Electrolytic Remediation of Chromated Copper Arsenate Wastes

by
Heather A. G. Stern

B.S. Engineering
Swarthmore College, 2000

M.S. Chemical Engineering Practice
Massachusetts Institute of Technology, 2002

Submitted to the Department of Chemical Engineering
in partial fulfillment of the requirements for the degree of

DOCTOR OF PHILOSOPHY IN CHEMICAL ENGINEERING

at the

MASSACHUSETTS INSTITUTE OF TECHNOLOGY

May, 2006

Signature of Author:_____
Department of Chemical Engineering
May 15, 2006

Certified by:_____
Professor Donald R. Sadoway
Thesis Supervisor

Certified by:_____
Professor Jefferson W. Tester
Thesis Supervisor

Accepted by:_____
Professor William M. Deen
Professor of Chemical Engineering
Chairman, Committee for Graduate Students

Electrolytic Remediation of Chromated Copper Arsenate Wastes

By Heather A. G. Stern

Submitted to the Department of Chemical Engineering on May 15, 2006 in partial fulfillment of the requirements of the Degree of Doctor of Philosophy in Chemical Engineering.

ABSTRACT

While chromated copper arsenate (CCA) has proven to be exceptionally effective in protecting wood from rot and infestation, its toxic nature has led to the problem of disposal of CCA-treated lumber and remediation of waters and soils contaminated by process wastes. The active ions in water-based CCA are hexavalent chromium, divalent copper, and pentavalent arsenic. The objective of this study was to develop the underlying engineering science for remediation of aqueous CCA wastes via electrolytic deposition of neutral arsenic, chromium, and copper in order to evaluate the technical feasibility of this process. The specific approach focused on electrochemical stability analysis of the metals; development and testing of a copper sulfate reference electrode (CSE); electrolytic deposition of arsenic, chromium, and copper from model aqueous CCA wastes; and characterization of the resulting deposits.

The electrochemical stability analysis of the individual components, As, Cr, and Cu, in an aqueous system was used to determined the most thermodynamically stable forms of the metals as a function of pH and electrochemical potential. This analysis predicted that under the conditions of codeposition of all three metals, hydrogen and arsine would also be produced.

A robust and accurate CSE was designed, constructed, developed and used as a reference electrode for the electrolytic deposition experiments in this study. The potential of the CSE as a function of temperature over the range of 5 to 45 °C was measured and related to the normal hydrogen electrode potential (317 mV at 25°C, slope of 0.17 mV/°C).

Electrolytic deposition was performed using working and reference electrodes specially designed and fabricated for this study. Despite the results of the electrochemical stability analysis, conditions were found experimentally where arsenic, chromium, and copper were deposited from model aqueous CCA type-C solutions over a range of concentrations without the formation of arsine or hydrogen. Three different types of deposits were observed. One type contained a ratio of metal concentrations similar to that of CCA type-C and is a good candidate for use in CCA remediation and recycling processes. This study indicated that CCA remediation via electrolytic deposition is probably feasible from an engineering perspective.

Thesis supervisors:

Jefferson W. Tester
H.P. Meissner Professor of Chemical Engineering

Donald R. Sadoway
John F. Elliott Professor of Materials Chemistry
Department of Materials Science and Engineering

Acknowledgements

I would like to thank my advisors, Jeff Tester and Don Sadoway, for all of their hard work and understanding throughout my years at MIT. They always pushed me to try to find the answers to the difficult questions. Prof. Tester went beyond his role as academic advisor and on to that of life advisor during the annual bike and ski trips that he organized for the lab group. Prof. Sadoway never seems to want to stop teaching, even during dinner parties at his house he gathers a crowd to explain the physics behind his special coffee maker.

Gwen Wilcox is the glue that holds the Tester lab together. She knows how MIT works and how to get things done. I value both her management and story telling skills.

My time at MIT has been greatly enriched both intellectually and socially by my fellow lab members. I was lucky to be a member of two wonderful lab groups. The Tester group: A.J. Allen, Brian Anderson, Chad Augustine, Rocco Ciccolini, Kurt Frey, Morgan Fröling, Murray Height, Russ Lachance, Lai Yeng Lee, Scott Paap, Andy Peterson, Jason Ploeger, Jin Qian, Patty Sullivan, Joany Tarud, Mike Timko, Paul Yelvington; and the Sadoway group: Ken Avery, Simon Mui, Elsa Olivetti, Aislinn Sirk, Patrick Trapa, I would like to acknowledge the hard work and dedication of Michael Mock, Talia Gershon, and Christopher Post who worked with me through the MIT undergraduate research opportunity program.

Funding for this work was provided by the Martin Family of Fellows for Sustainability fellowship, the Army Research Office, the Singapore-MIT Alliance, and the Malaysia University of Science and Technology.

I would like to thank Hong He and Jianyi Cui of the Ying group for training me on and allowing me to use their XRD machine. SEM EDAX analysis would not have been possible without the training provided by Patrick Boisvert of the MIT Center for Materials Science and Engineering (CMSE). Similarly, I would like to thank Elizabeth Shaw of CMSE for her XPS analysis of my difficult samples.

In particular, I would like to acknowledge the love and support of my family who helped me get to MIT in the first place and to be happy once I was here. And last, but not least, I would like to recognize Nick Ortiz, who helped to calm me down when I was stressed and generally got me through my PhD. Thank you Nick for all of your encouragement and love.

Table of Contents

1 Introduction 9
1.1 Background 9
1.1.1 Chromated Copper Arsenate Characteristics and Disposal Methods 9
1.1.2 Electrolytic Deposition 15
1.1.3 Three-Electrode Cell 17
1.2 Objectives and Approach 19
1.3 References 20
2 Electrochemical Stability Analysis 22
2.1 Regions of Thermodynamically Favored Deposition 24
2.2 Conclusions 30
2.3 References 31
3 Copper - Copper Sulfate Reference Electrode 32
3.1 Previous Work 33
3.2 Solubility Measurements of Copper Sulfate 35
3.2.1 Calculations 36
3.2.2 Results 38
3.3 CSE Experimental Setup and Procedures 40
3.3.1 Dissolved Oxygen 41
3.3.2 Potential as a Function of Temperature 41
3.4 Experimental Results and Discussion 45
3.4.1 Dissolved Oxygen 46
3.4.2 Potential as a Function of Temperature 46
3.5 Electrolyte Physical Property Modeling 49
3.6 Conclusions 63
3.7 References 64
4 Deposition Experimental Setup and Procedures 66
4.1 Deposition Cells 66
4.1.1 Reaction Kettle Deposition Cell 67
4.1.2 Flask Deposition Cell 68
4.2 Electrodes 69
4.2.1 Solid Metal Working Electrode 69
4.2.2 Liquid Gallium Working Electrode 71
4.2.3 Counter Electrode 73
4.2.4 Reference Electrode 73
4.3 Arsine Collection and Analysis 75
4.4 Equilibrium Measurement Apparatus 76
4.5 Electrical Equipment and Control 77
4.6 Voltammetry Methods and Data Analysis 79
4.6.1 Direct Current – General Methodology 80
4.6.2 Direct Current – Applications to this Study 88
4.6.3 Alternating Current 91
4.7 Energy-Dispersive X-Ray with Scanning Electron Microscope 93
4.8 X-Ray Diffraction 95
4.9 X-Ray Photoelectron Spectroscopy 96

4.10 Conclusions 97
4.11 References 98
5 Single Component Solution Deposition Results and Discussion 100
5.1 Copper 100
5.1.1 Equilibrium Measurements 101
5.1.2 Kinetic Studies 104
5.2 Chromium 117
5.3 Arsenic 130
5.3.1 Solid Working Electrode 132
5.3.2 Liquid Gallium Working Electrode 138
5.4 Conclusions 142
5.5 References 143
6 Deposition from Multicomponent Solution: Results and Discussion 145
6.1 Copper and Chromium 145
6.2 Arsenic and Copper 146
6.3 Arsenic and Chromium 150
6.4 Arsenic, Copper, and Chromium 153
6.5 Conclusions 172
6.6 References 173
7 Assessment of Electrolytic CCA Remediation 174
8 Conclusions 177
8.1 Copper sulfate reference electrode 177
8.2 Electrochemical stability analysis 178
8.3 Electrolytic deposition 178
8.4 Practical implications for CCA remediation 180
8.5 References 180
9 Recommendations 181
9.1 Copper sulfate electrode modeling 181
9.2 Electrolytic deposition 182
9.3 Analysis of the deposits 182
10 Appendix 184
10.1 Symbols 184
10.2 Abbreviations 185
10.3 XRD Spectra 185
10.4 XPS Spectra 188

List of Figures

Figure 1-1: Electrolytic deposition of copper 16
Figure 1-2: Three-electrode cell 17
Figure 2-1: Water electrochemical stability diagram, 25°C 25
Figure 2-2: Copper electrochemical stability diagram, 25°C 26
Figure 2-3: Chromium electrochemical stability diagram, 25°C 27
Figure 2-4: Arsenic electrochemical stability diagram, 25°C 28
Figure 3-1: Solubility of copper sulfate in water as a function of temperature 39
Figure 3-2: Molality of copper sulfate at saturation condition as a function of sulfuric acid concentration and temperature 40
Figure 3-3: Copper sulfate reference electrode schematic 43
Figure 3-4: Plan view of copper sulfate reference electrode testing apparatus 44
Figure 3-5: Effect of sparging reaction kettle with argon on dissolved oxygen concentration 46
Figure 3-6: Potential of the copper sulfate electrode vs. the saturated calomel electrode as a function of temperature with linear fit 47
Figure 3-7: Potential of the copper sulfate electrode vs. the saturated calomel electrode as a function of temperature with second order regressed fit 47
Figure 3-8: Activity of Cu^{2+} as a function of temperature for the ELECNRTL model 55
Figure 3-9: Activity of Cu^{2+} as a function of temperature for experimental data, the ELECNRTL and the Meissner models 58
Figure 3-10: Calculated and experimental CSE potential 59
Figure 3-11: Percent deviation of model molality (M_{model}) from calculated molality (M_{calc}) as a function of position x 62
Figure 4-1: Plan view of flask deposition cell 69
Figure 4-2: Solid metal working electrode 70
Figure 4-3: Liquid gallium working electrode schematic 73
Figure 4-4: Copper sulfate reference electrode schematic 75
Figure 4-5: Gas bubbler system including chloroform solution bubblers 76
Figure 4-6: Potentiostat and equivalent cell with resistance and capacitance schematic 78
Figure 4-7: DC voltammetry cyclic linear potential sweep method 81
Figure 4-8: AC voltammetry traces for reversible and quasireversible system 92
Figure 5-1: Equilibrium potential of Cu – Cu^{2+}, at 25°C 103
Figure 5-2: Copper linear sweep voltammogram, 20 mV/s 105
Figure 5-3: Copper linear sweep voltammogram, 20 mV/s, expanded section 106
Figure 5-4: Effect of gold activation on copper deposition 108
Figure 5-5: Copper deposition on gold WE with varying scan rate 109
Figure 5-6: Peak current as a function of the square root of scan rate 110
Figure 5-7: Copper deposition onto copper working electrode 112
Figure 5-8: AC voltammograms for copper deposition, 100 Hz, 20 mV/s 114
Figure 5-9: AC voltammograms for copper deposition for a range of frequencies 115
Figure 5-10: Maximum cotan(ϕ) as a function of $\omega^{1/2}$ 116
Figure 5-11: Chromium deposition from 0.5 M CrO_3, 5 mM H_2SO_4 onto Cu WE 122
Figure 5-12: Magnified view of Cr deposition from 0.5 M CrO_3, 5 mM H_2SO_4 on Cu WE 122
Figure 5-13: Cr deposition from 0.25 M CrO_3, 2.5 mM H_2SO_4 on Cu WE 123
Figure 5-14: Cr deposition from 25 mM CrO_3, 0.25 mM H_2SO_4 on Gold WE 124

Figure 5-15: Cr deposition from 25 mM CrO_3, 0.25 mM H_2SO_4 on copper WE 125
Figure 5-16: Cr deposition from 25 mM CrO_3, 0.25 mM H_2SO_4 on 304 stainless steel WE 125
Figure 5-17: Chromium stability diagram for 0.25 mM CrO_3 126
Figure 5-18: Chromium stripping 127
Figure 5-19: Chromium deposition from 0.5 M $K_2Cr_2O_7$, 5 mM H_2SO_4 on copper WE 128
Figure 5-20: Chromium deposition from 60 mM $K_2Cr_2O_7$, 5 mM H_2SO_4 on copper WE 129
Figure 5-21: Arsenic deposition on gold WE 133
Figure 5-22: Arsenic deposition on copper WE 134
Figure 5-23: SEM GSE images of arsenic deposited on copper WE 135
Figure 5-24: Arsenic deposition on stainless steel WE 136
Figure 5-25: SEM GSE images of arsenic deposited on stainless steel WE 136
Figure 5-26: Arsenic deposition on solid gallium WE 137
Figure 5-27: Gallium striping from a solid gallium WE 138
Figure 5-28: Arsenic deposition from 5 mM As_2O_5, 61 mM H_2SO_4 on liquid gallium WE 140
Figure 5-29: Arsenic deposition from 41 mM As_2O_5, 61 mM H_2SO_4 on liquid gallium WE 141
Figure 5-30: SEM BSE image of arsenic deposited on liquid gallium WE 142
Figure 6-1: Copper deposition from a copper and chromium solution on a Cu WE 146
Figure 6-2: Copper and arsenic codeposition onto a liquid Ga WE 147
Figure 6-3: SEM GSE image of arsenic and copper deposit formed on liquid Ga WE 149
Figure 6-4: Arsenic and chromium codeposition onto a stainless steel WE 152
Figure 6-5: SEM images of arsenic and copper deposited on a stainless steel WE 153
Figure 6-6: Voltammograms for solution A on copper WE 156
Figure 6-7: Voltammograms for solution A on gold WE 157
Figure 6-8: Deposition on copper WE from solution C 158
Figure 6-9: SEMs of type two deposit on copper working electrode from solution C 159
Figure 6-10: Deposition on copper WE from solution B 160
Figure 6-11: BSE SEM of deposits on copper WE from solution B 161
Figure 6-12: Voltammograms for gold WE in solution C 162
Figure 6-13: Deposition on gold WE from solution C 163
Figure 6-14: BSE SEM of deposit on gold WE from solution C 163
Figure 6-15: Deposition on gold WE from solution B 164
Figure 6-16: BSE SEM of type two deposit on gold WE from solution B 165
Figure 6-17: Deposition on stainless steel WE from solution B 166
Figure 6-18: Deposition on clean stainless steel WE from solution C 167
Figure 6-19: Deposition on type one deposit on stainless steel WE from solution C 168
Figure 6-20: SEMs of type two deposit on stainless steel working electrode from solution C 169
Figure 6-21: Deposition on liquid gallium WE from solution B, higher switching potentials 170
Figure 6-22: Deposition on liquid gallium WE from solution B, lower switching potential 171
Figure 6-23: BSE SEM image of type one deposited on liquid gallium WE 171

List of Tables

Table 3-1: Saturated copper sulfate density 38
Table 3-2: Average measured potential 49
Table 3-3: Species mobilities 52
Table 3-4: Model conditions for ELECNRTL model 55
Table 3-5: Comparison of the trendline parameters for E_{CSE} 59
Table 5-1: Chromium species in solution as a function of concentration 118
Table 5-2: Chromium deposition and stripping peak potentials 130
Table 6-1: Concentration of solutions for arsenic, copper, and chromium codeposition 153
Table 7-1: Concentration of solutions for arsenic, copper, and chromium codeposition 174
Table 7-2: Atom percent of As, Cr, and Cu in CCA type-C and the three deposit types 175
Table 8-1: Concentration of solutions for arsenic, copper, and chromium codeposition 179
Table 8-2: Atom percent of As, Cr, and Cu in CCA type-C and the three deposit types 179

1 Introduction

1.1 Background

1.1.1 Chromated Copper Arsenate Characteristics and Disposal Methods

Chromated copper arsenate (CCA) has been the most commonly used inorganic, waterborne wood preservative since at least the 1970s (Thompson 1991; Preston 2000). It is employed to protect wood from rot and infestation, particularly in outdoor applications, and is one of the most cost-effective treatment options. In North America 70-85,000 tons of CCA are used annually to treat approximately 6-7 billion board feet of lumber, and other wood products (Preston 2000). The active ions in water-based CCA are hexavalent chromium, divalent copper, and pentavalent arsenic. The copper acts as a fungicide and the arsenic protects the wood from insect attack. The chromium serves to fix the copper and arsenic in the wood matrix by complexing with the lignin in the wood.

The CCA pressure treatment process consists of filling a long cylindrical pressure cell with dry, debarked wood and CCA treatment solution. CCA treatment solutions are highly acidic (pH 1.5 to 2.5) and pressurized (862 to 1,207 kPa is the commonly used range) to enhance penetration into the wood fiber matrix. The operating pressure and exposure times are dependent on the species and thickness of the lumber being treated. The duration of the treatment process usually ranges from one to six hours (Humphrey 2002). After treatment, a vacuum is applied to the cell to remove excess CCA solution from the surface of the lumber, and the CCA-treated lumber is allowed to drip dry before being shipped to consumers. The CCA fixation process continues while the lumber is drying. Retention levels of CCA vary from 0.25 to 2.50 lb/ft^3, resulting in a gray-green hue. CCA-treated lumber is considered to be leach-resistant during its

useful lifetime and is commonly used anywhere from the interior portion of a structure to saltwater immersion (American Wood-Preservers' Association 2001).

CCA reacts with and is fixed to the wood during the pressure treatment process through a variety of reactions. Chromium (VI) complexes with lignin and is then reduced to Cr(III). Copper reacts with wood by ion exchange and then participates in a series of condensation reactions to form copper arsenate, copper chromium, and possibly copper chromium arsenate complexes. These complexes are associated with wood components through coordination or covalent complexes, and others are fixed by insolubilization within the wood structure. The pH of the solution within the wood pores rises to about 5.5 by the end of the reactions (Thompson 1991). The final equilibrium products are Cu fixed by ion exchange, chrome arsenate ($Cr(III)AsO_4$), basic copper arsenate ($Cu(OH)CuAsO_4$), chrome hydroxide ($Cr(III)(OH)_3$), and trace amounts of copper chromium ($CuCr(VI)O_4$).

CCA type C is the most commonly used formulation of CCA and accounts for about 90% of CCA sales worldwide. It consists of a mixture by weight of the following: chromium trioxide (CrO_3, 47.5%), cupric oxide (CuO, 18.5%), and arsenic pentoxide (As_2O_5, 34.0%). Converting the oxide percents of CCA type C into an elemental molar basis reveals that arsenic is present in the largest molar concentration: 33.8% chromium, 10.5% copper, 55.7% arsenic. The active ingredients can be added in the form of potassium or sodium dichromate ($K_2/Na_2Cr_2O_7$), chromium trioxide, copper sulphate ($CuSO_4$), basic copper carbonate ($CuCO_3.Cu(OH)_2$), cupric oxide or hydroxide, arsenic pentoxide, arsenic acid (AsH_3O_4), sodium arsenate ($AsHNa_2O_4$), or pyroarsenate ($H_4As_2O_7$). The most common formulation of the liquid concentrated CCA is CrO_3, CuO, and AsH_3O_4, in large part because the components have high solubility and a lower molecular weight than their salt counterparts. All of the compounds used in the CCA

formulation must be at least 95% pure on an anhydrous basis (American Wood-Preservers' Association 2001).

While CCA has proven to be exceptionally effective in protecting wood from rot and infestation, its toxic nature has led to the problem of disposal of CCA-treated lumber and remediation of waters and soils contaminated by process wastes. All three heavy metals are classified as toxic release inventory chemicals and their discharge is therefore monitored and regulated by the US EPA. Arsenic is ranked in the top ten percent of the most hazardous compounds to human health. It is a recognized carcinogen and developmental toxicant (Agency for Toxic Substances and Disease Registry 2000). Hexavalent chromium has been classified by the International Agency for Research on Cancer as being carcinogenic to humans (International Agency for Research on Cancer 1990). Long term exposure to copper can cause kidney and liver damage (U.S. Environmental Protection Agency 2006).

Although CCA-treated wood *per se* is not overly toxic if left in an undisturbed natural state for about the first 30 years of its life, old CCA-treated wood, incineration of waste CCA treated wood, or CCA-contaminated soils and waters at active and abandoned wood preservation factories pose severe environmental hazards. Approximately 1100 tons of CCA wastes are generated directly from wood pressure-treating in North America each year, but the actual amount of waste generated may be far higher than reported. One expects the amount of CCA in these solid and liquid wastes to range from 18 to 94% by weight with arsenic compounds accounting for as much as half of the total (Kazi and Cooper 2002). An additional source of CCA-containing waste is approximately 2.5 billion board feet per year (6 million m^3/yr) of discarded and construction waste CCA-treated wood that enters the industrial and municipal solid waste stream (Wilson 1997). An order of magnitude analysis suggests that the CCA-

treated wood discarded each year contains at least 10 thousand tons each of arsenic, chromium, and copper valued at over $100 million (Florida Center for Solid and Hazardous Waste Management 2002). Since CCA-treated wood has a service life of approximately 30 years, the wood industry's self-regulated departure from using CCA-treated lumber for non-industrial uses as of December 2003 will not significantly affect the volume of waste CCA-treated wood for a long time (U.S. Environmental Protection Agency 2002).

There are strict federal and state regulations for the disposal of the contaminants in CCA and for the level of these contaminants in drinking water. For the application of solid waste to land, such as CCA-treated wood chips for mulch, the limit is 75 ppm As and 4300 ppm Cu (Cr is not listed) (1995). The standard for wood-preserving industries that introduce process wastewater pollutants into a publicly owned treatment works is a maximum of 4 ppm arsenic, 4 ppm chromium, and 5 ppm copper (1981). The drinking water standards are more stringent, with maximum enforceable levels of 0.010 ppm As, 0.1 ppm Cr, and 1.3 ppm Cu (2002).

CCA wastes can be divided into several categories: construction waste and used CCA-treated lumber; CCA-contaminated surface and groundwater and CCA aqueous wastes generated by the CCA pressure-treating industry; industrial wood preservative sludge; and CCA-contaminated soils. Far more difficult to remediate than point-source CCA wastes are CCA-contaminated soils and ground- and surface waters at abandoned wood preservation factory sites. Many of these sites pose such a severe environmental hazard that they are often designated as Superfund sites. Remediation of each type of CCA waste is often accomplished using a separate treatment method.

Conventional wastewater treatment techniques are commonly employed to treat aqueous CCA wastes. These techniques include, but are not limited to, coagulation and filtration,

adsorption, ion exchange, membrane processes, and electrodialysis reversal (U.S. Environmental Protection Agency 1993; Office of Ground Water and Drinking Water 2000). These CCA treatment methods are often rudimentary and do not concentrate on recovering the arsenic, chromium, and copper in a reusable form. They thus produce large quantities of secondary wastes that must be treated or securely isolated. The processes are, however, effective at producing clean water (< 3 micrograms of metal per liter for many of the processes).

Removal of more than just small amounts of soil from the ground and transportation to a treatment facility is prohibitively expensive. Therefore, *in situ* immobilization is the preferred approach. The EPA-recommended immobilization remedies for CCA-contaminated soil include the use of lime and concrete, do not remove the arsenic or chromium from the soil (final permeability of the contaminants is $<1x10^{-7}$ m/s), and render the land unsuitable for further use (Office of Solid Waste and Emergency Response 1993). As a part of the *in situ* remediation process, physical barriers may be used to help prevent the spread of the contaminates to the adjacent soil and ground water. More recently-developed technologies, such as *in situ* washing or flushing of the soil and electroremediation, can achieve significant *in situ* metal removal from waters and soils depending on the soil conditions. Water solubility of the contaminants is the controlling removal mechanism and additives are often used to enhance removal efficiencies (Mulligan 2001). In electroremediation processes, direct current is applied through the soil between appropriately distributed electrodes. The charged contaminants are transported through the soil and concentrated in the soil near the electrodes due to electro-osmosis, electromigration and diffusion. The soil adjacent to the electrodes is then collected for further treatment (Page and Page 2002). Bioremediaton methods are under development and, in the case of uptake of the metals by surface plants, are often most appropriate for treatment of surface soils. The plants are

then collected and disposed of by such methods as incineration, gasification, pyrolysis, and acid extractions (Mulligan 2001). While some of these methods can be effective at removing waste from soil, a secondary process to recover and recycle the arsenic, chromium, and copper is lacking.

The only currently available option for the disposal of CCA-treated lumber is disposal in a lined landfill since incineration will produce toxic vapors and hazardous ash (if the wood waste contains 5% or greater CCA-treated wood). There are a variety of remediation technologies for CCA-treated wood, waste sludges, and ashes from the incineration of CCA-treated lumber, such as acid leaching and biological processes in the early development stages that have met with moderate success (Wilson 1997; Kazi and Cooper 2002; Velizarova 2002). Acid leaching treatment can be followed by the emerging technique of electrodialytic removal of Cu, Cr, and As. The electrodialytic remediation works on a principle similar to electroremediation of soils and can be used for acid-treated CCA-contaminated wood and CCA-contaminated soils (Ottosen 1997; Ribeiro 2000). It consists of a central compartment containing the contaminants, a cathode in a chamber separated from the central compartment by a cation-exchange membrane, and an anode in a chamber separated by an anion-exchange membrane. When current is passed through the cell, the negatively charged contaminants are concentrated in the anolyte and the positively charge contaminants are concentrated in the catholyte. While it effectively removes As, Cr, and Cu from CCA-contaminated substances and concentrates them in aqueous solutions, it is only the first step in producing As, Cr, and Cu in a form that can be reused in a wide variety of processes.

A remediation method that could take the secondary wastes produced by the treatment of CCA-contaminated waters, soils, and lumber and recycle the As, Cr, and Cu to recover their potentially large economic value (<$100 million/yr) would provide a more sustainable and cost-

effective solution for the complete remediation of CCA-contaminated wastes. The ideal method would be able to remove As, Cr, and Cu from either a solid or liquid waste matrix and shift the valences of the ion to their neutral metal/semi-metal state. Our approach for accomplishing this type of remediation and recovery involves electrolytic deposition of the As, Cr, and Cu from an aqueous solution since the process of electrolytic deposition plates out an ion from a solution onto an electrode by affecting a valence shift. Given the complex nature of this system, it is necessary to first develop the underlying engineering science of electrolytic deposition of As, Cr, and Cu by modeling and experimentally investigating their deposition behavior in aqueous media before designing a remediation technique. If the remediation technique is successful for CCA wastes, it may also be applicable to other wastes containing metals such as cadmium, lead, nickel, and zinc.

1.1.2 Electrolytic Deposition

In the electrolytic deposition process an external power source applies a potential (E_{apl}) to an electrochemically active system to force the deposition of a substance on an electrode. In the case of a positively charged metal ion, M^{n+}, the ion combines with n electrons at the cathode and is reduced to neutral metal, M.

$$M^{n+} + ne^- \rightarrow M \tag{1-1}$$

The current in the system flows out of the power source, into the anode, through the solution carried by ions, into the cathode, and back into the power source to complete the current loop. Figure 1-1 shows a copper deposition system. One reaction that allows the current to pass from the anode into the solution is the oxidation of OH^- to oxygen.

$$\text{Cathodic reaction:} \quad Cu^{2+}(aq) + 2e^- \rightarrow Cu(s) \tag{1-2}$$

$$\text{Anodic reaction:} \quad 2OH^- \rightarrow O_2(g) + 2H^+(aq) + 2e^- \tag{1-3}$$

The deposited copper forms a conductive layer on the cathode and grows thicker as the deposition process continues. If the deposited species were poorly conductive, such as arsenic, the thickness of the deposited layer would be limited by its ability to conduct current from the cathode to the newly formed solution interface.

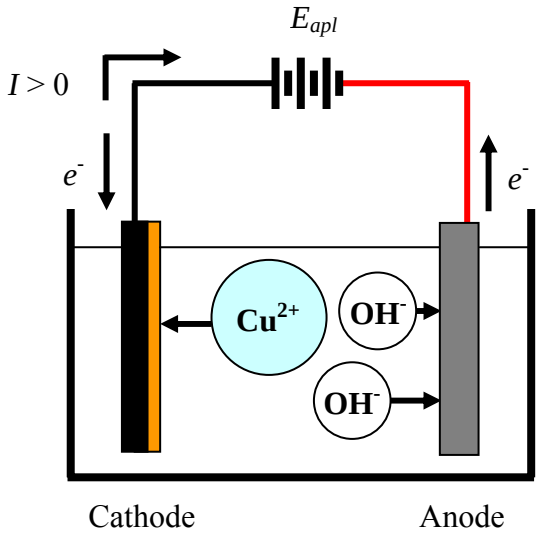

Figure 1-1: Electrolytic deposition of copper

The electrodes and the conductive solutions compose what is known as the electrochemical cell. Each electrode/electrolyte combination is considered to be a half-cell. Under open-circuit conditions (in the limit of zero current), the cell voltage is the difference in potential between the anode potential and the cathode potential.

When current flows through the system, it is no longer in electrochemical equilibrium. The potential that the external power source applies to the deposition system is always greater than the potential difference across the deposition solution since there are resistive and capacitive losses throughout the system. Some of the losses are due to the resistance of the solution, the electrodes, and the wire connectors and the capacitance of the electrode-electrolyte interfaces where there is a double layer of oppositely charged species.

1.1.3 Three-Electrode Cell

While only two electrodes are necessary to perform electrolytic deposition, the addition of a third electrode allows for the more accurate measurement of the potential of a single electrode when current flows through the cell. A standard three-electrode cell consists of a working electrode (WE), a reference electrode (RE), and a counter electrode (CE), as shown in Figure 1-2. A computer-controlled potentiostat provides the power and measures the potential and current of the cell. The potentiostat can be programmed to control a wide range of experiments such as constant potential, constant current, and the potential or current as a particular function of time.

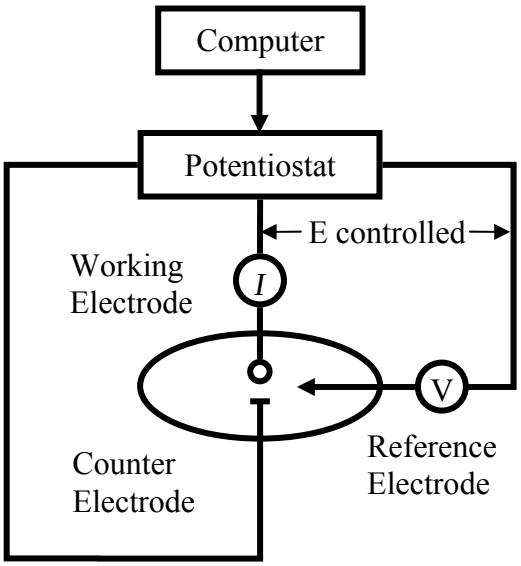

Figure 1-2: Three-electrode cell

The working electrode is where the reaction of interest occurs; for electrolytic deposition of a metal it is the cathode. The potential of the system is measured as a difference between the working electrode and the reference electrode with the reference electrode taken as a zero potential baseline. The reference electrode consists of a stable electrochemical couple. To compare the measured potential to values reported in the literature, it is necessary to know the potential of the reference electrode compared to the standard reference electrode – the normal

hydrogen electrode (NHE) - which is defined as zero for all temperatures. The most commonly employed reference electrodes are the NHE, the saturated calomel electrode (SCE), and the silver-silver chloride (Ag/AgCl) electrode. To help ensure a stable electrochemical reference potential, the current through the reference electrode is controlled so that it is almost zero. The bulk of the current is passed through the counter electrode to the working electrode. The potential on the counter electrode is allowed to float to a value that yields enough current for the electrochemical reaction to proceed on the working electrode. It is important that the current passing through the counter electrode is not the rate determining step in the current flow. The counter electrode, therefore, usually has a larger surface area than the working electrode and in aqueous systems is often made of pure platinum. The reaction on the counter electrode is not important as long as the products from this reaction do not interfere with the reactions occurring on the other electrodes. When this interference is a problem, the counter electrode can be separated from the other electrodes by a semi-permeable membrane.

In this study, a three-electrode cell was used to probe the deposition of copper, chromium, and arsenic. The reference electrode was connected to the deposition solution via a porous glass frit. The deposition solutions were composed of water, sulfuric acid, and copper, chromium, and arsenic ions. The choice of the reference electrode for a solution is often driven by ease of use, prevention of contamination of the deposition solution by the reference electrode solution, and minimization of the liquid junction potential between the reference electrode and the deposition solution. The liquid junction potential is the potential due to the passage of current between two different solutions. The normal hydrogen electrode can be difficult to use because it requires hydrogen gas. The calomel and silver-silver chloride electrodes both contain chloride that can complex with metals and thereby change the deposition potential of the metal.

The ramifications of the liquid junction potential are explored in chapter 3. One way to minimize the liquid junction potential is to match the components in the reference solution to the deposition solution components as closely as possible. The electrolyte in a copper-copper sulfate electrode (CSE) is the closest match to the composition of the deposition solution of the available reference electrodes. It contains copper, copper sulfate, and sometimes sulfuric acid, all of which are in the deposition solution. The problem with using the CSE is that its potential has not been as carefully characterized as the standard reference electrodes. Part of this study consisted of characterizing the CSE as a function of temperature (5 to 45°C) relative to known standard electrodes in order to be able to use the electrode as the reference in deposition studies.

1.2 Objectives and Approach

The overall aim of this study was to develop the underlying engineering science to enable the effective design of processes for removing and recovering elemental species (copper, chromium, and arsenic) from chromated copper arsenate (CCA) wastes.

This study combined experiments with theoretical modeling to explore deposition conditions for pentavalent arsenic, divalent copper, and hexavalent chromium from aqueous sulfuric acid solutions. The approach consisted of six separate tasks.

(1) *Prediction of the deposition behavior of arsenic, copper, and chromium.* Before deposition experiments were designed and performed, the thermodynamic stability landscape of arsenic, copper, and chromium was mapped and used to identify the optimal deposition conditions.

(2) *Characterization of copper-copper sulfate electrode behavior*. Measured the potential of the CSE as a function of temperature (5 to 45°C). Modeled the CSE electrolyte solution to predict the CSE potential and the liquid junction potential.

(3) *Design and construction of deposition apparatus.* A three-electrode system was fabricated to probe arsenic, chromium, and copper reduction processes. The electrodes were specially made for the deposition system.

(4) *Electrodeposition of elements from solution.* Deposition of pentavalent arsenic, divalent copper, and hexavalent chromium from single component systems was first characterized to understand the behavior of the individual components. Next, multicomponent solutions over a range of concentrations, with the components in the same ratio as CCA type C treatment solution, were studied to determine the effect of co-deposition on each component. A variety of solid and liquid metal working electrodes were employed to explore the influence of the working electrode material on deposition behavior.

(5) *Characterization of deposition products.* The composition of the deposited material was determined with X-ray diffraction and energy-dispersive X-ray with scanning electron microscope.

(6) *Evaluation of deposition results.* The results of the deposition experiments were analyzed to determine if conditions exist where arsenic, copper, and chromium can safely be removed from solution via electrolytic deposition.

1.3 References

(1981). 40 Code of Federal Regulations. Timber Products Processing Point Source Category - Subpart H - Wood Preserving - Pretreatment standards for existing sources. **429.95**.

(1995). 40 Code of Federal Regulations. Standards for the use or disposal of sewage sludge, Subpart B-Land application. **503.13**.

(2002). 40 Code of Federal Regulations. National primary drinking water regulations. **141.51:** 425.

Agency for Toxic Substances and Disease Registry (2000). Public Health Statement for Arsenic, ASTDR Information Center. **2002**.

American Wood-Preservers' Association (2001). Book of Standards. Granbury, TX, American Wood-Preservers' Association.

Florida Center for Solid and Hazardous Waste Management (2002). Metal Concentrations in CCA-Treated Wood and Wood Ash. **2003**.

Humphrey, D. G. (2002). "The chemistry of chromated copper arsenate wood preservatives." Reviews in Inorganic Chemistry **22**(1): 1-40.

International Agency for Research on Cancer (1990). IARC Monographs on the Evaluation of Carcinogenic Risks to Humans: Chromium, Nickel and Welding. Lyon, France, International Agency for Research on Cancer Press.

Kazi, F. K. M. and P. A. Cooper (2002). "Rapid-extraction oxidation process to recover and reuse copper chromium and arsenic from industrial wood preservative sludge." Waste Management **22**: 293-301.

Mulligan, C. N., R. N. Yong and B. F. Gibbs (2001). "Remediation technologies for metal-contaminated soils and groundwater: an evaluation." Engineering Geology **60**: 193-207.

Office of Ground Water and Drinking Water (2000). Technologies and Costs for Removal of Arsenic from Drinking Water. Washington, D.C., United States Environmental Protection Agency.

Office of Solid Waste and Emergency Response (1993). Presumptive Remedies: Technology Selection Guide for Wood Treater Sites. Washington, D.C., United States Environmental Protection Agency**:** 8.

Ottosen, L. M., H. K. Hansen, S. Laursen and A. Villumsen (1997). "Electrodialytic Remediation of Soil Polluted with Copper from Wood Preservation Industry." Environmental Science Technology **31**: 1711-1715.

Page, M. M. and C. L. Page (2002). "Electroremediation of Contaminated Soils." Journal of Environmental Engineering **128**(3): 208-219.

Preston, A. F. (2000). "Wood Preservation: Trends of today that will influence the industry tomorrow." Forest Products Journal **50**(9): 12-19.

Ribeiro, A. B., E. P. Mateus, L. M. Ottosen and G. Bech-Nielsen (2000). "Electrodialytic Removal of Cu, Cr, and As from Chromated Copper Arsenate-Treated Timber Waste." Environmental Science Technology **34**: 784-788.

Thompson, R., Ed. (1991). The Chemistry of Wood Preservation. Cambridge, The Royal Society of Chemistry.

U.S. Environmental Protection Agency, Ed. (1993). Mercury and Arsenic Wastes: Removal, Recovery, Treatment, and Disposal. Park Ridge, NJ, Noyes Data Corporation.

U.S. Environmental Protection Agency (2002). Whitman Announces Transition from Consumer Use of Treated Wood Containing Arsenic. **2003**.

U.S. Environmental Protection Agency (2006). List of Drinking Water Contaminants & MCLs. **2006**.

Velizarova, E., A. B. Ribeiro and L. M. Ottosen (2002). "A comparative study on Cu, Cr and As removal from CCA-treated wood waste by dialytic and electrodialytic processes." Journal of Hazardous Materials **B94**: 147-160.

Wilson, A. (1997). "Disposal: The Achilles' Heel of CCA-Treated Wood." Environmental Building News **6**(3).

2 Electrochemical Stability Analysis

Electrochemical stability analysis permits estimation of the thermodynamically stable phases and compounds, as a function of the pH of the solution and electrochemical potential (*E*), that would be present in an electrochemical reacting system at or near equilibrium conditions. This analysis gives important information about limiting states but contains no kinetic information. The results of the analysis are presented in electrochemical stability diagrams, where the most thermodynamically stable species is designated in the space defined by pH and potential of the system.

For the analysis done here, it is assumed that all solutions are aqueous; the temperature, pressure, and total amount of the component of interest (e.g. As, Cu, Cr) are fixed; even though a solid compound may be the predominant phase, it is in equilibrium with the aqueous and gaseous phase; the aqueous phase is in equilibrium with the gaseous phase; the non-predominant phases contain a smaller percentage of the species of interest than the predominant phase. To simplify the diagrams shown in this work, only the predominant phase is indicated.

The objective of electrochemical stability analysis in this work is to determine the conditions under which solid arsenic, copper, and chromium could be formed. The initial conditions are an aqueous solution of pentavalent arsenic, divalent copper, and hexavalent chromium at atmospheric pressure and room temperature. Electrochemistry stability analysis was used to determine the proper range of pH for the solution to avoid oxide formation, the required electrochemical potential for formation of the desired solids, and the expected byproducts at those conditions. Multi-species diagrams are not shown because only one multi-metal species – Cu_3As – was found using the E-pH module of the HSC5 program (Haung 1999) and these diagrams are difficult to decipher.

The first step in constructing an electrochemical stability diagram is to determine which species will be included. Choices are often based on experimental data and chemical intuition. Next the electrochemical potentials - as a function of pH and species concentration - for the relevant reactions are determined from experimental data and thermodynamic modeling. At equilibrium, the electrochemical potential of a single reaction (E) can be related to its standard state potential (fixed T, P, total concentration of each element) (E^0) and the activities of the reactive species (a_i) through the Nernst equation.

$$E = E^0 - \frac{RT}{nF} \ln \prod a_i^{\nu_i}$$

where R = universal gas constant, T = temperature (K), (2-1)
n = number of electrons,
ν_i = stoichiometric coefficient of species i in the electrochemical reaction

The activity of a species is related to the concentration (c_i) through an activity coefficient (γ_i) as shown in equation 2-2 that is referred to an infinite-dilution state at T and P of the mixture. In the limit of infinite dilution, the activity coefficient goes to one and the activity is equal to the concentration.

$$a_i = \gamma_i c_i \tag{2-2}$$

The electrochemical potential of the reaction can be related to the change in Gibbs free energy for the reaction (ΔG) through equation 2-3.

$$\Delta G = -nFE \tag{2-3}$$

There are two common ways to construct stability diagrams. Before the widespread availability of personal computers, the electrochemical potential equations for the reaction system were solved at a given component of interest concentration as a function of pH and electrochemical potential to determine the predominate species. The current method for constructing a stability diagram is to divide the pH and potential region into a finely spaced grid

and solve for the species concentrations that yield the minimum Gibbs free energy of the system at each point on the grid. Points with the same solution makeup are then grouped together into regions and the stability diagram lines are drawn at the border of these regions. Additionally, the predominant aqueous species for all conditions may be calculated. For a good primer on electrochemical stability diagrams, also known as Pourbaix diagrams, see Pourbaix (1974) and Guy (1962).

2.1 Regions of Thermodynamically Favored Deposition

All electrochemical stability diagrams in this chapter were based on the equations in Pourbaix (1974) and drawn using graphing software. For all diagrams the conditions are 25°C, 1 atm, a total concentration of $1x10^{-6}$ mol of active species distributed between the gas, liquid, and solid phases (Cu/Cr/As) in an aqueous environment. The bold lines indicate the boundary of a solid species, normal weight lines indicate the boundary of two dissolved species, and the dashed lines are the water stability lines shown on all stability diagrams. Figure 2-1 shows only the water stability lines, A and B, which are defined in equation 2-4.

$$\begin{aligned} &\text{line A: } \mathrm{H^+(aq)} + 2e^- \leftrightarrow \mathrm{H_2(g)} \\ &\qquad E_{\mathrm{H^+/H_2}} = -0.059\mathrm{pH} \\ &\text{line B: } \mathrm{O_2(g)} + 4\mathrm{H^+(aq)} + 4e^- \leftrightarrow 2\mathrm{H_2O(l)} \\ &\qquad E_{\mathrm{O_2/H_2O}} = 1.229 - 0.059\mathrm{pH} \end{aligned} \tag{2-4}$$

On all stability diagrams, the species shown in bold are solid, those in standard type are aqueous, and those italicized are gaseous. To simplify the diagrams, only the oxidation state of the dissolved species is indicated instead of the actual species. The electrochemical potential, *E* plotted on the y-axis, is in reference to the normal hydrogen electrode (NHE) which has a value of zero for all temperatures.

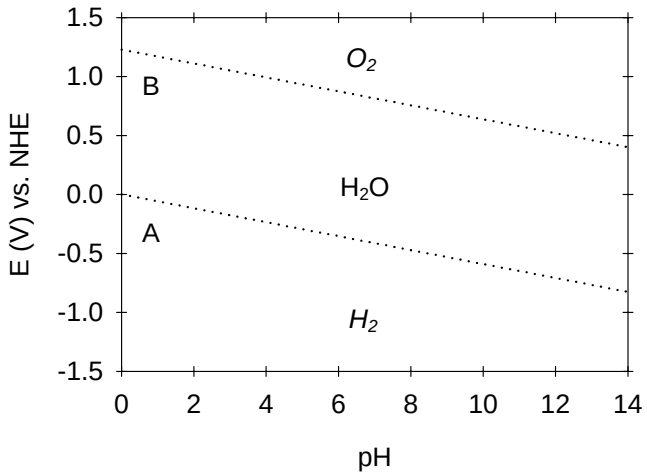

Figure 2-1: Water electrochemical stability diagram, 25°C
(Pourbaix 1974)

According to the copper electrochemical stability diagram given in Figure 2-2, copper metal deposition at $1x10^{-6}$ mol Cu in an acidic solution will occur at 0.17 V vs. NHE. The pH range for Cu deposition is wide, <5.5 pH. For deposition, the initial solution concentration will be greater than $1x10^{-6}$ mol Cu. At higher copper concentrations, the area of stability of the aqueous divalent copper is smaller in all directions. For example, if a concentration of 1 molal Cu with an activity coefficient of 1 is assumed, then the boundary of aqueous divalent copper and CuO shifts to 3.9 pH and the lowest pH edge of the Cu_2O region shifts to 2.2 pH. The potential boundary between Cu(II) and Cu metal increases to 0.34V. Since 0.17V is still within the Cu range, it is an acceptable potential for deposition. At 25°C the operating conditions for copper deposition from a concentrated to a dilute solution should be a solution pH < 2.2 and a potential < 0.17 V vs. NHE.

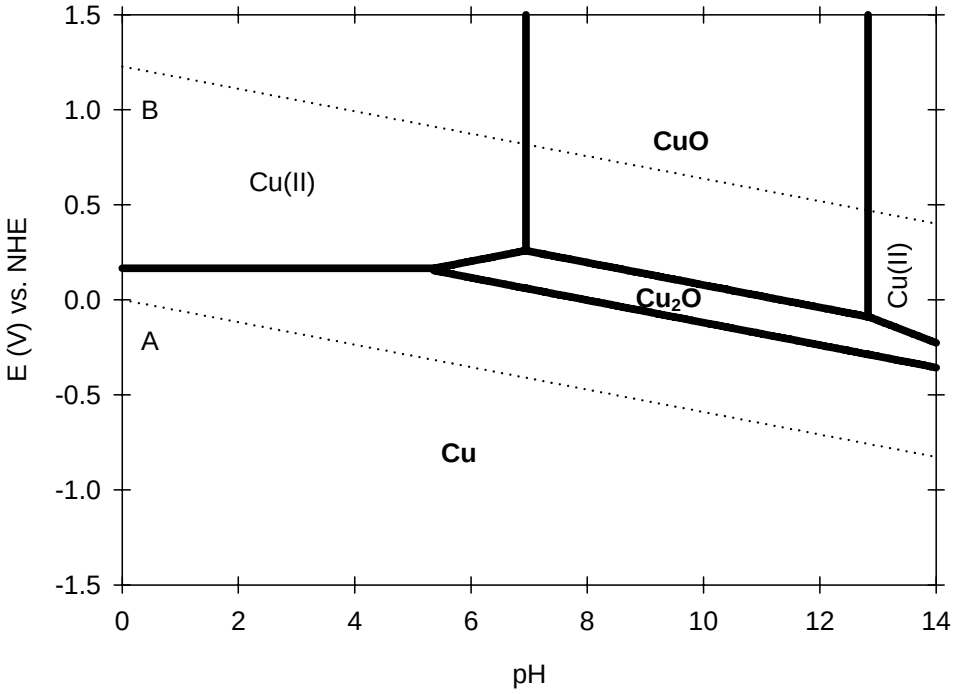

Figure 2-2: Copper electrochemical stability diagram, 25°C
(Pourbaix 1974)

The chromium electrochemical stability diagram is similar to the copper diagram in that it has a area of oxide at neutral and basic pH with a stable base metal at negative potentials. Chromium however has several stable oxide states, as is shown in Figure 2-3. To deposit chromium from a $1x10^{-6}$ mol hexavalent chromium solution, a potential of -1.1 V vs. NHE is necessary. The overall efficiency, defined as the percent of the total current that is used to drive the reaction of interest, is decreased because hydrogen is produced under the same conditions as that for base metal chromium deposition. If the initial solution condition is 1 molal Cr with an assumed activity coefficient of 1, then the Cr(III) and Cr_2O_3 boundary shifts to 2.1 pH. The conditions for Cr deposition from a concentrated solution down to a dilute solution; therefore, are a pH < 2.1 and a potential < -1.1 V vs. NHE, which are similar to the range for copper deposition. A comparison of the stability diagrams for Cu (Figure 2-2) and for Cr (Figure 2-3) shows that Cu and Cr could be deposited under the same conditions.

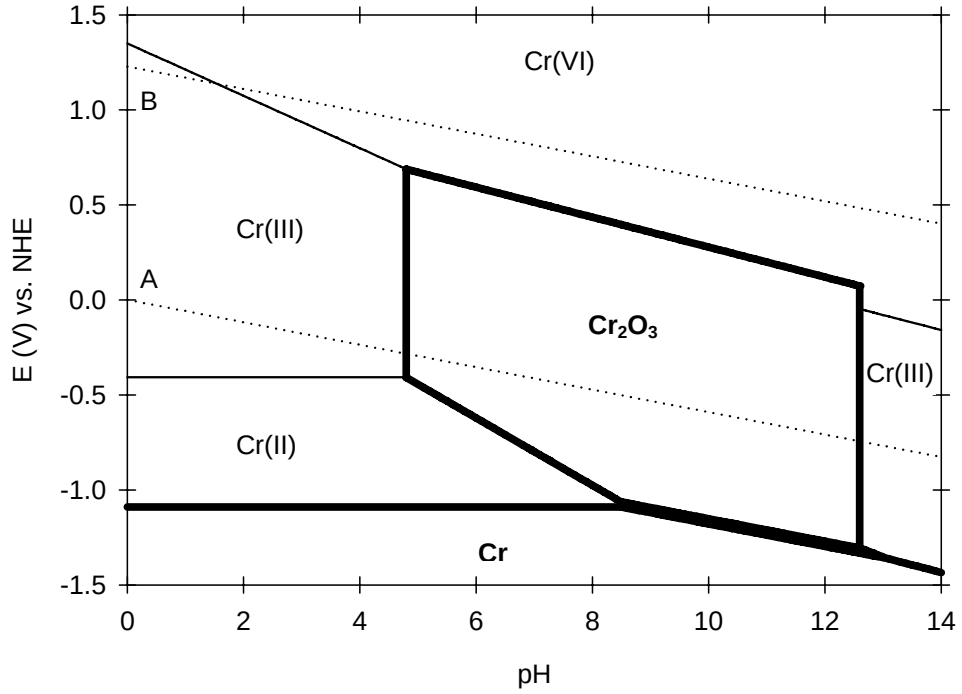

Figure 2-3: Chromium electrochemical stability diagram, 25°C
(Pourbaix 1974)

Arsenic is a semi-metal and has a different type of electrochemical stability diagram from copper and chromium. In order to deposit arsenic from an acidic solution containing As(V), the potential must be lowered to about 0 V (relative to the NHE). If the pH is held constant, the stability diagram shows that during the acid As deposition process it starts as aqueous As (V), becomes As(III), and then has to move through As_2O_3 in order to reach $As^0(s)$. For many systems, an oxide phase would be an impediment to deposition; however, studies have shown (Tomilov 2001) that it is possible to deposit arsenic from an acidic solution. This indicates that the oxide phase is probably not actually formed during As deposition.

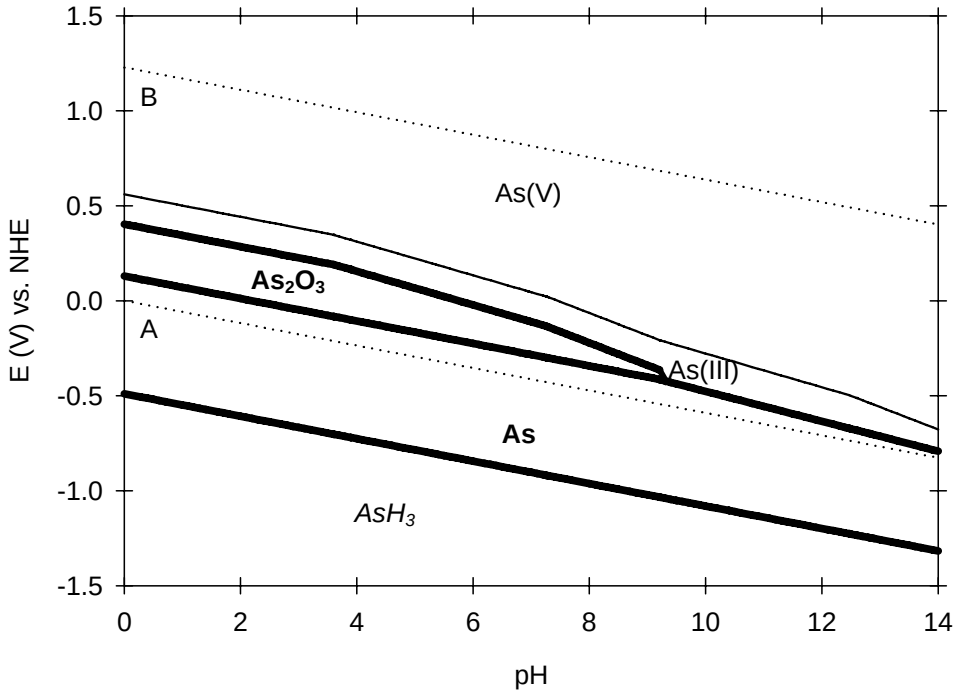

Figure 2-4: Arsenic electrochemical stability diagram, 25°C
(Pourbaix 1974)

A more serious complication with arsenic stability is that arsenic is converted to arsine, a highly toxic gas, by decreasing the electrochemical potential.

$$As\ (s) + 3H^+ + 3e^- \rightarrow AsH_3(g) \qquad (2\text{-}5)$$

The stability conditions under which copper is deposited are more anodic (positive potential) than arsenic formation, so both arsenic and copper could be formed under the same conditions. Unfortunately, the conditions that form chromium (< -1.1 V and pH <2.1), also produce arsine. Remediation of CCA wastes by electrolytic deposition would not be feasible if the byproduct of the remediation was arsine – a more toxic substance than the original waste.

One possible way to avoid arsine formation would be to completely remove all of the arsenic from the solution by electrolytic deposition before moving on to chromium deposition. This multi-step approach is much more complicated and therefore expensive than a single deposition step and would have to be carefully controlled to prevent arsine evolution.

Another possible method to avoid arsine formation would be to have the freshly formed arsenic immediately bond with another substance, such as liquid gallium, that would prevent its conversion to arsine. This work examines the use of a liquid gallium working electrode in section 5.3.2. In principle, arsenic should react with gallium to form gallium arsenide because gallium arsenide is more thermodynamically stable than arsine by about 20 kcal/mol.

$$As_{(s)} + Ga_{(l)} \rightarrow GaAs_{(s)} \quad (2\text{-}6)$$

Liquid gallium is better than solid gallium because, in general, metals are more reactive in their liquid state. Gallium has a low melting point of 29.78°C, making it easy to liquefy at temperatures of interest in this study. A possible problem with forming gallium arsenide instead of arsine is that gallium arsenide formation has a change in Gibbs free energy that is less negative than that of arsine formation by at least 20 kcal/mol depending on the pH and arsine pressure (Pourbaix 1974; Haung 1999). Thus arsine formation is thermodynamically favored over gallium arsenide formation, so the electrochemical stability diagram for arsenic given in Figure 2-4 is unchanged in the presence of gallium. Experiments may show that it is kinetically more favorable to combine solid arsenic with liquid gallium to form a solid than it is to combine solid arsenic with hydrogen ions to form a gas. The addition of an overpressure to suppress arsine gas formation would have to be very high, rendering the process unfeasible.

The addition of $1x10^{-6}$ mol Cu to the electrochemical stability diagram of arsenic introduces one notable deviation from the individual arsenic diagram. The entire region where As solid is most stable plus about 0.1 V above and below the entire region is replaced by Cu_3As since Cu_3As formation has a change in Gibbs free energy of about -3 kcal/mol (Haung 1999).

$$3Cu_{(s)} + As_{(s)} \rightarrow Cu_3As_{(s)} \quad (2\text{-}7)$$

Thus the addition of copper to the arsenic system helps to prevent arsine formation, although not under the conditions of chromium deposition.

The calculated combined electrochemical stability diagram of arsenic, copper, and chromium does not show any effect of the components on each other beyond the formation of Cu_3As (Haung 1999). However, the diagram is incomplete in that it does not include any interaction parameters between the dissolved species. The interactions may affect the stability of the components.

Since the analysis of the stability diagrams reveals that the conditions required to deposit As, Cr, and Cu from a multicomponent solution would probably also produce arsine, another approach to As, Cr, and Cu removal from acidic solutions may be needed. A comparison of the stability diagrams for Cr (Figure 2-3) and for As (Figure 2-4) shows that in the acidic region where As is stable, Cr(III) is also stable. Cr(III) is considerably less toxic than Cr(VI) and would be a positive step towards remediation of a CCA waste solution. The process could be stopped after Cr(III) formation, and a shift in the pH towards a more neutral solution would produce chromium oxide that would be stable and could be recycled or disposed.

2.2 Conclusions

The stability diagram analysis of the individual components, As, Cr, and Cu, revealed that deposition of all three components may not be possible without also producing arsine (AsH_3), a toxic gas. Hydrogen would be an additional byproduct of the deposition. The addition of Cu to the arsenic system does not move the As/AsH_3 stability boundary far enough in the negative potential direction to allow chromium deposition without arsine evolution. The use of a liquid gallium electrode may help prevent or reduce arsine evolution by reacting with the arsenic preferentially over hydrogen. If deposition of all three components without arsine evolution is

not possible, then deposition of only As and Cu and production of Cr(III) would be the next best alternative. There is always the possibility that experimental deposition from a multicomponent solution will produce one or more stable arsenic-chromium-copper species that were not considered in the stability diagram analysis and thus avoid arsine formation by either trapping the As in a more stable compound/alloy or forming a Cr(III) containing species.

2.3 References

Guy, A. G. and F. N. Rhines (1962). "Pourbaix diagrams. A firm basis for understanding corrosion." Metal Treatment and Drop Forging **29**(No. 197): 45-54.

Haung, H.-H., K. Anttila and A. Roine (1999). Outokumpu HSC Chemistry. Pori, Finland, Outokumpu Research Oy.

Pourbaix, M. (1974). Atlas of Electrochemical Equilibria in Aqueous Solutions. Houston, National Association of Corrosion Engineers.

Tomilov, A. P., A. V. Smetanin, I. N. Chernykh and M. K. Smirnov (2001). "Electrode Reactions Involving Arsenic and Its Inorganic Compounds." Russian Journal of Electrochemistry **37**(10): 997-1011.

3 Copper - Copper Sulfate Reference Electrode

The copper – copper sulfate reference electrode, or the copper sulfate electrode (CSE), is composed of a copper wire in contact with an aqueous copper sulfate solution and, often, with sulfuric acid present as well. The active electrochemical couple is Cu (s) with Cu^{2+} (aq). For the current study, the electrode filling solution was saturated copper sulfate and approximately 0.5% sulfuric acid. The sulfuric acid in the electrode filling solution serves two purposes. First, sulfuric acid is needed to prevent copper oxidation. Second, this specific level of sulfuric acid was chosen to match the bulk solution used for deposition experiments because the copper sulfate electrode was used as the reference electrode for the deposition studies, see chapters 5 and 6.

In order to be able to compare the electrical potential measured using the CSE in reference to other studies, it is necessary to relate the CSE electrical potential (E_{CSE}) to the normal hydrogen electrode (NHE) which is defined as 0 V for all temperatures. The electrical potential of the CSE was measured as a function of temperature over the range of 5 to 45°C versus the saturated calomel electrode (SCE). Since the SCE electrical potential relative to the NHE as a function of temperature has been well characterized (Chateau 1954), the CSE potential can be related to the NHE. An attempt was made to use electrolyte property modeling to calculate the activity of the copper ion in the electrode solution in order to estimate the potential of the Cu (s) / Cu^{2+} (aq) couple and, thereby, the error in the physical measurements of the potential that was introduced by the liquid junction potential. By removing the liquid junction potential error, the equilibrium electrical potential of the CSE can be found. Measured solubilities of copper sulfate in the sulfuric acid solutions are needed as an input for the electrolyte property modeling.

3.1 Previous Work

The CSE is most commonly used in cathodic or anodic corrosion protection applications of buried metal, such as steel storage tanks and building foundations, which means that it is usually in direct contact with soil. The majority of the literature on CSEs is focused on its use in field work, rather than on precise laboratory measurements.

Ewing's (1939) work laid the foundation for CSE work. He found that the measured potential difference between a CSE and an SCE at 25°C is "about 75 mV." He also measured the temperature dependence of saturated and unsaturated copper sulfate electrodes with reference to an electrode of the same composition held at a constant temperature, over a range from 1 to 51°C. The slope of the saturated curve is approximately 0.9 mV/°C. Ewing did not include a correction for the Soret effect due to the temperature gradient in the liquid bridge between the two half-cells because the same effect would occur when the soil and half-cell were at different temperatures. Ewing's CSE was designed for field use and there was probably a small amount of sulfuric acid added to his copper sulfate solutions.

Aker (1957) reports on his handmade CSE half-cell for field use. The half-cell contained saturated copper sulfate in water and a porous wooden plug to make the electrical connection. His CSE, versus an SCE, with the half-cells connected by tap water, gave a potential of 70 mV on average, varying from 68 to 73 mV.

A more analytical approach to determining the CSE potential was taken by Scott (1958). He claimed that he could extrapolate the activity coefficient of divalent copper ion to the saturation point of copper sulfate (1.41 molal) by using data for cadmium and zinc sulfate that spanned that concentration since copper, cadmium, and zinc sulfate activities were similar at

lower concentrations. The Nernst equation for $Cu \rightarrow Cu^{2+} + 2e^-$ at 25°C (assuming an activity of one for solid copper) simplifies to

$$E_{CSE} = E^{\circ}_{CSE} - 0.02958 \log\left(a_{Cu^{2+}}\right) \tag{3-1}$$

The value for E°_{CSE} was taken as -0.337 V from Latimer (1952), which is close to the value of -0.340 V found in Bard (2001). With the value of the activity coefficient of the copper ion approximated as 0.0390, the calculated value of E_{CSE} is -0.300 V vs NHE. Taking into account the reversed sign convention of Scott, the potential would be written today as E_{CSE} = +0.300 V versus NHE and +0.060 V vs. SCE. Thus Scott's results are approximately 10 to 15 mV smaller than the previously published studies.

More recent studies have focused on the factors affecting the accuracy of the CSE. Since copper salts are photosensitive, light can be an important factor when using a CSE outside. The difference in potential between a CSE is bright sunshine at noon versus a CSE in the dark was found to be -52 mV; however, when the light source was a fluorescent light the shift was only -2 mV (Ansuini and Dimond 1994). Ansuini and Dimond also found that a change in concentration of copper sulfate resulted in a potential shift of about 20 mV/decade of g/L. (Each decade of g/L is an order of magnitude.) The logarithmic dependence of the potential on concentration is expected given equation 3-1, since the activity is approximately proportional to the concentration (a better assumption at lower concentrations). Ansuini and Dimond also found that chlorides in the electrolyte solution of a CSE have a pronounced effect on the CSE potential. At 10 parts per thousand (ppth) chloride, the CSE potential was shifted negatively by 100 mV.

Further work was done by Pawel (1998) on the effect of temperature on CSE. The cooled/heated CSEs were measured against a room temperature CSE in a similar manner to Ewing. The result was the same with a slope of ~0.9mV/°C. Pawel's measurement of the

concentration effect on CSEs yielded almost the same result as Ansuini and Diamond, 17 mV/decade. Pawel also studied the effect of chloride contamination on the CSE potential and found that cells with a lot of excess copper sulfate were more resistant to chloride contaminant than those with only a few crystals of copper sulfate at saturation. The fully saturated CSEs were relatively insensitive to chloride contamination and required concentrations of 10 to 20 ppth chloride to produce a deviation of 15 mV in the CSE potential. The CSE potential was found to be relatively insensitive to contaminations of up to 18.8 ppth sulfide, 10 ppth iron, sulfuric acid or nitric acid to bring the solution to pH ~1, or sodium hydroxide to bring the solution to pH ~13. A 50/50 mixture of antifreeze and water resulted in 15mV decrease in potential after a few days. These tests show that the CSE is nearly unchanged after contamination with a variety of species and could be used to measure the reference potential in a range of aqueous solutions. Pawel found that formation of different types of oxide films on the solid copper in the CSE had an effect of < 5 mV on the CSE potential and was eliminated once the oxide films were scrubbed off the copper. Pawel also investigated the effect of light on the CSE potential and reported that overhead fluorescent or incandescent light had no measurable influence, while direct sunlight had a variable effect and was often related to the heating of the CSE due to the sunlight. For this study, laboratory light was assumed not to affect the potential of the CSE (and was already partially blocked due to the experimental configuration).

3.2 Solubility Measurements of Copper Sulfate

In order to model the copper sulfate electrode (CSE) potential, it is necessary to determine the composition of the saturated copper sulfate filling solution. The copper concentration and the sulfuric acid concentration vary with temperature as will be shown in Section 3.3.2. The results of the experimental measurements are used in the liquid junction

potential calculations. Once the sulfuric acid concentration of the filling solution is known, it is possible to minimize the liquid junction potential in the deposition experiments by matching the bulk solution sulfuric acid concentration to the CSE filling solution.

3.2.1 Calculations

The CSE electrolyte filling solution was made by first combining 3.85 mL of 96.1% sulfuric acid with water to make up 1 L of 69.5 mM sulfuric acid at room temperature (21 to 23°C). Next, this solution was heated or cooled to the temperature of the experiment and crystals of copper sulfate pentahydrate were added until saturation was achieved. The density of the solution at each temperature was measured gravimetrically using a glass volumetric flask that was heated or cooled to the temperature of the solution prior to measurement.

By measuring the copper concentration of the final solution, it is possible to determine the solubility of copper sulfate and the sulfuric acid concentration at each temperature. Copper concentration was measured using the bathocuproine method (Greenberg 1992), which gives the mass percent of copper and titration with ethylenediaminetetraacetic acid (EDTA), which gives the molarity of the copper. The data from the bathocuproine method at 35 and 45°C was not used due to poor temperature control at those conditions resulting from employing a temperature-controlled heat and stir plate for the solubility measurements at those temperatures because a portion of the normal temperature control system was broken. Later measurements at those conditions that were analyzed with the EDTA method used the standard experimental set-up that is described in Section 3.4.2. The EDTA method is easier to perform and more accurate than the bathocuproine method because it directly measures the copper ion concentration instead of requiring the solution to be diluted by several orders of magnitude.

The calculations used to determine constituent molality and molarity from each method are listed below.

1. For EDTA titration, calculate the mass % Cu using the density (ρ) and the molecular weight ($\mathfrak{M}$).

$$\text{mass \% solute} = \left(\frac{\text{molarity of solute}}{\rho_{solution}}\right)\mathfrak{M}_{\text{solute}}\left(\frac{1\text{kg}}{1000\text{g}}\right) \tag{3-2}$$

2. From the mass % Cu determine the mass % water added to the solution by addition of $CuSO_4 \bullet 5H_2O$ assuming complete dissociation

$$\text{mass \% additional } H_2O = (\text{mass \% } CuSO_4)\left(\frac{5 \text{ mol } H_2O}{1 \text{ mol } CuSO_4}\right)\left(\frac{\mathfrak{M}_{H_2O}}{\mathfrak{M}_{CuSO_4}}\right) \tag{3-3}$$

3. Calculate the remaining mass % that is not $CuSO_4$ and additional H_2O

$$\text{remaining mass \%} = 100 - \text{mass \% } CuSO_4 - \text{mass \% additional } H_2O \tag{3-4}$$

4. This remaining mass % is the original solution of H_2SO_4 and H_2O.

The mass % H_2SO_4 in the final solution is

$$\text{mass \% } H_2SO_4 \text{ in final solution} = (\text{remaining mass \%})(\text{mass \% } H_2SO_4 \text{ in orginal solution}) \tag{3-5}$$

5. Convert mass % into molality (mol solute / kg H_2O) and molarity (mol solute / 1L solution)

First calculate mass % H_2O total

$$\text{mass \% } H_2O \text{ total in final solution} = (\text{mass \% additional } H_2O) + (\text{remaining mass \%})(100 - \text{mass \% } H_2SO_4 \text{ in orginal solution}) \tag{3-6}$$

Then calculate the molality of H_2SO_4 and $CuSO_4$ (solute)

$$\text{molality of solute} = \left(\frac{\text{mass \% solute}}{\text{mass \% } H_2O \text{ total}}\right)\left(\frac{1}{\mathfrak{M}_{\text{solute}}}\right)\left(\frac{1000\text{g}}{1\text{kg}}\right) \tag{3-7}$$

6. For the bathocuproine method, the molarity of the solute can be calculated using the measured density of the solution at temperature

$$\text{molarity of solute} = \left(\frac{\text{mass \% solute}}{\mathfrak{M}_{\text{solute}}} \right) \rho_{solution} \left(\frac{1000\text{g}}{1\text{kg}} \right) \tag{3-8}$$

3.2.2 Results

The measured density of the saturated copper sulfate solutions as a function of temperature is shown in Table 3-1.

Table 3-1: Saturated copper sulfate density

Temperature (°C)	Solution Density (g/mL)
5.0	1.16
10.0	1.17
15.0	1.19
25.0	1.21
35.0	1.25
45.0	1.28

The results from the bathocuproine method (5-25°C) and the EDTA method (35-45°C) are shown as the mass percent of copper sulfate in Figure 3-1. The measured data is slightly lower than the data from Miles and Menzies (1937) who measured saturated copper sulfate solution with no sulfuric acid. The decreased copper sulfate solubility is expected given the common ion effect with sulfuric acid.

Crockford and Warrick (1930) measured copper sulfate solubility over a range of sulfuric acid concentrations that include those employed in the current study. Since the temperature range of Crockford and Warrick spans that of the current study (0 - 55 as compared to 5 – 45°C) but was not measured at the same temperatures as the current study, the measured sulfuric acid concentration was interpolated from their conditions and the resulting copper sulfate solubility

was determined. There appears to be significant error in their results (which may be due in part to the interpolation), which underscores the need for the current experimental study. The Miles and Menzies and the Crockford and Warrick studies provided the best available measurements of copper sulfate solubility in or near the range of sulfuric acid concentration relative to the CSE conditions used in this study.

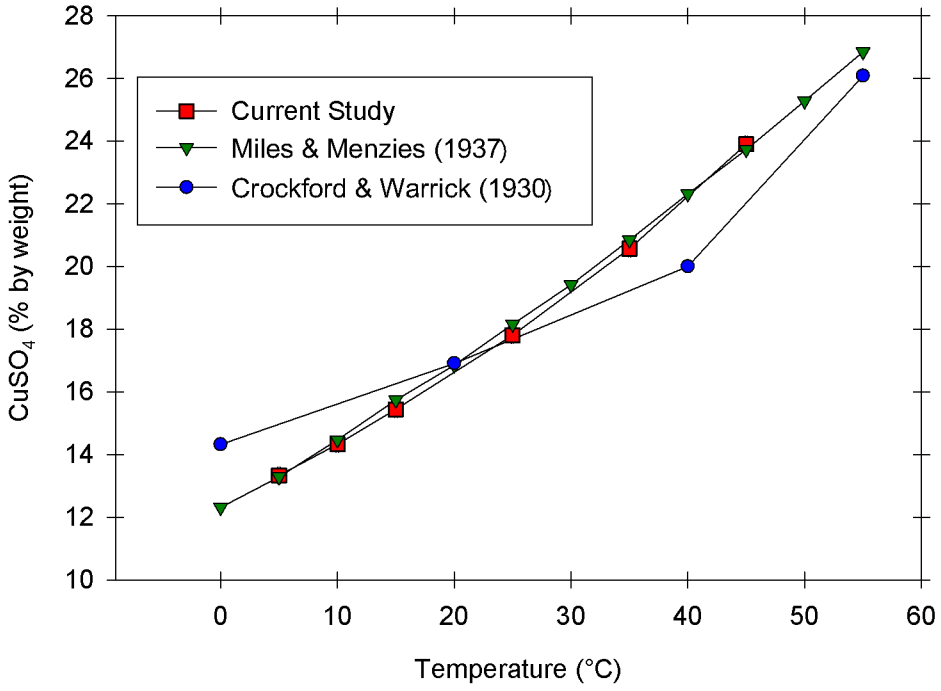

Figure 3-1: Solubility of copper sulfate in water as a function of temperature

Using the calculations outlined in Section 4.3.1, the molality of saturated copper sulfate in a sulfuric acid solution can be calculated from the mass percent copper sulfate and are shown in Figure 3-2. These saturation molalities are used as inputs for the electrolyte physical property modeling explained in Section 3.5.

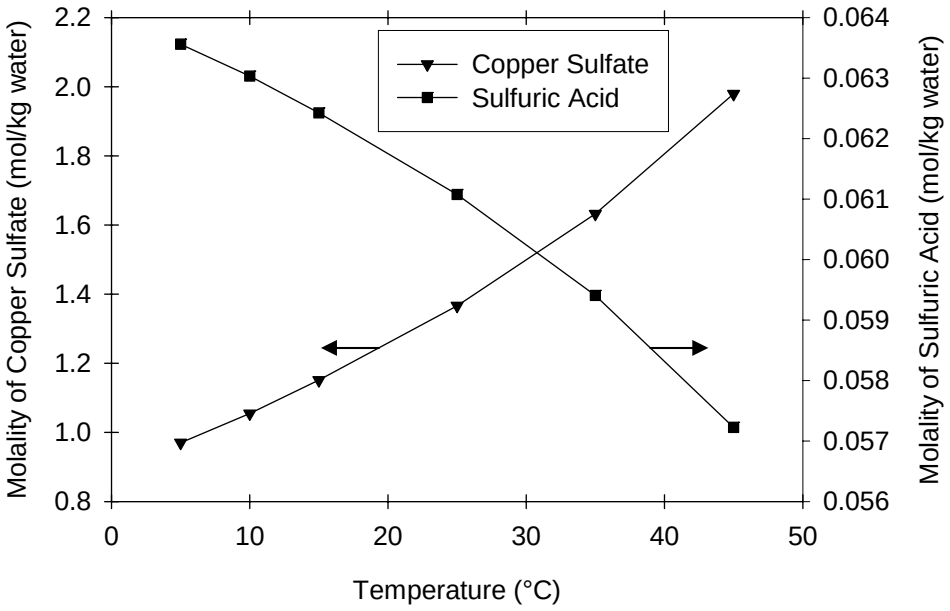

Figure 3-2: Molality of copper sulfate at saturation condition as a function of sulfuric acid concentration and temperature

3.3 CSE Experimental Setup and Procedures

The measurement apparatus for the CSE potential versus the calomel reference electrode potential was designed with the goal of measuring a stable open circuit potential. To achieve this goal, it was important to maintain a constant temperature and form reproducible liquid junctions. By their nature, liquid junctions are unstable since they are formed by the mixing of two liquids, in this case saturated copper sulfate and saturated potassium chloride solutions. The liquid junction potential is dependent on the nature of the concentration transition layer between the solutions. There are a variety of different types of liquid junctions, but it has been shown that liquid junctions with cylindrical symmetry give the most reproducible results (Guggenheim 1930). For this reason, a double liquid junction with frits was used instead of a single junction. The porosity of the frits determines their permeability which controls the time over which the liquid junction is stable because they control the rate of diffusion from the bulk solution into the

liquid junction. More porous frits establish a liquid junction more quickly, but the bulk solution rapidly diffuses into the reference electrode and changes the potential. A less porous frit takes longer to reach a steady potential, but this potential is held for a longer time and can be more accurately measured. For this study, Vycor® 7930 glass frits were utilized for their low porosity (average pore diameter of 40 Angstroms). Several other types of fine porosity frits were found to be both too porous and too variable in their porosity.

3.3.1 Dissolved Oxygen

The copper – copper sulfate reference electrode (CSE) experiments were carried out in a 2-L glass reaction kettle. In order to decrease the effect of oxygen on the measured potential of the CSE, the reaction kettle was sparged with 5.7 research grade (99.9997%) argon before the experiments and then blanketed with argon during the experiments. To determine the time necessary to remove oxygen by sparging with argon and stirring, the dissolved oxygen concentration was measured with a dissolved oxygen probe with an accuracy of 0.02 mg/L (Sension 6 , Hach) as a function of time.

3.3.2 Potential as a Function of Temperature

The copper – copper sulfate reference electrode (CSE) experiments provided a measurement of the potential of the CSE vs. the saturated calomel reference electrode (SCE) every 10°C over the range of 5 to 45°C. Three electrodes of each type were employed in order to minimize the experimental error. The copper sulfate electrodes (bold type) were connected to the calomel electrodes (underlined) via a potassium chloride salt bridge to make the following electrical couple: **Cu(s)/$CuSO_4$(sat),H_2SO_4(0.06 M)**//KCl(sat)//<u>KCl(sat)/Hg_2Cl_2(s)/Hg(l)</u>.

The single junction SCE electrodes were purchased from Radiometer Analytical (type REF421, p/n E21M004, batch 356-11) through their U.S. distributor, Hach Company. Their

operating range is -10 to 60°C, which is more than sufficient for the CSE experiments. The Radiometer Analytical electrodes were chosen because they use “Red Rod” technology to ensure a higher reproducibility than the average SCE electrode (Radiometer Analytical 2000). The saturated potassium chloride fill solution was made by heating or cooling water to the temperature of interest and adding potassium chloride crystal to saturation.

The CSEs were specially fabricated for these experiments. The general design as shown in Figure 3-3 consists of a 0.64 mm (0.025in) diameter copper wire (99.999%, oxygen free, Alfa Aesar p/n 00098) in a 5 mm inner diameter glass tube bent into a “J” shape with two Vycor glass frits (7930 porous glass, Advanced Glass and Ceramics) that measured 1/8 inch in diameter and 1/4 inch long attached with plastic tubing to form two liquid junctions. The length of the frits was sealed in heat-shrink Teflon® tubing with length-wise slits cut out of the center half of the tubing to increase solution diffusion when soaking the frits before assembling the electrode. A few grains of copper sulfate crystals sat on the bottom of the glass tubing to ensure saturation conditions. The CSE filling solution was made as described in Section 3.3.

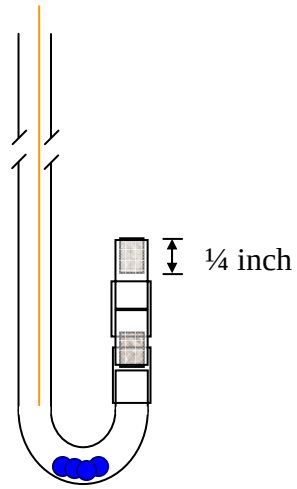

Figure 3-3: Copper sulfate reference electrode schematic
Figure not drawn to scale. The total length of the glass portion of the electrode is approximately 9" and the inside diameter of the glass tube is 5mm. The frits are inside 1/8" inside diameter flexible PVC tubing held together by 1/4" inside diameter PVC tubing. This tubing is connected to the glass tube by 3/8" inside diameter PVC tubing. The top of the glass tube is covered with two layers of parafilm to reduce solution evaporation. The copper wire is poked through the parafilm. To make the electrical connection with the Potentiostat, a gold-plated screw BNC fitting is attached to the end of the copper wire.

To ensure thermal and compositional equilibrium of the electrodes, the CSEs were placed in a 1 L flask of saturated copper sulfate solution and the SCEs were placed in a 2 L reaction kettle of saturated potassium chloride at temperature for at least 24 hours prior to the start of the experiments, as illustrated in Figure 3-4. The flask of the saturated copper sulfate solution and the reaction kettle of potassium chloride solution were immersed in a 16L agitated bath to regulate and maintain constant temperature. At 5°C and 15°C, the bath was a mixture of 30% ethylene glycol in water, and its temperature was regulated with a 120-V chiller (model # 1109, PolyScience) and a glass stick heater (model # CN9122A , Omega Engineering, Inc). At 25°C, the bath was changed to pure water. For 35°C and 45°C, the chiller was removed and only the heater was used to maintain a constant temperature. Three stir plates and a variable-speed impeller mixer (model #500002-30, Cole-Palmer Instrument Co.) were used to disperse solutes throughout the liquids in the flask, kettle, and bath and to maintain a uniform temperature.

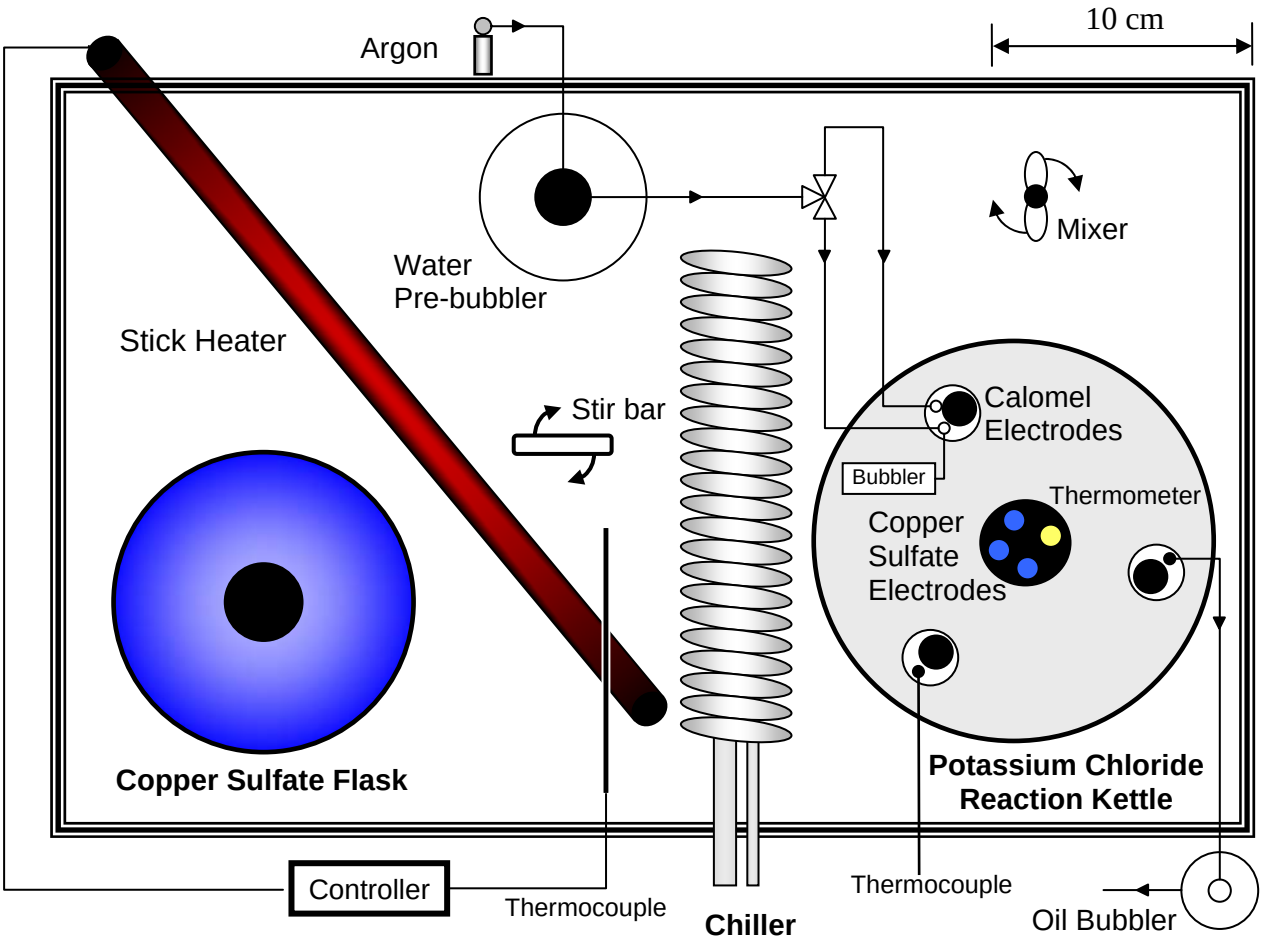

Figure 3-4: Plan view of copper sulfate reference electrode testing apparatus
The CSEs are moved from the copper sulfate flask to the potassium chloride reaction kettle at the start of the experiment, when the potential difference between the electrodes is measured. The Figure is not drawn to scale

As described in Section 3.3.1, forty-five minutes of sparging 5.7 research grade argon gas was found to remove the dissolved oxygen concentration in the 2 L reaction kettle down to zero within accuracy of the dissolved oxygen probe; therefore, the saturated potassium chloride solution was sparged with 5.7 research grade argon gas for forty-five minutes prior to the transfer of copper sulfate electrodes to the kettle. The CSEs were removed from the saturated copper sulfate bath and rinsed thoroughly with water. A layer of water was allowed to remain on the top of the Vycor® frits since it was found that drying the ends of the frits introduced scatter in the data. The argon was switched to blanket the kettle as the copper sulfate electrodes were

transferred to the saturated potassium chloride solution and for the duration of the experiment. The stirring in the reaction kettle was stopped during the actual measurement phase of the experiments to prevent convection currents from interfering with the electrical potential measurements. The temperature was maintained within 0.2°C of the target for 5 and 25°C and with 0.1°C of the target for 15, 35 and 45°C during the experiments.

The open circuit potential difference between each of the CSEs and a single SCE, the difference between all of the SCEs, and the temperature of the saturated potassium chloride solution were logged for at least twenty-four hours to ensure a stable potential difference. The potential was measured with a high-impedance potentiostat (model # 197 Autoranging Microvolt DMM, Keithley).

At the end of each experiment, the CSEs were removed and disassembled. The glass and plastic portions were rinsed with water and dried. The frits and copper wire were soaked in fresh, room temperature copper sulfate solution, with a separate bottle for each piece of the electrode. The SCEs were removed from the reaction kettle, emptied, filled with room temperature saturated potassium chloride solution, and set aside with their tips soaking in the same solution.

3.4 Experimental Results and Discussion

The dissolved oxygen results were used to set the argon sparge time for the experiments to determine the CSE potential as a function of temperature. The results for the CSE potential are related to the SCE potential and the normal hydrogen electrode (NHE) potential as a function of temperature.

3.4.1 Dissolved Oxygen

Following the procedure described in Section 3.4.1, the dissolved oxygen concentration in the saturated potassium chloride solution in the 2-L reaction kettle was measured as a function of argon sparging time. After forty-five minutes of sparging with argon, the dissolved oxygen concentration was 0.02 mg/L, which is one tenth of the accuracy of the probe (Hach Company 2000), as shown in Figure 3-5.

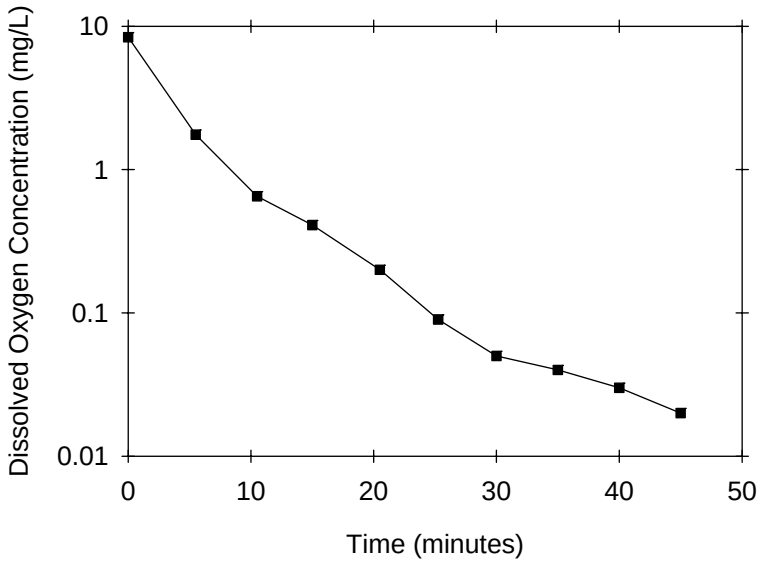

Figure 3-5: Effect of sparging reaction kettle with argon on dissolved oxygen concentration
The 2 L reaction kettle was sparged with argon at a rate of approximately 60 mL/min.

3.4.2 Potential as a Function of Temperature

The results from measuring the potential of the CSE verses the SCE as a function of temperature are presented in Figures 3-6 and 3-7. Each point on the graph represents one CSE electrode verses the average potential of the three SCEs. The variation of the potential of the SCEs was significantly less than the variation of the CSEs. There are three points at every temperature, but at some temperatures the values are so similar that it is not possible to see all of the individual points.

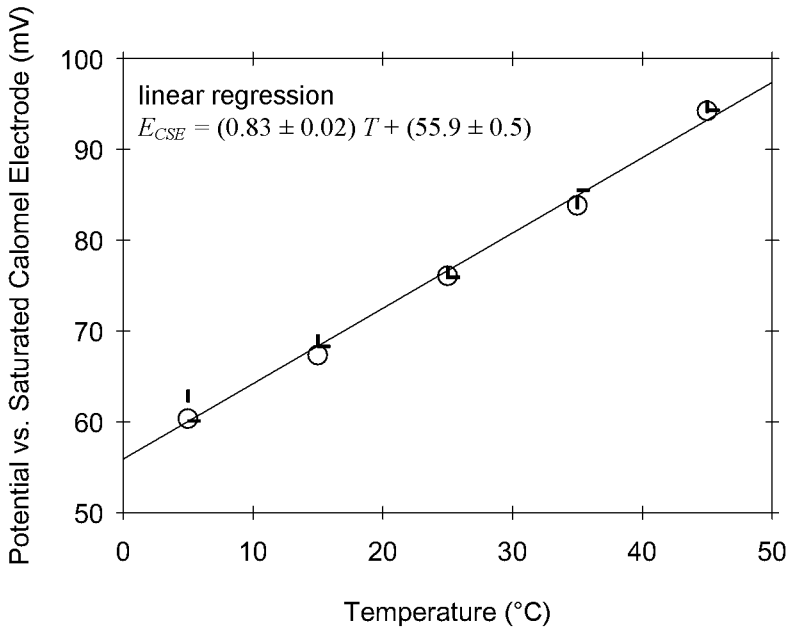

Figure 3-6: Potential of the copper sulfate electrode vs. the saturated calomel electrode as a function of temperature with linear fit

Three different symbols (I , —, ○) were used to represent the data points at each temperature so that when three data points had the same coordinates all three points would be visible.

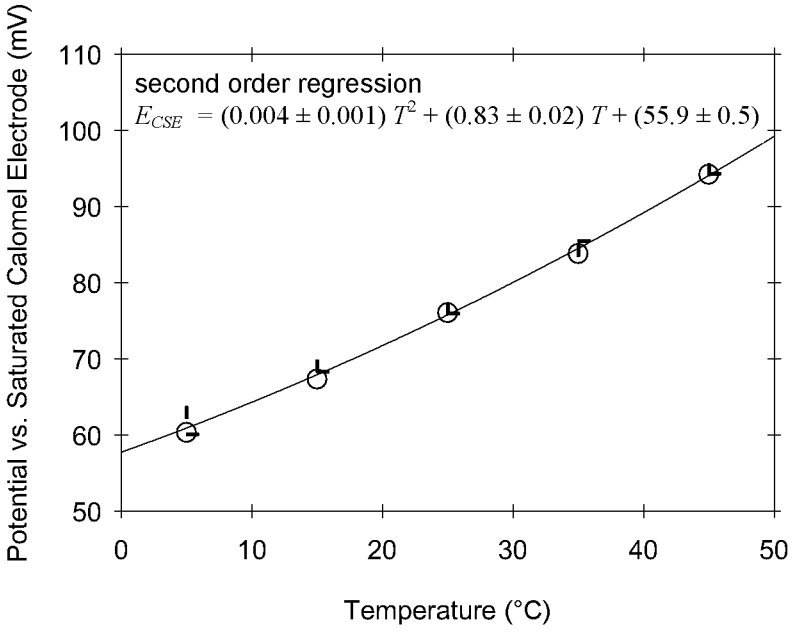

Figure 3-7: Potential of the copper sulfate electrode vs. the saturated calomel electrode as a function of temperature with second order regressed fit

Three different symbols (I , —, ○) were used to represent the data points at each temperature so that when three data points had the same coordinates all three points would be visible.

The linear fit to the potential of the CSE versus the SCE is good, but the second order fit more accurately represents the values, particularly at the standard state temperature of 25°C. Since the change in copper sulfate solubility is not linear with temperature (Figure 3-2), it is to be expected that the potential is nonlinear. The slope of the linear fit is 0.83± 0.02 mV/°C which is close to Ewing's (1939) and Pawel's (1998) value of 0.9 mV/°C.

The SCE has been related to the NHE with no liquid junction potential effects over the range of 5 to 70°C (Chateau 1954). The liquid junction potential was circumvented by using experimental data and the Debye-Huckel equation to determine the activity of chloride ions in a saturated potassium chloride solution. The potential of the SCE in reference to the NHE within an error of 0.1 mV is

$$E_{SCE}\,(\text{mV}) = 241.2 - 0.661(T - 25) - 1.75 \times 10^{-3}\,(T - 25)^2 - 9.0 \times 10^{-7}\,(T - 25)^3 \qquad (3\text{-}9)$$

where T is in degrees Centigrade. Equation 3-9 was used to convert the data from SCE to NHE reference. The linear fit of the potential CSE vs. NHE in mV and degrees Centigrade is

$$E_{CSE} = (0.17 \pm 0.02)\,T + (313.2 \pm 0.4) \qquad (3\text{-}10)$$

and the second order fit is

$$E_{CSE} = (0.003 \pm 0.001)\,T^2 + (0.04 \pm 0.06)\,T + (314.4 \pm 0.6) \qquad (3\text{-}11)$$

The second order fit more accurately represents the values, but the linear fit is simpler to use to quickly approximate the CSE potential.

The average value at each measured temperature is shown in Table 3-1.

Table 3-2: Average measured potential

Temperature (°C)	Potential (CSE vs. NHE, mV)
5.0	314.6
15.0	315.6
25.0	317.1
35.0	318.7
45.0	321.5

One of the most valuable aspects of the CSE is that it is relatively insensitive to temperature changes relative to the NHE which by definition is zero at all temperatures. Its potential relative to NHE only changes by 7 mV over the entire temperature range measured. The potential of the CSE vs. NHE at 25°C is one mV higher than Ewing's value of 316 mV (75mV vs. SCE), one of the commonly accepted values (Uhlig and Revie 1985) and one mV lower than another commonly accepted values (Potter 1956; Jones 1996).

3.5 Electrolyte Physical Property Modeling

The electrolyte physical property modeling is focused on estimating the activity of the components in the copper sulfate electrode solution (solution I) and the saturated potassium chloride solution (solution II). Solution II was used to form a salt bridge between the CSEs and the SCEs in the open circuit potential measurement experiments. The activity (a_i), transference number (t_i), electronic charge (z_i) and concentration in molarity (c_i) of each species in the solutions in the junction may be used to approximate the liquid junction potential (LJP, E_j) as shown in equation 3-12 (Bard and Faulkner 2001). The transference number is related to the electronic mobility (u_i) and concentration of all y components in solution as defined in equation 3-13. The calculated LJP at each temperature is then subtracted from the measured potential to more closely approximate the thermodynamic potential difference between the two electrochemical half-cells as shown in equation 3-14. The potential of the copper sulfate electrode in reference to the NHE (E_{CSE}) can be calculated from the activity of the bivalent

copper ion as will be shown later in this Section. The potential of the saturated calomel electrode in reference to the NHE (E_{SCE}) is already known from the literature.

$$E_j = \frac{-RT}{F}\int_I^{II}\sum_{i=1}^{y}\frac{t_i}{z_i}d\ln a_i \tag{3-12}$$

$$t_i \equiv \frac{|z_i|u_i c_i}{\sum_{i=1}^{y}|z_i|u_i c_i} \tag{3-13}$$

$$E_{CSE} - E_{SCE} = E_{Measured} - E_j \tag{3-14}$$

The liquid junction in the experiments was formed by a vertical tube with a frit on either end. The saturated copper sulfate solution was at the bottom of the tube and the saturated potassium chloride solution was at the top of the tube. In order to integrate equation 3-12, several assumptions need to be made about the transport profile in the liquid junction and the electronic mobility of the species. Since at each experimental temperature the density of the saturated copper sulfate solution is greater than that of the saturated potassium chloride solution and the tube itself is stationary, it can be assumed that there is no transport in the tube due to natural convection. The mixing of the two solutions is driven solely by diffusion due to the concentration gradient. Furthermore, since the mixing occurs slowly over at least 24 hours, it can be assumed that the concentration of each species in the mixture varies linearly from one end of the junction to the other end. This assumption means that the concentration of each species can be linearly related to its position in the tube (x) through equation 3-15. By convention at x = 0 we are at the solution I interface (CSE electrolyte solution) and at x = 1 we are at the solution II interface (SCE electrolyte solution). The superscripts in equation 3-15 refer to the solution number.

$$c_i = c_i^I + \left(c_i^{II} - c_i^I\right)x \tag{3-15}$$

In addition it is assumed that the electronic mobility of each species is constant for all experimental concentrations and can be approximated by the infinite dilution mobility. While not strictly true, the ionic mobilities for many concentrated species are usually about 5% to 20% less than at infinite dilution (Washburn 1929). For example, the bivalent copper ion has a mobility of $9.9\text{x}10^{-4}$ $\text{cm}^2\text{s}^{-1}\text{V}^{-1}$ at infinite dilution. The mobility drops to $8.0\text{x}10^{-4}$ $\text{cm}^2\text{s}^{-1}\text{V}^{-1}$ at a concentration of about 0.5 molar. The transport assumptions in this derivation are the same as those made to derive the most commonly used simplified version of the liquid junction potential – the Henderson equation (MacInnes 1961). The derivation in this work deviates from the Henderson derivation in that the activity of a component is not assumed to be equal to its concentration.

In order to integrate equation 3-12 the transference number and the activity have to be related to x. Combining equations 3-13 and 3-15 yields equation 3-16, the relationship between the transference number and x.

$$t_i = \frac{|z_i| u_i c_i}{\sum_{i=1}^{y} |z_i| u_i c_i^I + x \sum_{i=1}^{y} |z_i| u_i \left(c_i^{II} - c_i^I \right)} \tag{3-16}$$

$d\ln a_i$ is related to x as shown in equation 3-17.

$$d \ln a_i = d \ln a_i \left(\frac{dx}{dx} \right) = \left(\frac{d \ln a_i}{dx} \right) dx \tag{3-17}$$

Combining equations 3-12, 3-16 and 3-17 yields equation 3-18.

$$E_j = \frac{-RT}{F} \int_0^1 \sum_{i=1}^{y} \frac{\frac{|z_i| u_i c_i}{z_i} \left(\frac{d \ln a_i}{dx} \right)}{\sum_{i=1}^{y} |z_i| u_i c_i^I + x \sum_{i=1}^{y} |z_i| u_i \left(c_i^{II} - c_i^I \right)} dx \tag{3-18}$$

The electronic mobilities have been measured for all charged species except for HSO_4^-. The electronic mobility is defined as the limiting velocity of the ion (v_i) in an electric field ($\mathscr{E}$) of unit strength. The magnitude of the force exerted by the electric field is $|z_i|e\mathscr{E}$, where e is the electronic charge, and is balanced by the frictional drag on the ion that can be approximated (from Stokes law for a sphere) as $6\pi\eta r v_i$, where η is the viscosity of the medium, and r is the radius of the ion. Therefore,

$$u_i = \frac{v_i}{\mathscr{E}} = \frac{|z_i|e}{6\pi\eta r} \tag{3-19}$$

The electronic mobility of HSO_4^{-1} is approximated as half that of SO_4^{-2} since it is half its charge but almost the same size. The electronic mobility of each species used in the liquid junction potential calculations is listed in Table 3-3. The values for all species are for infinite dilution (Bard and Faulkner 2001) except for Cu^{2+}, which was calculated based on the transference number for a $CuSO_4$ solution of 0.5 M using the infinite dilution mobility of SO_4^{2-} (Washburn 1929).

Table 3-3: Species mobilities

Species	u ($cm^2sec^{-1}\ V^{-1}$)
K^+	$7.619x10^{-4}$
Cl^-	$7.91x10^{-4}$
Cu^{2+}	$8.04x10^{-4}$
$SO4^{-2}$	$1.654x10^{-3}$
H_3O^+	$3.625x10^{-3}$
HSO_4^-	$8.270x10^{-4}$

The concentration and the activity of the saturated potassium chloride solution is already known from previous studies (Chateau 1954). The concentrations and activities of all of the species in the copper sulfate solution and the copper sulfate / potassium chloride solution in the liquid junction are unknown and have to be calculated. The derivative of the natural log of the

activity with respect to the position in the liquid junction can be determined from the activity results.

Aspen Plus 2004 was used for the calculations with ELECNRTL (Aspen Technology 2004). The electrolyte Non-Random Two Liquid equation of state (ELECNRTL) was chosen over the Pitzer electrolyte model because it is better able to handle concentrated solutions (Abovsky 1998). The database in Aspen Plus 2004 was used for all the inputs into ELECNRTL except for two equilibrium constants, potassium chloride and copper sulfate solubility. The default value for the equilibrium constant for potassium chloride solubility resulted in a potassium chloride solubility limit much lower than the literature value. The database value was replaced with a value based on a regression of the mean activity of potassium and chloride ion data assuming that the activity of potassium chloride was equal to one (Chateau 1954). The inputted values are shown in equation 3-20. In Aspen Plus 2004, the KCl equilibrium reaction is written as a dissociation reaction, so the ions are the products.

$$\ln K_{KCl} = \ln\left(\frac{a_{K^+}a_{Cl^-}}{a_{KCl}}\right) = \ln\left(a^2_{K^+Cl^-}\right) = -34.3 - \frac{0.679}{T} + 6.38\ln T \qquad (3\text{-}20)$$

The Aspen Plus 2004 database assumed complete dissociation for copper sulfate in solution. Spectrophotometric studies have shown that at high concentrations copper sulfate is also present as a neutral ion pair species in solution (Dadgar 1982; Méndez De Leo 2005). An equilibrium constant equation as a function of temperature was developed from the limited equilibrium constant data available at atmospheric pressure and was used in some of the simulations. Méndez De Leo assumed that the activity coefficient of neutral ion pair copper sulfate in solution (γ_{CuSO_4}) was equal to one in order to calculate the equilibrium constant. In Aspen Plus 2004, the

neutral copper sulfate reaction was written as an equilibrium reactions so the ions are the reactants.

$$\ln K_{CuSO_4} = \ln\left(\frac{a_{CuSO_4}}{a_{Cu^{2+}} a_{SO_4^{2-}}}\right) = \ln\left(\frac{c_{CuSO_4}\gamma_{CuSO_4}}{c_{Cu^{2+}}\gamma_{Cu^{2+}} c_{SO_4^{2-}}\gamma_{SO_4^{2-}}}\right) = -20.9 + \frac{0.381}{T} + 4.61\ln T \qquad (3\text{-}21)$$

The equilibrium constant for copper sulfate pentahydrate ($CuSO_4*5H_2O$ (s)) solubility was left at its default value and yielded results slightly above the experimental values.

The following set of reactions were employed in the calculation of the saturated copper sulfate and sulfuric acid system over the range of temperatures 5 to 45 °C assuming the presence of neutral copper sulfate species in solution. The double-ended arrows indicate an equilibrium reaction. All species are aqueous unless marked with (s) to indicate a solid.

$$\begin{aligned}
&2H_2O \leftrightarrow H_3O^+ + OH^- \\
&H_2SO_4 + H_2O \leftrightarrow H_3O^+ + HSO_4^- \\
&HSO_4^- + H_2O \leftrightarrow H_3O^+ + SO_4^{2-} \\
&CuSO_4 \leftrightarrow Cu^{2+} + SO_4^{2-} \\
&CuSO_4 \cdot 5H_2O\,(s) \leftrightarrow Cu^{2+} + SO_4^{2-} + 5H_2O
\end{aligned} \qquad (3R\text{-}1)$$

The set of reactions assuming no neutral copper sulfate is the same as above except that the fourth equation was changed to be irreversible in the direction of dissociation.

The activities of all components in solutions were determined for four different conditions as shown in Table 3-4. The conditions were varied such that half employed equilibrium for neutral copper sulfate in solution and half did not. Within each half, one condition used the value of copper sulfate concentration based on the simulation, and the other half used a value of copper sulfate concentration set to match the experimental value. Every condition was evaluated every 10°C from 5 to 45°C.

Table 3-4: Model conditions for ELECNRTL model

Case #	$CuSO_4$ equilibrium included?	$CuSO_4$ concentration
1	Yes	Simulated saturation
2	Yes	Set to match experimental value
3	No	Simulated saturation
4	No	Set to match experimental value

Figure 3-8 shows the values of the activity coefficient of Cu^{2+} calculated for each case using the ELECNRTL model. Cases 1 and 3 and Cases 2 and 4 give similar results. It appears that the controlling factor for the activity of Cu^{2+} in the ELECNRTL model is the total concentration of copper with the speciation of copper playing a smaller role.

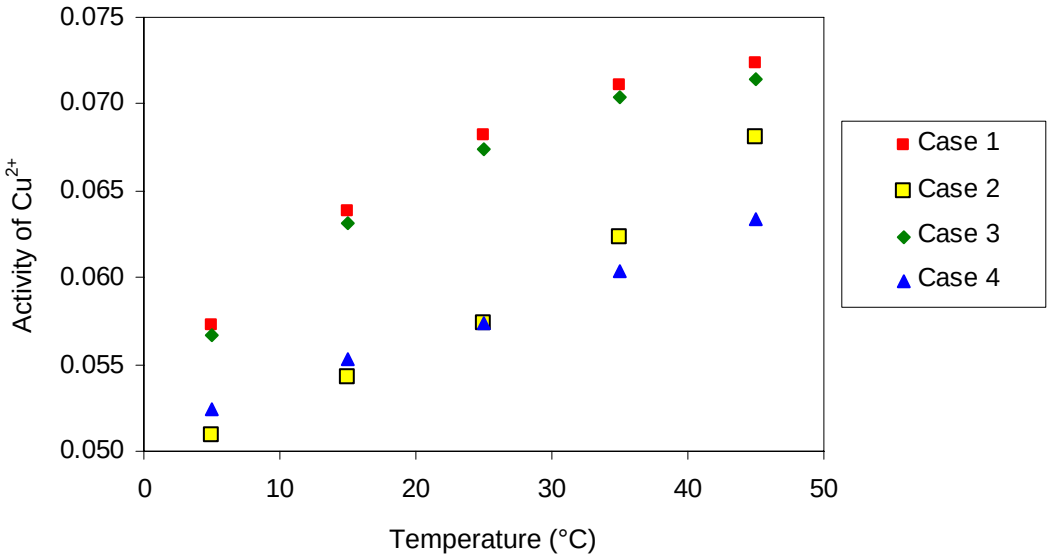

Figure 3-8: Activity of Cu^{2+} as a function of temperature for the ELECNRTL model

In addition to the ELECNRTL model, the activity of the bivalent copper ion in the saturated copper sulfate and sulfuric acid solution was also calculated using the Meissner model. The Meissner corresponding states model is based on generalizing the non-ideal behavior of the mean activity coefficient of strong electrolytes and is not completely internally consistent (Tester and Modell 1997). It allows the calculation of the mean activity coefficient of copper sulfate in a

sulfuric acid solution. The activity coefficient of the copper ion is then determined from the mean activity coefficient using the Debye-Hückel model as shown in equation 3-22.

$$\gamma_{Cu^{2+}} = e^{-\left(\frac{\left(z_{Cu^{2+}}\right)^2}{z_{Cu^{2+}} z_{SO_4^{2-}}}\right) \ln\left(\gamma_{Cu^{2+}SO_4^{2-}}\right)} = \gamma_{Cu^{2+}SO_4^{2-}} \tag{3-22}$$

The reaction system for the Meissner model (equation 3R-2) is simplified from that used in the ELECNRTL model shown in reaction scheme 3R-1.

$$\begin{aligned} H_2SO_4 &\leftrightarrow 2H^+ + SO_4^{2-} \\ CuSO_4 &\leftrightarrow Cu^{2+} + SO_4^{2-} \end{aligned} \tag{3R-2}$$

HSO_4^- was not used in the reaction system because no data for $Cu(HSO_4)_2$ is available as would be required by the Meissner model. The copper sulfate was modeled using available data (Tester and Modell 1997). Extended Debye-Hückel behavior was assumed for the sulfuric acid because it was at moderately low concentrations (molality ~0.6) and the sulfuric acid mean activity coefficient is not well behaved in the Meissner model (Meissner and Tester, 1972). The experimental values for the copper sulfate and sulfuric acid concentrations (Figure 3-2) were used as inputs to the Meissner model. Equations 3-23 through 3-30 were solved to calculate the mean activity coefficient of sulfuric acid. Ion 1 = Cu^{2+}, 2 = SO_4^{2-}, and 3 = H^+. I = ionic strength of the $CuSO_4$ only for equations 3-25 through 3-28, the sulfuric acid only for equation 3-29, and the entire system for equation 3-30, m_i = molality of species i, all z_i (charge on the species i) are taken as positive numbers, and $q_{12}^o = 0$ (Tester and Modell 1997).

$$\Gamma_{ij} = \left(\gamma_{ij}\right)^{1/z_i z_j} \tag{3-23}$$

$$I \equiv \frac{1}{2} \sum_{k=1}^{\text{all ions}} m_k z_k^2 \tag{3-24}$$

$$\Gamma_{12}^o = \left[1 + B\left(1 + 0.1I\right)^{q_{12}^o} - B\right] \Gamma_{12}^{DH} \tag{3-25}$$

$$\log_{10}\Gamma_{12}^{\mathrm{DH}} = -\frac{0.5107 I^{1/2}}{1 + C I^{1/2}} \tag{3-26}$$

$$B = 0.75 - 0.065 q_{12}^{o} \tag{3-27}$$

$$C = 1 + 0.055 q_{12}^{o}\left(e^{-0.023 I^{3}}\right) \tag{3-28}$$

$$\log\Gamma_{23}^{o} = \frac{-0.510 I^{1/2}}{1 + I^{1/2}} \tag{3-29}$$

$$\begin{aligned}\log\Gamma_{12} = {} & \frac{z_1}{z_1 + z_2}\left(\frac{(z_1 + z_2)^2}{2 z_1 z_2}\frac{0.5 m_2 z_2^2}{I}\log\Gamma_{12}^{o}\right) \\ & + \frac{z_2}{z_1 + z_2}\left(\frac{(z_2 + z_2)^2}{2 z_2 z_1}\frac{0.5 m_1 z_1^2}{I}\log\Gamma_{12}^{o} + \frac{(z_2 + z_3)^2}{2 z_2 z_3}\frac{0.5 m_3 z_3^2}{I}\log\Gamma_{32}^{o}\right)\end{aligned} \tag{3-30}$$

Figure 3-9 shows the results of the calculations of the activity of Cu^{2+} using both the Meissner and ELECNRTL models. The figure also includes the experimental value, which were calculated using the Nernst equation (3-31), the experimental potential of the CSE (Figure 3-6) in reference to the NHE, and the assumption of a value of E^{0} equal to 0.340 V (Bard and Faulkner 2001).

$$E_{CSE} = E_{CSE}^{\circ} - \frac{RT}{nF}\ln\left(a_{Cu^{2+}}\right) \tag{3-31}$$

Both models predict an activity of Cu^{2+} that is significantly less than the experimental value. In addition, all model-predicted slopes are smaller than the experimental value. The ELECNRTL-predicted slopes are positive as is the experimental value whereas the Meissner model is slightly negative. Based on the activity data, the ELECNRTL model more accurately predicts the experimental values than does the Meissner model.

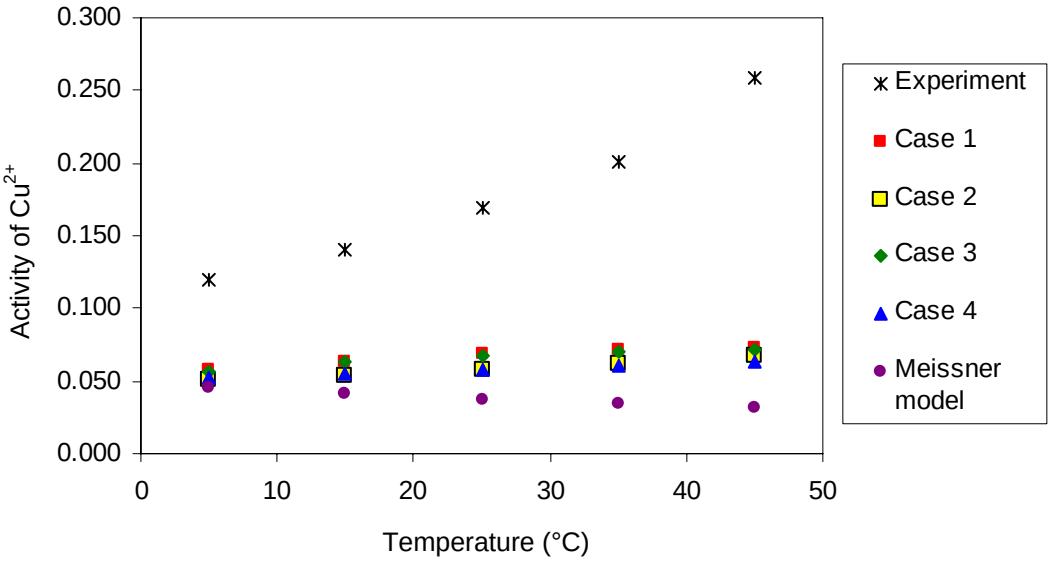

Figure 3-9: Activity of Cu^{2+} as a function of temperature for experimental data, the ELECNRTL and the Meissner models

The first step in calculating the liquid junction potential, which is included in the experimental value of the CSE, is to calculate the true potential of the CSE in reference to the NHE. In order to calculate the true potential, it is necessary to determine the set of conditions that best represent the values of the activity in solution. Equation 3-31 can be used to convert the calculated values of activity of Cu^{2+} to E_{CSE} as a function of temperature for each case as illustrated in Figure 3-10.

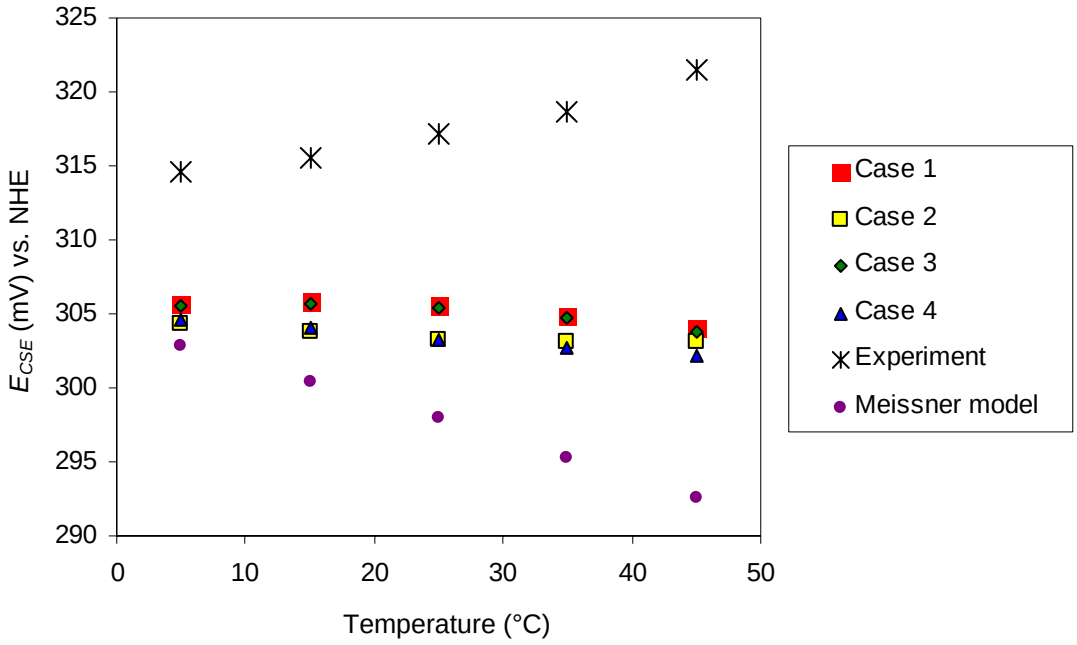

Figure 3-10: Calculated and experimental CSE potential

The slope and intercept of the best fit line for each case, compared to the experimental values, is shown in Table 3-5.

Table 3-5: Comparison of the trendline parameters for E_{CSE}

Condition	Slope (mV/°C)	Intercept (mV) vs. NHE
Experiment	0.17	313
Case 1	-0.04	306
Case 2	-0.03	304
Case 3	-0.05	306
Case 4	-0.06	305
Meissner model	-0.26	304

As with the activity of Cu^{2+}, the models underpredict the values of E_{CSE} for all temperatures. The ELECNRTL model has almost no temperature dependence whereas the Meissner model, again, has a negative temperature dependence. The experiment showed a positive temperature dependence. The models seems to predict the enthalpic contribution (ΔH) to the potential relatively accurately (the intercepts have less than 10% deviation) but do a poor job of predicting the entropic (ΔS) contribution to the potential (slope variation).

$$E = -\frac{\Delta G}{nF} = -\frac{\Delta H}{nF} + \frac{T\Delta S}{nF} \tag{3-32}$$

The best match to the experimental results is Case 1 (included neutral solvated $CuSO_4$ equilibrium, simulated saturation) although there is little difference between it and Case 3 (no neutral solvated $CuSO_4$ equilibrium, simulated saturation). Given the difficulty of correctly predicting the activity of concentrated ions in a multicomponent solution, the ELECNRTL model with the Aspen Plus 2004 database does a decent job of modeling the activity of Cu^{2+} (within 94% for all temperatures), though there is still room for improvement. Since the model does not include the liquid junction potential, it is expected that the model predictions would have small deviations from the experimental results. Case 1 and 2 (included neutral solvated $CuSO_4$ equilibrium, experimental value of $CuSO_4$ saturation) are the more realistic models (because they include the neutral solvated $CuSO_4$) and vary from the experimental conditions by 13 mV on average. This deviation can be used to estimate an upper bound on the liquid junction potential of about 13 mV.

All of the Cases produced similar values of the E_{CSE}. Even though the inclusion of the neutral copper sulfate in solution does not have a significant effect on the potential, it will have a significant impact on the liquid junction potential because it changes the ratio of neural ($CuSO_4$) to charged (Cu^{2+}, SO_4^{2-}) species. Since the liquid junction potential is concentration dependent, Case 2, which is based on the experimental value of copper in solution, was chosen as the model to calculate the liquid junction potential.

To calculate the liquid junction potential all parameters and functions in equation 3-18 must be measured or calculated. The electronic mobility that was used for each species is listed in Table 3-3. The concentrations of the charged species in the SCE electrolyte solution is known from experimental measurements. The concentration of the charged species in the CSE

electrolyte solution was determined from a combination of experimental measurements and calculations using the conditions for Case 2. The concentration of each species as a function of position *x* was found using equation 3-15 at increments of 0.1 in *x* with the points 0.01, 0.95, and 0.99 added to improve the curve fit of the natural log of the activity of each charged species as a function of *x*. All species activities were fit using a fifth order polynomial. The integral in equation 3-18 was calculated using Maple software (Waterloo Maple Inc. 2000). Since the smallest deviation between the experimental and calculated values of E_{CSE} was at 5°C, it is likely that more accurate results can be obtained for that temperature than for the higher temperatures. The liquid junction potential was found to be equal to 9 V at 5°C. The liquid junction potential is very sensitive to the mobility of the ions. For instance, changing the copper ion mobility from its value at 0.5 M (8.0×10^{-4} $cm^2 sec^{-1} V^{-1}$) to its infinite dilution value (9.9×10^{-4} $cm^2 sec^{-1} V^{-1}$) shifts the liquid junction potential to 13 V. The liquid junction potential result is orders of magnitude from reality and indicates that there are serious flaws in the assumptions used to calculate the liquid junction potential, such as that the mobility can be approximated with the infinite dilution values for most species; therefore, the liquid junction potential calculation for other temperatures was not performed.

The assumption of linear variation of the concentration across the liquid junction leads to a major error in the liquid junction potential calculation. While this assumption is good for the potassium chloride species, it ignores the equilibrium reactions of the neutral copper sulfate species and sulfuric acid. At each position *x* the Aspen Plus 2004 model has as inputs the total concentration of neutral copper sulfate species, copper, sulfate, bisulfate, and hydronium ions as solid copper sulfate and pure sulfuric acid. The model then determines the actual concentration of each species in solution. Figure 3-11 shows a plot of the percent deviation of the

concentration in molality predicted by the Aspen Plus 2004 model (M_{model}) from the concentration calculated with the assumption of linear variation of the concentration across the liquid junction (M_{calc}) as a function of x. There is significant deviation of the model from the calculated values of the concentration of the species in the CSE electrolyte solutions. This deviation can lead to large errors in the calculated liquid junction potential.

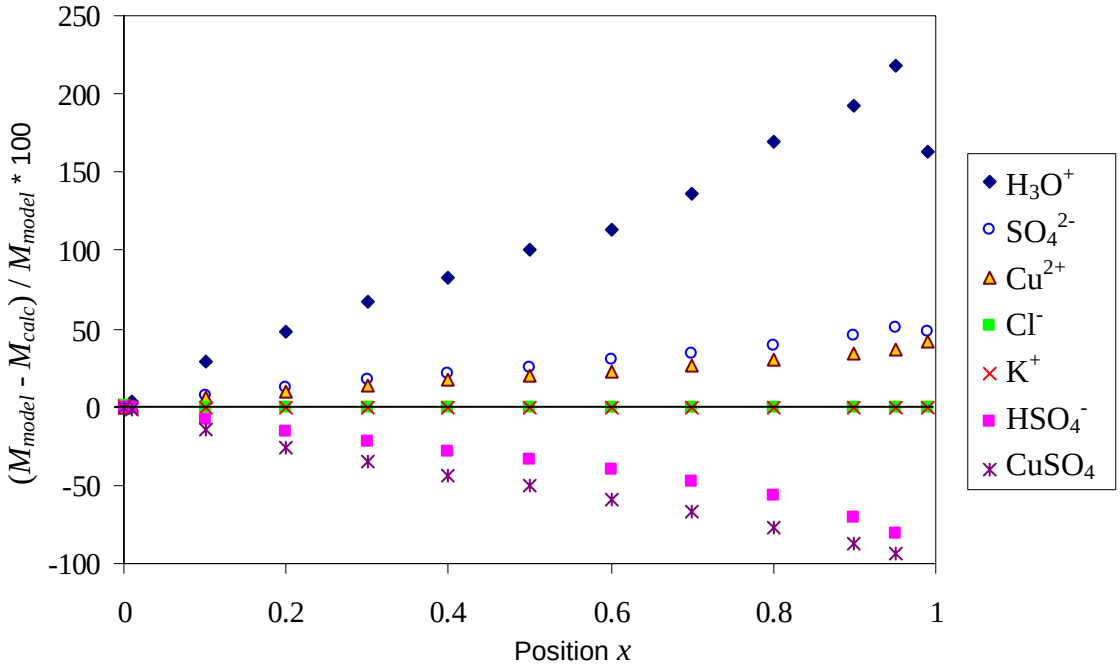

Figure 3-11: Percent deviation of model molality (M_{model}) from calculated molality (M_{calc}) as a function of position x

A better way to approach the calculation of the liquid junction potential is with digital simulation of the behavior of the liquid junction region. The general approach is to divide x into small steps and simultaneously solve for the concentration and activity of all species at each step point. By using small steps, the operational equations for the model could be linearized. This model would need to include the ELECNRTL model for the reaction system, the diffusion equation for transport of the species between each Section, and the boundary conditions of the composition of the electrolyte solutions at either end of the liquid junction region. There would

need to be a trace amount of all components in both boundary conditions to avoid evaluating the natural log of a zero activity in solving equation 3-18. The most difficult part of the digital simulation would probably be incorporation of the ELECNRTL model since Aspen Plus 2004 does not have an appropriate interface. One way to attempt to work around this problem would be to use Aspen Plus 2004 to find the concentration and activity of all the species in the system for a set of concentrations that span the range of expected concentrations. The results would require a large number of runs to yield detailed data and could be curve fit to multiple species concentrations. The resulting simplified equations for the property model would then be input into the digital simulation. For a good primer on how to apply digital simulation methods to electrochemical problems see Britz (2005). Digital simulation of the liquid junction region to determine the liquid junction potential was beyond the scope of this work.

3.6 Conclusions

The potential of the CSE as a function of temperature from 5 to 45 °C was successfully measured and related to the NHE potential. Data were fit with both linear and second-order models. The linear regressed slope was found to be similar to previously measured values that used slightly different experimental setups (Ewing 1939; Pawel 1998). The value of the CSE in reference to the NHE at 25°C, 317 mV, is bracketed by the commonly accepted values of 316 and 318 mV (Potter 1956; Uhlig and Revie 1985; Jones 1996). Simulation of the CSE electrolyte solution using the ELECNRTL property model yielded the activity of Cu^{2+} for four different model assumptions. The Meissner model, which is significantly simpler than the ELECNRTL model, calculated values of the activity of Cu^{2+} which were similar to the ELECNRTL values. The assumption of a standard potential for the Cu/Cu^{2+} couple resulted in calculated values of the CSE potential from the ELECNRTL model that were 94% to 97% of the

experimental value for all measured temperatures. The experimental values had a positive temperature dependence. In comparison, the Meissner model values had a negative temperature dependence and the ELECNRTL model values had almost no temperature dependence. Thus, the ELECNRTL model more accurately predicted the experimental data than the Meissner model. The results using the ELECNRTL model indicate that the liquid junction potential present in the experimental apparatus was small, probably less than 13 mV. The aqueous system in the liquid junction region involved reacting species and concentrated solutions and proved to be too complicated to be modeled using the assumptions described in Section 3.5. Digital simulation of the liquid junction region would be necessary to calculate a more accurate liquid junction potential. Once determined, the liquid junction potential would be subtracted from the measured values of the CSE to yield a more accurate CSE potential. In any case, the overall effect of the liquid junction potential appears to be small.

3.7 References

Abovsky, V., Y. Liu and S. Watanasiri (1998). "Representation of nonideality in concentrated electrolyte solutions using the Electrolyte NRTL model with concentration-dependent parameters." Fluid Phase Equilibria **150-151**: 277-286.

Aker, L. P. (1957). "A simplified method for making and maintaining half-cells." Corrosion **13**(9): Tech. Topics, 122.

Ansuini, F. J. and J. R. Dimond (1994). "Factors affecting the accuracy of reference electrodes." Materials Performance **33**(11): 14-17.

Aspen Technology (2004). Aspen Plus. Cambridge, MA, Aspen Technology.

Bard, A. J. and L. R. Faulkner (2001). Electrochemical Methods: Fundamentals and Applications. New York, John Wiley & Sons, Inc.

Britz, D. (2005). Digital Simulation in Electrochemistry. Berlin Heidelberg, Springer-Verlag.

Chateau, H. (1954). "Determinations précises des potentiels de référence données par les electrodes au calomel entre 5 et 70° C." Journal de Chimie Physique et de Physico-Chemie Biologique **51**(1): 590-593.

Crockford, H. D. and L. E. Warrick (1930). "The system: $CuSO_4$-H_2SO_4-H_2O." Journal of Physical Chemistry **34**: 1064-70.

Dadgar, A., D. Khorsandi and G. Atkinson (1982). "Effect of pressure and temperature on copper sulfate ion association in water." Journal of Physical Chemistry **86**(19): 3829-3834.

Ewing, S. (1939). "The copper-copper sulfate half-cell for measuring potentials in the earth." American Gas Association, Proceedings **21**: 624-634.
Greenberg, A. E., L. S. Clesceri, A. D. Eaton and M. A. H. Franson, Eds. (1992). Standard Methods for the Examination of Water and Wastewater. Washington DC, American Public Health Association.
Guggenheim, E. A. (1930). "A study of cells with liquid-liquid junctions." Journal of the American Chemical Society **52**(4): 1315-1337.
Hach Company (2000). sension™6 Portable Dissolved Oxygen Meter Instruction Manual. USA, Hach Company.
Jones, D. A. (1996). Principles and Prevention of Corrosion. Upper Saddle River, NJ, Prentice Hall.
Latimer, W. M. (1952). The Oxidation States of the Elements and Their Potentials in Aqueous Solutions. New York, Prentice-Hall.
MacInnes, D. A. (1961). The Principles of Electrochemistry. New York, Dover.
Meissner, H. P. and J. W. Tester (1972). "Activity Coefficients of Strong Electrolytes in Aqueous Solutions." Industrial & Engineering Chemistry Product Research and Development **11**(1): 128-133.
Méndez De Leo, L. P., H. L. Bianchi and R. Fernández-Prini (2005). "Ion pair formation in copper sulfate aqueous solutions at high temperatures." Journal of Chemical Thermodynamics **37**: 499-511.
Miles, F. T. and A. W. C. Menzies (1937). "Solubilities of Cupric Sulfate and Strontium Chloride in Deuterium Water." Journal of the American Chemical Society **59**: 2392-2395.
Pawel, S. J., R. J. Lopez and E. Ondak (1998). "Chemical and environmental influences on copper/copper sulfate reference electrode half cell potential." Materials Performance **37**(5): 24-29.
Potter, E. C. (1956). Electrochemistry Principles & Applications. London, Cleaver-Hume Press Ltd.
Radiometer Analytical (2000). Reference Electrodes Operating Instructions. Villeurbanne Cedex, France, Radiometer Analytical.
Scott, G. N. (1958). "The copper sulfate electrode." Corrosion **14**: 136t-140t.
Tester, J. W. and M. Modell (1997). Thermodynamics and Its Applications. Upper Saddle River, New Jersey, Prentice Hall.
Uhlig, H. H. and R. W. Revie (1985). Corrosion and Corrosion Control An Introduction to Corrosion Science and Engineering. New York, John Wiley & Sons.
Washburn, E. W., Ed. (1929). International Critical Tables of Numerical Data, Physics, Chemistry and Technology. New York, McGraw-Hill.
Waterloo Maple Inc. (2000). Maple 6.01, Waterloo Maple Inc.

4 Deposition Experimental Setup and Procedures

The deposition experiments encompass the deposition of arsenic, chromium, and copper from single- and multi-component solutions of arsenic pentoxide, potassium dichromate, chromium trioxide, copper sulfate, and sulfuric acid in water. This chapter focuses on the setup for these experiments and the analysis methods for the deposition process and products. The deposition experiments were performed in either a reaction kettle deposition cell or a flask deposition cell using a three-electrode configuration. Direct current and alternating current voltammetry were used to perform the deposition and analyze the deposition process. Both X-ray diffraction and energy-dispersive X-ray with scanning electron microscope were employed to analyze some of the deposition products.

4.1 Deposition Cells

Two types of cells were used for the deposition experiments. The reaction kettle deposition cell was used in all of the copper deposition and some of the chromium deposition and sulfuric acid baseline experiments. All other experiments were performed in the flask deposition cell. The major advantages of the flask deposition cell are the ability to remove the working electrode without disassembling the cell, better positioning of all of the electrodes, and greatly improved seals to prevent the ingress of oxygen and the egress of arsine. All experiments were performed in a fume hood. The gas handling systems were the same for both cells.

Argon of grade 5.0 (99.999% pure) or greater was used to sparge the deposition cells. Since the argon passed through oxygen-permeable plastic lines to reach the cell, oxygen was removed from the gas with a gas purifier (Supelco 2-3906) shortly before reaching the cell. All tubing after the gas purifier is 1/8 inch O.D. Tefzel® which has an oxygen permeability of only 100cc / 100in^2 * 24h * atm / mil @ 25° C. The dissolved oxygen level in the solutions was

reduced to a value that was less than the accuracy of the dissolved oxygen probe (0.2 mg/L) (Hach Company 2000). To prevent the argon from drying out the bulk deposition solution, the argon was saturated with deionized water after the gas purifier. The argon then passed through a three way valve. One line from the valve leads to a metal-free filter (Alltech 32170) placed at the bottom of the cell to disperse the argon and sparge the solution. The other line blankets the top of the solution with argon during a deposition run. The solution was not sparged during the experiments to avoid disturbing the solution.

For all experiments the effluent gas flowed at a rate of approximately 60 mL/min from the cell to a bubbler filled with approximately six inches of light mineral oil. The oil bubbler was used to apply a small back pressure to the cell, increasing the effectiveness of oxygen sparging. To trap any arsine that may have been produced the gas from the oil bubbler was sent to a system of bubblers as described in Section 4.3. When arsine was not a concern, the effluent gas was released into the fume hood. The tubing in the post-cell gas system is 1/8 inch O.D. Teflon®.

In between deposition runs the flasks and the non-PVC components were washed with 18.2 mega-ohm water (US Filter, Purelab Ultra Scientific) and 8 molar nitric acid or 6 molar hydrochloric acid. The PVC components were only washed with the hydrochloric acid solution and water because nitric acid is incompatible with PVC. All of the components were allowed to air dry.

4.1.1 Reaction Kettle Deposition Cell

The reaction kettle deposition cell is a 50 mL 3-neck kettle (Labglass, ML-1281-700) held together with a three-screw clamp (Labglass, ML-1288-700). An 1/16 inch thick expanded PTFE gasket (McMaster, 8903K13) was cut down to size for the reaction kettle. The necks of

the kettle were 14/20 and arranged in a line. The electrodes and gas lines were secured in the necks with rubber stoppers with specially bored holes. The working and reference electrodes were held in the center neck while the counter electrode, thermocouple, and gas-out line were in one side neck, both argon-in lines were in the remaining neck. Silicone grease was applied to the rubber stoppers to improve their seals. Since rubber stoppers may absorb and then slowly leak arsine gas, they are inappropriate for work with arsenic. The reaction kettle deposition cell could, therefore, not be used for arsenic deposition experiments.

4.1.2 Flask Deposition Cell

The flask deposition cell is a specially made borosilicate glass 5-neck European-style flask (Ace Glass Inc.). It has a 34/45 center neck with four angled side necks evenly spaced around it as shown in Figure 4-1. Two side necks opposite each other are 24/40, the third neck is 14/20, and the fourth is a #7 Ace-Thred. All nuts and ferrules in the deposition cell are Teflon® in order to withstand highly acidic solutions. The working electrode (WE) is held in place in the center neck by a specially fabricated glass adapter that goes from 34/45 to #7 Ace-Thred. Similarly, the Pt wire lead of the counter electrode (CE) is secured by a 14/20 to 1/2 mm electrode glass adapter (5038-04) with Teflon®-faced septa (8787-40) and a 1/2 mm bushing for the electrode adapter (5037-08 Teflon®). The reference electrode (RE) and the gas-out line share a 24/40 neck by using a 24/40 to #7 Ace-Thred and hose connection (5261-16). The hose connection was attached to the gas-out line by a hose-connection-to-1/8-inch-Swagelok adapter that was held in place with PVC tubing. The two gas in lines are in the other 24/40 neck and are connected via a twin adapter from 24/25 to two #7 Ace-Threds (5031-10). The thermocouple is fed through the #7 Ace-Thred and secured with a specially fabricated #7 Ace-Thred ferrule with a 2 mm hole. All other ferrules are #7 Ace-Thred with a 1/8 inch hole (11710-03) and all

bushings are #7 Ace-Thred (5029-45) except where noted. The Ace-Thred style was chosen because the nut-and-ferrule combination provide a secure seal against gas leakage.

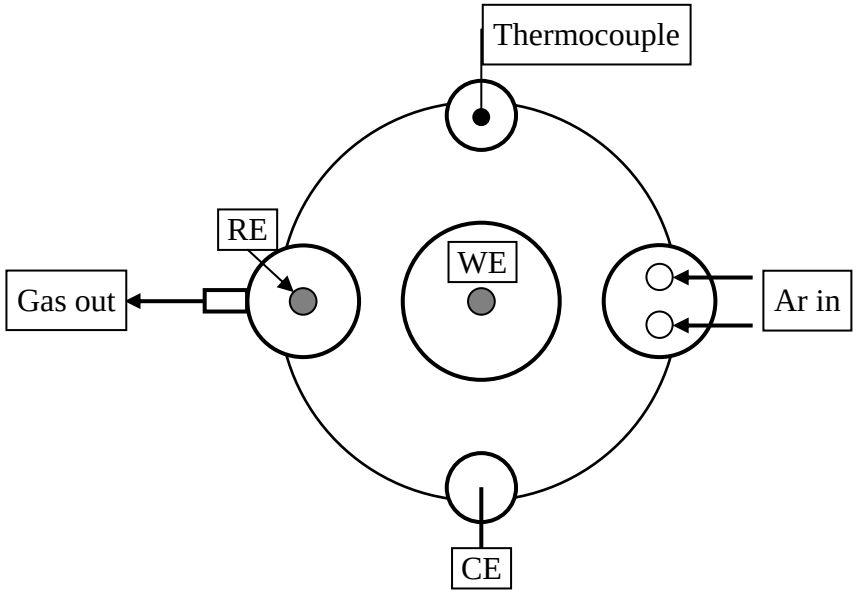

Figure 4-1: Plan view of flask deposition cell
The five necks are shown with the main body of the flask. WE = working electrode, RE = reference electrode, CE = counter electrode. The argon-in lines were connected to the argon via a water bubbler and the gas-out line was connected to the gas bubbler system shown in Figure 4-5. The type-K thermocouple was connected to a digital thermocouple reader (Extech Instruments, 421501).

4.2 Electrodes

Three electrodes were used in the deposition experiments. The same counter electrode was used for all experiments. Slight variations on the main design of the reference electrode were used in the reaction kettle and flask deposition cells. Only one working electrode was used for each experimental run. The reaction kettle deposition cell used solid metal working electrodes exclusively while the flask deposition cell used both solid metal and liquid gallium working electrodes.

4.2.1 Solid Metal Working Electrode

The basic design of the solid metal working electrodes was a short metal cylinder with a

polished end to make the face of the electrode. The metal cylinder was attached to a longer copper wire via solder (Solder-It, Inc., SP-7) or conductive epoxy (Creative Materials, Inc., 118-06(SD)) as shown in Figure 4-2. The copper wire served as the electrode lead. The metal cylinder and the connection to the copper wire were encased in non-conductive acid-resistant epoxy (Master Bond Inc., EP21AR) cast into a cylindrical shape using a pipette tip as the mold. The copper lead was insulated from the solution with 1/8" O.D. Teflon® or Tefzel® tubing. The tubing and epoxy were connected by wrapping them in Parafilm. The tip of the electrode was bent upward into a "J" shape as shown. In this configuration, the electrode faces upwards to help gas bubbles leave the electrode surface. The seal with the deposition cell was made on the Teflon® or Tefzel® tubing. The electrodes were polished to an average roughness of 0.05 microns.

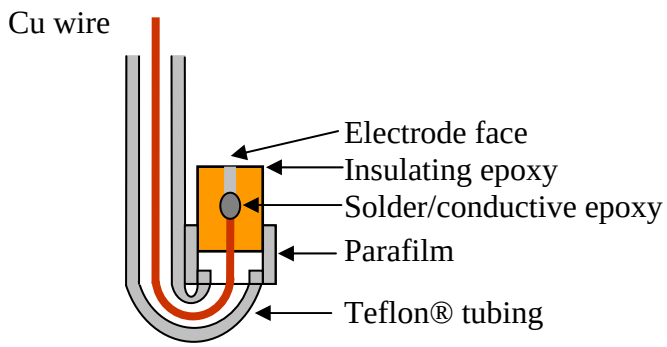

Figure 4-2: Solid metal working electrode

To help ensure one-dimensional transport of the electroactive species to the working electrode surface, the planar surface of the electrode should be either inside a tube or surrounded by a flat surface that is flush with the electrode. For the most commonly employed electrode diameter of 2.0 mm, the diameter of the surrounding epoxy was 9.5 mm. Electrodes with 0.5 mm diameter were encased in 6.4 mm diameter epoxy. Gold, copper, and platinum were used for the small diameter electrodes while 304 stainless steel, copper, and gold were used for the large diameter electrodes. The small diameter electrodes can only be used for reactions that do

not produce gas since the gas bubbles quickly cover and insulate the electrode, whereas in the larger electrodes enough gas is produced before the electrode is covered to allow the bubble to lift off of the surface.

The original solid metal working electrode designs used a series of dual heat-shrink PTFE/FEP tubing to insulate the working electrode. However, the hydrophobic nature of this tubing caused the bubbles evolved on the electrode surface to stick to it, blocking it. The epoxy reduces the sticking of the evolved bubbles because it is hydrophilic.

4.2.2 Liquid Gallium Working Electrode

Gallium is unusual in that it is one of four metals that can be liquid near room temperature (gallium melts at 29.77°C and boils at 2205°C) (Lide 1992), thus it is relatively easy to keep gallium liquefied in a laboratory using a hot plate. One of the main challenges of working with gallium is its high surface tension which makes it difficult to force gallium through a small tube. In addition, the surface tension of gallium under water is a function of its electrical potential and the species on its surface (Bockris 2000).

$$d\sigma = -q_M dE - \frac{q_M}{z_i F} d\mu_i - \sum \Gamma_i d\mu_i \qquad (4\text{-}1)$$

Where σ = surface tension, q_M = charge density,
E = applied potential, z_i = charge on species i,
F = Faraday's constant, μ_i = chemical potential of species i,
Γ_i = surface excess

At electrical potentials where gallium oxidizes to water soluble species, which is the same electrical potential region of interest for copper stripping, the surface tension of gallium under water greatly decreases. If the surface of the liquid gallium is too close to the top of the tube, the gallium will overflow under oxidizing potentials. This phenomenon is a particular problem for smaller-diameter glass tubes such as 2.0 mm, the diameter of the solid working electrodes. In

addition to surface tension, the wetting properties of gallium are important design parameters for the liquid gallium working electrode. Gallium will wet glass and metal, but it has great difficulty wetting plastic. For this reason, and because it is electrically insulating, glass was used as the material for the electrode holder. In addition, a tube with a 4.5 mm inner diameter, which is larger than the diameter of the solid working electrodes, was chosen to hold the liquid gallium.

The general shape of the gallium working electrode is similar to the solid metal working electrodes. It is a "J" shape with the gallium surface facing upwards out of the shorter end as shown in Figure 4-2. A copper wire is used to make electrical contact with the gallium. The seal is made between the Ace-Thred of the flask and the 1/8 inch Tefzel® tubing. Since gallium forms a thin oxide layer when exposed to air, the liquid gallium working electrode was designed to allow the user to form a fresh gallium surface when the gallium was immersed in the bulk deposition solution (Wang 1994). Forming a fresh electrode surface is also a way to remove deposition product between experimental runs. The height of the gallium surface exposed to the deposition solution was controlled by adjusting the argon pressure above the other end of the gallium. The connection to the argon system was made via a polypropylene "T" connector attached to the Tefzel® tubing with soft PVC tubing. The air-tight seal between the copper wire and the top of the "T" connector was made with dual heat-shrink PTFE/FEP tubing. The liquid gallium working electrode was only used in the flask deposition cell.

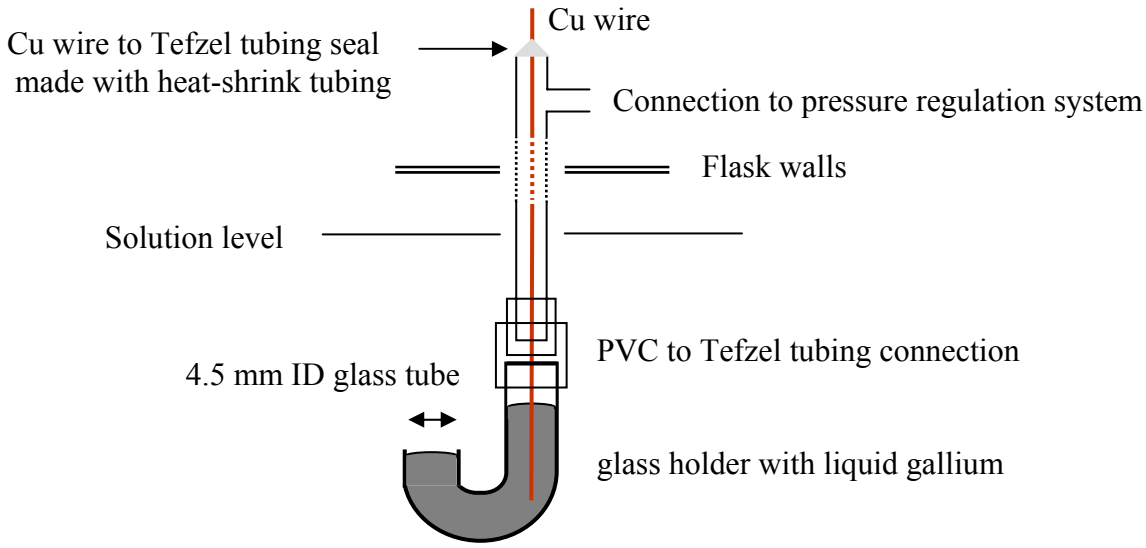

Figure 4-3: Liquid gallium working electrode schematic
Figure not drawn to scale. Dotted lines indicate where the lines have been shortened.

4.2.3 Counter Electrode

The bulk of the current in a three-electrode cell is passed through the counter electrode to the working electrode in order to allow nearly zero current to pass through the reference electrode. The counter electrode used in this study consisted of a Pt gauze 52 mesh woven from 0.1 mm diameter 99.9% pure wire (Alpha Aesar, 10283) attached to a 0.5 mm diameter Pt 99.95% pure wire (Alpha Aesar, 10286) by threading the wire through the mesh and crimping them together. The surface area of the mesh is approximately 4.5 cm^2 which is over an order of magnitude greater than the surface area of the largest working electrode used in this study. The counter electrode should always have a larger surface area than the working electrode to ensure that the electrochemical processes on the working electrode are the rate determining factor for the flow of current through the cell and not those on the counter electrode.

4.2.4 Reference Electrode

A copper-copper sulfate reference electrode (CSE) was used in all deposition

experiments. The design of the electrode varied slightly from the work described in Chapter 3. A side view of the CSE design is shown in Figure 4-4. For the deposition experiments, a triple junction design was used instead of a double junction. The first junction is between the reference electrode solution with the copper wire and the bridge reference electrode solution. The second junction is between the bridge reference electrode solution and the bulk deposition solution. The third junction is between the bulk deposition solution in the electrode and the bulk deposition solution in the deposition cell, serving to prevent contamination of the bulk deposition solution with the reference electrode solution. Similarly, the other two junctions prevent contamination of the innermost reference electrode solution with the bulk deposition solution. The frits forming the first and second junctions were soaked in reference electrode solution and the frit forming the third junction was soaked in bulk deposition solution before assembling the electrode. The CSE configuration used in the reaction kettle deposition cell has the first junction outside the cell and the other junctions inside the cell. In contrast, the CSE configuration used in the flask deposition cell has all three junctions and the end of the copper wire in contact with the reference electrode solution inside the cell in order to ensure temperature equilibrium when working at elevated temperatures with the liquid gallium working electrode. An additional benefit of the CSE configuration for the flask deposition cell is that the saturation of the copper sulfate solution directly in contact with the copper wire is ensured by the presence of copper sulfate crystals.

The frits are inside 1/8” (3.2 mm) O.D. flexible PVC tubing and are held together by 3/8” (9.5 mm) O.D. PVC tubing. In both configurations, 1/8” O.D. Teflon® tubing is used to make the seal with the cell. The outside diameter of the more rigid Teflon® tubing was slightly enlarged with Teflon® heat-shrink tubing to ensure a secure fit inside the flexible PVC tubing.

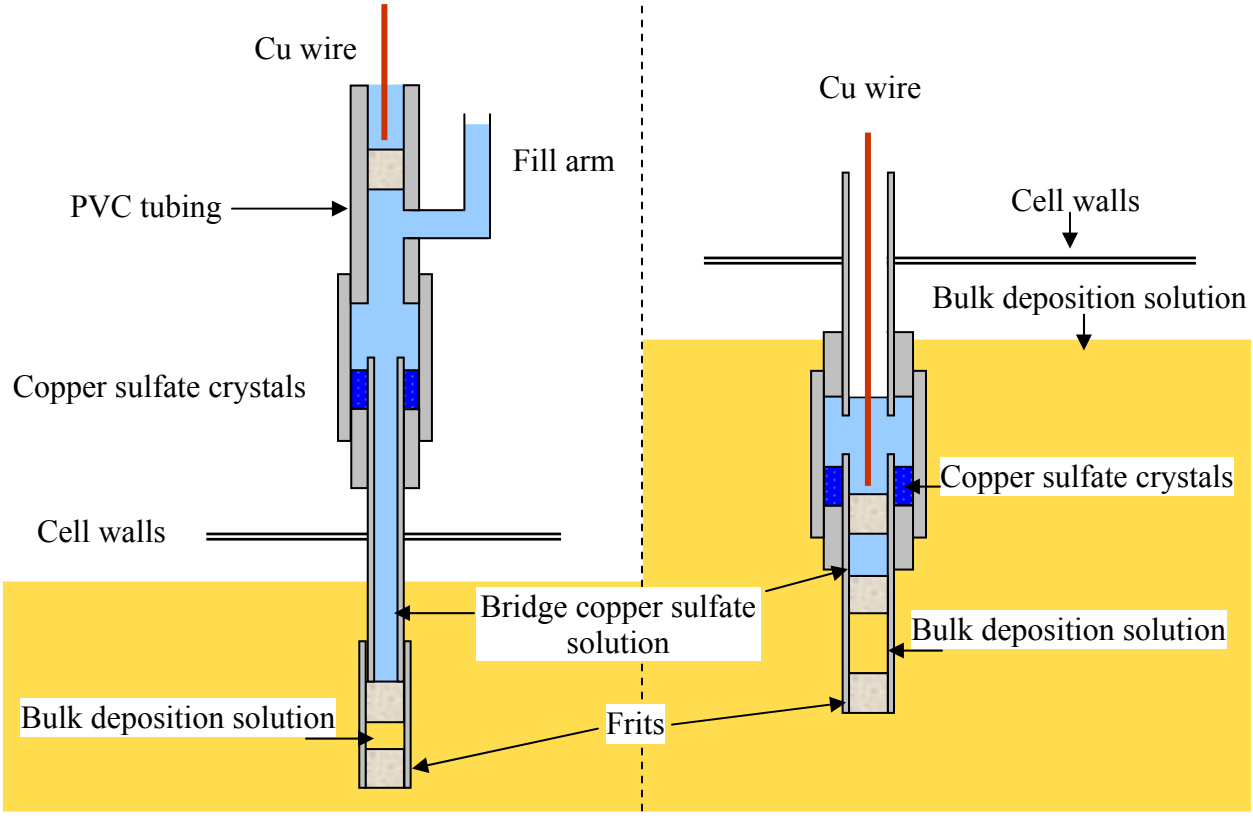

Figure 4-4: Copper sulfate reference electrode schematic
The electrode configuration on the left was used in the reaction kettle deposition cell and the configuration shown on the right was employed in the flask deposition cell. The width of the cells was enlarged to illustrate the cell construction. The frit diameter is 1/8".

4.3 Arsine Collection and Analysis

When arsine (AsH_3) was produced during the arsenic electrodeposition experiments, it was captured using two bubblers in series. Each contained a solution of 0.3% w/v of silver diethyldithiocarbamate and 1 % v/v of morpholine in chloroform that was either made following Standard Methods (Greenberg 1992) or purchased (Ricca Chemicals, 6810-16). In the presence of arsine the solution changes color from pale yellow to red. The concentration of reacted arsine in solution was determined by measuring the absorbance at 520 nm using a spectrophotometer (Varian, Cary 50) following the procedure in Greenberg (1992). The actual amount of arsine evolved is unknown because no standard with a known concentration of arsenic was used to

calibrate the spectroscopic measurements. Instead, the unreacted solution was used as a baseline and intensitites greater than the baseline were considered to have reacted with arsine. The absorbance was assumed to be proportional to the reacted arsine concentration in order to determine a qualitative amount of arsine evolved.

The entire effluent gas handling system connected to the gas-out tube of the flask deposition cell consisted of three bubblers, including the two used in the arsine capture and detection system, as shown in Figure 4-5. The first bubbler was the mineral oil bubbler described in section 4.1. The second and third bubblers contained the chloroform solution. Separating the deposition solution from the arsine detectors ensured that no reaction would occur between the chloroform and the oxidizers. The second bubbler was a 50 mL bubbler with a fine frit to aid gas dispersion (Ace Glass Inc., 7534-10) that was connected to a larger bubbler with no frit (Pyrex, 250 mL). In all of the experiments, the arsine was completely trapped in the second bubbler. The solution in the third bubbler never changed color.

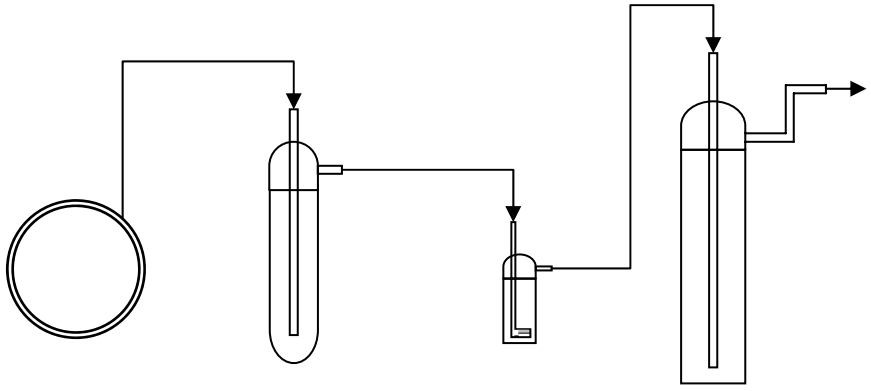

Cell oil bubbler chloroform solution bubblers

Figure 4-5: Gas bubbler system including chloroform solution bubblers

4.4 Equilibrium Measurement Apparatus

A set of experiments was conducted to determine the equilibrium potential of copper deposition. Data were collected by measuring the open circuit potential of a copper rod (3.1 mm

diameter, 99.999% Cu, Alfa Aesar) in copper sulfate solutions of varying concentrations [$1x10^{-6}$ to 1.4 molal (copper sulfate solubility limit)] with reference to a double-junction 3.5 M potassium chloride, silver-silver chloride reference electrode with a 10% KNO_3 salt bridge (Omega Engineering, Inc., PHE 3211). A high-impedance voltmeter (Keithley 197) was used to measure the open circuit potential. All copper sulfate solutions had a concentration of 47 mM sulfuric acid to prevent oxidation of the copper rod. The measurements occurred in a 500 mL three-neck round bottom flask. The solution was sparged with grade 5.6 (99.9996%) argon for at least half an hour and a back pressure was applied using a bubbler with six inches of water. A metal-free filter (Alltech 32170) was placed at the bottom of the cell to disperse the argon evenly throughout the solution. A pH meter was used to monitor the pH of the solutions during the open circuit potential measurements and to determine the appropriate amount of sulfuric acid to add during the initial experiments. The connections between the flask necks and the instruments were made with rubber stoppers with appropriately sized holes. The temperature of the solution was measured with a thermocouple and was set to 25.0 ± 0.3°C using the same bath set-up as shown in Figure 3-4. A stir bar in the flask was used to make sure the solution temperature was uniform and to improve the oxygen removal process. The stir bar was turned off during all open circuit potential measurements.

4.5 Electrical Equipment and Control

Electric power for the deposition experiments were supplied and controlled by a potentiostat (Solartron Analytical, 1286) (for the DC experiments) in combination with a frequency response analyzer (Solartron Analytical, 1250) (for the AC experiments). A computer running CorrWare (Johnson 2002) ran the DC experiments while the program ZPlot (Johnson

2002) was used for the AC experiments. Shielded BNC cables with BNC-to-binding-post attachments connected the electrodes to the potentiostat.

A key part of effectively controlling a cell is ensuring stable conditions. A cell becomes unstable when the output current and the measured voltage are independent of the input polarization voltage. A general schematic of the control system for a potentiostat with an equivalent cell circuit with resistance and capacitance is shown in Figure 4-6. For the three-electrode cell used in the experiments, the second reference electrode is tied to the working electrode.

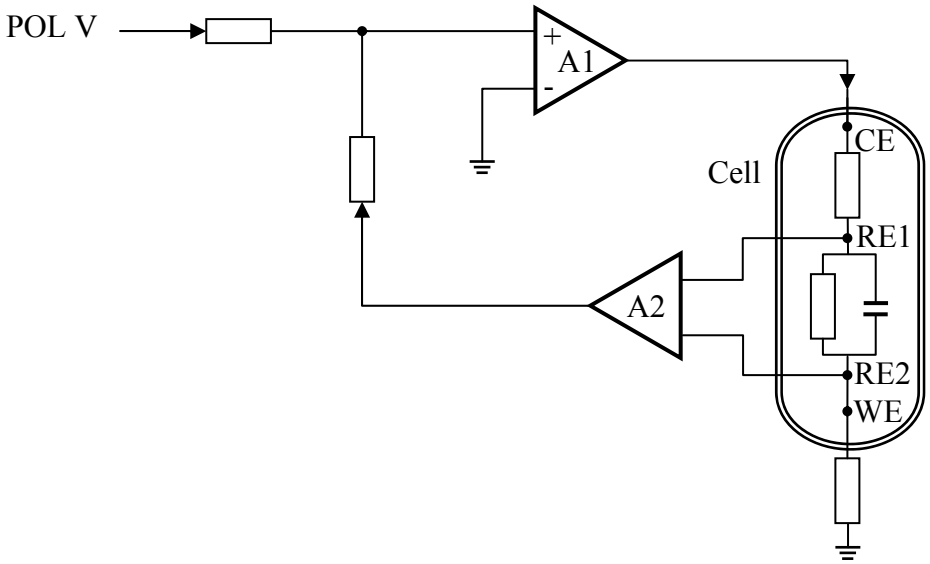

Figure 4-6: Potentiostat and equivalent cell with resistance and capacitance schematic
The polarization voltage (POL V) is selected by the user. The op amps, shown as triangles, provide negative feedback to control the cell. The rectangles are resistive elements and the double parallel lines are capacitors. The outline of the cell is a double line. The schematic is adapted from several schematics in Schlumberger Technologies (1988).

The stability of the cell can be tuned by adjusting the pole of op amp A1. As the pole is decreased, the range of available frequencies, also known as the bandwidth, decreases, which dampens the system. The ideal bandwidth enables the cell to respond quickly to new polarization voltages with minimal overshoot of the desired value. When a cell is unstable, it oscillates when the input is changed. This phenomenon is also known as ringing, and the cell is

said to be underdamped. When the bandwidth is too narrow, it unnecessarily restricts the available measurement frequencies and the cell's response is sluggish (Schlumberger Technologies 1988).

Bandwidth C (> 1 MHz, as defined for the Solarton Analytical potentiostat employed in this study) resulted in a stable response for solid metal working electrodes of 0.25 mm diameter or less. When larger diameter solid and liquid working electrodes were measured for current ranges of 2 mA or greater, the cell was unstable with bandwidth C. The current-range-dependent stability behavior is reasonable since the resistor used to measure current is unique for each range. The largest bandwidth that produced a controlled response was bandwidth E (25 kHz). Since bandwidth E is larger than the greatest frequency used in AC voltammetry, it was acceptable for all large diameter working electrode experiments.

4.6 Voltammetry Methods and Data Analysis

Voltammetry methods that were employed in this study can be categorized based on the use of direct current (DC) only or a combination of DC and alternating current (AC). The bulk of the voltammetry experiments were DC because it is simpler and faster to find DC conditions that yield meaningful results than AC conditions. In general, however, AC can yield more precise results than DC experiments because AC measures current responses that are linearly related to the AC potential. One of the major sources of difficulty with using voltammetry methods to analyze the reactions of interest in this study comes from the fact that most of the available derivations for analysis are for systems where all components are soluble in either the bulk solution or in the electrode (such as a mercury electrode) and not for the case of deposition, where the products are by design insoluble in the bulk solution and the electrode. The bulk of the discussion in this section is based on Bard and Faulkner (2001) except where noted.

4.6.1 Direct Current – General Methodology

Direct current voltammetry is a method for studying electrochemical reactions by controlling the DC electrical potential as a function of time and measuring the current response. Some of the important reaction parameters that can be determined for some types of electrochemical reactions with this method are the standard state potential (E^0), standard reaction rate (k^0), and the transfer coefficient (α), which will be explained later in this section. The two most common methods are the potential step and linear potential sweep methods.

In the potential step method, the potential (E) is initially held at a value where there is no reaction. Then, at time zero, the potential is stepped to a value where the reaction of interest occurs, and the current (I) is measured as a function of time.

The linear potential sweep method is illustrated in Figure 4-7. The potential is swept from a value where the reaction does not occur through the region of interest as illustrated in Figure 4-7(a). In cyclic linear potential sweep voltammetry, the potential is reversed at the switching potential, $E_{\lambda,}$ and swept back to the starting potential. The current is plotted as a function of potential in Figure 4-7(b). Using this method both the cathodic and anodic reactions can be examined. The rate at which the electrical potential is changed with time is called the scan rate (v). In cyclic DC linear potential sweep voltammetry, this potential sweep cycle is usually repeated multiple times to improve experimental precision.

Although the potential step method produces more accurate results than the potential sweep method, it takes many more experiments using the potential step method to get almost the same information that can be collected using the potential sweep method. The potential step method, therefore, is not as well suited for exploring new electrochemical reactions and was not

used in this study. In other sections of this work it should be understood that DC voltammetry refers only to the linear potential sweep method.

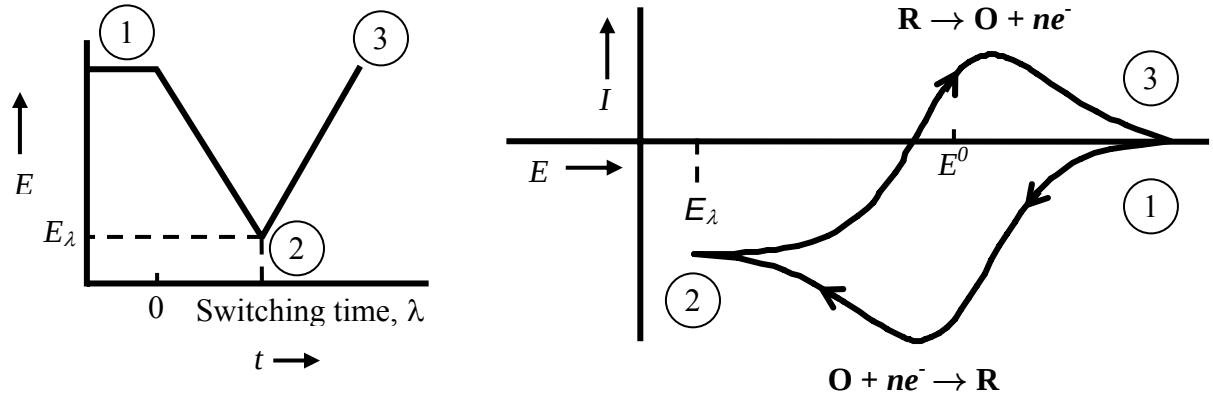

Figure 4-7: DC voltammetry cyclic linear potential sweep method
Each pair of numbered circles corresponds to the same time in each diagram. Diagram (a) shows the electrical potential profile with time. Diagram (b) portrays the ideal current response as a function of electrical potential. The idealized current response assumes reversible kinetics and semi-infinite linear diffusion to an electrode in a quiescent solution. The current response curve was drawn based on the solution to the current function in Bard and Faulkner (2001).

Several key assumptions were made in deriving the ideal current response shown in Figure 4-7 (b): the bulk solution is initially homogeneous and quiescent during the entire experiment; there is semi-infinite linear transient diffusion of the reacting species to the electrode (defined as $c \rightarrow c^*$ at $x = \infty$ for $t > 0$, and $c = c^*$ all x at $t = 0$, where c^* = bulk concentration); all reactions are heterogeneous and occur on the working electrode surface; the reaction rate is mass-transfer controlled, in other words, the heterogeneous charge-transfer kinetics are rapid relative to the transport rate of the active species to the electrode. (This type of system is called reversible.); over the course of the experiments, the amount of species reacted is much smaller than the total amount in solution, and the concentration in the bulk solution is essentially constant; and transport of the reacting species to the electrode occurs only via diffusion, so the flux of species *i* at location *x* (*x* = 0 at the electrode surface) and time *t* ($J_i(x,t)$) is governed by a

simplified form of the Nernst-Planck equation as shown in equation 4-2 where D_i is the diffusion coefficient and c_i is the concentration. The diffusion coefficient is a function of the bulk solution concentration, which was assumed to be constant.

$$J_i(x,t) = -D_i \frac{\partial c_i(x,t)}{\partial x} \tag{4-2}$$

The flux of the species is related to the current of the species (I_i) through the surface area (A) of the electrode, the charge of species i (z_i) and Faraday's constant (F) in equation 4-3.

$$I_i = -J_i z_i F A \tag{4-3}$$

When charge-transfer kinetics are reversible, then the Nernst equation 4-4 applies to the species behavior at the electrode surface.

$$E = E^0 - \frac{RT}{nF} \ln \prod a_i^{\nu_i}$$
where E^0 = standard state potential, R = universal gas constant, (4-4)
T = temperature (K), n = number of electrons,
a_i = activity of species i, ν_i = stoichiometric coefficient of species i

The Nernst equation sets the reversible thermodynamic equilibrium (zero net current) value of the potential based on the activity of the species in the electrochemical reaction. The electrochemical stability diagrams presented in chapter 2 are based on the set of Nernst equations for all possible species in a reaction system. At small solute concentrations, the activity of each species is approximately equal to its concentration and equation 4-4 can be replaced by equation 4-5.

$$E = E^0 - \frac{RT}{nF} \ln \prod c_i^{\nu_i} \tag{4-5}$$

Equation 4-3 was employed in the derivation of the ideal current response in Figure 4-7 as a boundary condition to dictate the ratio of species O (oxidized species) to R (reduced species) at

the electrode surface. Each peak of the ideal current response corresponds to a reaction. The cathodic reaction corresponds to the negative current peak and the anodic reaction corresponds to the positive current peak.

The peak shape is due to the nature of the mass-transfer of the reactant(s) to the electrode as the potential is swept. As the potential is swept to a value where the reaction first occurs, current starts to flow. As the reaction continues, the reactant concentration at the surface decreases and diffusion carries the reactant to the surface down the concentration gradient. Thus the flux of the reactant to the electrode, and in turn the current, increases. As the potential increases to a value greater than E^0, the concentration of the reactant at the surfaces approaches zero and the maximum flux of the reactant to the surface is achieved. The current then reaches its peak value. A further increase of potential with time causes the diffusion layer of the reactant at the electrode surface to grow, in turn decreasing the flux of the reactant to the surface until it approaches zero. The decreasing reactant flux causes the current to decrease and tail off to a constant value. The product then diffuses into the bulk solution. For the ideal current response in Figure 4-7(a) it is assumed that both the reactants and products are soluble in the bulk solution. For a reversible reaction, the value of the potential at the current peak is independent of scan rate.

The peak current (I_p) for a reversible reaction can be related to the mass transport conditions including the bulk concentration of species i (c_i^*) through equation 4-6.

$$I_p = 0.4463\left(\frac{F^3}{RT}\right)^{1/2} n^{3/2} A D_i^{1/2} c_i^* v^{1/2} \tag{4-6}$$

If one and only one of the parameters on the right hand side of equation 4-6 is unknown (such as area or diffusion coefficient), measurement of the peak current as a function of the scan rate can

be used to determine the unknown parameter. This technique was used to confirm the working electrode area as part of this study.

The potential at half of the peak current ($E_{p/2}$) is related to the equilibrium potential through the diffusion coefficients of the reactant and product in equation 4-7.

$$E_{p/2} = E^0 + \frac{RT}{nF}\left(1.09 + \ln\left(\frac{D_{\text{product}}}{D_{\text{reactant}}}\right)^{1/2}\right) \tag{4-7}$$

The relation between the peak potential (E_p) and the half peak potential can be employed to determine if a current wave was produced by a reversible reaction. If it is reversible, then it should follow equation 4-8.

$$\left|E_p - E_{p/2}\right| = 2.20\frac{RT}{nF} \tag{4-8}$$

To move beyond the purely reversible case, it is helpful to look at the general relation for the applied potential and the current through the Butler-Volmer equation for the reaction $\mathrm{O} + ne^- \rightleftharpoons \mathrm{R}$.

$$i = nFAk^0\left[a_O(0,t)e^{-\alpha f\left(E-E^0\right)} - a_R(0,t)e^{(1-\alpha)f\left(E-E^0\right)}\right]$$

where i = current, k^0 = standard reaction rate,
$a(0,t)$ = activity at the electrode surface (x=0) as a function of time, t,
α = transfer coefficient, $f \equiv \frac{F}{RT}$ (4-9)

The transfer coefficient is a measure of the symmetry of the energy barrier between the reactants and products and ranges from 0 to 1, with ½ indicating a symmetrical barrier, < ½ favoring the reactants, and > ½ favoring the products. Equation 4-9 shows that as ($E - E^0$), also known as the overpotential (η), increases, the current increases exponentially. Equation 4-4, in combination with Fick's laws and a concentration-to-activity relationship yields the time dependent surface

concentrations of species O and R regardless of the reversibility of the system. For the very rapid kinetics, compared to the sweep rates that are present in a reversible system, equation 4-8 can generally be simplified to an equation similar to equation 4-4 where the kinetic parameters k^0 and α are not present in the equation.

The anodic portion of equation 4-9 is the portion multiplied by a_O while the cathodic portion is the portion multiplied by a_R. For an irreversible system, the anodic and cathodic portions of equation 4-9 are of different orders of magnitude, so only the larger portion has to be included as a boundary condition in the current response derivation. For a quasireversible system both portions of equation 4-9 are of the same order of magnitude, and thus the entire equation has to be employed as a boundary condition in the current response derivation. A general way to classify the reversibility of a system under study at a particular scan rate was developed by Matsuda and Ayabe (1955) using the parameter Λ.

$$\Lambda \equiv \frac{k^0}{\left(D_O^{1-\alpha} D_R^{\alpha} fv\right)^{1/2}} \tag{4-10}$$

$$\begin{aligned} &\text{Reversible:} && \Lambda \geq 15 \\ &\text{Quasireversible:} && 15 \geq \Lambda \geq 10^{-2(1+\alpha)} \\ &\text{Irreversible:} && \Lambda \leq 10^{-2(1+\alpha)} \end{aligned} \tag{4-11}$$

For an irreversible system where $n = 1$, the peak current and the peak potential have been related to the mass-transport and heterogeneous charge-transfer parameters with equations 4-12 to 14.

$$I_p = \left(2.99\text{x}10^5\right) \alpha^{1/2} A c_i^* D_i^{1/2} v^{1/2} \tag{4-12}$$

$$E_p = E^0 - \frac{RT}{\alpha F}\left[0.780 + \ln\left(\frac{D_i^{1/2}}{k^0}\right) + \ln\left(\frac{\alpha F v}{RT}\right)^{1/2}\right] \tag{4-13}$$

$$\left|E_p - E_{p/2}\right| = \frac{1.857RT}{\alpha F} \tag{4-14}$$

Unlike the reversible system current response, for the irreversible system, E_p is a function of scan rate. Increasing the scan rate shifts E_p away from E^0 to a more negative potential for a cathodic reaction and to a more positive potential for an anodic reaction. If the irreversible process is more complicated than a one-step, one-electron process, then digital simulations are employed instead of theoretical derivations.

The current response for a quasireversible system is a function of the same parameters as the reversible current response plus another parameter ($\Psi(E)$) that was only defined graphically in Bard and Faulkner (2001). It is useful to note that for a quasireversible system, unlike a reversible system, I_p is not a proportional to $v^{1/2}$. As the parameter Λ increases, the current wave becomes narrower and taller and approaches the reversible current response.

In the preceding portion of this section, it was assumed that the reactants and products of the heterogeneous electrochemical reaction were soluble either in the bulk solution or in the electrode. Berzins and Delahay (1953) have considered the case of deposition of an insoluble reduction product assuming reversible deposition. They follow a development similar to the derivation for a soluble reduction product. The key difference in their derivation is that the boundary condition for the reduction product is not its activity in solution at the electrode surface, but a specified standard state of activity of unity for the insoluble reaction product in a pure, solid form. This assumption is good if there is at least a monolayer of the product present on the electrode and that the deposition product is elementally pure. These conditions are not met when the deposit is first formed as small islands at the most active sites on the electrode surface. In this study, these conditions were best met for copper deposition on a copper electrode. The theoretical current response as a function of potential for an insoluble reduction

product is shown in equation 4-15.

$$I = 2nF\left(\frac{nF}{\pi RT}\right)^{1/2} Ac_i^* D_i^{1/2} v^{1/2} \Phi\left[\left(\frac{nF}{RT}\right)^{1/2}\left(E^0 - E + \frac{RT}{nF}\ln a_i\right)^{1/2}\right] \tag{4-15}$$

$$\text{where } \Phi[s] \equiv e^{-s^2}\int_0^s e^{z^2} dz$$

Substituting the maximum value of function Φ, 0.5410 (at a value of $\alpha = 0.9241$), yields the peak current and potential as shown in equations 4-16 and 4-17.

$$I_p = 1.082nF\left(\frac{nF}{\pi RT}\right)^{1/2} Ac_i^* D_i^{1/2} v^{1/2} \tag{4-16}$$

$$E_p = E^0 + \frac{RT}{nF}\ln a_i - 0.854\frac{RT}{nF} \tag{4-17}$$

The major problems with applying this derivation to real systems are determining an accurate activity for the reactant and assuming unit activity for the product. When a metal is deposited on a dissimilar substrate, there is not a monolayer of material on the electrode during the early portion of the peak, so the activity of the species is not unity. Experimental deposition of cadmium from a solution of 0.5 mM cadmium and 1 M potassium chloride on a platinum electrode has shown that although the peak heights had a linear dependence on the square root of the scan rate, the measured peak heights were about 20% lower than the predicted values. Berzins and Delahay (1953) attribute this difference to uncertainty in the area of the electrode and the use of the infinite dilution diffusion coefficient that overestimates the actual diffusion coefficient. The shape of the experimental current curve was significantly narrower than the predicted curve. Berzins and Delahay hypothesized that this difference was due to the changing activity of the cadmium deposit as the first layer of cadmium built up on the electrode. An improved model of deposition would have to include a model of the changing activity of the

deposit as deposition progresses and would need to include a general scheme of the initial islands of deposits and their growth to form a layer that completely covers the electrode surface.

For all systems, regardless of their reversibility, the sweeping of the electrochemical potential with time gives rise to a charging current (I_c) that is not related to the current due to the electrochemical reaction. The charging current arises from the differential capacitance of the electrical double layer at the electrode surface (C_d) and is proportional to the scan rate.

$$\left|I_c\right| = AC_d v \tag{4-18}$$

For a reversible system, the ratio of charging current to peak current increases with increasing scan rate and decreasing bulk concentration of the reactant, O.

$$\frac{\left|I_c\right|}{I_p} = \frac{C_d v^{1/2}\left(10^{-5}\right)}{2.69 n^{3/2} D_i^{1/2} c_i^*} \tag{4-19}$$

A charging current is not the only case where multiple currents can obscure the current response. For a system with multiple electrochemical reactions, a potential sweep voltammogram can give rise to multiple peaks. These can be consecutive reaction systems (A → B → C) or they can be separate reaction systems. When electrochemical reactions occur simultaneously as in the second case the current responses are additive. As the potential difference between the current peaks decreases it becomes increasingly difficult to determine the baseline current for the second peak. In the case of a reaction with the solvent found in excess, such as hydrogen or oxygen formation in water, the peak never decreases.

4.6.2 Direct Current – Applications to this Study

The conditions and reactions studied in this work differ from the reversible current response in several important ways. First, the total current in a quiescent solution is the sum of the current due to diffusion of charged species to the electrode plus the current due to migration

of charged species in an electric field. The first term on the right hand side of equation 4-20 is the diffusion contribution and the second term is the migration contribution, where ϕ is the electrostatic potential.

$$I = FA\sum_i z_i D_i \frac{\partial c_i}{\partial x} + \frac{F^2 A}{RT}\frac{\partial \phi}{\partial x}\sum_i z_i^2 D_i c_i \tag{4-20}$$

In order to ensure that the majority of the current for the electroactive species is due to diffusion instead of migration, there needs to be a supporting electrolyte (capable of carrying charge but not electroactive) several orders of magnitude greater than the electroactive species. Equation 4-21 illustrates the need for a supporting (inert) electrolyte by showing the ratio of the total current to the current due to diffusion (I_D) for an electroactive cation with charge $+z_C$ and an anion with charge $-z_A$ in an inert electrolyte with the same two charges on its ion, and with g the concentration ratio of electrolyte to electroactive ion (Britz 2005).

$$\frac{I}{I_D} = \left(1 + \left|\frac{z_C}{z_A}\right|\right)(1+g)\left(1 - \left(\frac{g}{1+g}\right)^p\right)$$
$$\text{where } p = \left(1 + \left|\frac{z_C}{z_A}\right|\right)^{-1} \tag{4-21}$$

In the great majority of the experimental runs performed in this study, the electroactive species concentration is of the same order of magnitude or greater than the concentration of the supporting electrolyte, sulfuric acid. Thus, there is significant error in determining the standard electrochemical potential of a deposition reaction from a DC voltammogram due to migration of the electroactive species.

Copper deposition at low scan rates is close to reversible. The deposition of chromium has been found experimentally, however, to be quasireversible, and that of arsenic is probably irreversible, and thus the Nernst equation does not dictate the ratio of species O to R at the

electrode surface for the arsenic and chromium DC voltammetry results. Instead of having a mass-transfer-limited current response, as in the case of a reversible reaction, the quasireversible and irreversible current responses are under the mixed control of mass- and charge-transfer. Given that the arsenic and chromium systems included multiple reduction steps and multiple electron transfer, it is not feasible to derive a theoretical solution for their current responses. The voltammograms are further complicated by the generation of hydrogen in parallel with the metal reduction. Since the addition of chromium trioxide, one of the reactants, affects the pH, it is not possible to obtain a completely accurate background scan. In order to try to make the system behave more reversibly, a slow scan rate was used for most of the experimental runs.

The derivation of the equations for reversible deposition of an insoluble substance can be applied to copper deposition. It cannot, unfortunately, be applied to the case of codeposition of two insoluble substances since their activities on the working electrode are not unity. When an alloy or compound is deposited from a multicomponent solution, the activity of the individual elements deviates even further from unity.

The DC linear potential sweep voltammetry method can be used to determine the approximate value of the electrochemical potential at which a deposition reaction occurs; however, it possible to further refine the value by using a method similar to the potential step method. A clean working electrode is initially held at a potential at which no deposition occurs. The potential is then stepped to a value slightly below where the potential sweep method suggests that deposition should begin and held at that value for approximately ½ hour to 2 hours depending on the rate of deposition. The experiment is terminated and the working electrode is examined for the presence of a deposit. These experimental steps are repeated with more cathodic potential each time until a deposit is found. The precision of the deposition potential

measurement depends on the gradation between the potential steps. In the case where the deposit can be electrically stripped from the working electrode without affecting the electrode (or multiple working electrodes are available), it is possible to overshoot the deposition potential and then work backwards to find it. If the stripping of the deposit can be seen using a linear sweep voltammogram of the anodic sweep, then that can also be used to determine if deposition has occurred.

4.6.3 Alternating Current

Alternating current (AC) voltammetry includes a wide variety of methods. This section will focus on the method employed in the current study in which the DC potential (E_{DC}) was varied linearly on a long time scale compared to that of the superimposed AC variation of the potential ($\dot{E}$, with the dot indicating a phasor, or rotating vector, with magnitude and frequency). The DC potential was varied in the same manner as the linear method discussed in the previous section. The important measured quantities were the magnitude of the AC component of the current and the phase angle between the alternating current and the alternating potential as a function of the DC potential.

AC voltammetry has the potential to yield important thermodynamic and kinetic parameters without much distortion due to charging current. The DC potential is swept slowly (10 mV/sec for the current study) to minimize charging currents. The magnitude of the AC variation of the potential (10mV for this study) is small enough to stay within the linear range of the current-to-potential relationship.

The conditions to yield meaningful AC voltammetry results are more complicated than DC voltammetry. It was found in this study that for some systems only a limited range of AC frequencies yielded clearly defined peaks for the reaction(s) of interest. The maximum AC

frequency is also limited by the maximum skew rate (change in potential per unit time) of the potentiostat. DC voltammetry was always done before AC voltammetry in order to find the DC potential range of interest.

The theory for AC voltammetry that is available in the literature is only for the case of a soluble product and reactant. The theory is considerably more complicated than for DC voltammetry, although it may be possible to derive a similar theory for the case of an insoluble product assuming unit activity. There would probably be similar distortion with the AC results as there are with the DC result because the product does not have unit activity throughout the deposition.

The plot of the magnitude of the AC component of the current as a function of the DC potential yields two positive peaks. For a reversible reaction, the peaks directly overlap each other. As the irreversibility of the reaction increases, the peaks move apart in the DC potential scan direction and their heights decrease unevenly, as shown in Figure 4-8.

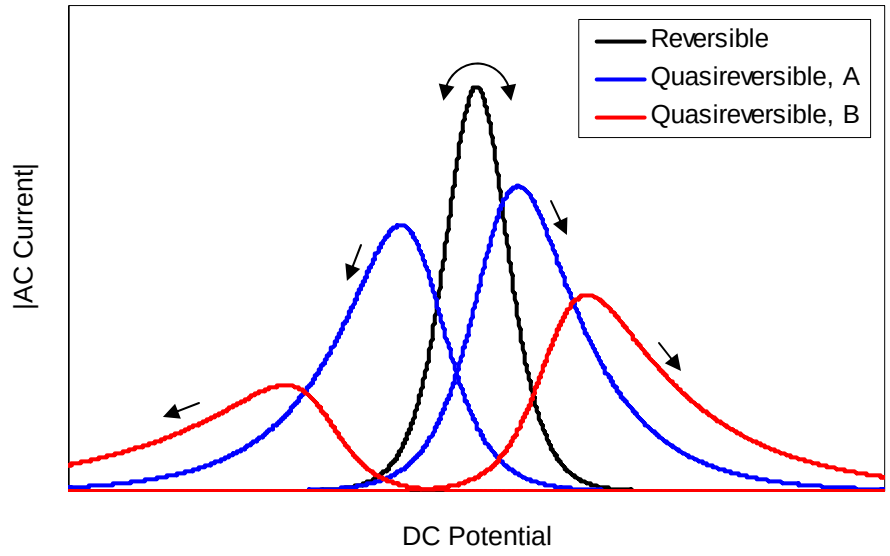

Figure 4-8: AC voltammetry traces for reversible and quasireversible system
Trace A has a larger heterogeneous reaction rate than trace B. Traces of reversible and quasireversible systems based on equations from Bard and Faulkner (2001). Arrows indicate direction of DC potential scan.

For the reversible case, the peak potential is related to the equilibrium potential.

$$E_p = E^0 + \frac{RT}{nF} \ln \left(\frac{D_{\text{product}}}{D_{\text{reactant}}} \right)^{1/2} \tag{4-22}$$

Kinetic parameters can be found for the quasireversible and irreversible cases by measuring the maximum peak phase angle between the alternating current and the alternating potential as a function of frequency. Once the kinetic parameters have been found, they can be used to relate the potential at the peak of the magnitude of the AC component of the current to the equilibrium potential. AC voltammetry can be used to push a reversible reaction into a quasireversible regime by increasing the frequency of the AC potential and thus allowing measurement of kinetic parameters that would not have been obtainable with DC voltammetry. For soluble reactants and products, AC voltammetry usually yields more precise kinetic parameters than DC voltammetry because AC measurements occur in the range of the linear current-potential relationship. Theoretical development of the AC cyclic voltammetry for insoluble products would be required before a determination of its measurement accuracy for kinetic parameters can be formulated.

4.7 Energy-Dispersive X-Ray with Scanning Electron Microscope

Energy-dispersive X-ray microanalysis of the electro-deposited samples was performed in a scanning electron microscope (FEI/Philips XL30 FEG ESEM, MIT Center for Materials Science), abbreviated as ESEM. This discussion of the ESEM is based on Garratt-Reed and Bell (2003). In ESEM, the SEM probes the sample with a focused column of electrons at a user preset beam energy and with a user preset beam spot size. The beam is scanned across the sample and the resulting excited radiation is detected by the energy-dispersive X-ray detector. The result is a spectrum of varying intensity as a function of electron energy. Each element has a

unique fingerprint of intensity as a function of electron energy that allows it to be identified. This analysis provides a semiquantitative determination of the weight percent of each element in the sample, but it provides no information about the compounds actually present in the sample. The accuracy of the determination increases with the atomic weight of the element. Thus, the weight percent analysis is particularly poor for oxygen in comparison to copper, arsenic, and chromium. The ESEM analysis of the recorded spectrum used a computer program (Genesis Spectrum, EDAX Inc, 2003) to deconvolute overlapping peaks from multiple elements in order to determine the response due to each element. A quantitative elemental analysis could be achieved by calibrating the machine with a series of samples of known compositions that span the range of the unknown sample. ESEM calibration was not performed for this study.

ESEM analysis was used to determine the elemental composition of the electro-deposits that were fabricated in this study. An additional degree of uncertainty was introduced in the ESEM analysis of many of the electro-deposited samples because they were not completely planar, nor were they homogeneous or polished, all three of which are requirement for a good ESEM analysis. For thin electro-deposited samples, the uncertainty in the ESEM results is also increased because the underlying substrate may be contributing to the measured X-ray spectrum. The depth of penetration of the ESEM varies directly with the beam strength and is dependent on the sample composition. In general the depth of penetration is in the range of 0.1 to 5 microns.

ESEM can be used to analyze a spot or an area of a sample. As the electron beam penetrates the sample, the volume of interaction with the substrate grows such that a cross-section of the sample parallel to the beam direction shows a teardrop shape. Thus, the results of a spot ESEM analysis would also include, to a lesser extent, a small circle of the surrounding material.

A picture of the areas where an element is present in the sample can be made using X-ray mapping. In this technique, a spectrum of the entire sample is taken and the peaks corresponding to each element are identified. The sample is then broken up into a grid of evenly spaced squares. There is one map for each element. Each square is scanned for a set amount of time and if an element is detected, then the square on the map of that element is darkened. This process is repeated multiple times for each element. The entire process can be repeated to improve the resolution of the X-ray map.

In addition to the energy-dispersive X-ray detector, information about the sample can be collected using the gaseous secondary electron detector (GSE) and the backscatter electron detector (BSE). The GSE produces a grayscale topographical image of the sample. In contrast, the BSE provides no topographical information, instead it shows the average atomic weight of the sample. The BSE is useful in quickly identifying regions of different elemental composition with images.

4.8 X-Ray Diffraction

The X-ray diffraction (XRD) method is based on bombarding a sample with monochromatic X-rays over a range of angles. The angle is defined as being between the incident X-ray and the plane of the sample and can range from ~0 to 90 degrees. The intensity of the resulting diffracted beam of scattered X-rays is measured as a function of the angle of incidence. The diffraction patterns are a function of the crystal lattices present in the sample and can be matched to the structure of known samples, thus allowing identification of the compounds in the unknown sample. The matching procedure, assisted by a computer program, first determines a list of possible substances based on the possible elements present in the unknown sample. (The elements present could first be determined using ESEM.) Next, the spectrum of

each known substance is compared to the unknown spectrum. If the tallest three peaks of the known substance's spectrum are at the same angle and have the same ratio of intensities, it is usually considered to match the unknown spectrum and thus is present in the sample (Cullity and Stock 2001).

In order for XRD to be effective, the sample should diffract nearly all of the incoming X-rays. The sample thickness required varies with the elements present and the particular XRD machine employed, and is inversely proportional to the sample density. For metal samples it is usually on the order of tens of microns (Pecharsky and Zavalij 2003). XRD requires a larger sample size than ESEM, so all samples that can be analyzed with XRD can also be analyzed with ESEM.

XRD was used to determine the compounds present in electro-deposited samples. The solid working electrodes did not fit in the XRD machine used in this study (Siemens X-Ray Diffractometer D5000, Cu k-alpha radiation), although it is possible that they would fit in an XRD machine with a different type of sample holder. Only samples that could be removed from the working electrode and that were large enough to produce a good signal could be analyzed using XRD. The only electro-deposits that fit this criteria were those produced in a solution with at least three components, including sulfuric acid. All of the samples were analyzed from an angle of 10 to 60 degrees with a point taken for 3 seconds every 0.025 degrees.

4.9 X-Ray Photoelectron Spectroscopy

X-ray photoelectron spectroscopy (XPS), also known as electron spectroscopy for chemical analysis, is based on the photoelectric effect. In this technique, the surface of a sample is bombarded with protons of a preset energy, resulting in the ejection of photoelectrons (Walker and Morton 1998). The energy of the photoelectrons is measured using a concentric

hemispherical analyzer. The energies are plotted as a function of photoelectron energy, and the result is an energy spectrum with a series of peaks that correspond to the elements in each species in the sample. The area under each peak directly corresponds to the surface concentration of the species. The peaks are shifted based on the chemical bonding of the elements and are identified via comparison either to databases of known samples or to known samples measured as a reference. XPS is sensitive to all elements except hydrogen and helium. XPS is performed under ultra high vacuum (UHV) conditions ($<10^{-9}$ millibar) to ensure that the sample surface is free of adhered gas molecules.

XPS was employed in this study in an attempt to determine the chemical bonding of the electrodeposited samples. Since the epoxy that was part of the electrodes could contain trapped gases that would prevent the machine (Axis Ultra, Kratos Analytical, aluminum K alpha source) from reaching UHV conditions, the samples were removed from the electrodes before analysis (Shaw 2006). The only electro-deposits that were large enough to be removed from the working electrodes were those produced in a solution with at least three components, including sulfuric acid. The powder samples quickly became charged and could not easily be dropped onto the copper tape sample mount. Carbon 1s was used as the internal reference peak. Elizabeth Shaw of the MIT Center for Materials Science and Engineering mounted the samples, operated the XPS machine, and curve fitted the spectrums. The authors attempted to identify the peaks in the spectrums based on the NIST XPS database (Wagner 2003) and the LaSurface.com XPS database (Benoit 2006).

4.10 Conclusions

Two types of three-electrode deposition cells were fabricated and utilized for deposition experiments. The flask deposition cell was used for the majority of the experiments because it

was better able to prevent diffusion of oxygen into the cell and diffusion of arsine out of the cell. Working, reference, and counter electrodes were specially designed and fabricated for the deposition studies for use in the deposition cells. The working electrode surfaces faced upwards to aid in the release of bubbles produced on their surface. The reference electrodes were of the copper sulfate reference electrode type and a triple-junction design was used to minimize cross-contamination between the reference electrolyte and the bulk solution.

Two types of voltammetry methods were used for the deposition studies – DC and AC cyclic voltammetry. DC voltammetry was used more frequently because it is a better tool for finding deposition conditions and the theoretical analysis for insoluble deposition products has been published (Berzins and Delahay 1953). AC voltammetry had the potential of yielding more accurate results than DC voltammetry because it measures the current response in the linear range of the current-potential relationship, but the theory for insoluble products in not currently available.

The deposition products were characterized using energy-dispersive X-ray microanalysis in a scanning electron microscope. This method determined the elemental composition of the samples and their morphology. XRD analysis of a limited number of samples was performed to identify the compounds present in the deposits. XPS analysis was performed an attempt to confirm the XRD results and to characterize the non-crystalline portion of the electro-deposited samples.

4.11 References

Bard, A. J. and L. R. Faulkner (2001). Electrochemical Methods: Fundamentals and Applications. New York, John Wiley & Sons, Inc.

Benoit, R. (2006). LaSurface.com XPS Database, Centre National de la Recherche Scientifique and ThermoElectron Corp. **2006**.

Berzins, T. and P. Delahay (1953). "Oscillographic polarographic waves for the reversible deposition of metals on solid electrodes." Journal of the American Chemical Society **75**: 555-559.

Bockris, J. O'M., A. K. N. Reddy and M. Gamboa-Adeco (2000). Modern Electrodchemistry: Fundamentals of Electrodics. New York, Kluwer Academic/Plenum Publishers.

Britz, D. (2005). Digital Simulation in Electrochemistry. Berlin Heidelberg, Springer-Verlag.

Cullity, B. D. and S. R. Stock (2001). Elements of X-Ray Diffraction. Upper Saddle River, NJ, Prentice Hall.

Garratt-Reed, A. J. and D. C. Bell (2003). Energy-Dispersive X-Ray Analysis in the Electron Microscope. Oxford, UK, BIOS Scientific Publishers Limited.

Greenberg, A. E., L. S. Clesceri, A. D. Eaton and M. A. H. Franson, Eds. (1992). Standard Methods for the Examination of Water and Wastewater. Washington DC, American Public Health Association.

Hach Company (2000). sension™6 Portable Dissolved Oxygen Meter Instruction Manual. USA, Hach Company.

Johnson, D. (2002). CorrWare for Windows. Southern Pines, NC, Scribner Associates Incorporated.

Johnson, D. (2002). ZPlot for Windows. Southern Pines, NC, Scribner Associates Incorporated.

Lide, D. R., Ed. (1992). CRC Handbook of Chemistry and Physics. Boca Raton, CRC Press.

Matsuda, H. and Y. Ayabe (1955). "The theory of the cathode-ray polarography of Randles-Sevcik." Zeitschrift fuer Elektrochemie und Angewandte Physikalische Chemie **59**: 494-503.

Pecharsky, V. K. and P. Y. Zavalij (2003). Fundamentals of Powder Diffraction and Structural Characterization of Materials. Boston, Kluwer Academic Publishers.

Schlumberger Technologies (1988). 1286 Electrochemical Interface Operating Manual. Hampshire, England.

Shaw, E. (2006). H. Stern. Cambridge, MA.

Wagner, C. D., A. V. Naumkin, A. Kraut-Vass, J. W. Allison, C. J. Powell and J. R. R. Jr. (2003). NIST X-ray Photoelectron Spectroscopy Database, U.S. Secretary of Commerce. **2006**.

Walker, C. and S. Morton (1998). Surface Science Techniques, UK Surface Analysis Forum. **2006**.

Wang, Y. L., Y. Y. Doong, T. S. Chem and J. S. Haung (1994). "Oxidation of liquid gallium surface: Nonequilibrium growth kinetics in 2+1 dimensions." Journal of Vacuum Science Technology A **12**(4): 2081-2086.

5 Single Component Solution Deposition Results and Discussion

The deposition behavior of single-component solutions of copper, chromium, and arsenic in dilute sulfuric acid was studied on solid working electrodes in order to set a baseline for the multicomponent solutions that are examined in Chapter 6. Arsenic deposition was also examined on a liquid gallium working electrode.

Industrial processes for copper and chromium deposition exist and use high concentrations (>1 M) of the metals. For remediation of CCA wastes using electrolytic deposition, it is important to be able to deposit copper, chromium, and arsenic over a wide range of solution concentrations. In general, as the concentration of the species to be deposited decreases, it becomes increasingly difficult to deposit it. For this reason, the bulk of the experimental work is focused at lower metal concentrations. This chapter characterizes the deposition behavior of copper, chromium, and arsenic in dilute sulfuric acid solutions in order to better understand the role of each of these metals in the multi-component deposition experiments that are presented in Chapter 6.

5.1 Copper

Copper is one of the most commonly plated metals. Standard industrial copper plating baths include complex ion systems, such as alkaline cyanide and pyrophosphate, and simple ion systems, such as acid sulfate and fluoroborate. The most frequently used bath solution consists of a mixture of copper sulfate and sulfuric acid in water (Dini 2000). The sulfuric acid concentration has a large influence on the polarization of the cathode and anode with the polarization reaching a minimum at 0.4 M sulfuric acid. Copper can be deposited from a wide range of solution concentrations, although a higher concentration of copper sulfate (~1 M) is

required to achieve high current densities. Conventional solutions for an acid copper sulfate bath are 0.8 to 1.0 M copper sulfate pentahydrate and 0.5 to 1.0 M sulfuric acid.

5.1.1 Equilibrium Measurements

The electrochemical stability analysis of copper in Chapter 2 shows that deposition of neutral copper from an acidic solution is dependent on the bivalent copper concentration.

$$Cu^{2+} + 2e^{-} \rightarrow Cu$$

The equilibrium deposition potential for copper ($E_{Cu^{2+}/Cu}$) is related to the standard state potential ($E^{0}_{Cu^{2+}/Cu}$) (25°C, 1 atm, and 1 molal Cu^{2+}) through the Nernst equation (5-1) (Pourbaix 1974). It is assumed that the activity of solid copper is one; the activity of Cu^{2+} ion can be approximated by its molality (the activity coefficient is equal to one); copper sulfate dissociates completely into Cu^{2+} and SO_4^{2-}; the solution temperature is 25°C; and n, the number of electrons transferred in the deposition of Cu^{2+}, is two.

$$E_{Cu^{2+}/Cu} = E^{0}_{Cu^{2+}/Cu} - \left(\frac{RT}{nF}\right)\ln\left(\frac{a_{Cu}}{a_{Cu^{2+}}}\right) \approx 0.337 + 0.0295\log\left(c_{Cu^{2+}}\right) \qquad (5\text{-}1)$$

As the concentration of copper sulfate increases, the predicted equilibrium potential will increasingly deviate from the measured potential as the activity coefficient of Cu^{2+} deviates from unity. Open circuit (equilibrium) potential measurements of copper in contact with copper sulfate solutions of varying concentrations were performed to determine the range of applicability of equation 5-1. A small amount of sulfuric acid (47 mM) was added to the copper sulfate solutions to prevent copper oxidation. All experiments were run at 25.0±0.3°C using the experimental set-up described in Section 4.4. The copper wire was connected to the silver-silver chloride reference electrode through the following electrical couple, where / indicates a phase boundary and // denotes a porous frit: Cu(s)/ $CuSO_4$ (varying concentration), H_2SO_4 (47 mM) //

KNO_3 (10%) // KCl (3.8M), AgCl (sat) /AgCl/ Ag The electrochemical potentials are given in reference to the normal hydrogen electrode (NHE). Figure 5-1 shows the results of the experimental measurements, calculated values for equation 5-1, and the available literature results (Pawel 1998) over the copper sulfate concentration range from $1x10^{-6}$ to 1.4 molal (copper sulfate saturation) at 22°C. The results from Pawel were given in reference to the saturated copper sulfate reference electrode and have been referenced to NHE based on the results in Chapter 3. The experimental results are about 4 mV less than those predicted by equation 5-1 over the concentration range of $1x10^{-5}$ to $1x10^{-1}$ molal. This systematic error may be due to an error in the assumed potential of +205 mV for the 3.8 M KCl silver-silver chloride reference electrode in reference to the NHE. The potential value was provided by Omega Engineering, Inc. (2003) and is the same as the value listed for the 3.5 M KCl silver-silver chloride reference electrode (Bates 1973). Alternatively, the small systematic error may arise from the common ion effect due to the 47 mM sulfuric acid that was added to the copper sulfate solutions. Since the deviation of the experimental results from Pourbaix (1974) is small, equation 5-1 is a good approximation of the experimental results over the copper concentration range of $1x10^{-5}$ to $1x10^{-1}$ molal. Pawel's results only measured the potential at the high end of the concentration range and show a larger deviation from Pourbaix than do the experimental results of the current study; however, they do display the trend that their deviation from the Pourbaix results increases as copper concentration increases which is the same trend shown in the results from this study. The difference between the experimental results and Pawel's results probably arises from the use of different reference electrodes and salt bridges in the experimental set-up which would lead to different liquid junction potentials.

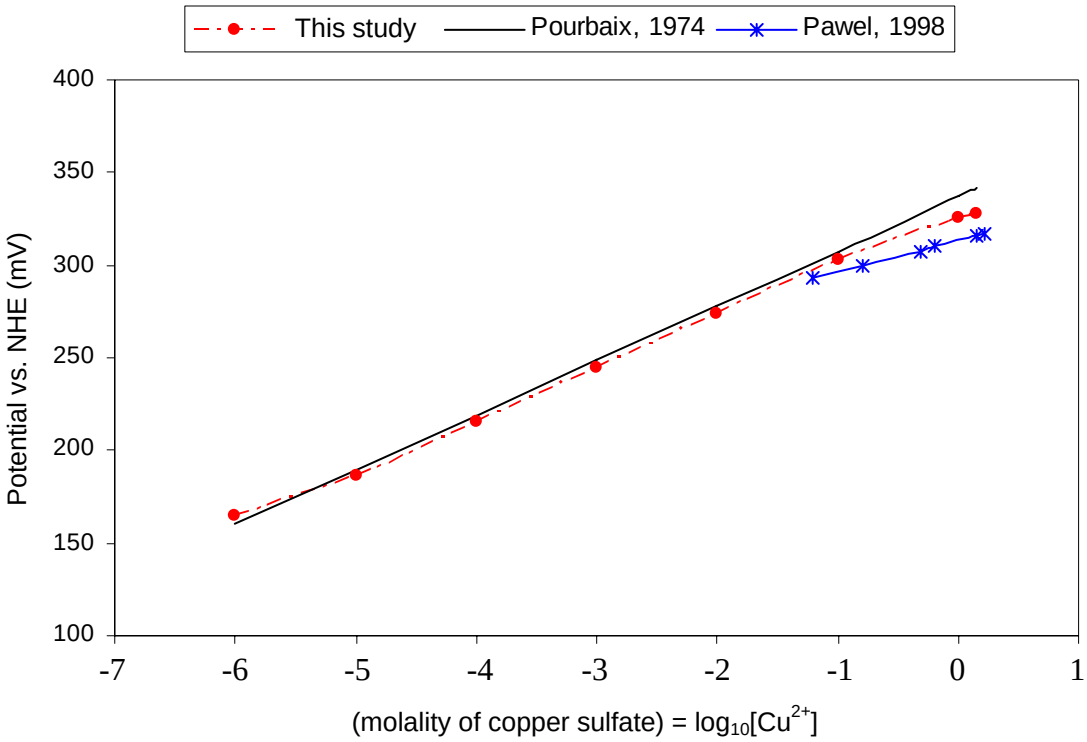

Figure 5-1: Equilibrium potential of Cu – Cu^{2+}, at 25°C

The greatest source of measurement error at high copper sulfate concentrations (> 0.1 molal $CuSO_4$) is probably the liquid junction potential (LJP) between the reference electrode and the bulk copper sulfate solution. The LJP of the silver-silver chloride reference electrode with a 10% KNO_3 salt bridge in contact with the bulk solution increases as the copper sulfate bulk concentration increases. At lower copper sulfate concentrations (< 0.01 molal $CuSO_4$), K^+ and NO_3^- ions, which have almost the same mobility, carry the majority of the current across the liquid junction, and thus serve to nearly cancel out the liquid junction potential.

The error in the potential measurements at the lowest copper sulfate concentration in Figure 5-1 is most likely largely due to dissolved oxygen in solution since the rubber stoppers used to make the hose and electrode connections are permeable to oxygen. This phenomenon is particularly evident at a copper concentration of $1x10^{-6}$ molal where the potential is greater than

that predicted by equation 5-1. Dissolved oxygen in equilibrium with water gives rise to a positive potential.

$$O_2 + 4H^+ + 4e^- \leftrightarrow 2H_2O \; ; \; E_{O_2/H_2O} = 1.229 - 0.059\text{pH} \qquad (5\text{-}2)$$

As the concentration of copper decreases, the percent of total current due to the oxygen reaction increases. Thus, the dissolved oxygen would significantly increase the measured open circuit potential at low copper concentrations ($\leq 1x10^{-6}$ molal). Experiments at copper concentrations lower than $1x10^{-6}$ molal did not yield repeatable results. Even though grade 5.6 (99.9996%) argon was used to sparge the solution, it was not completely free of oxygen contamination (<0.5 ppb oxygen). Further steps to remove the oxygen from the argon, such as a gettering furnace, could have been used in order to obtain more accurate data. The rubber stoppers that were employed to make the seals between the three-neck flask and the inserted instruments are oxygen permeable (on the order of 1×10^{-8} $cm^2/(s*atm)$) (Massey 2003). A better shield against oxygen diffusion, such as the Ace Glass fittings that were used in the flask deposition kettle, would have decreased the dissolved oxygen concentration in the bulk solution.

5.1.2 Kinetic Studies

Kinetic measurements of copper deposition were characterized using both DC and AC voltammetry as described in Section 4.6. All copper deposition experiments had a concentration of 1 mM copper sulfate with a supporting sulfuric acid electrolyte of either 500 mM or 61 mM. The set of experiments with 500 mM sulfuric acid were done with a 0.5 mm diameter polycrystalline gold working electrode and were performed in order to compare the results to Motheo (1996), who studied similar conditions. The 61 mM sulfuric acid set of experiments used a 2.0 mm copper working electrode.

Copper deposition is a two step process.

$Cu^{2+} + e^- \rightarrow Cu^{1+} + e^- \rightarrow Cu(s)$.

In a sulfuric acid solution the first step is the rate controlling step, so the entire process appears as one in voltammograms. In contrast, chloride ions stabilize Cu^{1+} and both electron transfer steps can be observed when chloride is present (Ponce de Leon and Walsh 2003). This chemistry is one of the reasons why it was important that a chloride-containing reference electrode was not used for the deposition studies.

The basic shape of copper deposition current versus potential using the potential sweep method is two deposition peaks and two stripping peaks as shown in Figure 5-2 (a magnified partial view of the peaks is shown in Figure 5-3). The dependent variable is the current density, which is defined as the current divided by the electrode area. The small black arrows on Figure 5-2 denote the direction of the potential scan and will be used in this manner on voltammograms throughout this chapter.

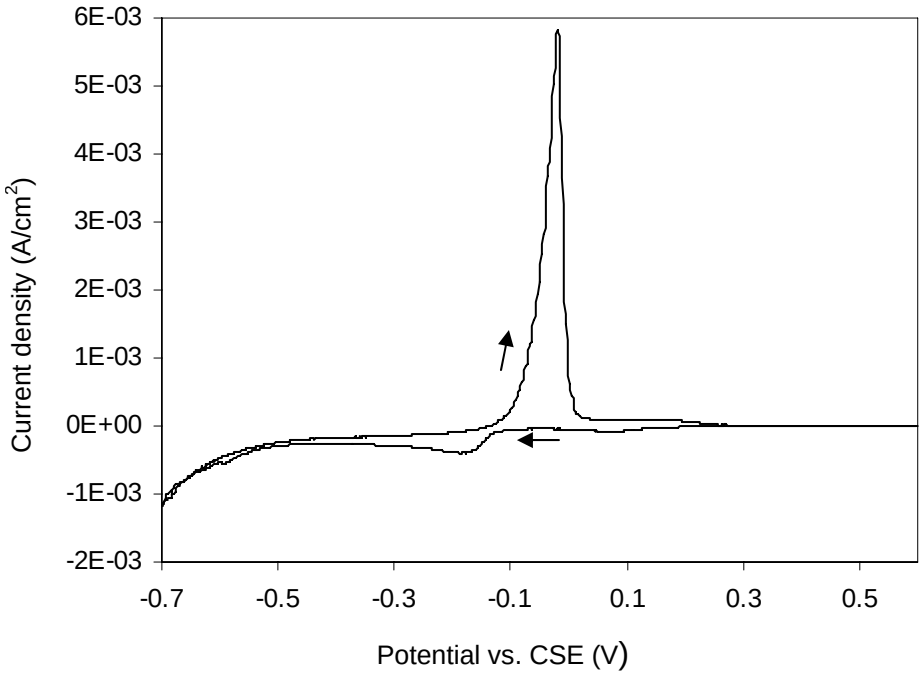

Figure 5-2: Copper linear sweep voltammogram, 20 mV/s
The black arrows indicate the direction of the scan.

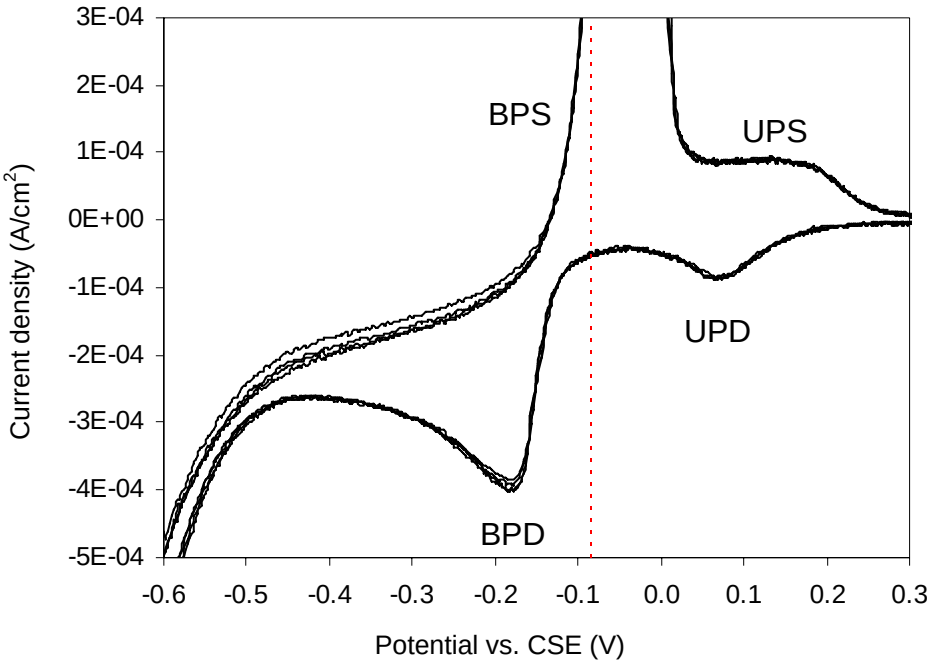

Figure 5-3: Copper linear sweep voltammogram, 20 mV/s, expanded section
Four cycles are shown. The dotted red line indicates the measured equilibrium potential as shown in Figure 5-1.

The deposition peaks (actually minima, but will be considered as "peak" negative currents) have a negative current while the stripping peaks have a positive current. The largest deposition and stripping peaks correspond to bulk potential deposition (BPD) and bulk potential stripping (BPS). As illustrated in Figure 5-3, the bulk deposition peak occurs at a more negative, or cathodic, potential than the equilibrium potential. The smaller set of peaks correspond to underpotential deposition (UPD) and underpotential stripping (UPS). Underpotential deposition is the chemical adsorption of a monolayer or submonolayer of a metal onto a foreign metal substrate at a potential that is less cathodic than the equilibrium potential. This process occurs when the adsorbate atoms (in this case copper) are more strongly bound to the foreign substrate (in this case gold) than to a substrate of their own type (Zhang 1996). This phenomenon has been extensively studied for the underpotential deposition of copper onto gold. The basic shape of Figures 5-2 and 5-3 matches that of Motheo (1996), although Motheo found smaller peaks

surperimposed on the larger ones. Motheo attributed these smaller peaks to a changing interaction between the gold substrate and the adsorbed copper and sulfate ions. Shi (1995) reported that on a (111) gold surface in a solution of 0.1 M $HClO_4$, 10^{-3} M $Cu(ClO_4)_2$, and 10^{-3} M K_2SO_4, the layer formed by the underpotential deposition consisted of 2/3 of a monolayer of copper with interspersed sulfate ions. At bulk potential deposition the first layer on the electrode was a complete monolayer of copper.

The current cycle shown in Figures 5-2 and 5-3 goes from +0.6 to -0.7V. At the negative end of the cycle, the current becomes increasingly negative due to hydrogen evolution. At the positive end of the cycle, the current is approximately zero for potentials greater than +0.3V. At the anodic potentials, although there is nearly zero current, a thin layer of gold is stripped from the surface of the working electrode to reveal a fresh surface, free of adsorbed molecules. An alternate method to activate the gold electrode surface is to anneal the gold with a flame and transfer the gold electrode to the solution covered with a drop of deionized water (Motheo 1996). The *in situ* method of gold surface activation developed in this study is simpler than the flame annealing process and provides a fresh gold surface for every voltammetry cycle. The effects of not activating the gold surface are illustrated in Figure 5-4. The cycle with no gold activation (a maximum positive voltage of +0.3 V) has deposition peaks occurring about 0.2 V more negative than the cycle with gold activation (a maximum positive voltage of +0.6 V). A clean (free of adsorbed substances), fresh gold surface provides a better surface for copper deposition than an unclean surface resulting in a smaller overpotential for deposition reactions. The non-activated trace shows no UPS peak, although the BPS peaks are similar for both traces. This behavior also indicates that a clean surface is a better surface for copper deposition.

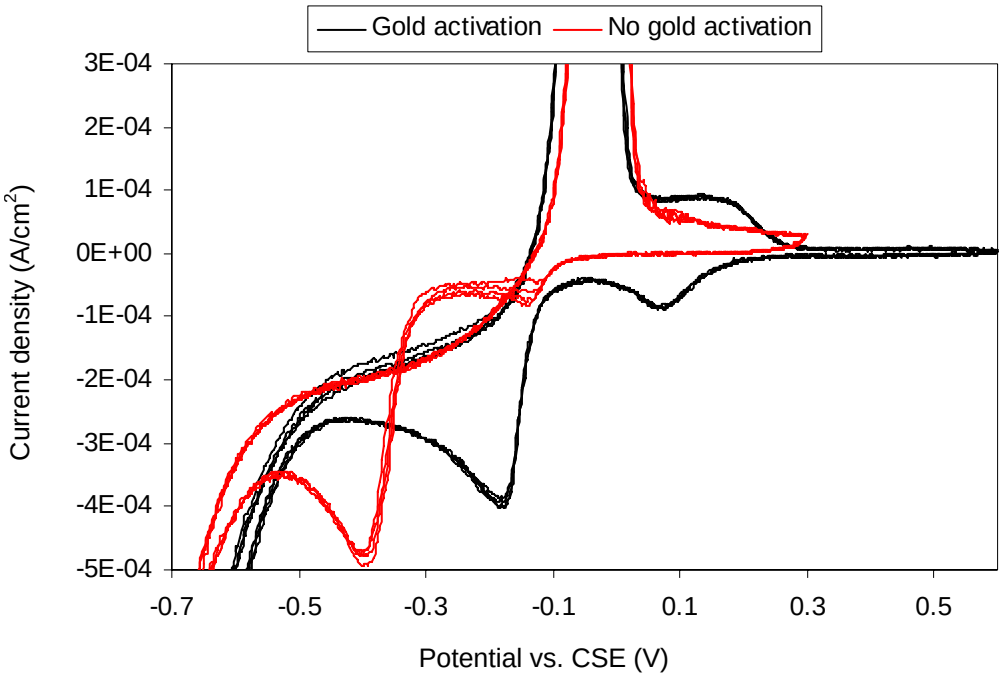

Figure 5-4: Effect of gold activation on copper deposition
Sweep rate is 20 mV/s for both voltammograms. The potential range for the activated gold trace is +0.6 to -0.7V and the potential range for trace with no gold activation is +0.3 to -0.7V. The traces are partially cut off to magnify the area of interest.

Scan rates of 1 mV/s to 100 mV/s were employed for the potential sweep studies. It was found that below 10 mV/s the deposition peaks were of the same order of magnitude as the noise. The potentiostat could not consistently produce scan rates faster than 100 mV/s, so scan rates greater than 100 mV/s were not studied. For 50 mV/s and greater the current peaks (I_p) were no longer directly proportional to the square root of the scan rate (v) as they were for the range of 10 to 30 mV/s. This deviation from linearity indicates a change from approximately reversible, mass-transfer-controlled deposition of an insoluble species to a partially kinetic-controlled deposition (see discussion around equation 4-15). Voltammograms for 10, 20 and 30 mV/s scan rates are shown in Figure 5-5. Further support for reversibility of the copper deposition process under these conditions comes from the fact that the potential of the peak current is nearly the same for all scan rates (see equation 4-16).

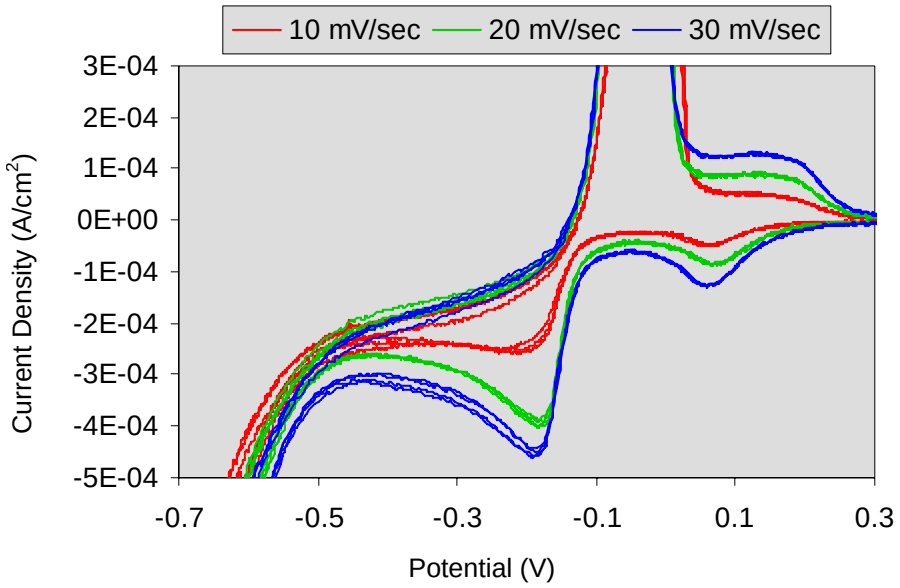

Figure 5-5: Copper deposition on gold WE with varying scan rate

The current density reported in the voltammograms has been calculated by assuming a working electrode area based on the wire diameter used to fabricate the electrodes. Equation 5-3 (Berzins and Delahay 1953) can be used to calculate the area of the electrode based on the known bulk solution concentration (c_i^*), diffusion coefficient for copper at 1 mM (D_i) ($7.60 \times 10^{-6} cm^2 s^{-1}$) (Quickenden and Xu 1996), temperature (T), and measured slope of the peak current versus the square root of the scan rate as shown in Figure 5-6 assuming one-dimensional diffusion to the working electrode.

$$A = \frac{(\pi RT)^{1/2}}{1.082 nFc_i^* (nFD_i)^{1/2}} \left(\frac{I_p}{v^{1/2}} \right) \tag{5-3}$$

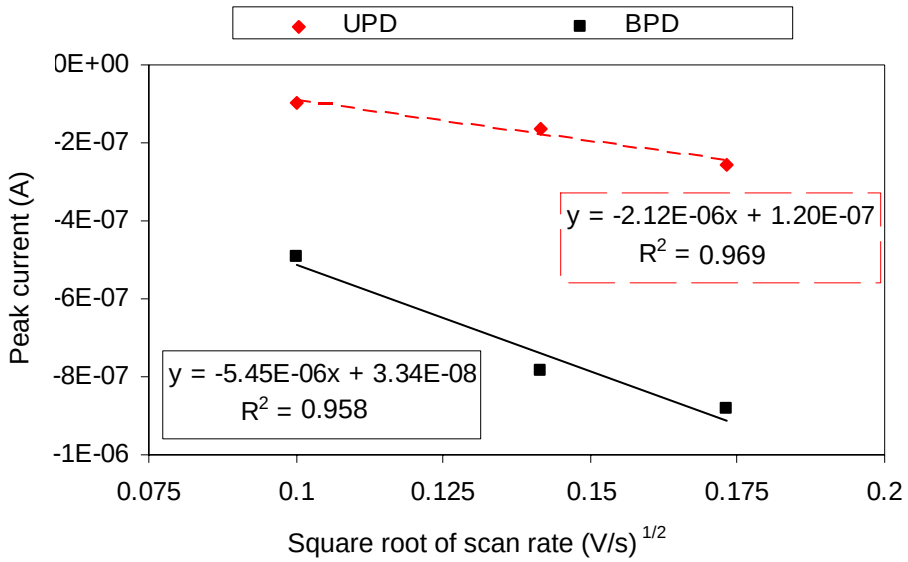

Figure 5-6: Peak current as a function of the square root of scan rate

Extensive earlier studying of the structure the copper deposited at the underdeposition potential indicates that deposits do not uniformly and totally cover the cathode. The slope from both the UPD and the BPD were used to calculate the area of the working electrode. The UPD slope was $7.39 \times 10^{-4} cm^2$ is significantly smaller than the area of $1.96 \times 10^{-3} cm^2$ calculated from the wire diameter, while the BPD slope was $1.90 \times 10^{-3} cm^2$ which is reasonably in agreement with the wire area. This analysis using the BPD slope validates the use of the wire diameter as an acceptable method for estimating the electroactive area of the working electrode. The coverage area of the copper deposited during the UPD is 39% of the total electrode area. Shi et al (1995) found the coverage of the copper for UPD was 2/3 of the total electrode, about twice that of this study. Although their solution of 0.1 M $HClO_4$, 10^{-3} M $Cu(ClO_4)_2$, and 10^{-3} M K_2SO_4 had the same copper concentration, it had chlorates present and significantly less sulfate. The differences between the solutions could account for the differences between calculated UPD coverages.

While gold provides a good surface for laboratory studies of the deposition behavior of copper, it would not practical for an industrial processes where a copper working electrode

would most likely be used. Also, in bulk deposition of copper, each copper layer is deposited on top of another layer of copper, keeping the electrode properties roughly constant throughout the process. Consequently the deposition of copper onto copper electrodes was studied for 1 mM $CuSO_4$ (the same concentration as the gold working electrode studies) and 61 mM H_2SO_4. The sulfuric acid concentration was changed from the previous value of 500 mM in order to match the concentration of sulfuric acid in the copper sulfate reference electrode.

Figure 5-7 shows copper deposition on a 2.0 mm diameter copper working electrode for a range of scan rates. Only a bulk deposition peak is observed since underpotential deposition requires a species be deposited on a foreign substrate. There is no apparent end to the stripping peak as the potential is swept in an anodic direction because the working electrode is removed at the same potential as the newly deposited copper. The potential of the deposition peak on copper is about the same as it was for is deposition on gold. But it shows a tendency to move to increasingly cathodic potentials with scan rate, for example the peak potential moves from -0.17 V at 10 mV/s to -0.21 V at 30 mV/s, indicating that the deposition is not reversible for this range of scan rates. The fact that potentials are similar is reasonable since the bulk deposition peak of copper on a gold working electrode starts on a mixed gold and copper surface and ends on a completely copper surface. The reduced concentration of the supporting electrolyte (from 500 to 61 mM) may be contributing to some of the irreversibility observed in the deposition peak since the concentration of the supporting electrolyte is inversely proportional to the current due to migration of the electroactive species (Cu^{2+}).

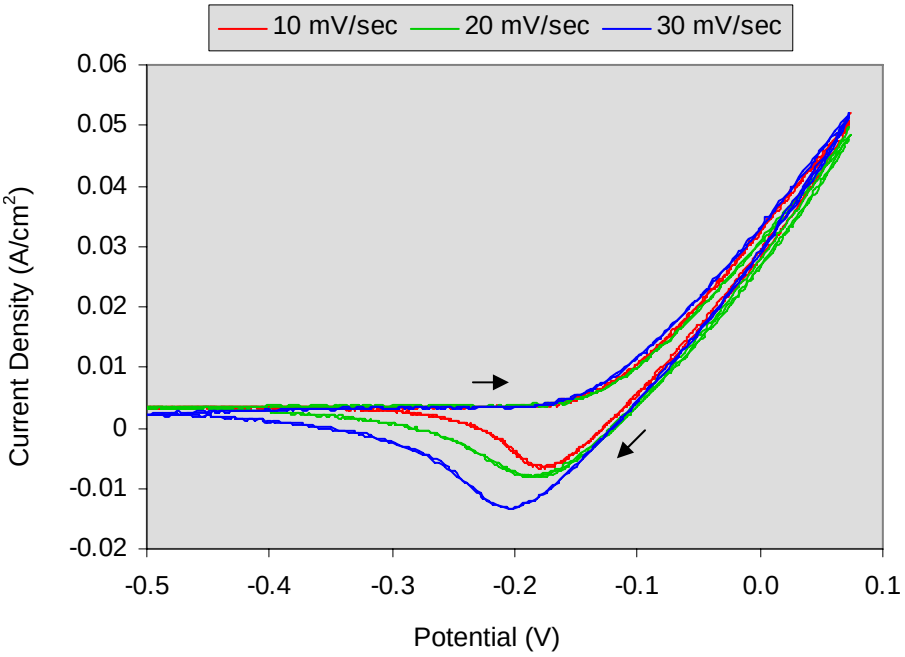

Figure 5-7: Copper deposition onto copper working electrode

In addition to DC voltammetry, AC voltammetry was employed to study the deposition of copper. Gold was chosen for the electrode because the deposition behavior was shown to be nearly reversible using DC voltammetry and has more interesting features. The same solution (1 mM $CuSO_4$, 0.5M H_2SO_4) and working electrode (0.5 mm diameter) conditions were used as in the DC voltammetry study. The DC scan rate for all AC voltammetry was either 10 or 20 mV/s to reduce the charging current due to the changing potential. The magnitude of the AC potential was 10 mV and the frequency ranged from 25 to 50,000 Hz. See Section 4.6.3 for further background on AC voltammetry.

The impedance (Z) is defined as the ratio of the AC potential ($\dot{E}$, with the dot indicating a phasor, or rotating vector, with magnitude and frequency) to the AC current ($\dot{I}$) The admittance (Y) is the inverse of the impedance. The cotangent of the phase angle (ϕ) between the current and potential is related to the real part of the impedance (Z_{Re}) and the imaginary part of the impedance (Z_{Im}) as shown in equation 5-6.

$$Z = \frac{\dot{E}}{\dot{I}} = \text{impedance} \tag{5-4}$$

$$|Z| = \frac{1}{|Y|} = \frac{1}{|\text{admittance}|} \tag{5-5}$$

$$\text{cotan}(\phi) = \frac{Z_{\text{Re}}}{Z_{\text{Im}}} \tag{5-6}$$

For constant AC potential magnitude, as was used in these studies, the admittance is directly proportional to the AC current. Figure 5-8 shows the variation of the absolute value of admittance and the cotan(ϕ) as a function of the DC potential at 100 Hz for solutions with 1 mM $CuSO_4$, 0.5 M H_2SO_4 and with only 0.5 M H_2SO_4. The peaks are easier to see in the cotan(ϕ) versus potential plot than they are in the admittance plot because there is less background noise. The deposition potential maximum is approximately -0.15 V, whereas it was -0.19 V for the DC voltammetry scans. The small positive shift in the peaks between AC and DC voltammetry represents a decrease in the charging current due to the changing potential; therefore, the AC voltammetry peak potential is the more accurate value because it does not include the charging potential. The bulk stripping potential peak is the same within error for both DC and AC voltammetry, approximately -0.02V (the value is slightly higher in Figure 5-8 because it was measured at a DC scan rate of 20 mV/s whereas most of the AC voltammetry scans were performed at 10 mV/s).

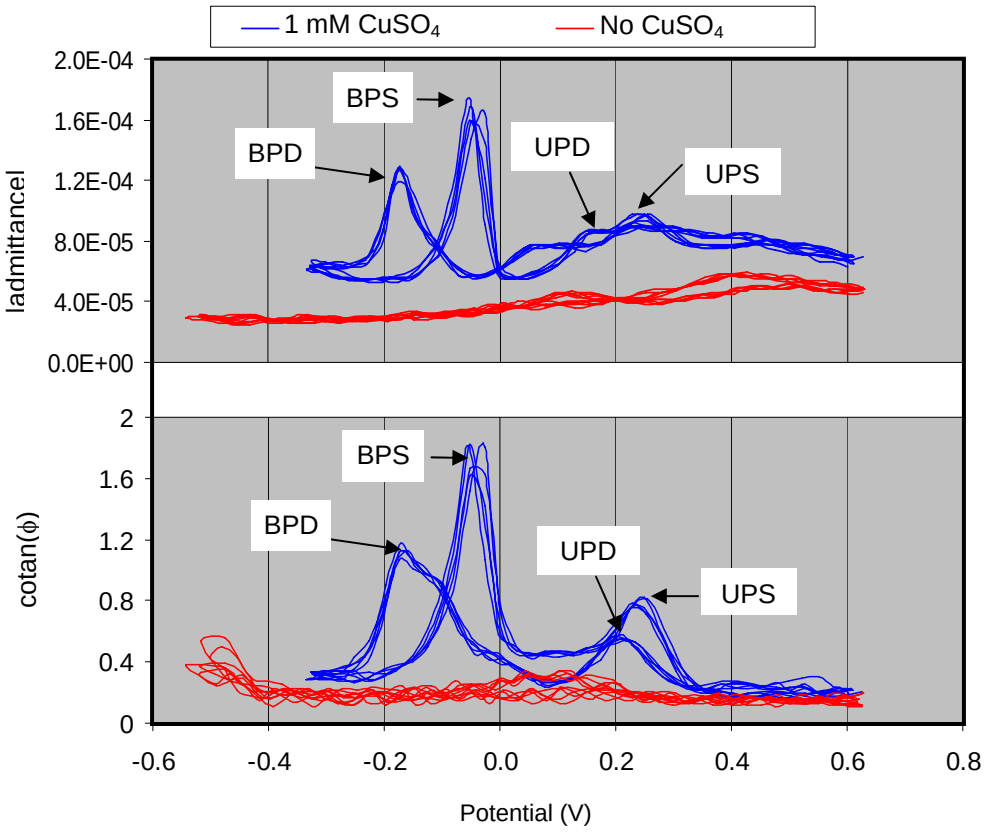

Figure 5-8: AC voltammograms for copper deposition, 100 Hz, 20 mV/s

The height of the peaks of cotan(ϕ) versus potential vary as a function of the frequency. Figure 5-9 shows cotan(ϕ) versus potential for a range of frequencies where we see that the peak height increases with decreasing frequency.

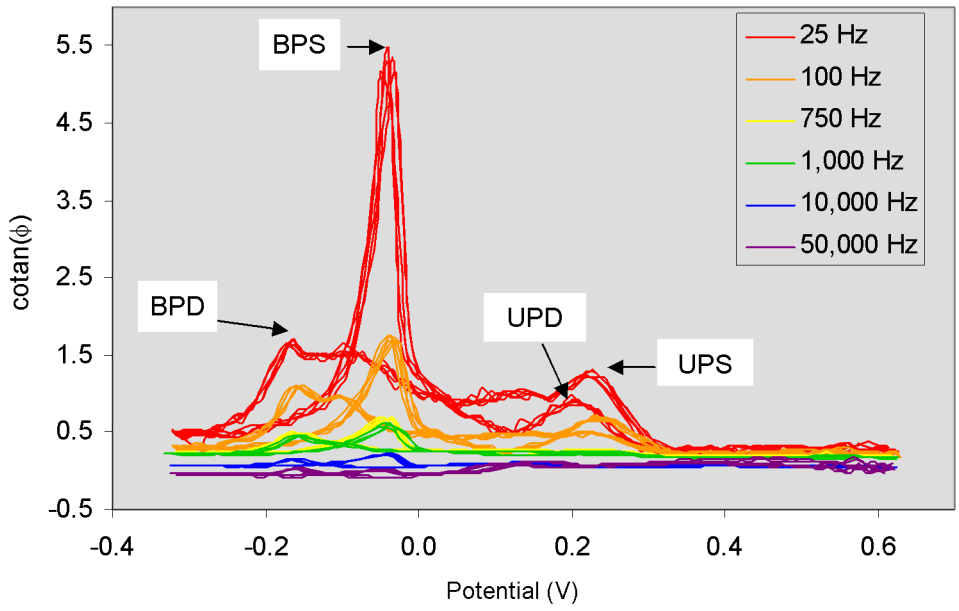

Figure 5-9: AC voltammograms for copper deposition for a range of frequencies

Figure 5-10 is a plot of the maximum value of cotan(ϕ) as a function of the square root of the angular frequency (ω).

It has been shown that, regardless of the reversibility of a reaction, for the case of soluble reactants and products cotan(ϕ) is directly proportional to the square root of the angular frequency as seen in equation 5-7 (Smith 1971; Bond 1978). β is defined as (1-α) and ranges from 0 to 1, so the denominator of equation 5-7 will always be positive. Since the diffusion coefficients (D_i) for the general reaction $O + ne^- \rightarrow R$ are always positive, the numerator will also be positive.

$$\left[\text{cotan}(\phi)\right]_{max} = 1 + \frac{\left(2D_O^{\beta} D_R^{\alpha}\right)^{1/2}}{k^0\left[\left(\frac{\alpha}{\beta}\right)^{-\alpha} + \left(\frac{\alpha}{\beta}\right)^{\beta}\right]}\omega^{1/2} \qquad (5\text{-}7)$$

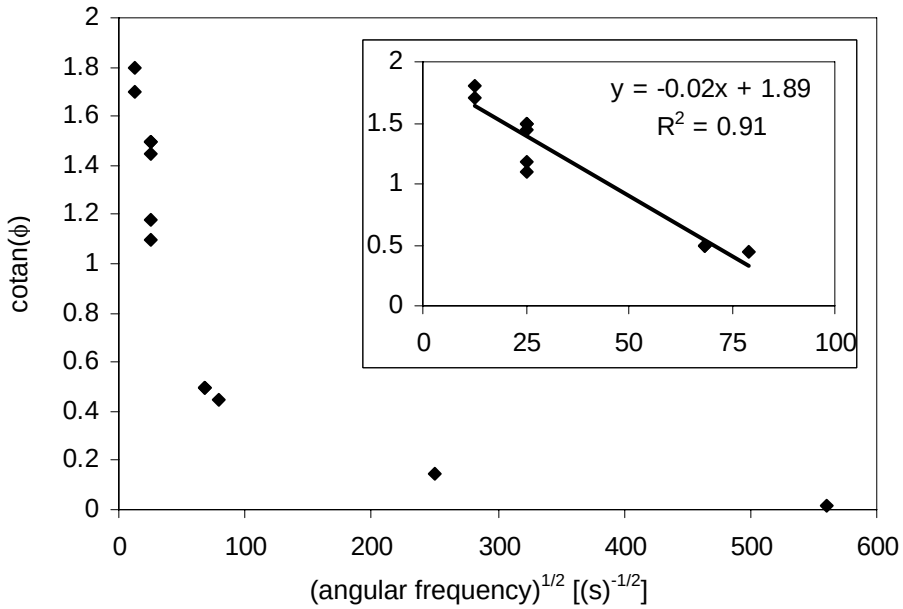

Figure 5-10: Maximum cotan(ϕ) as a function of $\omega^{1/2}$
The multiple data points at a frequency represent the results of multiple experimental runs. The inset graph is a magnified view of the smaller angular frequency results with a linear curve fit of the results.

If this general type of equation applied to the current study, then the slope of the data in Figure 5-10 should be positive, not negative as observed. The maximum cotan(ϕ) of the smaller angular frequencies (< 100Hz) have a linear dependence as predicted by equation 5-7 (Figure 5-10). However, this equation cannot be directly applied to this study because the diffusion coefficient of the reduced species (Cu) is zero, which removes all dependence on the angular frequency. No earlier studies of AC cyclic voltammetry for an insoluble product were found in the literature, an independent analysis was performed to determine kinetic parameters from experimental data. Because we concluded similar assumptions to those used for DC cyclic voltammetry of an insoluble product similar levels of uncertainty were expected (Section 4.6.1). Given the complexity of the AC cyclic voltammetry analysis, it was considered to be beyond the scope of the current study. Because the peaks in the AC cyclic voltammograms were at nearly the same

position as in the DC cyclic voltammograms, they provided limited new information and further measurements using AC cyclic voltammetry were not performed.

5.2 Chromium

Chromium deposition is different from most other metal deposition processes in that it cannot be deposited from an aqueous solution containing only chromium ions (either hexavalent or trivalent chromium). The plating solution must also contain one or more acid radicals to act as catalysts for hexavalent chromium and complexers for trivalent chromium. The most commonly used bath additives are sulfate, silicofluoride, and proprietary organic additives. Sulfate and silicofluoride additives are often used together (Mandich and Snyder 2000). The basic sulfate bath for chromium plating consists of 2.5 M CrO_3 and 0.026 M H_2SO_4, which translates to a 100:1 weight ratio (also nearly equivalent to 100:1 on a molar basis). This bath is of most interest to this study because it closely mimics the conditions used, although at a higher concentration. The lowest reported CrO_3 concentration for chromium plating is 0.5 M. The ratio between the chromium and sulfate is crucial for the successful deposition of chromium. For industrial chromium plating baths, it is suggested that this ratio should be kept within 50:1 to 250:1 (Dubpernell 1974). Within this range, the current efficiency (the percent of the current that results in the product) for chromium is relatively constant at about 18%. Below a ratio of about 25:1 and above about 500:1 the current efficiency drops off rapidly and no chromium is deposited (Dubpernell 1977).

To understand the importance of the ratio of chromium to sulfate catalyst, it is necessary to have a general understanding of chromium deposition chemistry. At the molecular mechanistic level, the entire chromium deposition process is complex and even after eighty years of research it is still not fully understood. The solutions start with hexavalent chromium. The

species of hexavalent chromium in solution is dependent on the chromium concentration and multiple species can be present in equilibrium with each other. Table 5-1 shows the species present as a function of concentration (Mandich 1997). The polychromate structures are composed of tetrahedral CrO_4 structures, and their appearance in solution changes from yellow to red as their size increases. Thus, the changing ion speciation with concentration accounts for the change in the solution color. Since the bulk of the work on chromium deposition has been at high chromium concentrations, chromium deposition at low concentration may proceed via a slightly different mechanism due to the different species present.

Table 5-1: Chromium species in solution as a function of concentration

CrO_3 concentration (mol/L)	Ions in equilibrium
$<10^{-2}$	$HCrO_4^-$
10^{-2} to 10^{-1}	$HCrO_4^- \leftrightarrow Cr_4O_7^{2-} + H_2O$
10^{-1} to 1.5	$Cr_4O_7^{2-}$
1.5 to 3.5	$3Cr_2O_7^{2-} + 2H^+ \leftrightarrow 2Cr_3O_{10}^{2-} + H_2O$
3.5 to 7.5	$Cr_3O_{10}^{2-}$
7.5 to 10	$4Cr_3O_{10}^{2-} + 2H^+ \leftrightarrow 2Cr_4O_{13}^{2-} + H_2O$

According to (Mandich 1997), during the chromium deposition process two different films form on the cathode surface. The film closest to the surface, known as the C-film because it is compact, forms first and contains very few sulfate ions. The second film, known as the L-film because it is liquid-like, contains the sulfate ions and dissolves easily in the bulk solution. The cathodic films are mostly composed of Cr^{3+} complexes, but their exact valences have not been determined. Chromium is not directly deposited from the films, but from chromium that reacts with the films and then passes through them to plate out on the cathode. The cathodic films form slowly and can result in a start-up time for chromium deposition that can be observed in cyclic voltammograms. In these voltammograms, the first cycle does not show chromium deposition, but the following cycles do.

Mandich and coworkers (1997; Mandich and Snyder 2000) have proposed a series of reaction steps from hexavalent chromium that lead to chromium deposition; however, their explanations lack complete clarity (in some cases, the published reaction structures appear to have several errors and, in one case, the space for the reaction was accidentally left blank). The authors have done their best to interpret the reaction scheme as it may have been originally conceived. Under industrial plating conditions, hexavalent chromium complexes contain three chromium atoms (trichromate). After the cathodic films have been formed, one of the chromium atoms in the trichromate molecule is reduced to trivalent chromium and then to bivalent chromium to produce a trichromate ion. This ion reacts with hydronium as shown in reaction R5-1 to form Cr^{2+} hydroxide. The hydroxide forms a complex with the bisulfate ion via hydrogen bonding (indicated by the dashed lines) as illustrated in reactions R5-2 and R5-3. The reaction proceeds such that the positively charged chromium specifically adsorbs onto the cathode (R5-4). Two electrons are transferred from the electrode surface to produce metallic chromium and release the bisulfate ion to restart the cycle in reaction R5-3.

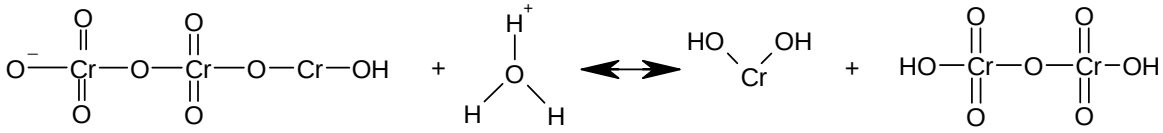

(R5-1)

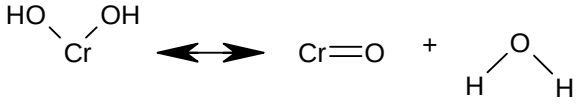

(R5-2)

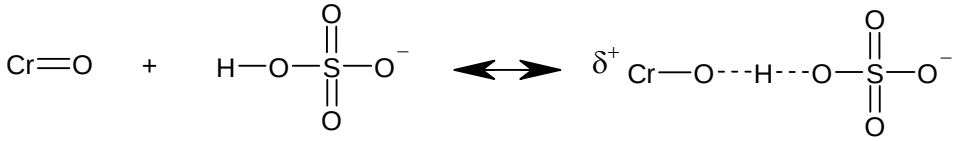

(R5-3)

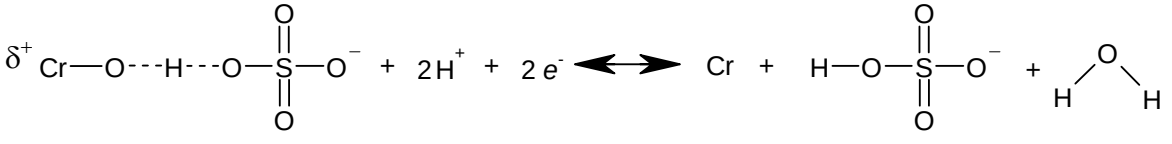

(R5-4)

Where: dichromate ion = 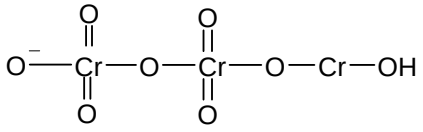 , Cr^{2+} hydroxide = 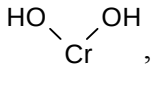 ,

dichromic acid = 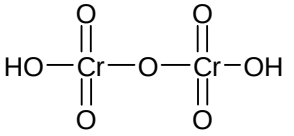 , chromium monoxide = ,

chromium – bisulfate complex = 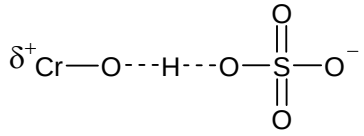 , solid chromium = Cr.

Mandich (1997) has further proposed that the trichromate ion is protected from reduction to Cr^{3+} aquo-complexes (Dubpernell 1977) by hydrogen bonding between bisulfate ions (HSO_4^-) and the oxygen atoms that are double bonded to the chromium atoms. These aquo-complexes can polymerize to form large, unreactive complexes that trap the Cr^{3+} and prevent its reduction to chromium. If the concentration of bisulfate ions is too high, they could block reaction R5-1 by hydrogen bonding to all of the oxygen atoms of the trichromate ion. Thus, it is possible to have either too much or too little sulfate present.

In this study, chromium concentrations range from 0.5 to 0.0025 M CrO_3, so hexavalent chromium would be present as mono- and dichromate, not trichromate, according to Table 5-1. Mandich's reaction scheme suggests that the important ratio for successful chromium deposition is actually that of chromium complexes to bisulfate ions, not total chromium concentration to sulfuric acid. As the chromium concentration decreases, the size of the chromium complexes decrease (as shown in Table 5-1), so the number of chromium complexes relative to chromium atoms increases. Therefore, the optimal 100:1 ratio of chromium trioxide to sulfuric acid may decrease with decreasing chromium trioxide concentration.

Since the lowest reported concentration of chromium (VI) plating solution is 0.5 M, this concentration was used as the upper limit for chromium deposition experiments (Dubpernell

1974). The optimal weight ratio of chromium trioxide to sulfuric acid of 100:1 was used in most experimental runs in an attempt to yield compact chromium deposits. Experiments at three concentrations of chromium trioxide, 0.5 M, 0.25 M, and 0.025 M, with appropriate amounts of sulfuric acid to maintain at 100:1 ratio, were performed. All chromium deposition experiments were performed on solid metal electrodes of 2.0 mm diameter.

Figure 5-11 shows the results for a solution of 5 mM sulfuric acid with and without 0.5 M chromium trioxide on a copper working electrode. For the 5 mM sulfuric acid trace the peaks on the right are copper deposition and stripping on the copper electrode, while the cathodic peak on the left is hydrogen evolution. In the chromium solution, the copper deposition and stripping peaks are suppressed. The new cathodic peaks are a combination of hydrogen evolution and chromium deposition and stripping. The addition of chromium trioxide acidifies the solution and causes a large increase in hydrogen evolution over the solution without chromium. Figure 5-12 shows the approximate hydrogen peak that would be seen if there was no chromium activity. This approximated hydrogen peak can serve as a baseline for chromium activity as indicated on Figure 5-12. The chromium deposition peak potential is -1.12V and that of the stripping peak is -0.96V.

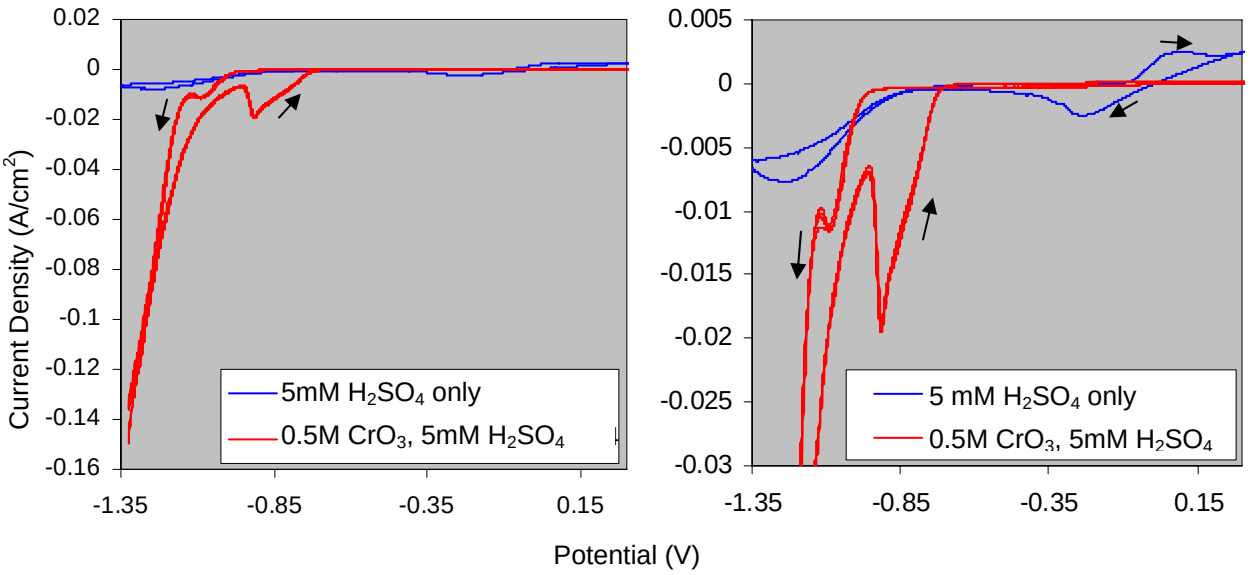

Figure 5-11: Chromium deposition from 0.5 M CrO_3, 5 mM H_2SO_4 onto Cu WE
The graph on the right is a magnified portion of the graph on the left. All scans were performed at 10 mV/s. The black arrows indicate the direction of the scan.

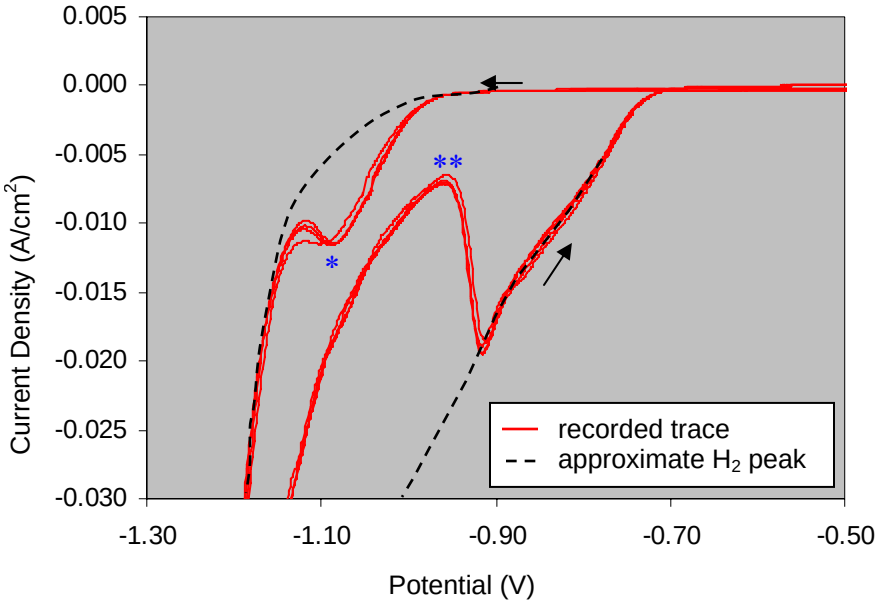

Figure 5-12: Magnified view of Cr deposition from 0.5 M CrO_3, 5 mM H_2SO_4 on Cu WE
The black arrows indicate the direction of the scan. The red line is the recorded voltammogram trace. The dashed black line is approximately the contribution to the scan from hydrogen evolution. The peak marked with * is chromium deposition and the other peak marked with ** is chromium stripping.

The same experiment was repeated at half the concentration of CrO_3 and H_2SO_4. The results for 0.25 M CrO_3, 2.5 mM H_2SO_4 on a Cu working electrode are shown in Figure 5-13.

The same general shape of the curve is similar to the earlier run (Figure 5-11), but the chromium stripping peak is broader and less distinct. The chromium deposition peak potential of -1.13V is nearly the same value as before and the chromium stripping peak potential of -0.96V is the same.

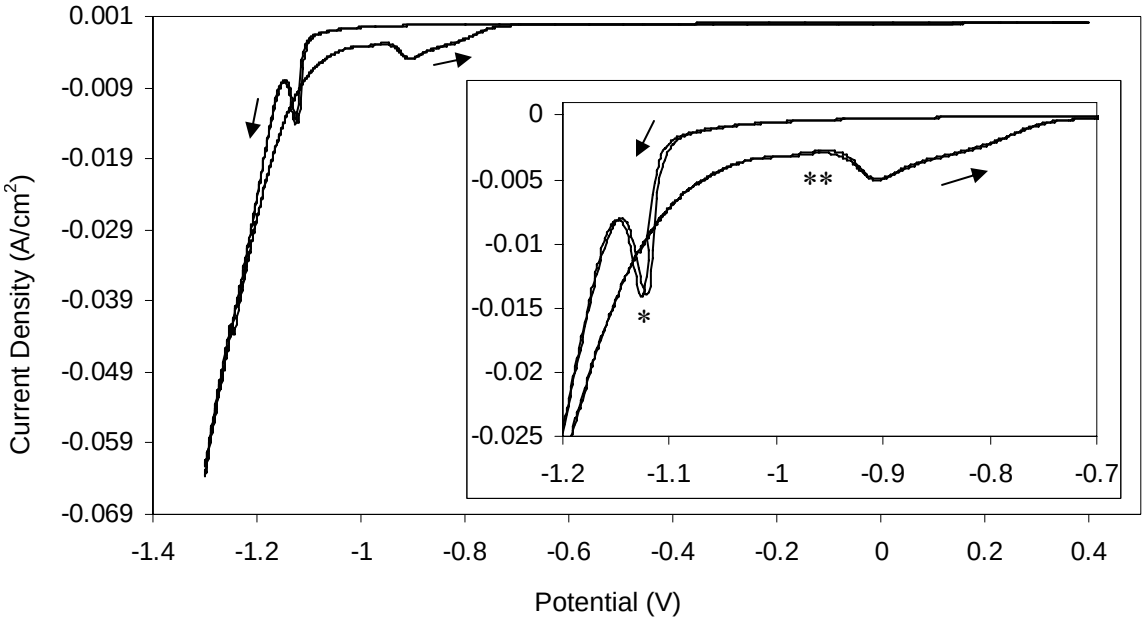

Figure 5-13: Cr deposition from 0.25 M CrO_3, 2.5 mM H_2SO_4 on Cu WE
Inset graph is a magnified view of larger graph. Scan rate is 10 mV/s. Two scan cycles are shown. Arrows indicate direction of scan. The * indicates the Cr deposition peak and the ** denotes the broad Cr stripping peak.

Dropping the solution concentration by an order of magnitude markedly changes the chromium deposition and stripping behavior as shown in Figures 5-14 through 5-16. The chromium deposition peak is no longer visible because the hydrogen peak completely masks it. The deposition of chromium was ascertained visually for all working electrode materials (copper, gold, and 304 stainless steel). EDAX with SEM confirmed that the gray, slightly rough deposit that was observed on all working electrodes was chromium. On the gold and stainless steel electrodes a peak on the anodic sweep is observed at about +1.0 V. This peak was determined to be the chromium stripping peak by holding the potential and visually monitoring the disappearance of the deposited chromium after the experimental run. The anodic sweep with

the copper electrode is dominated by the stripping of copper, although the small inflection in the peak at about +0.7 V may be the beginning of the chromium stripping peak or instrumental error (Figure 5-15). In order to fully remove the chromium deposit from the copper electrode, the layer of copper onto which it had been deposited also had to be removed because the chromium could not be removed from the copper.

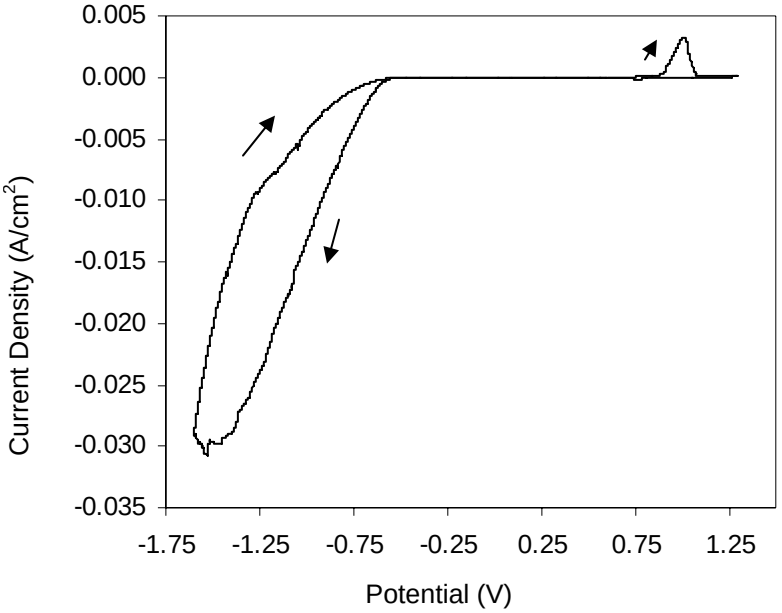

Figure 5-14: Cr deposition from 25 mM CrO_3, 0.25 mM H_2SO_4 on Gold WE
Scan rate is 10 mV/s. Arrows indicate direction of scan.

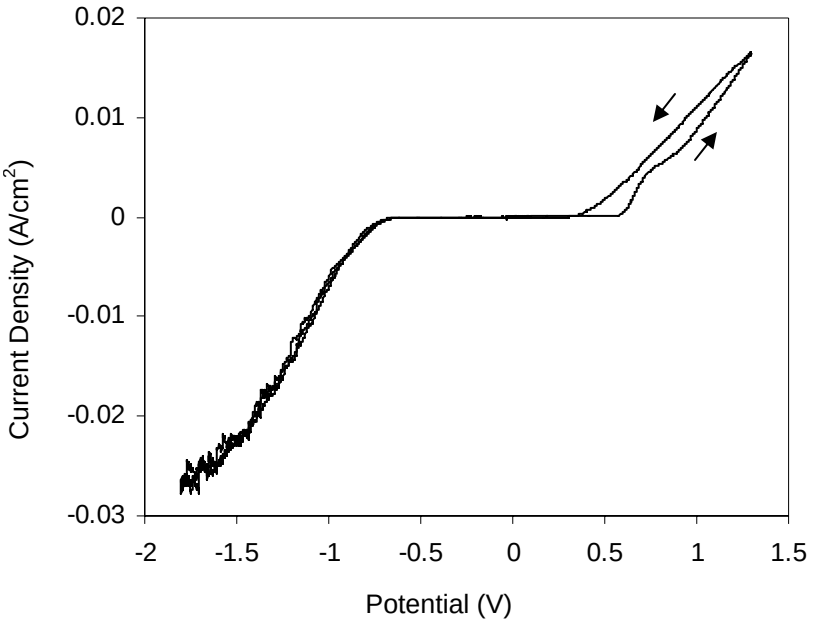

Figure 5-15: Cr deposition from 25 mM CrO_3, 0.25 mM H_2SO_4 on copper WE
Scan rate is 10 mV/s. Arrows indicate direction of scan.

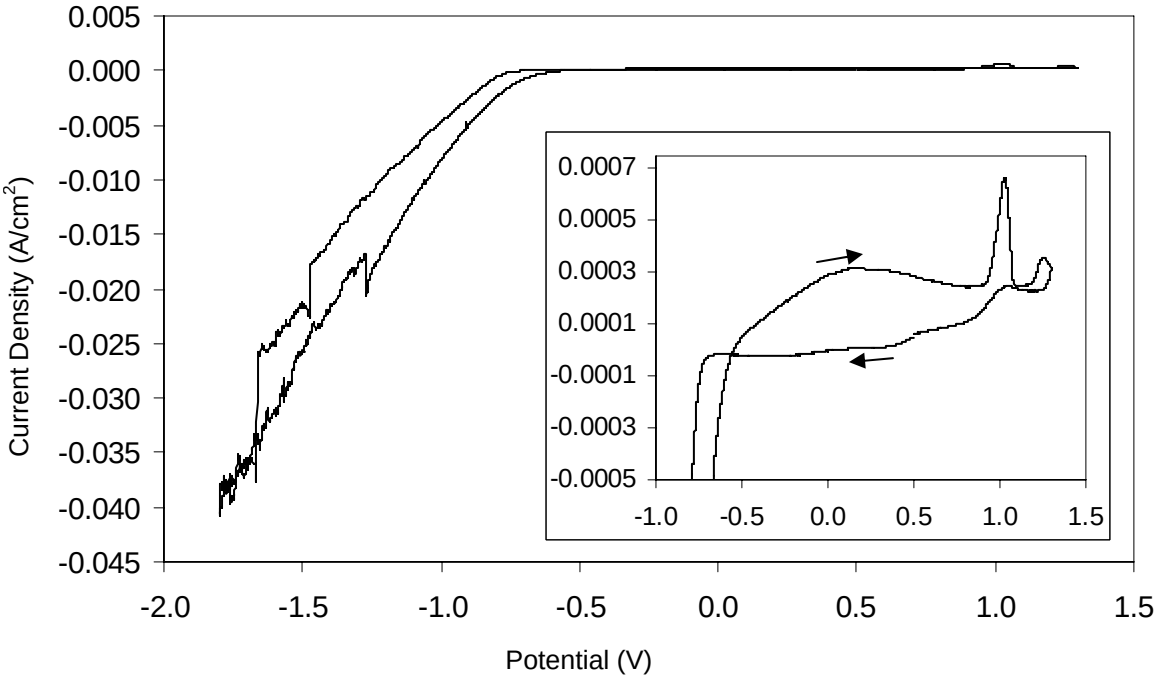

Figure 5-16: Cr deposition from 25 mM CrO_3, 0.25 mM H_2SO_4 on 304 stainless steel WE
Inset graph is a magnified view of larger graph. Scan rate is 10 mV/s. Arrows indicate direction of scan.

The large increase in the potential of the chromium stripping peak from the higher concentration runs can be explained with the help of the chromium stability diagram shown in Figure 5-17. At higher concentrations, chromium stripping occurs at a low enough pH (less than 1) that neutral chromium goes through the Cr(II) and Cr(III) regions to arrive at Cr(VI), and hence chromium stripping can occur at about -1 V. Decreasing the chromium concentration to 25 mM in turn increases the pH of the solution such that neutral chromium was protected by the chromium oxide. In this range, Cr has to go through the passive region, where it is protected by a layer of chromium oxide, in order to be converted to Cr(VI) at about +1 V. The increase in the stripping peak potential with a decrease in chromium concentration is consistent with the chromium stability diagram.

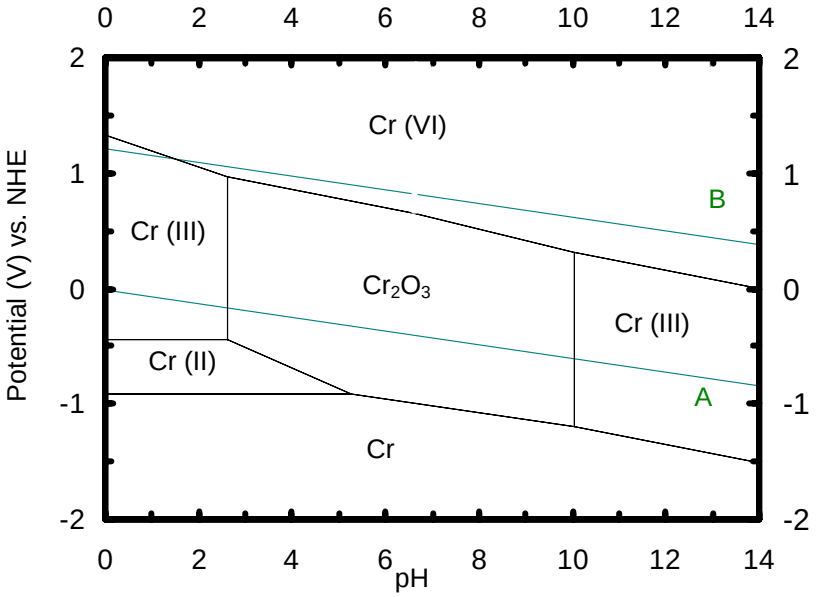

Figure 5-17: Chromium stability diagram for 0.25 mM CrO_3
Diagram drawn using HSC with an activity coefficient of one for all species (Haung 1999).

Although the chromium deposition peak is masked by the hydrogen peak, the chromium stripping peak can be used as a probe to determine the potential at which chromium is first deposited. The potential is held for 10 minutes at a series of values that span the possible deposition potential. After each hold period, the voltage is swept through the chromium

stripping potential to see if a peak appears. The highest potential at which a chromium stripping peak is detected is the potential at which chromium starts to deposit. This stripping technique could only be used on the stainless steel and gold working electrodes because they did not have any appreciable stripping at the chromium stripping potential. Figure 5-18 shows that chromium first deposits on stainless steel at -1.55 V and on gold at -1.25 V from a solution of 0.25 mM CrO_3 and 0.25 mM H_2SO_4.

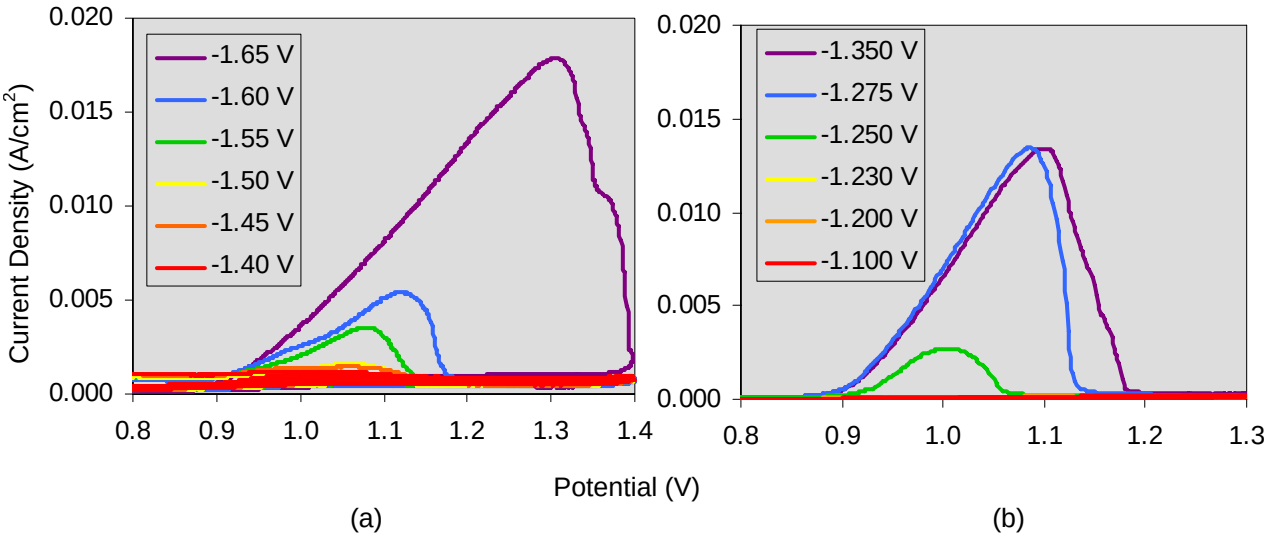

Figure 5-18: Chromium stripping

Graph (a) is for a 304 stainless steel working electrode and graph (b) is for a gold working electrode. The potential at which the electrode was held for 10 minutes before the voltage sweep that is shown is indicated in the legend.

Although chromium trioxide is the most common way that chromium is added to chromated copper arsenate solutions, other compounds such as sodium or potassium dichromate are also used. The discussion in Dubpernell (1974) indicates that salts can have a deleterious effect on chromium plating. To characterize this effect, potassium dichromate ($K_2Cr_2O_7$) was used for some chromium plating baths. A concentration of 0.25M $K_2Cr_2O_7$ with 5 mM H_2SO_4 was chosen because it gives the same chromium concentration as 0.5 M CrO_3, which gave the best chromium deposits of the CrO_3 experiments. Figure 5-19 compares these voltammograms:

0.25M $K_2Cr_2O_7$ with 5 mM H_2SO_4; 0.5 M CrO_3 with 5 mM H_2SO_4; and a background scan of 5 mM H_2SO_4. With the addition of potassium, the chromium deposition peak was confounded and the chromium stripping peak was reduced. Chromium deposition started at around -1.3 V, about 0.2 V more cathodic than the potassium-free chromium solutions. The chromium deposit when viewed under an optical microscope did not smoothly cover the surface. Instead, the deposit was patchy with thin tendrils. Clearly, the potassium was inhibiting the chromium deposition process.

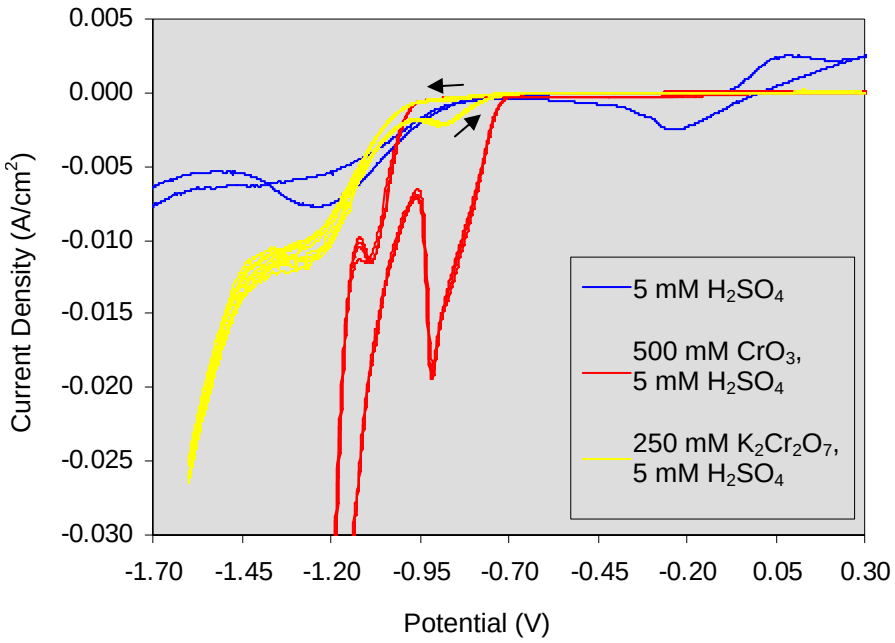

Figure 5-19: Chromium deposition from 0.5 M $K_2Cr_2O_7$, 5 mM H_2SO_4 on copper WE
All scans were performed at 10 mV/s.

The limits of the chromium deposition conditions were probed by reducing the $K_2Cr_2O_7$ concentration to 60 mM while holding the H_2SO_4 concentration at 5 mM. The reduction in chromium concentration mimics chromium removal during a batch deposition process. The limit of the chromium-to-sulfuric acid ratio for good deposition has been found to be approximately a molar ratio of 25:1, these conditions, 24:1, are just past this boundary. Visual examination of the copper working electrode showed extremely limited chromium deposition from these conditions.

The chromium deposit was significantly more sparse than that from the 0.5 M $K_2Cr_2O_7$ run. Figure 5-20 compares the 60 mM potassium dichromate voltammogram to the scans shown in Figure 5-19. The chromium deposition chemistry is even more suppressed than in the 0.25 M potassium dichromate run. The additional peaks on the anodic scan may be Cr(0) → Cr(III) and then Cr(III) → Cr(VI). It is possible that because these processes are less favored than before due to the reduction of the chromium-to-sulfuric acid ratio, the kinetics have been slowed down so that there is a separate peak for each reaction.

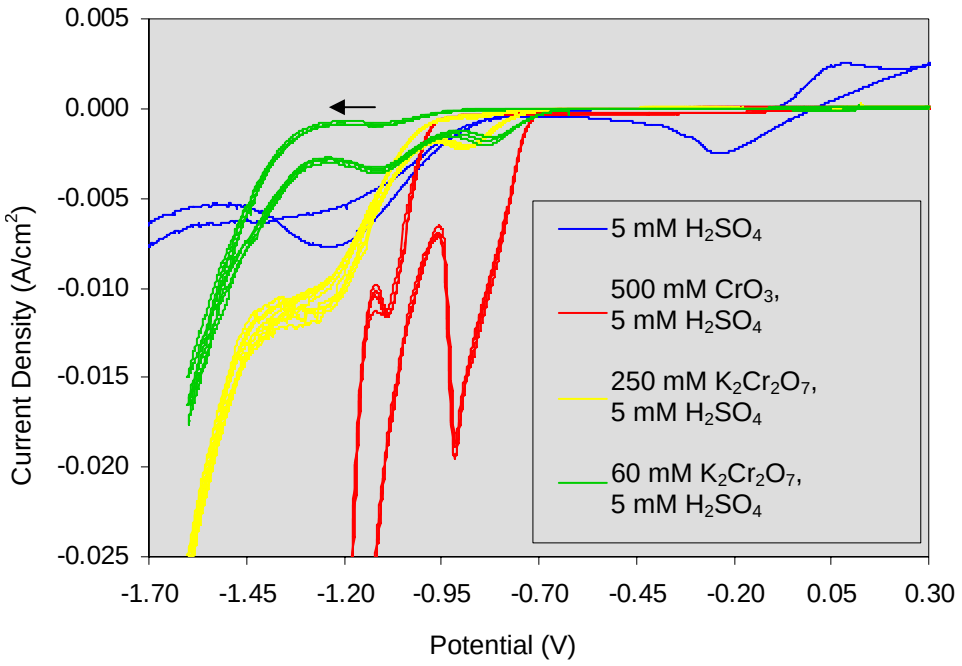

Figure 5-20: Chromium deposition from 60 mM $K_2Cr_2O_7$, 5 mM H_2SO_4 on copper WE
All scans were performed at 10 mV/s. The cathodic peaks on the 60 mM $K_2Cr_2O_7$ and 5 mM H_2SO_4 are from the anodic scan.

Table 5-2 summarizes the deposition and stripping conditions of chromium. The accuracy of the reported deposition potentials in some cases is limited when the deposition peak and/or stripping peak is not clear in the voltammograms. For these cases, a separate run at each potential of interest and then visual inspection of the working electrode was required. For the copper working electrode, the deposition peak is shifted in the cathodic direction with decreasing

chromium concentration, as predicted by the Nernst equation (Pourbaix 1974) which is in reference to the NHE in equation 5-8.

$$E_{Cr} = -0.913 + 0.0295 \log\left[Cr^{2+}\right] \quad (5\text{-}8)$$

Table 5-2: Chromium deposition and stripping peak potentials

Composition	W.E. material	Deposition Potential (V)	Stripping Potential (V)
500 mM CrO_3, 5 mM H_2SO_4	Cu	-1.12, good deposit	-0.96
250 mM CrO_3, 2.5 mM H_2SO_4	Cu	-1.13, good deposit	-0.96
25 mM CrO_3, 0.25 mM H_2SO_4	Cu	> -1.8, good deposit	Not visible
25 mM CrO_3, 0.25 mM H_2SO_4	Au	-1.25, good deposit	1.0
25 mM CrO_3, 0.25 mM H_2SO_4	Steel	-1.55, good deposit	1.1
250 mM $K_2Cr_2O_7$, 5 mM H_2SO_4	Cu	~ -1.3, poor deposit	Not visible
60 mM $K_2Cr_2O_7$, 5 mM H_2SO_4	Cu	undetermined	Not visible

5.3 Arsenic

Arsenic is a semi-metal and, as such, its properties do not readily allow it to be electrolytically deposited. The main application of arsenic reduction has been arsine formation for use in the semiconductor industry. Publications have focused on the minimization of arsenic deposition and a maximization of arsine evolution (Tomilov 2001). Arsenic deposition is not currently performed industrially, although several arsenic deposition processes have been developed for both aqueous and nonaqueous solvents (Holt 1974). Co-deposition of gallium(III) and arsenic(III) from aqueous and molten salt solutions has been employed to deposit gallium arsenide (Schlesinger 2000). When deposited alone from a trivalent solution, arsenic forms a brown or black mass resembling graphite (Tomilov and Chomutov 1974).

Chernykh et al (2001) have performed the most recent thorough examination of electrochemical reduction of arsenic acid (H_3AsO_4). They found that the reduction of aqueous arsenic (V) compounds to arsenic and arsine begins at a pH of about 4 or 5 and continues as the

pH is decreased with a marked increase in reaction rate for pH < 2. The current efficiency, defined as the percent of the total current that results in the product, for arsine production is greatest at neutral pHs and decreases as the pH decreases. The current efficiencies for both arsenic deposition and arsine evolution were found to be dependent on the working electrode material. A general trend for the working electrode, regardless of the material, is that the current efficiency of arsine evolution increases with increasing arsenic acid concentration and with an increase in the temperature from 25 to 50°C. The current efficiency of hydrogen formation increased with decreasing pH, as expected for most hydrogen-producing reactions.

White and Bard (1966) studied the behavior of arsenic acid with pyrogallol in an aqueous 1-3 M $HClO_4$ solution on a mercury electrode and identified three polargraphic waves corresponding to the following reactions:

$$As^{5+} + 2e^- \rightarrow As^{3+} \quad \text{(R5-5)}$$

$$As^{3+} + 3e^- \rightarrow As^{0} \quad \text{(R5-6)}$$

$$As^{0} + 3e^- \rightarrow As^{3-} \quad \text{(R5-7)}$$

Although under most deposition conditions these reactions are not seen individually, it does not mean that the individual reactions are not occurring in a quick series.

Chernykh et al (2001) found that the current efficiency of arsine evolution for solutions of 1 to 3 M arsenic acid was about 10 to 100 times that of arsenic deposition. Also, no perceptible quantities of arsenous acid [$As(OH)_3$] (the stable form of As^{3+}) were found in the reduction product. These observations led them to conclude that the reduction of arsenic acid proceeds via the eight electron scheme shown in the following reaction.

$$H_3AsO_4 + 8e^- + 5H^+ \rightarrow As^{3-} + 4H_2O \quad \text{(5-R8)}$$

This reaction is followed by the formation of arsine gas.

$$As^{3-} + 3H^{+} \rightarrow AsH_3(g) \qquad (5\text{-}R9)$$

It is highly unlikely that any single reaction involves eight electrons. It is more plausible that the reaction proceeds through a series of reaction steps. Since Chernykh and coworkers found no evidence of arsenous acid, and very little arsenic metal, they postulated that the energy required to activate the first electron transfer step under the conditions they studied is greater than the energy required for all of the following reactions to produce arsine. Thus, the arsine production reaction behaves as if it were a single eight-electron reaction.

Regardless of the correctness of their mechanistic interpretation, the results of Chernykh and coworkers' study does not lead to any deposition conditions that would result in deposition of arsenic from a pentavalent solution without the formation of arsine, which is a key goal of this research. Arsenic deposition and arsine evolution are sensitive to the working electrode material, so multiple materials have been explored. Deposition from a trivalent arsenic solution on a mercury working electrode reduces the formation of arsine to an insignificant level (Tomilov and Chomutov 1974). We anticipated that a liquid gallium working electrode might behave in a similar manner to mercury and help to suppress arsine formation during arsenic deposition.

As a result of these evaluations, four working electrode materials were employed in this study for the deposition of arsenic from a dilute sulfuric acid solution: copper, gold, 304 stainless steel, and gallium in liquid and solid forms. The deposition behavior of arsenic was probed and measured using DC voltammetry, SEM with EDAX, arsine detection, and visual observation of deposits on the electrodes.

5.3.1 Solid Working Electrode

Arsenic was successfully deposited from a solution of 5 mM As_2O_5 and 61 mM H_2SO_4 onto copper, gold, and 304 stainless steel electrodes with 2.0 mm diameter. The concentration of

arsenic was chosen so that the sulfuric acid could act as supporting electrolyte. There were probably trace amounts of copper in the bulk solution due to the slow leach of copper ions from the copper sulfate reference electrode.

Arsine was always detected by the bubbler system described in Section 4.3 whenever arsenic was deposited. Arsenic deposited the slowest on gold, with deposition starting at a potential between -1.8 and -2.5 V. Given the very slow arsenic deposition at -2.5 V, the arsenic deposition potential was probably close to -2.5 V. Figure 5-21 shows the DC voltammogram for 5 mM As_2O_5 and 61 mM H_2SO_4 onto gold. The arsenic deposition peak and arsine evolution peaks are lost in the noise of the hydrogen evolution. The hydrogen evolution peak is so noisy because gas bubbles are being generated and detaching from the working electrode surface. The magnified view of Figure 5-21 reveals the copper deposition and stripping peaks that are also seen in Figure 5-3. The most anodic peak at about +0.7 V is gold stripping.

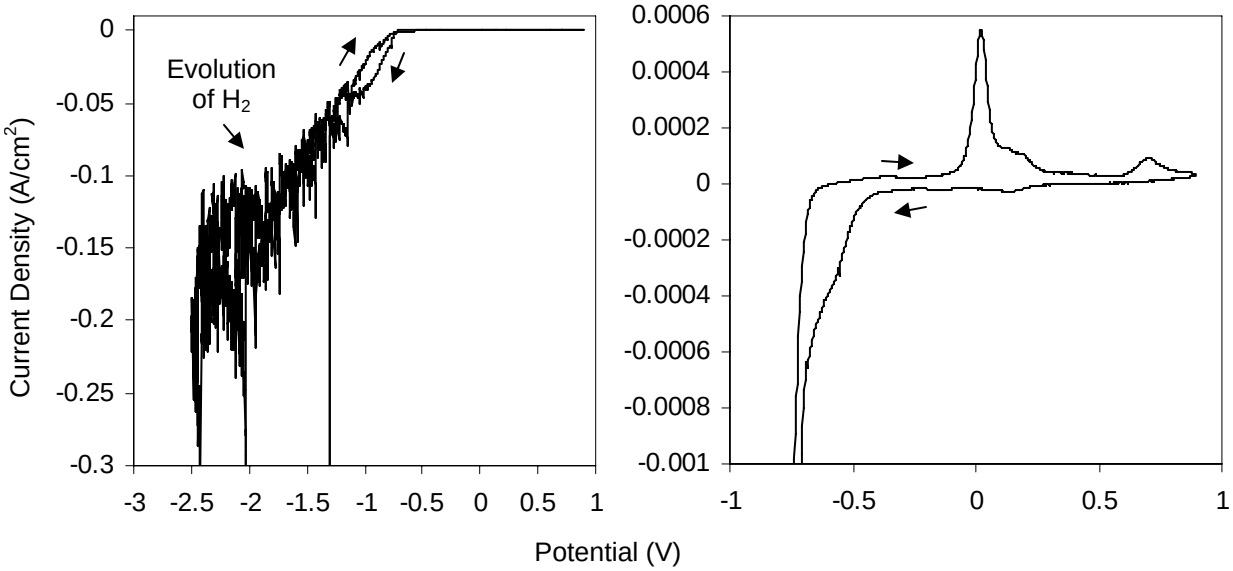

Figure 5-21: Arsenic deposition on gold WE
Scan rate is 20 mV/s.

Arsenic deposits more readily on copper than on gold. Figure 5-22 shows the DC voltammogram for 5 mM As_2O_5 and 61 mM H_2SO_4 onto copper. This voltammogram is similar

to the gold voltammogram in that the arsenic and arsine peaks are masked by hydrogen evolution. A magnified view of Figure 5-21 reveals copper electrochemistry that is similar to the case of a copper WE with a 1 mM $CuSO_4$ and 61 mM H_2SO_4 bulk solution as illustrated in Figure 5-7. Arsenic deposition started at approximately -2.0V. The deposit was a very dark gray, sponge like layer. The first deposition layer adhered to the copper electrode and could not be removed by wiping the electrode whereas the rest of the deposit could be easily removed. Arsine was produced under the same conditions as arsenic deposition.

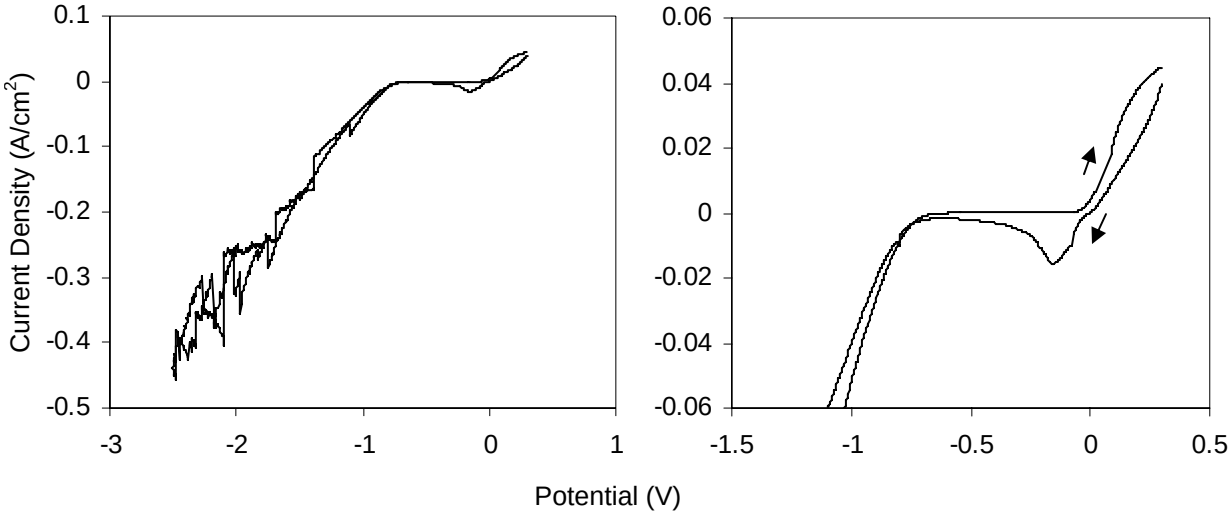

Figure 5-22: Arsenic deposition on copper WE
Scan rate is 20 mV/s.

Analysis of the deposit formed at -2.5 V on the copper working electrode using SEM with EDAX confirmed the presence of arsenic. SEM images taken with a gaseous secondary electron detector (GSE) are shown in Figure 5-23. Image (a) shows the arsenic deposit as light gray and the underlying copper electrode as dark gray. The black lines are grain boundaries in the polished copper surface. Image (b) is a magnified view of the arsenic deposit (light gray) and shows its porous nature.

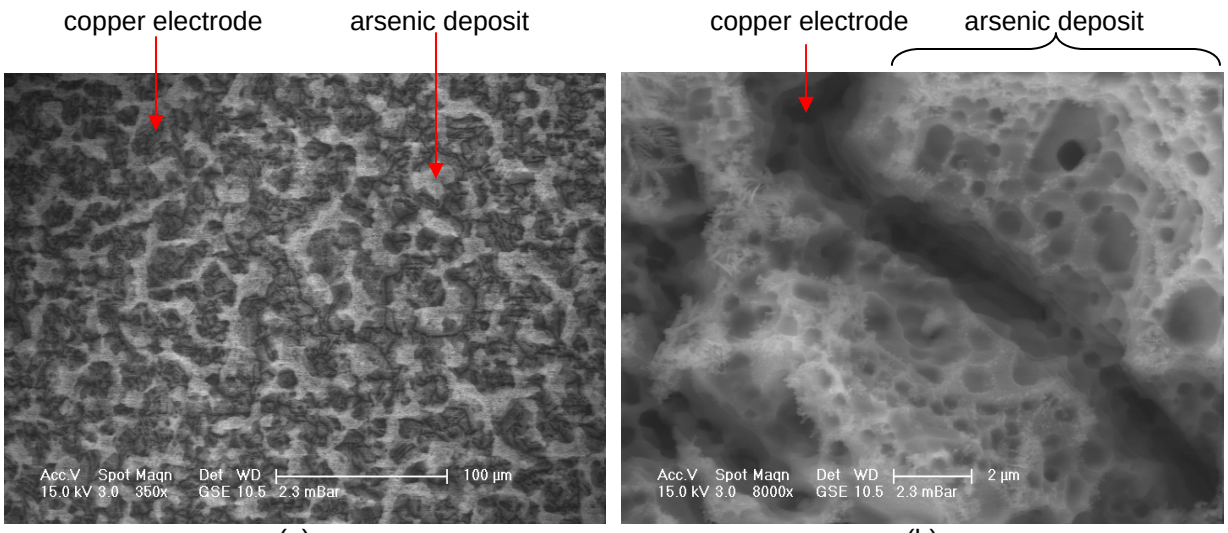

(a) (b)

Figure 5-23: SEM GSE images of arsenic deposited on copper WE

Arsenic first deposits on 304 stainless steel from a solution of 5 mM As_2O_5 and 61 mM H_2SO_4 at a potential between -1.5 and -2.5 V accompanied by arsine evolution as measured by the bubbler system described in Section 4.3. The very dark gray, spongy deposit appeared to be the same as the arsenic deposit on copper. Unlike the deposit on the copper electrode, the deposit on the stainless steel electrode could be wiped off to reveal the polished surface.

Gas evolution on the stainless steel electrode started between -0.5 and -1.0 V. The voltammograms shown in Figure 5-24 suggest that gas evolution started at about -0.7 V because that is where the cathodic current rapidly increases. As with all the voltammograms recorded on solid working electrodes in this study for a solution of 5 mM As_2O_5 and 61 mM H_2SO_4, the arsenic deposition and arsine evolution peaks are masked by hydrogen evolution. The magnified view of the voltammogram in Figure 5-24 shows two anodic peaks, one at about 0 V corresponding to copper stripping and one at about 1 V corresponding to chromium stripping from the stainless steel (see also Figure 5-16 for chromium stripping peak).

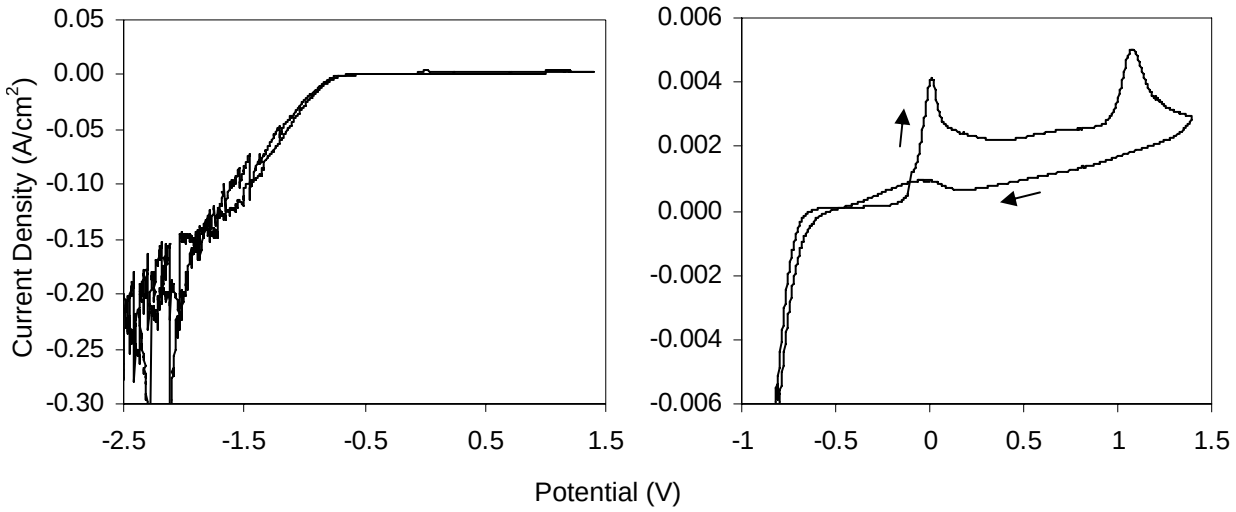

Figure 5-24: Arsenic deposition on stainless steel WE
Scan rate is 20 mV/s.

While the bulk properties of the arsenic deposit on stainless steel appear qualitatively to be the same as the deposit on copper, a SEM image taken with a GSE shows a different small-scale structure as seen in Figure 5-25. The length scale is the same as Figure 5-23 (b). The arsenic deposit (light gray) on the stainless steel (black) is more compact and is in clumps instead of a porous structure. SEM with EDAX confirmed the presence of arsenic.

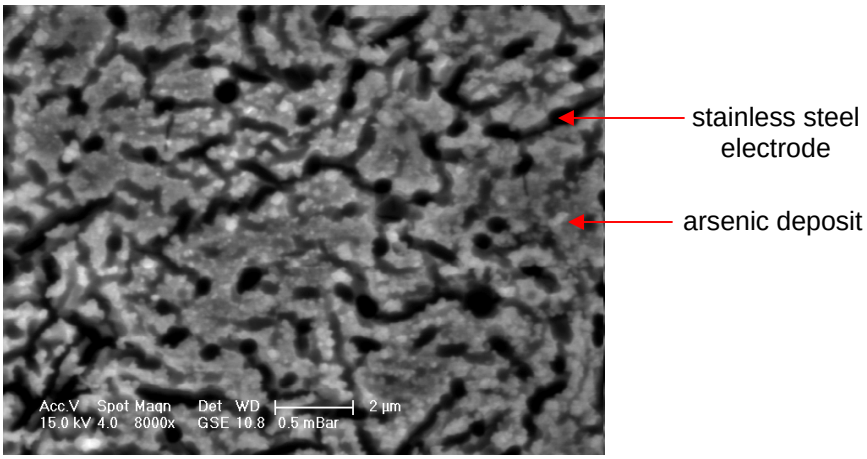

Figure 5-25: SEM GSE images of arsenic deposited on stainless steel WE

The solid gallium working electrode demonstrated similar arsenic deposition behavior to the gold working electrode, although the underdeposition peaks are not visible (Figure 5-26).

Minimal arsenic was deposited at -2.5 V accompanied by arsine evolution. Gas bubbles were visible on the solid gallium electrode starting at a potential of -0.72 V and continued as long as the voltage was below that limit. Hydrogen evolution again masked the arsenic deposition peak.

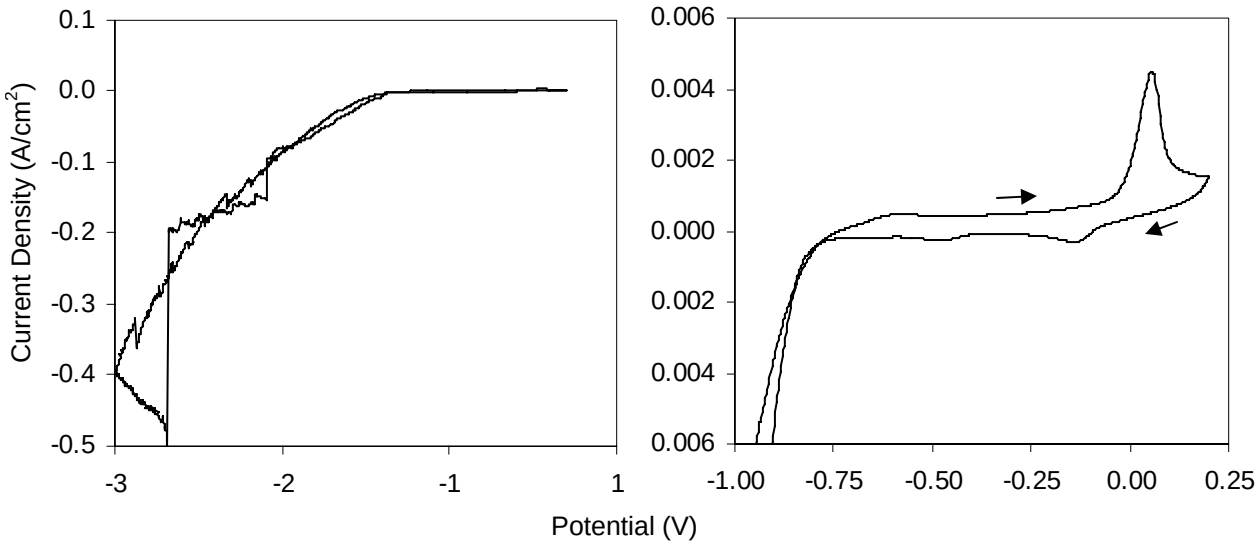

Figure 5-26: Arsenic deposition on solid gallium WE
Scan rate is 20 mV/s.

Like the copper working electrode, the gallium working electrode range is limited by the stripping of the electrode. Figure 5-27 shows gallium stripping starting at a potential of about 0 V, just beyond the copper stripping peak.

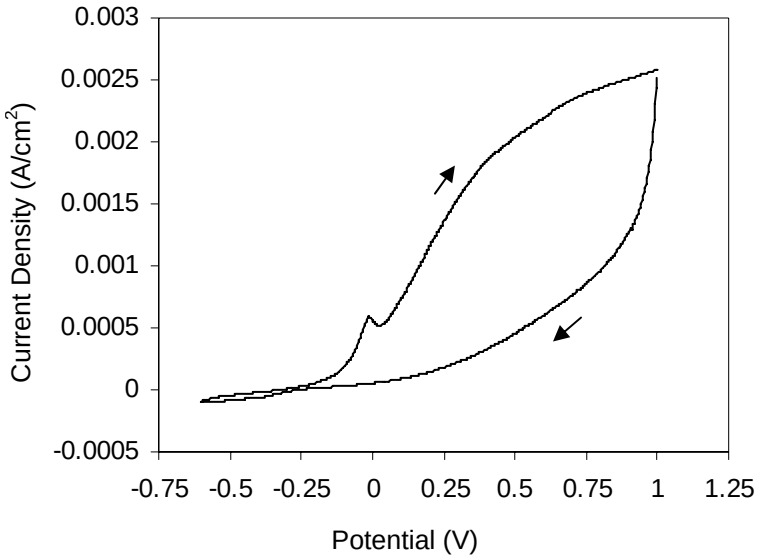

Figure 5-27: Gallium striping from a solid gallium WE
Scan rate is 20 mV/s.

5.3.2 Liquid Gallium Working Electrode

Three bulk solution concentrations were studied with a liquid gallium working electrode: 5 mM As_2O_5 and 5 mM H_2SO_4, 5 mM As_2O_5 and 61 mM H_2SO_4, 41 mM As_2O_5 and 61 mM H_2SO_4. The 5 mM As_2O_5 matches the concentration used for deposition on solid working electrodes. The solution with only 5 mM H_2SO_4 as a supporting electrolyte was found to have a low conductivity (10 mS/cm). When current was applied across the bulk solution between the working electrode and the counter electrode, the high resistivity of the solution resulted in a large potential drop in the voltammogram that covered any relevant peaks. The solutions with 61 mM H_2SO_4 had higher conductivities (>18 mS/cm) so that they did not suffer from the same problem. In preparation for the multi-component experiments, a concentration of 41 mM As_2O_5 was chosen because it fits the CCA type-C concentration ratio with respect to the previously explored 25 mM CrO_3 solutions. If a higher acid concentration was not needed to increase the conductivity of the solution, a lower acid concentration that matched the CrO_3 solution (0.25 mM H_2SO_4) would have been used.

The temperature of the liquid gallium working electrode experiments ranged from 33 to 39°C with the average at 35°C. At 35°C the CSE potential versus NHE was found to be 318.7 mV (see Section 3.4.2) and the potential varies less than 2 mV over this temperature range. The area of the working electrode that was used to calculate the liquid junction was approximated by the diameter of the working electrode holder. The actual area of the working electrode was probably slightly larger due to the curved surface of the liquid gallium working electrode. With the pressure-balanced liquid gallium working electrode, an attempt was made to flatten out the gallium surface by slightly lowering the pressure holding the gallium up in order to move the liquid gallium surface into its final position.

Just like with the solid working electrodes, arsenic deposition is not visible on the DC voltammograms due to hydrogen evolution. Arsine evolution always accompanied arsenic deposition, but it seemed to evolve at a slower rate than on the solid working electrodes. Arsenic deposition on the liquid gallium electrode was also slower, particularly in comparison to copper and stainless steel electrodes. Due to the slow deposition rate, only small amounts of arsenic were deposited over the course of the experiments. Deposition of arsenic did occur at -2.5 V from solutions of 5 and 41 mM As_2O_5 with 61 mM H_2SO_4. Arsine evolution started at a potential between -1.4 and -1.75 V. For the 5 mM As_2O_5 with 61 mM H_2SO_4 solution, hydrogen bubbles were first visible at -0.85 V on the cathodic sweep, and for the 41 mM As_2O_5 solution, hydrogen bubbles were first observed at -1.1 V. Both solutions evolved hydrogen before arsine.

The DC voltammogram for 5 mM As_2O_5 with 61 mM H_2SO_4 is shown in Figure 5-28 with each cycle separately marked. A cathodic peak at -1.2 V is seen on the first cycle and is an order of magnitude smaller on subsequent scans. This behavior was repeated in another cyclic voltammogram. The cathodic peak cannot correspond to either bulk arsenic deposition or arsine

evolution since neither of these phenomena start until more cathodic potentials. This peak may indicate a redox reaction between the trace copper in solution, the arsenic and the gallium surface. Once the gallium surface has mostly reacted, further sweeps would then show a limited current due to the reaction.

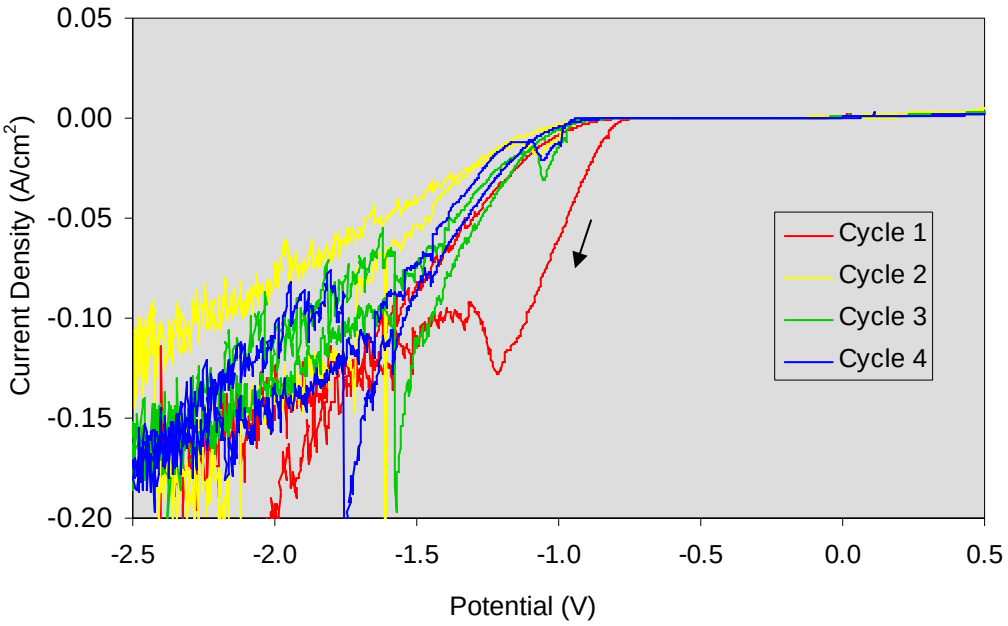

Figure 5-28: Arsenic deposition from 5 mM As_2O_5, 61 mM H_2SO_4 on liquid gallium WE
Scan rate is 20 mV/s.

The DC voltammogram of 41 mM As_2O_5 with 61 mM H_2SO_4, shown in Figure 5-29, also has a cathodic peak at -1.2 V. This peak was not observed in every voltammogram and, in contrast to Figure 5-28, the peak was not visible until cycle 3. This peak was not visible during DC voltammetry of sulfuric acid solutions on liquid gallium working electrodes, so it must be related to the arsenic in solution and might be the reduction of As(V) to As(III). The absence of a corresponding anodic peak indicates that the product produced in this process may be unstable or that the cathodic reaction is irreversible under the experimental conditions.

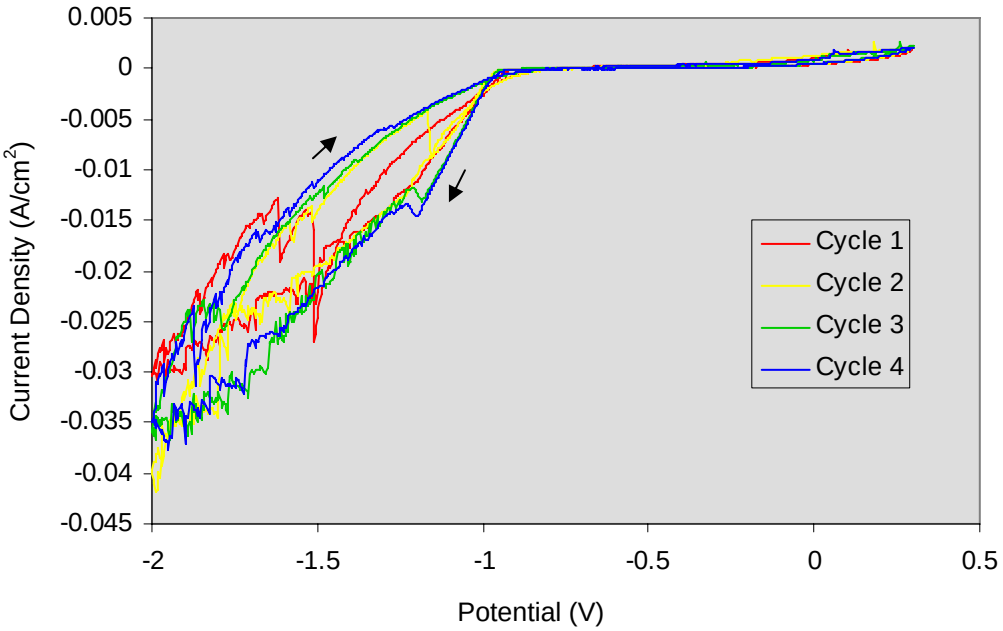

Figure 5-29: Arsenic deposition from 41 mM As_2O_5, 61 mM H_2SO_4 on liquid gallium WE Scan rate is 30 mV/s. The sudden drop in cycle 2 at -1.2 V is from the anodic sweep and is due to a hydrogen bubble detaching from the working electrode surface.

The deposition of arsenic at -2.5 V from both the 5 and 41 mM As_2O_5 solutions was confirmed with EDAX SEM analysis of the deposits. Approximately equal amounts of copper and arsenic were present in the deposit. While gallium was also detected, because the deposit layers were so thin it could not be determined if the gallium was from deposited gallium arsenide or if it was from the underlying gallium electrode surface. Further tests described in Chapter 6 reveal that no gallium arsenide was formed. Figure 5-30 shows SEM images taken with a backscatter secondary electron detector (BSE). The white/light gray areas are the gallium working electrode and the dark area are the deposit. The exact morphology of the deposit could not be ascertained because the liquid gallium was frozen, thawed to further level the sample, and then refrozen before the SEM analysis.

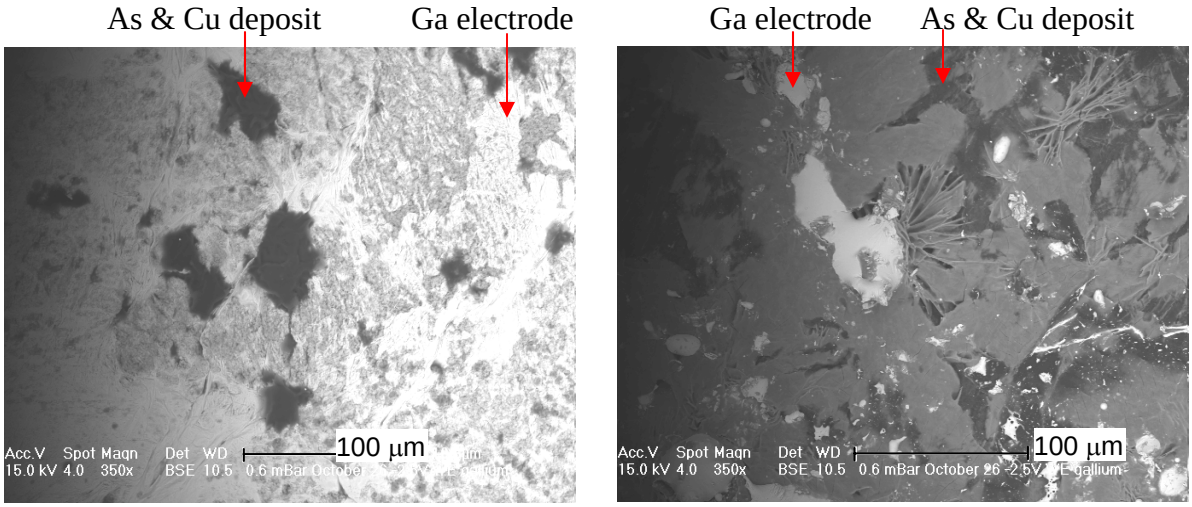

(a) (b)

Figure 5-30: SEM BSE image of arsenic deposited on liquid gallium WE

Image (a) is a deposit from a solution of 5 mM As_2O_5, 61 mM H_2SO_4 and image (b) is a deposit from a solution of 41 mM As_2O_5, 61 mM H_2SO_4. The light areas are gallium, the dark areas are arsenic and copper, and the gray areas are thin layers of arsenic and copper on gallium.

Liquid gallium working electrodes proved not to be effective (at least at the conditions studied) means for arsenic deposition from a 61 mM sulfuric acid solution without the evolution of arsine. Furthermore, arsenic deposition was slow under these conditions and hydrogen evolution was the dominant process. For a CCA remediation process, arsenic would most likely not be deposited from a single component solution, so there may be another route to avoid arsine formation during metal deposition. Chapter 6 reports on the behavior of multi-component solutions.

5.4 Conclusions

The deposition behavior of single-component solutions of copper, chromium, and arsenic in dilute sulfuric acid was studied on solid working electrodes in order to set a baseline for the multicomponent solutions detailed in Chapter 6. Deposition of arsenic, chromium, and copper from single component dilute sulfuric acid solutions was achieved. Since the analysis of the DC and AC cyclic voltammetry experiments for copper deposition revealed nearly the same deposition potentials, and DC voltammetry is simpler and faster, only DC voltammetry was used

for other deposition conditions. Chromium deposition was retarded by the addition of potassium to the bulk solution and by a decrease in the CrO_3:H_2SO_4 ratio from 100:1 to 24:1. Arsenic was deposited on solid working electrodes (Au, Cu, 304 stainless steel, and Ga) and on liquid Ga working electrodes as a loosely adhered black powder. All deposition conditions studied for arsenic also produced arsine, with the liquid Ga working electrode producing less arsine than the solid working electrodes.

5.5 References

Bates, R. G. (1973). Determination of pH; theory and practice. New York, John Wiley & Sons.

Berzins, T. and P. Delahay (1953). "Oscillographic polarographic waves for the reversible deposition of metals on solid electrodes." Journal of the American Chemical Society **75**: 555-559.

Bond, A. M., R. J. O'Halloran, I. Ruzic and D. E. Smith (1978). "Fundamental and Second Harmonic Alternating Current Cyclic Voltammetric Theory and Experimental Results for Simple Electrode Reactions Involving Amalgam Formation." Analytical Chemistry **50**(2): 216-223.

Chernykh, I. N., A. P. Tomilov, A. V. Smetanin and A. V. Khudenko (2001). "Electrochemical Reduction of Arsenic Acid." Russian Journal of Electrochemistry **37**(9): 942-946.

Dini, J. W. (2000). Electrodeposition of Copper. Modern Electroplating. M. Paunovic. New York, John Wiley & Sons Inc.**:** 61-138.

Dubpernell, G. (1974). Chromium. Modern Electroplating. F. A. Lowenheim. New York, John Wiley & Sons Inc.**:** 87-151.

Dubpernell, G. (1977). Electrodeposition of chromium from chromic acid solutions. New York, Pergamon Press.

Haung, H.-H., K. Anttila and A. Roine (1999). Outokumpu HSC Chemistry. Pori, Finland, Outokumpu Research Oy.

Holt, L. M. (1974). Uncommon Metals. Modern Electroplating. F. A. Lowenheim. New York, John Wiley & Sons Inc.**:** 461-485.

Mandich, N. V. (1997). "Chemistry & Theory of Chromium Deposition: Part I - Chemistry." Plating & Surface Finishing(May): 108-115.

Mandich, N. V. (1997). "Chemistry & Theory of Chromium Deposition: Part II - Theory of Deposition." Plating & Surface Finishing(June): 97-101.

Mandich, N. V. and D. L. Snyder (2000). Electrodeposition of Chromium. Modern Electroplating. M. Schlesinger and M. Paunovic. New York, John Wiley & Sons Inc.**:** 289-360.

Massey, L. K. (2003). Permeability Properties of Plastics and Elastomers: A Guide to Packaging and Barrier Materials. Norwich, NY, Plastics Design Library/William Andrew Publishing.

Motheo, A. J., E. R. Gonzalez, A. Rakotondrainibe, J.-M. Léger, B. Beden and C. Lamy (1996). "The Influence of Anions on the Underpotential Deposition of Copper on a Polycrystalline Gold Substrate." Journal of the Brazilian Chemical Society **7**(1): 1-6.

Omega Engineering Inc. (2003). Verbal communication. H. Stern.

Pawel, S. J., R. J. Lopez and E. Ondak (1998). "Chemical and environmental influences on copper/copper sulfate reference electrode half cell potential." Materials Performance **37**(5): 24-29.

Ponce de Leon, C. and F. C. Walsh (2003). "Research and Development Techniques 1: Potentiodynamic Studies of Copper Metal Deposition." Transactions of the Institute of Metal Finishing **81**(5): B95-B99.

Pourbaix, M. (1974). Atlas of Electrochemical Equilibria in Aqueous Solutions. Houston, National Association of Corrosion Engineers.

Quickenden, T. I. and Q. Z. Xu (1996). "Toward a reliable value for the diffusion coefficient of cupric ion in aqueous solution." Journal of the Electrochemical Society **143**(4): 1248-1253.

Schlesinger, T. E. (2000). Electrodeposition of Semiconductors. Modern Electroplating. M. Paunovic. New York, John Wiley & Sons Inc.

Shi, Z., S. Wu and J. Lipkowski (1995). "Coadsorption of metal atons and anions: Cu UPD in the presence of SO_4^{2-}, Cl^- and Br^-." Electrochimica Acta **40**(1): 9-15.

Smith, D. E. (1971). "Recent developments in alternating current polarography." CRC Critical Reviews in Analytical Chemistry **2**: 247-339.

Tomilov, A. P. and N. E. Chomutov (1974). Arsenic. Encyclopedia of Electrochemistry of the Elements. A. J. Bard. New York, Marcel Dekker Inc. **2:** 21-51.

Tomilov, A. P., A. V. Smetanin, I. N. Chernykh and M. K. Smirnov (2001). "Electrode Reactions Involving Arsenic and Its Inorganic Compounds." Russian Journal of Electrochemistry **37**(10): 997-1011.

White, M. C. and A. J. Bard (1966). "Polarography of metal-pyrogallol complexes." Analytical Chemistry **38**(1): 61-3.

Zhang, J., Y.-E. Sung, P. A. Rikvold and A. Wieckowski (1996). "Underpotential deposition of Cu on Au(111) in sulfate-containing electrolytes: A theoretical and experimental study." Journal of Chemical Physics **104**(14): 5699-5712.

6 Deposition from Multicomponent Solution: Results and Discussion

The results presented in Chapter 5 of deposition from solutions containing only one of the three target elements (copper, chromium, and arsenic) for removal are the foundation for the deposition studies of multiple target elements from multicomponent solutions discussed in this chapter. Sections 6.1 through 6.3 cover deposition of all three pairwise combinations of CCA components in dilute sulfuric acid solutions. Codeposition studies of all three target elements are presented in Section 6.4. Of all of the conditions studied, the behavior of the three-component solutions most closely represents CCA aqueous waste.

6.1 Copper and Chromium

The addition of chromium to a copper solution reduces the deposition rate of copper. Figure 5-11 illustrated how the addition of 0.5 M CrO_3 to a solution of 5 mM H_2SO_4 suppressed the deposition of pure copper on a copper working electrode as seen in the background scan with a solution of only 5 mM H_2SO_4. To further explore this effect a small amount of chromium (0.5 mM $K_2Cr_2O_7$) was added to a solution of copper sulfate and sulfuric acid. As shown in Figure 6-1, the copper stripping peak is unchanged, but the copper deposition peak current is smaller. The effect of chromium addition is more pronounced at greater chromium concentrations. Chromium deposition, however, can proceed from solutions containing copper and chromium can deposit on copper electrodes. In fact, copper can make chromium deposition more favorable. Studies on chromium deposition from industrial chromium plating solutions (2.5 M CrO_3, 0.025 M H_2SO_4) onto carbon steel working electrodes have shown that the addition of 0.01 M $CuSO_4$ to the plating solution shifts the onset of chromium ion reduction to a less negative potential and results in a larger current during chromium deposition (Baraldi 2001).

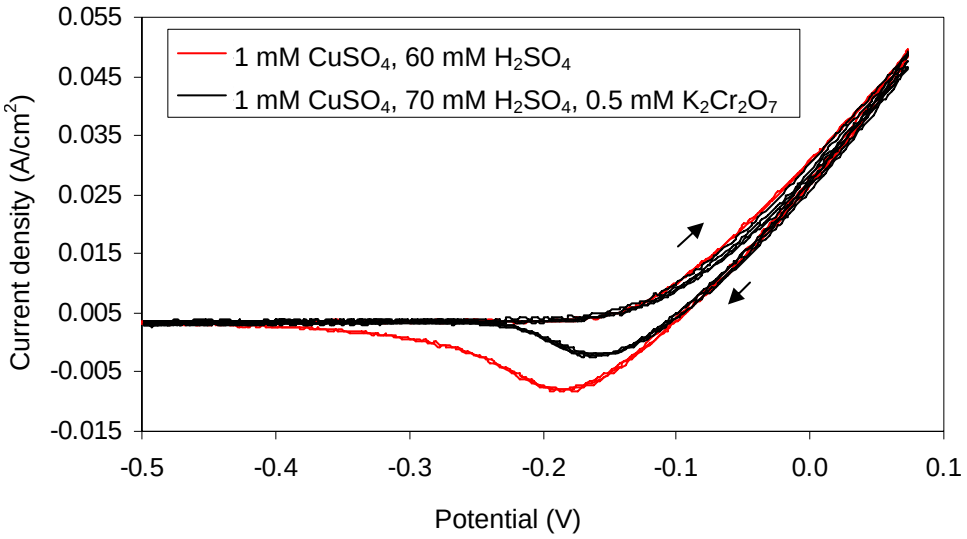

Figure 6-1: Copper deposition from a copper and chromium solution on a Cu WE
The black arrows indicate the direction of the DC potential scan. Scan rate is 20 mV/sec.

6.2 Arsenic and Copper

The codeposition of arsenic and copper was studied on a 4.5 mm diameter liquid gallium working electrode. Liquid gallium was chosen for the working electrode because it showed the lowest rate of arsine evolution during previous arsenic experiments. With an eye toward the three-component experiments (As, Cr, and Cu), concentrations of 41 mM As_2O_5 and 7.7 mM $CuSO_4$ were chosen. These levels match the CCA type-C concentration ratio with respect to the previously explored 25 mM CrO_3 solutions. A concentration of 61 mM H_2SO_4 was used in order to match the arsenic-only deposition studies on liquid gallium that were presented in Section 5.3.2.

Figure 6-2 shows the DC voltammogram for 41 mM As_2O_5, 7.7 mM $CuSO_4$, and 61 mM H_2SO_4 with a liquid gallium working electrode. The large anodic peak at 0.12 V is copper stripping. The peak is shifted 0.1 V in the anodic direction from the peak in Figure 5-2 for

copper deposition on a gold electrode. Scans that continued to more anodic potentials those shown in Figure 6-2 displayed stripping of the gallium electrode.

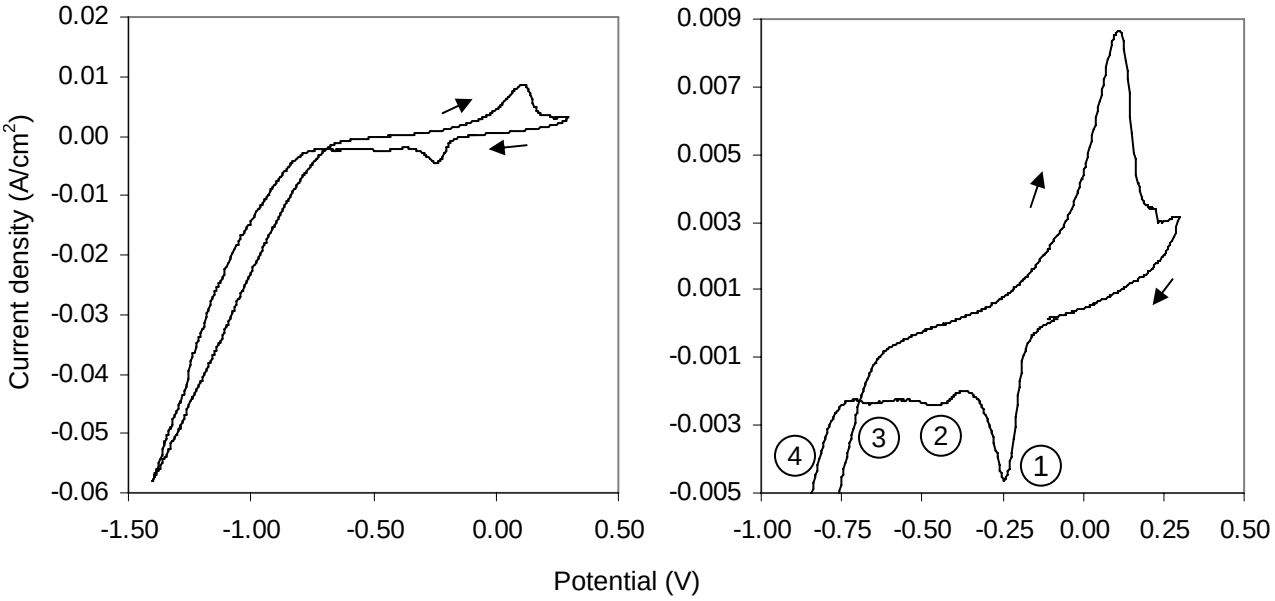

Figure 6-2: Copper and arsenic codeposition onto a liquid Ga WE
Scan rate is 30 mV/sec. Cycle 5 of 5 shown. Magnified plot of the area of interest on the left.

The behavior observed on the cathodic sweep of Figure 6-2 is more complicated than that seen on the anodic sweep. There are four cathodic peaks, numbered ①, ②, ③, and ④. Peak ①, at -0.25 V, corresponds to deposition of a reddish-brown powder that is probably copper. The second cathodic peak, ②, at -0.45 V, also corresponds to copper deposition. The powder at this potential is darker brown in color than that deposited at -0.25 V. Holding the potential at the third, and smallest, cathodic peak, ③ (-0.65 V), resulted in the deposition of a black, sponge-like powder with no detectable gas evolution, either visually or via the arsine detector/bubbler system described in Section 4-3. Gas evolution began at about -0.75 V at the start of the fourth cathodic peak, ④. The initial potential at which arsine was evolved was not determined, but it was apparent at -2.5 V. Also apparent was the rapid deposition of the same black, sponge-like

powder as at -0.65 V. Gas evolution at -2.5 V was so vigorous that the powder formed on the electrode was rapidly dispersed throughout the solution.

Unlike the limited deposition that was observed with the arsenic deposition alone from sulfuric acid solutions examined in Section 5.3.2, electrolysis of the binary copper-arsenic solutions generated enough powder to allow it to be removed from the gallium electrode for elemental and chemical analysis. EDAX SEM showed that the powder contained 75% arsenic and 25% copper by atom percent. No gallium peak was detected, which means that no gallium arsenide was in the powder formed during the deposition process. A SEM image of the powder is shown in Figure 6-3. XRD analysis of the black powder indicated the presence of Cu and Cu_3As (of the type domeykite high). See Appendix 10.3 for XRD data. Complete analysis of all of the XRD peaks in the spectrum was not possible due to high levels of background noise from the sample mounting material. The presence of Cu_3As is consistent with the electrochemical stability analysis from Section 2.1 for mixed copper-arsenic systems. Because the powder can be produced without arsine evolution, -0.65 V (peak number ③ from Figure 6-2) must be within the narrow range of potentials where this behavior is possible. XPS analysis of the powder yielded incomplete results because there was not a match in the databases to some of the peaks. See Appendix 10.4 for XPS data. The peaks that were identified correspond to As (~40% of the sample) and CuO (~55% of the sample). Cu_3As was not in the database. These peak identifications would be strengthened by collected XPS data on As, CuO, Cu_3As, and other arsenic and copper oxides.

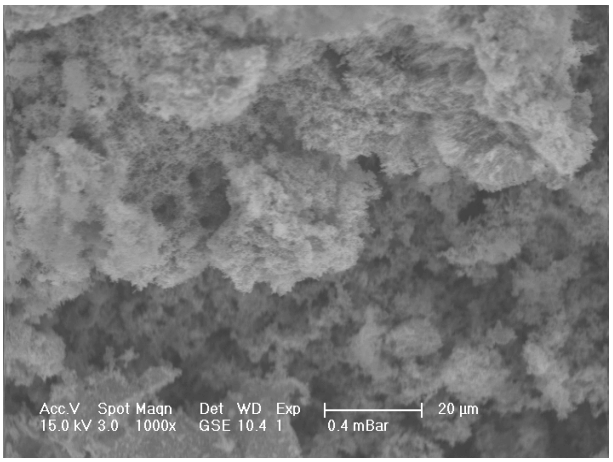

Figure 6-3: SEM GSE image of arsenic and copper deposit formed on liquid Ga WE

One of the major difficulties in using liquid gallium with solutions of arsenic and copper is that arsenic and copper are both more noble than gallium; hence, the latter can act as a reductant to produce elemental copper and arsenic by metallothermic displacement reactions without the application of an external electrical potential. This process occurs more rapidly with liquid gallium than solid gallium. The reactions that occur are shown as R6-1 to R6-3 along with their equilibrium potentials (versus CSE) calculated from Pourbaix (1974). The actual solution composition and its measured pH of 1.0 were used to calculate the equilibrium potentials. The arsenic reaction shown is the final step of arsenic deposition.

$$\mathrm{Ga\ (l,s)} \rightleftarrows \mathrm{Ga^{3+}} + 3e^- \qquad E_{\mathrm{Ga}} = -0.97\mathrm{V} \qquad \text{(R6-1)}$$

$$\mathrm{Cu} \rightleftarrows \mathrm{Cu^{2+}} + 2e^- \qquad E_{\mathrm{Cu}} = -0.04\mathrm{V} \qquad \text{(R6-2)}$$

$$\mathrm{As} + 2\,\mathrm{H_2O} \rightleftarrows \mathrm{HAsO_2} + 3\,\mathrm{H^+} + 3e^- \qquad E_{\mathrm{As}} = -0.16\mathrm{V} \qquad \text{(R6-3)}$$

Since the copper and arsenic equilibrium deposition potentials are more anodic than the equilibrium stripping potential of gallium, gallium dissolves as they are deposited. Copper, with the most anodic potential of the three, is deposited first as a reddish-brown powder with the same appearance as that deposited at peak ① of Figure 6-2. After about ten minutes of exposure with

the solution, a layer of black powder begins to form on top of the copper layer that was first deposited on the liquid gallium surface. EDAX SEM analysis of the entire powder mixture revealed that it is about 15% arsenic and 85% copper. Thus, the application of an external electrical potential to deposit arsenic and copper onto liquid gallium yields a higher percentage of arsenic (75%) in the final product than does the process without an externally applied potential. The voltammogram shown in Figure 6-2 was taken immediately after inserting the liquid gallium electrode into a deaerated solution in order to have a clean gallium surface for deposition. This method also ensured that the product collected after electrolytic deposition of copper and arsenic was not contaminated with the natural deposition product.

The non-electrolytic formation of solid arsenic on gallium cannot occur without copper present in solution. For complete removal of arsenic, copper would have to be present at a concentration of at least three times that of arsenic. For this method to be cost-efficient, it would have to include the recovery of gallium via deposition. A similar, cheaper, and potentially more effective method that is currently employed for metal removal from aqueous wastes uses iron in place of gallium. Iron has a more cathodic equilibrium potential with its dissolved ions than gallium and a wider pH range where no oxide is present.

6.3 Arsenic and Chromium

The codeposition of arsenic and chromium was studied using a 304 stainless steel 2.0 mm diameter working electrode. Stainless steel was chosen for the working electrode because it does not react with the bulk solution and had previously shown a reproducible chromium stripping peak (Section 5.2). As with the arsenic and copper deposition experiments, concentrations of 41 mM As_2O_5 and 25 mM CrO_3 were chosen because they matched the CCA type-C concentration ratio. Both arsenic and chromium were studied at those concentrations in single-component

solutions (Sections 5.2 and 5.3). A concentration of 0.25 mM H_2SO_4 was used in order to match the 100:1 CrO_3:H_2SO_4 ratio that has been shown to be optimal for chromium deposition (Section 5.2).

Figure 6-4 shows a DC voltammogram for the solution of 41 mM As_2O_5, 25 mM CrO_3, and 0.25 mM H_2SO_4 with a freshly polished stainless steel electrode. A mixture of a light bluish-gray and black material was deposited over the range of -0.65 V to -2.5 V. Gas evolution started at a potential of about -0.9 V and arsine was first detected at -1.0 V. Both arsine and total gas evolution increased with decreasing potential. It is important to note that deposition first occurred before the visible evolution of any gas. The deposit formed from the arsenic and chromium solution, unlike the deposit from the chromium-only solution, could not be electrolytically stripped from the working electrode. No chromium stripping peak was observed when the potential approached the chromium stripping region reported in Section 5.2. The first cycle in Figure 6-4 shows a distinct peak at -0.15 V which probably corresponds to deposition of the copper leached from the CSE. Later cycles show that this peak becomes less distinct as other deposition processes, such as arsenic, start to occur. It is possible that a cathodic film for chromium deposition has formed at the electrode surface by the second cycle and changed the deposition kinetics of all species present in solution.

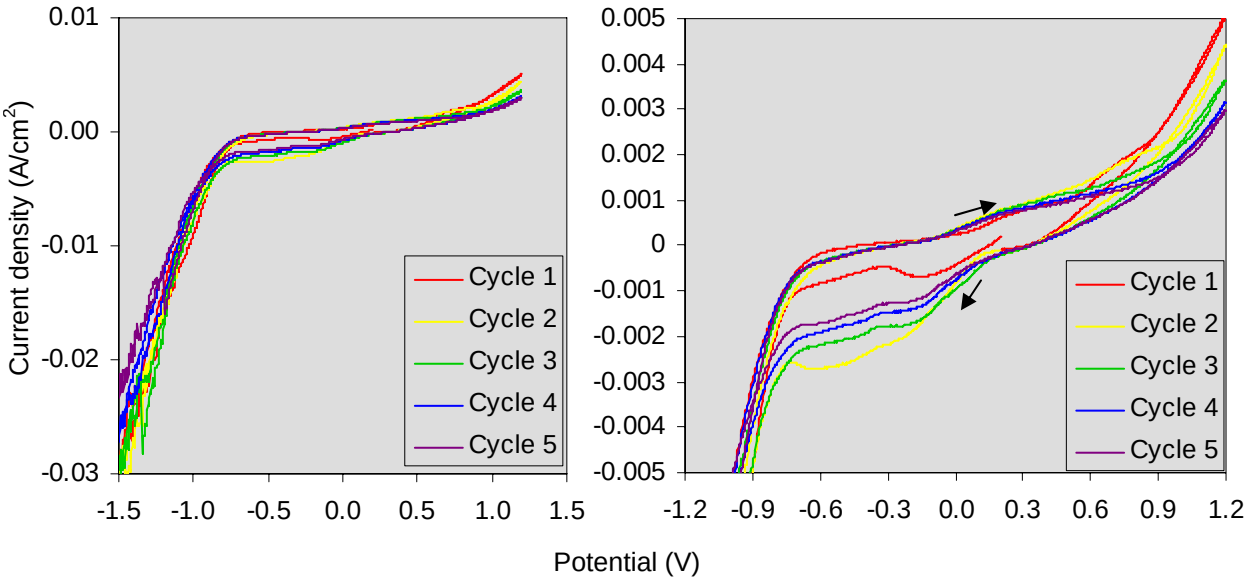

Figure 6-4: Arsenic and chromium codeposition onto a stainless steel WE
Scan rate is 30 mV/sec. Graph on the right is a magnified view of the area of interest.

Deposition was observed over a range of potentials ranging from -0.65 to -2.5 V. Deposition rates at all these potentials were slow, particularly in comparison to those associated with the codepositon of arsenic and copper on a liquid gallium working electrode. EDAX SEM analysis showed variation of the elemental content of the deposit across the electrode. The elemental metal percents varied from 45 to 65% arsenic and 35 to 55% chromium. Oxygen was also present in the deposits, since the sample was exposed to air between deposition and analysis.

The SEM images in Figure 6-5 reveal that the deposit consists of small islands of roughly 50 to 100 microns, somewhat similar to the morphology of the material deposited from the arsenic-only solution on the stainless steel electrode (Figure 5-25). The image taken with the BSE detector (b) shows that most of the deposit is the same color, hence the same average atomic weight, with underlying spots of lighter and heavier atomic weights. These spots may be areas of pure arsenic (lighter) and pure chromium (darker).

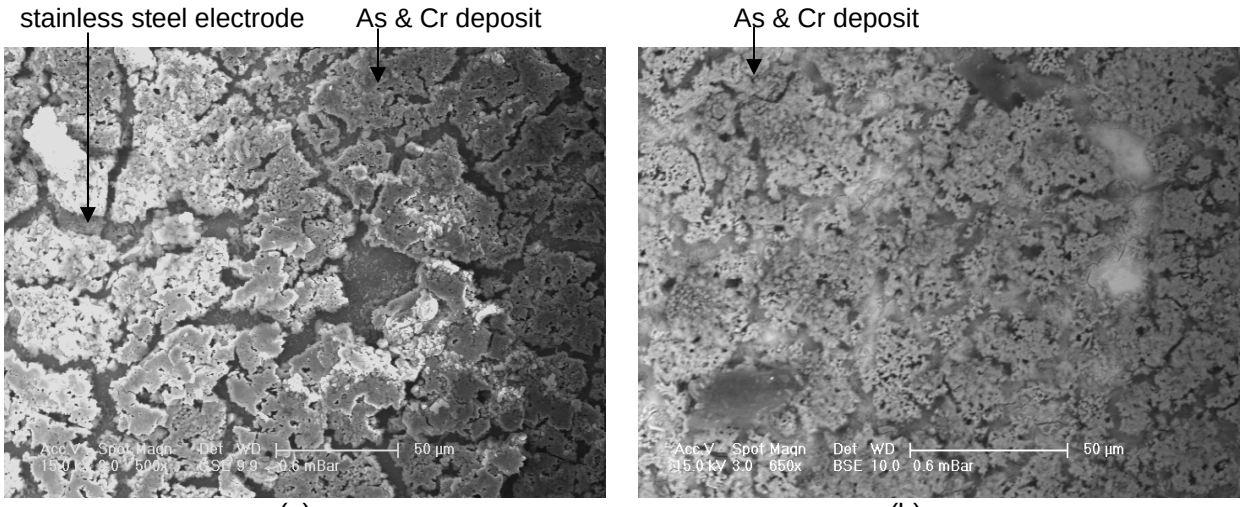

Figure 6-5: SEM images of arsenic and copper deposited on a stainless steel WE
Image (a) was taken using the GSE detector and image (b) was taken using the BSE detector. The images are of different locations on the same general deposit. The images become darker on the right side due to the sample angle relative to the detector.

6.4 Arsenic, Copper, and Chromium

Codeposition of arsenic, copper, and chromium was explored at three different total concentrations with the metal ratio always set to the CCA type-C ratio. These concentrations are shown in Table 6-1 in milli-molar values. Each solution has been labeled with a letter (A, B, or C) for future reference.

Table 6-1: Concentration of solutions for arsenic, copper, and chromium codeposition

Solution	Concentration, mM			
	As_2O_5	$CuSO_4$	CrO_3	H_2SO_4
A	4.1	0.77	2.5	0.025
B	41	7.7	25	0.25
C	206	39	125	2.5

The chromium-trioxide-to-sulfuric-acid ratio is 100 to 1 for solutions A and B and 50 to 1 for solution C. This change in ratio was the result of a calculation oversight, but the resulting ratio is still within the recommended range. Except for the change in sulfuric acid, solution C is five times as concentrated as solution B, and solution B is 10 times as concentrated as solution A.

Solution B matches the concentration used in all two-metal deposition experiments and in both the chromium and arsenic single-metal deposition experiments. Deposition from solutions A and C was performed on gold and copper working electrodes, while deposition from solution B was performed on gold, copper, stainless steel, and liquid gallium electrodes.

Deposition from solutions A, B, and C yielded three types of deposits. The first type, similar to that deposited in the arsenic-copper deposition experiments, was black and sponge-like. It was deposited from all three solutions and contained As (35%), Cr (20%), and Cu (45% of the total metal), with oxygen accounting for about half of the atoms detected. From all three solutions, this type of deposit was formed over a narrow potential range without arsine and then at more cathodic potentials along with arsine for all three solutions. This type of deposit was formed at a faster rate than the other types. The second type of deposit formed at more anodic potentials than the first type and only from solutions B and C. It changed from medium gray to light-bluish gray upon exposure to air. It contained a different balance of As (60%), Cr (30%), and Cu (10% of the total metal), with oxygen again accounting for about half of the atoms detected, and deposited only on solid electrodes without evolving arsine. The third type of deposit was thin and silvery, deposited as a smooth layer, and was only formed on gold and copper working electrodes. Its deposition was confirmed for solution A and C and was probably also formed from solution B, but the experiments to check for its existence were not performed. Type three was deposited at more anodic potentials than the other two types of deposits and did so without the evolution of any gas. It contained only As (35%) and Cu (65% total metal) with small amounts of oxygen and was only deposited in very limited quantities. The second type of deposit offers the best method for arsenic, copper, and chromium removal from both solutions B and C since it can be produced in larger quantities than type three, contains a distribution of the

metals close to that in CCA type-C, and can be produced without the evolution of arsine.

The equilibrium potentials for Cu, As, and Cr metal, in contact with aqueous solutions of their oxidized species become more negative with increasing concentration (Section 2.1). This decrease in equilibrium potential should translate to a decrease in deposition potential. This decrease in equilibrium potential should translate to a decrease in deposition potential as confirmed by measurements made in this study.

Type one deposit is the only option for bulk removal of CCA from solution A. Bulk codeposition of Cr, Cu, and As from solution A first occurred at a potential between -0.9 and -1.0V on copper and gold electrodes. The onset of deposition in solution A occurs at a potential that is more cathodic than for all types of deposition in solutions B and C. Since detectable arsine evolution does not begin until a potential that is more negative than -1.1 V, a type one deposit can be made without the evolution of arsine from solution A. The problem with this deposition for bulk CCA removal is that it occurs very slowly. For instance, after 6 hours of deposition from solution A at -1.1 V on 2.0 mm diameter copper and gold working electrodes, the surface of each electrode was less than half covered by a thin layer of the deposited powder. The slower rate of deposition and the more cathodic potential for deposition from solution A in comparison to solutions B and C was probably due to solution A being ten and fifty times more dilute than the other solutions, respectively.

Figure 6-6 compares the voltammograms in solution A recorded on a clean copper working electrode and an electrode that was about half covered by the type one deposit. The peak recorded during the anodic sweep at -0.62 V was observed only for the electrode with the deposit. This peak, therefore, probably represents electrochemistry that occurs only on the deposit and not on the copper electrode surface. Further studies on an electrode with the same

composition as the powder would be necessary to more accurately determine the electrochemical origins of the anodic peak.

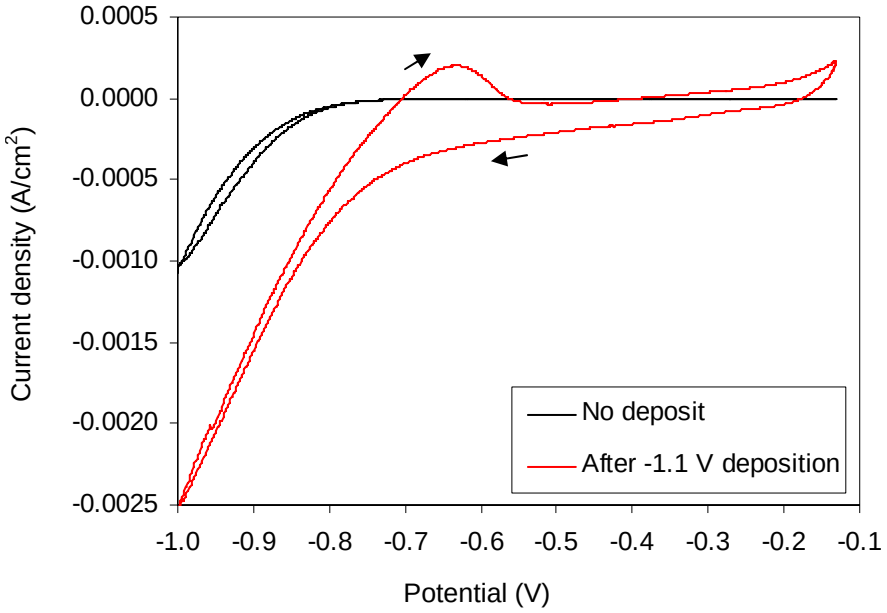

Figure 6-6: Voltammograms for solution A on copper WE
The trace in red shows the voltammogram with type one deposit covering half of the working electrode.

The voltammogram for solution A with a gold electrode, shown in Figure 6-7, includes three traces. The one for the clean gold surface (trace A) has a large peak on the cathodic sweep, probably copper deposition, followed by a small peak at -0.50 V. Deposition at -0.50 V appeared to produce a trace amount of the type three deposit, but the deposited layer was so thin that it was difficult to visually characterize. A linear sweep voltammogram of the electrode after holding the potential at -0.52 V for 3 hours (trace B) still displayed a small cathodic peak at -0.5 V. The copper deposition and stripping peaks are more distinct than on a clean gold surface. The shape of the voltammogram dramatically changed after type one deposition at -1.1 V for six hours (trace C). The peak at -0.65 V during the anodic sweep was in almost the same position as the one observed in Figure 6-6 for type one deposit on a copper electrode. The growth of the other peaks in reference to trace B is in large part due to the increase in the electroactive area

with the addition of the type one deposit. The peak at 0.75 V in Figure 6-6(b) during the cathodic sweep is from gold deposition back onto the working electrode. The same peak was observed in other voltammograms in that potential range on a clean gold surface. The anodic peak at 0.05 V is most likely copper stripping. In addition, copper stripping from a copper-arsenic or copper-chromium compound would probably be shifted in the anodic direction and could account for the large peak at 0.3 V.

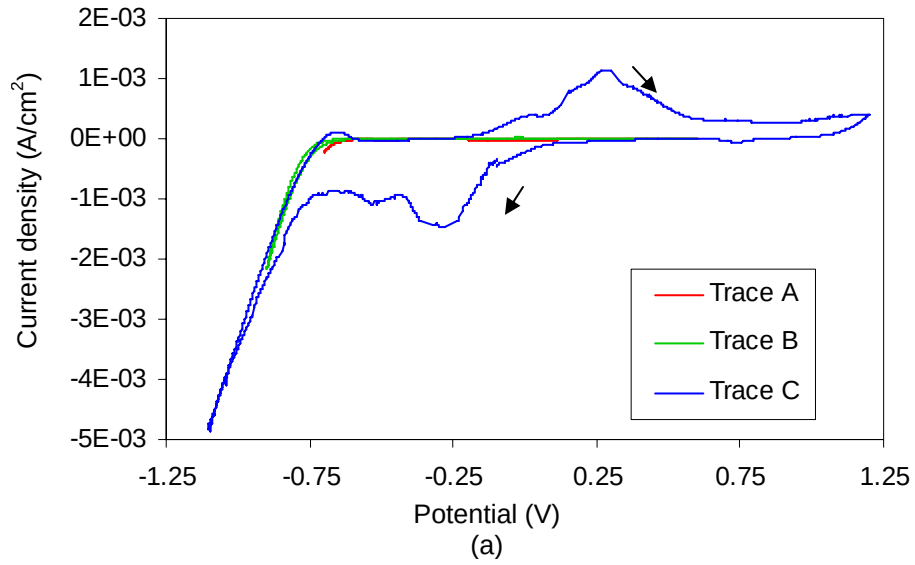

(a)

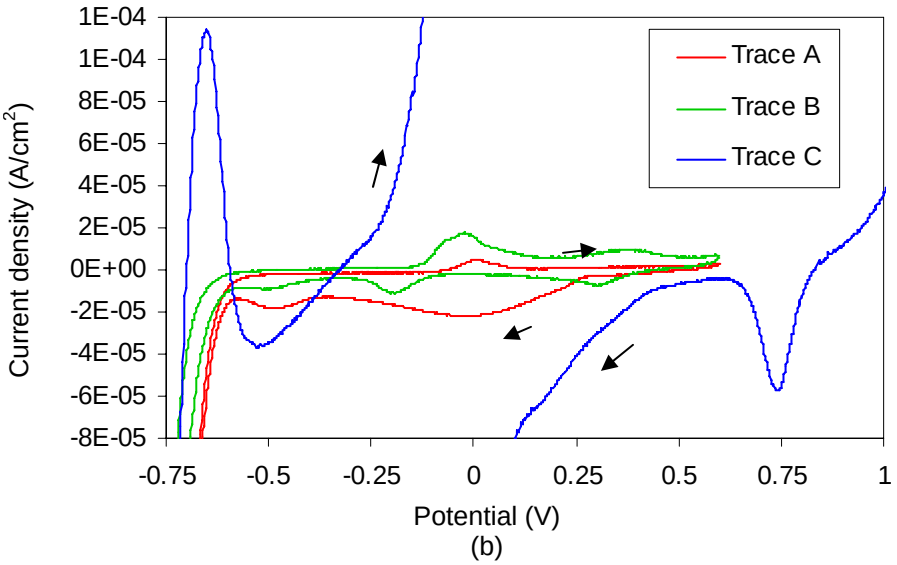

(b)

Figure 6-7: Voltammograms for solution A on gold WE

Scan rate is 10 mV/sec. Trace A was preformed on a clean electrode surface. Trace B was performed after a -0.52 V deposition. Trace C was after a -1.1 V deposition.

Type one and type two deposits were observed from solutions B and C onto copper, gold, and stainless steel working electrodes. Figure 6-8 illustrates the effect of the type two deposit on the voltammogram trace. The trace on the fresh copper electrode in solution C shows a deposition peak at -0.73 V corresponding to the type two deposit. After holding the system at -0.7 V for 3.5 hours, type two material covered the electrode surface. During the next potential sweep, the cathodic peak shifted to -0.66 V. The system was held at -0.65 V for 15.75 hours, and the cathodic potential of the peak current remained unchanged. The peak current was, however, slightly smaller, which may indicate that type two deposit has a lower conductivity than the copper working electrode. The type two deposit was formed without the evolution of any type of detectable gas.

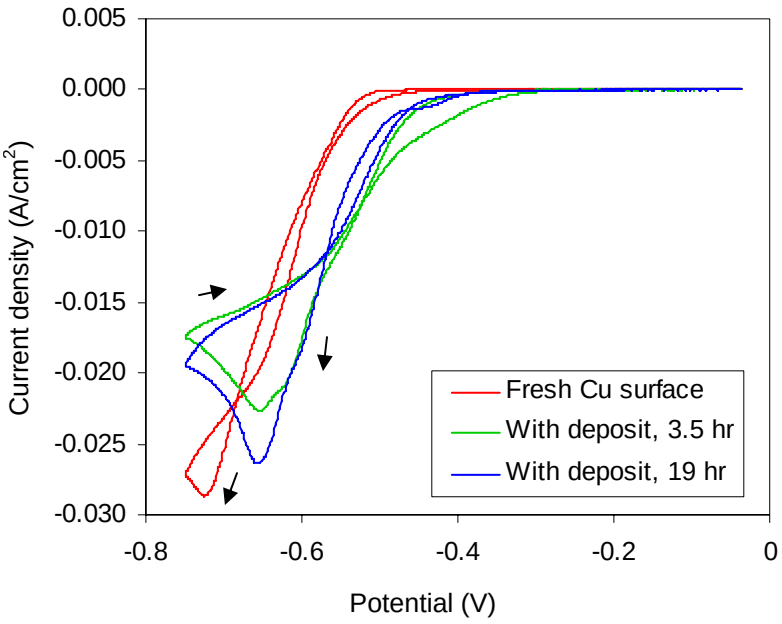

Figure 6-8: Deposition on copper WE from solution C
The line in blue was recorded after deposition at -0.7 V for 3.5 hours and the green line after depositing at -0.65 V for 15.75 hours on top of the original deposit. Scan rate is 10 mV/sec.

Figure 6-9(a) shows the SEM BSE of the type two deposit on copper working electrode from solution C as being nearly homogeneous in elemental composition (medium gray color,

60% As, 20% Cr, 20% Cu) with small cracks (dark gray) between the islands of deposit. There are a few white spots in the SEM BSE and they have a higher copper concentration (50% As, 10% Cr, 40% Cu) than the gray areas. The SEM GSE image in Figure 6-9(b) shows the topography of the deposit as being composed of nearly flat islands of deposit separated by small cracks.

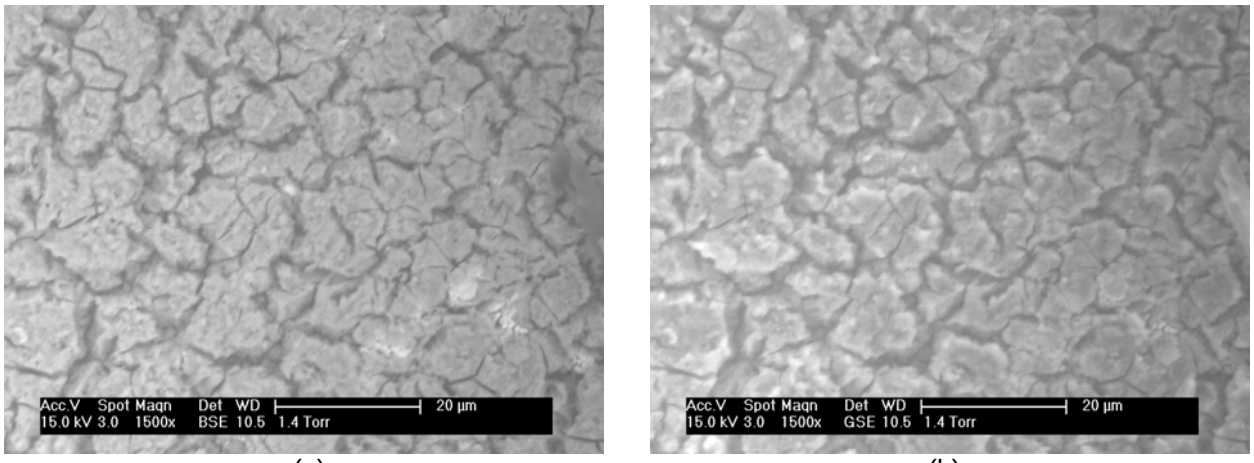

(a) (b)

Figure 6-9: SEMs of type two deposit on copper working electrode from solution C
Image (a) is BSE SEM and image (b) is GSE SEM.

Type three deposit was formed on a copper working electrode from solution C. It began depositing at a potential between -0.42 and -0.5 V and formed a thin, silvery, mirror-smooth layer. Holding the system at -0.5 V for over 16 hours did not result in a visible increase in the thickness of the initial deposit. Deposits of type one and two were still possible at more cathodic potentials. This deposition behavior suggests that type three deposit can occur on copper (and gold, as will be shown later), but not on a thick layer of itself. It also shows that type three deposit does not interfere with type one or type two deposition.

The voltammogram in Figure 6-10(a) is for a copper working electrode in solution B. The trace shows similar deposition behavior to solution C. Cycle one of the scan was performed on a clean copper surface and has a deposition peak for type two at -0.75 V (-0.73 V for solution

C). By cycle 5, after there has been growth of the deposit, the peak current decreases slightly and the potential shifts to -0.65 V (-0.66 V for solution C).

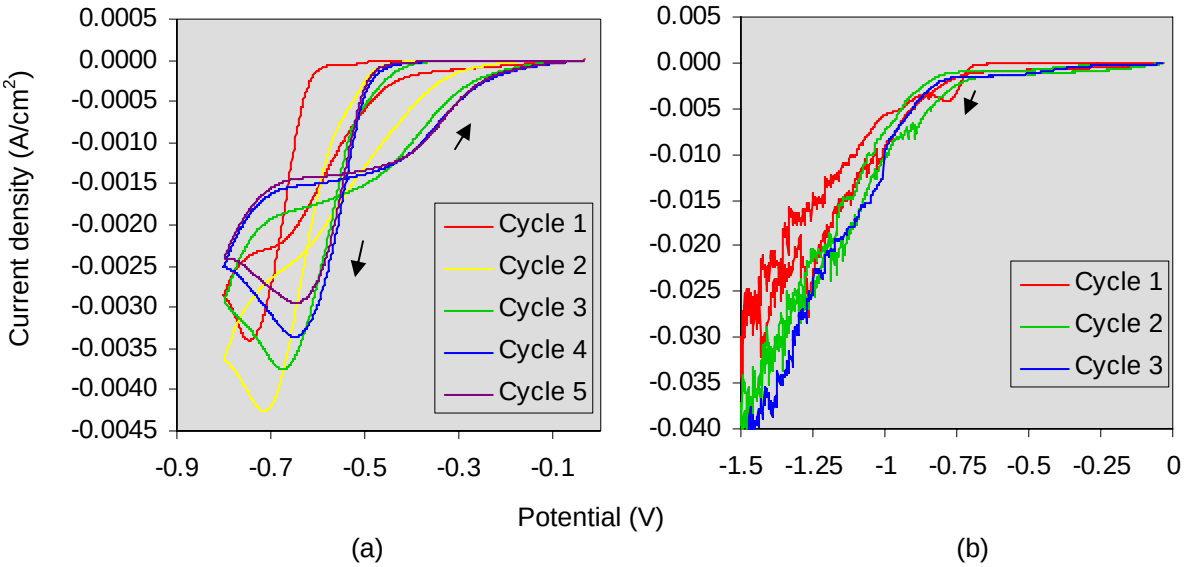

Figure 6-10: Deposition on copper WE from solution B
Plot (a) has a lower switching potential of -0.8 V while that for plot (b) is -1.5 V.
Scan rate is 10 mV/sec for all traces.

As seen in Figure 6-10(a) at -0.8 V mostly type two deposit is formed, along with a little bit of type one. Arsine evolution starts between -0.8 and -1.02 V for a copper working electrode in solution B. Thus, it is possible to make both type one and type two deposits without the evolution of arsine. Figure 6-10(b) displays the voltammogram with a switching potential of -1.5 V. For cycle one, the cathodic deposition peak observed in (a) at -0.8 V is also seen in (b). Over the course of the first sweep, type one deposit is formed. Cycles two and three no longer display the cathodic peak seen in cycle one. Therefore, the deposition that occurs on the bare copper surface does not occur on the surface of type one deposit.

SEM analysis of the type two deposit formed on a copper working electrode at -0.8 V from solution B revealed a mostly flat surface with many small cracks. String-like deposits can be seen in Figure 6-11(a) scattered over the flat surface. The elemental composition of the flat

surface is type two deposit while that of the string-like deposits was more similar to type one deposit and had a higher copper and lower arsenic content. The type one deposit is Figure 6-10(b) is a dendritic structure deposited on top of type two deposit at -1.5 V from solution B.

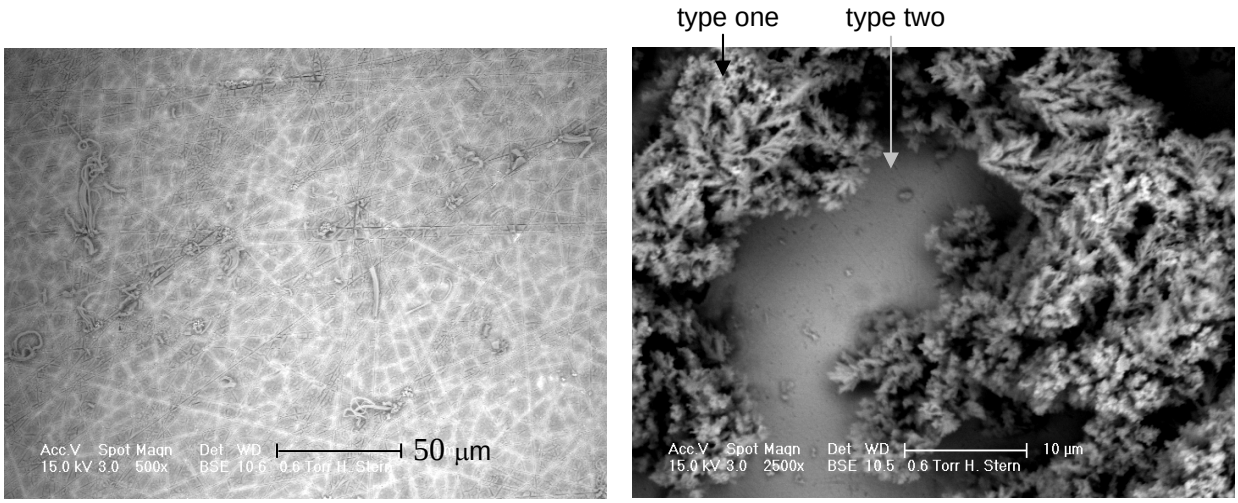

Figure 6-11: BSE SEM of deposits on copper WE from solution B
Image (a) is of type two deposit formed at -0.8 V and image (b) is of type one deposit on top of type two deposit formed at -1.5 V.

The gold working electrode behaved in a similar manner to the copper working electrode for solutions B and C. Figure 6-12 explores the effect of type three deposit on the voltammograms for a gold working electrode in solution C. Type three deposition began at less than -0.5 V. The first cycle on a clean gold electrode is almost flat. By the fifth cycle, a small amount of type one deposit has probably formed and a peak at -0.39 V during the cathodic sweep is visible. After deposition at -0.5 V for 0.5 hours, the electrode is covered with type one deposit and the scan shows a larger peak current at -0.39 V. No gas was observed during any of the scans. The cathodic process at -0.39 V may correspond to the deposition of the type one deposit; however, the total thickness of this deposit is limited and the peak may correspond to another reaction that does not form a solid or gaseous product.

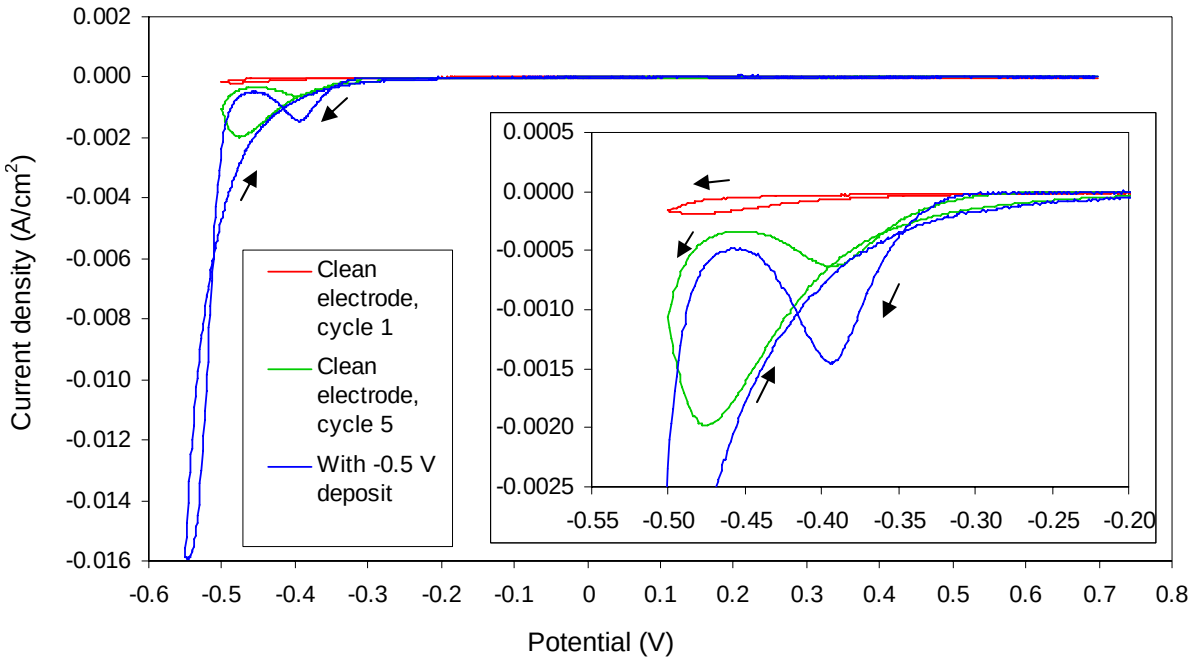

Figure 6-12: Voltammograms for gold WE in solution C
Scan rate is 10 mV/sec.

At more cathodic potentials, the deposit changes from type three to type two and then to type one. The peak in Figure 6-13 at -0.66 V during the cathodic sweep corresponds to type two deposition. Beyond this cathodic peak, where the current forms a local cathodic current minima (-0.8 V), the deposition switches from type two to type one. Thus, during the course of the trace both type two and type one deposits where formed. In Figure 6-13, the peak that was observed at -0.39 V in Figure 6-12 is absent. Thus, the process that formed that peak does not occur on type two or one deposit.

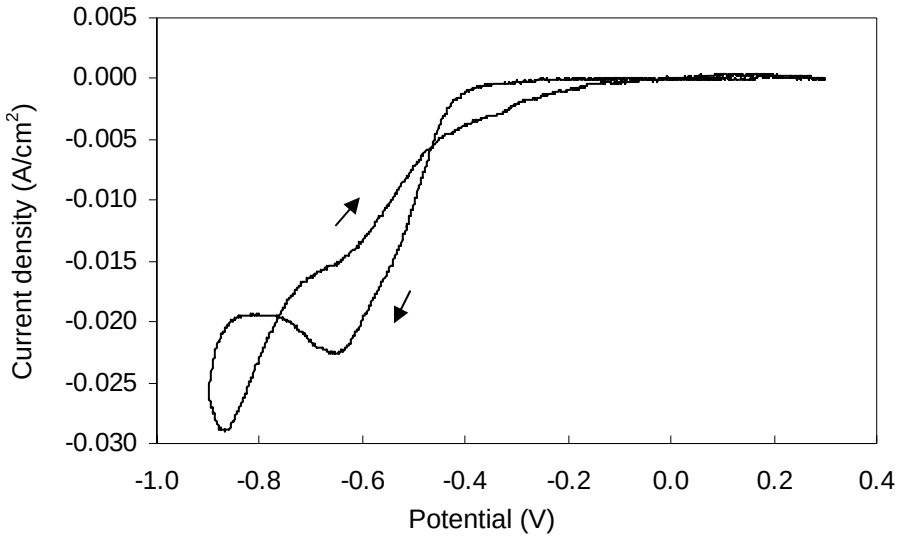

Figure 6-13: Deposition on gold WE from solution C
Trace recorded after deposition at -0.7 V. Scan rate is 10 mV/sec.

It was possible to observe visually the mix of the gray type two deposit and the black type one deposit formed by holding the potential at -0.8 V on a gold electrode in solution C on the electrode. Figure 6-14(a) shows that the mix of the deposits is visible in the BSE SEM image as areas of different average atomic weight. The plain gray areas (b) when analyzed with a spot beam of EDAX had the same composition as the type two deposits. The mixed white and gray bumpy clusters (c) had a similar composition to the type one deposit.

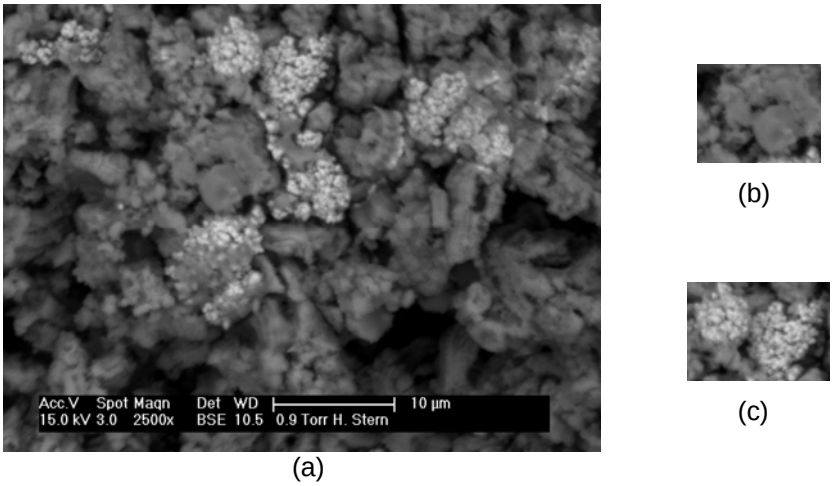

Figure 6-14: BSE SEM of deposit on gold WE from solution C
The SEM (a) shows a mixture of type two (gray) (b) and type one (white and gray) (c) deposit that was formed at -0.8 V from solution C.

When the concentration was reduced from solution C to solution B, formation of type two and type one deposits still occurred. Figure 6-15 shows the voltammogram for an initially clean gold surface compared to one with a type two deposit formed at -0.6 V. Both traces have a peak in the -0.48 to -0.46 V range, but the peak current increased after the type two deposition. The potential of this peak is between that for the type three deposit in Figure 6-12 and the type two deposit in Figure 6-13. A trace amount of arsine was detected at -0.6 V, so this peak is probably related to type two deposition since no gas was ever observed during type three deposition. It is not clear why this peak is shifted in the anodic direction from that observed in solution C for gold working electrodes and for solutions B and C for copper working electrodes. During this experiment, deposition was not held at a potential more anodic than -0.6 V to check for type three deposition because the existence of type three had not yet been identified.

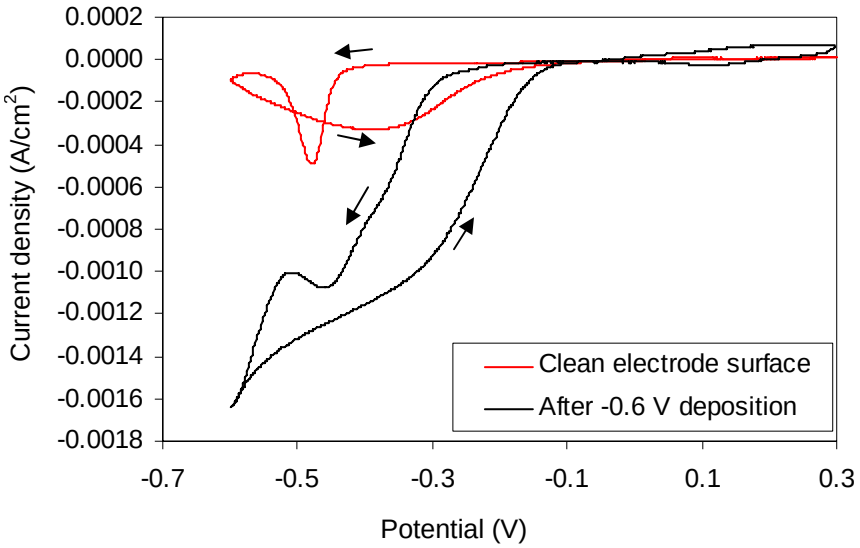

Figure 6-15: Deposition on gold WE from solution B
Scan rate is 10 mV/sec.

Figure 6-16 is a BSE SEM image of the type two deposit on a gold working electrode from solution B. It is a thinner deposit than that on the copper working electrode shown in

Figure 6-11(a). The deposit is light gray and the darker areas are cracks that reveal the underlying gold surface.

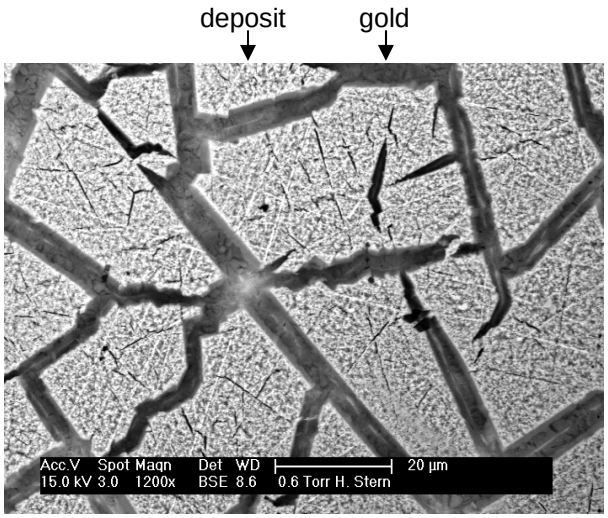

Figure 6-16: BSE SEM of type two deposit on gold WE from solution B

Type two deposit from solution B onto a stainless steel working electrode was achieved at a potential of -0.8 V. Deposition occurred slowly in comparison to both the gold and copper working electrodes. After two and a half hours of deposition, less than half of the electrode surface was covered, and the deposit layer was thin. Arsine was not detected during this deposition or during a later deposition potential of -0.85 V. The trace for the clean stainless steel surface in Figure 6-17 shows a peak at about 0 V. Holding the potential at -0.12 V for 16 hours yielded no visible deposit, which indicated that this peak does not correspond to a deposition product. The peak starting at -0.65 V increased significantly after the type two deposit covered half of the electrode surface. This behavior shows that the type two deposition occurs more quickly onto itself than onto stainless steel. Since deposition from solution B onto stainless steel was slower than with either the gold or copper working electrodes, experiments were not performed using solution A.

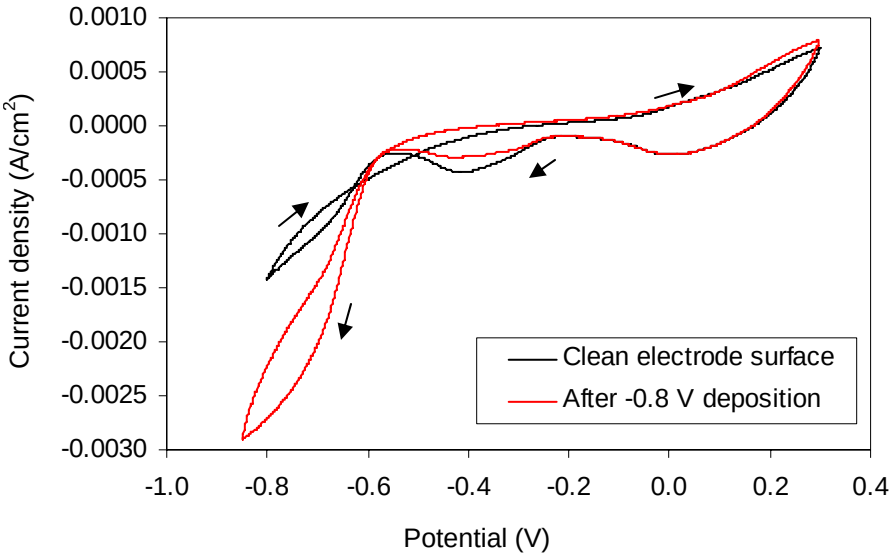

Figure 6-17: Deposition on stainless steel WE from solution B
Scan rate is 10 mV/sec.

Deposition onto a stainless steel working electrode from solution C yielded type one and type two deposits. The deposition process occurred at a faster rate from solution C than from solution B as would be expected with an increase of the bulk solution concentration. No gas evolution was observed at -0.75 V on a clean stainless steel working electrode. Figure 6-18 illustrates the deposition behavior onto an initially clean stainless steel working electrode. A peak at -0.87 V is not observed until after the first layer is deposited during cycle one. Peak current decreases with each successive scan. This behavior may indicate that the deposit is formed at a slower rate when deposited on itself or that the composition of the cathodic film changes with each cycle (similar to chromium only deposition) and affects the deposition rate. Deposition at -0.87 V for 16 hours resulted in the formation of a compact form of the black type one deposit with a thin layer of dark green deposit on the surface of the entire deposit. The dark green deposit was not observed in any other deposition experiments.

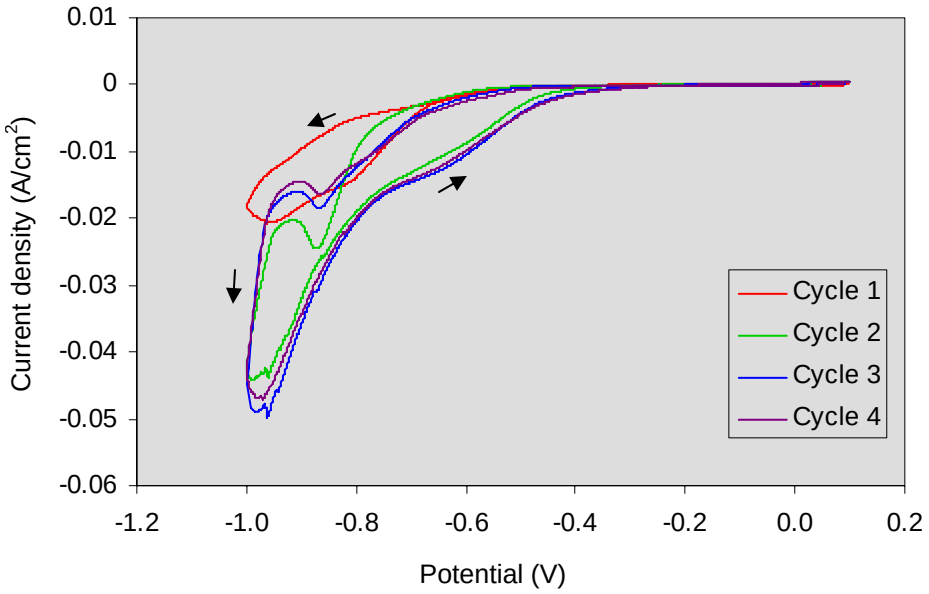

Figure 6-18: Deposition on clean stainless steel WE from solution C
Scan rate is 10 mV/sec.

After most of the type one deposit was removed from the stainless steel electrode by scrapping it with a metal spatula, a thin layer of type one deposit still remained. Figure 6-19 shows the deposition behavior on this layer. With each successive cycle the peak moves to a more anodic potential with the greatest jump occurring between cycle one (-0.84 V) and cycle two (-0.77 V). The cathodic current also decreases in proportional to the movement of the peak potential. This change in potential with cycle may indicate that deposition onto type one first occurs at a more cathodic potential than deposition onto type two which is deposited during each cycle. The potential was held for 6 hr 20 minutes at -0.72 V, the peak potential of cycle 5. At this potential, type two deposit was formed without the evolution of any gas, including arsine.

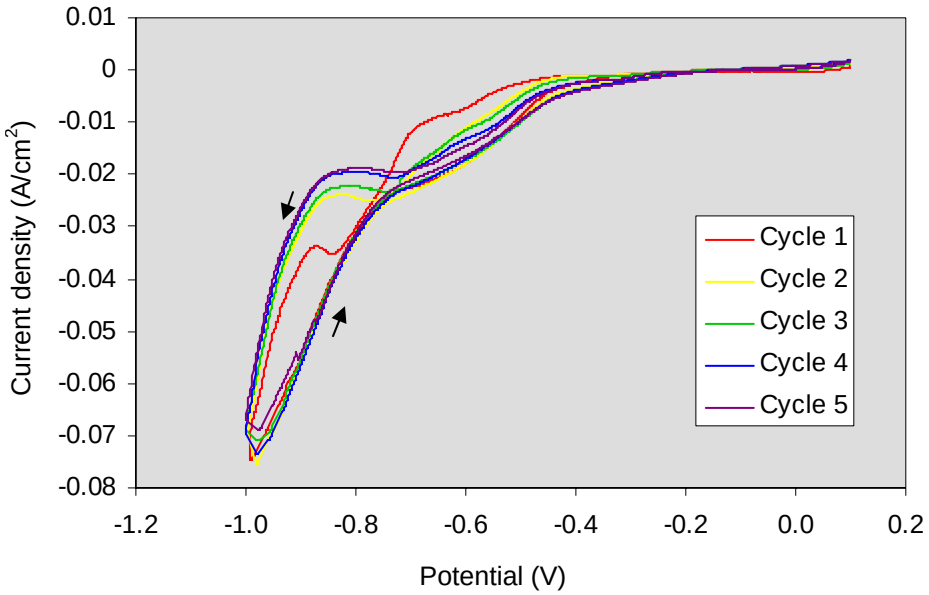

Figure 6-19: Deposition on type one deposit on stainless steel WE from solution C
Scan rate is 10 mV/sec.

Figure 6-20(a) shows the BSE SEM image and (b) shows the GSE SEM image of the type two deposit on a stainless steel working electrode from solution C at -0.72 V. The deposit is small gray compact clumps (55% As, 30% Cr, 15% Cu by atom of total metals) with the stainless steel working electrode occasionally visible as a smooth area in the GSE SEM and a plain white area in the BSE SEM. The few small white clumps in the BSE SEM may be the start of type one deposit since they have a higher Cu percent (50% As, 10% Cr, 40% Cu) than the gray clumps. This mixture of type one and two deposits is similar to Figure 6-14, which is for a deposit on a gold working electrode from solution C, although there is a smaller surface density of the type one deposit in Figure 6-20 than in Figure 6-14.

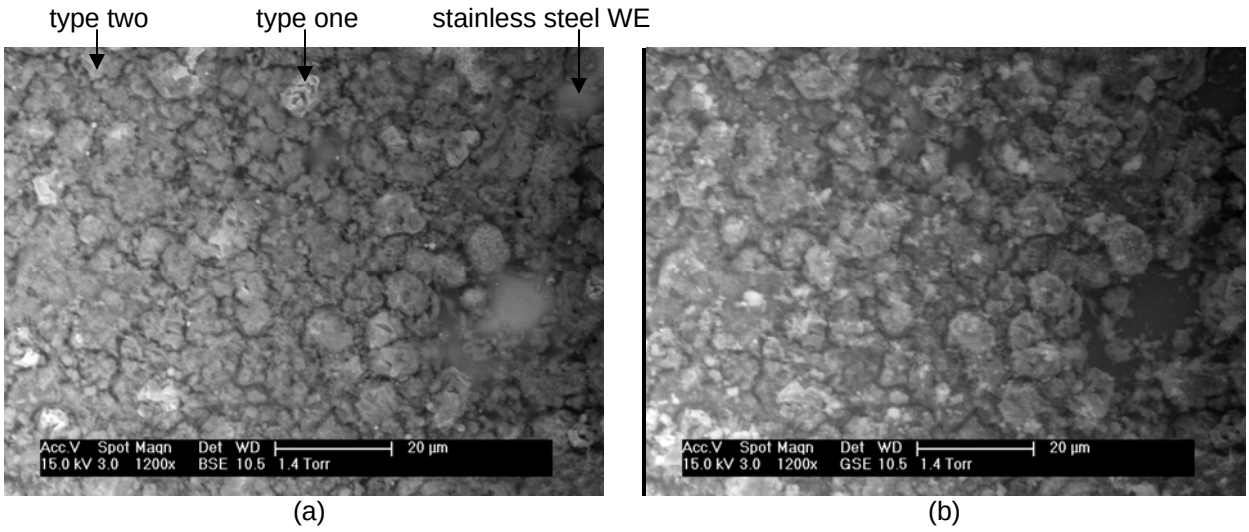

Figure 6-20: SEMs of type two deposit on stainless steel working electrode from solution C
Image (a) is BSE SEM and image (b) is GSE SEM.

A liquid gallium working electrode was studied only with solution B. Type one deposit first occurred at a potential between -0.9 and -1.2 V and arsine evolution did not begin until a potential between -1.2 and -1.5 V.

It appears possible to remove and deposit As, Cr, and Cu from solution B without evolving arsine; however, only type one deposit was observed on the liquid gallium electrode. This type of deposit is rich in copper (45 % total metal by atom of deposit; 10% of CCA type-C) and is a less effective method for arsenic (35% of deposit; 56% of CCA type-C) and chromium (20% of deposit; 34% of CCA type-C) removal from CCA solutions than type two deposit. Due to the absence of type two deposit in the experimental runs with solution B, liquid gallium working electrodes were not used with solution A or C.

Analysis of the type one deposit produced on liquid gallium working electrodes showed similarities with that produced from a copper and arsenic solution (Section 6.2). XRD analysis revealed definitive peaks for Cu_3As (of the type domeykite high) and possible peaks for As and Cr. See Appendix 10.3 for XRD data. XPS analysis was inconclusive as it was for the deposit

from the copper and arsenic solution because not all peaks could be identified from the databases and Cu_3As was not in the databases. Cu and As were good matches to the database values, and $Cu(OH)_2$ and $Cr(OH)_3$ were possible additional matches. See Appendix 10.4 for XPS data.

In Figure 6-21, the DC voltammogram for a liquid gallium electrode in Solution B with a switching potential at -0.9 V is nearly flat and shows no signs of reduction or oxidation of species in solution. After the first cycle of the voltammogram with a switching potential of -1.2 V, significant cathodic activity is visible in the voltammogram. The peak starting at -1 V corresponds to type one deposition and gas evolution.

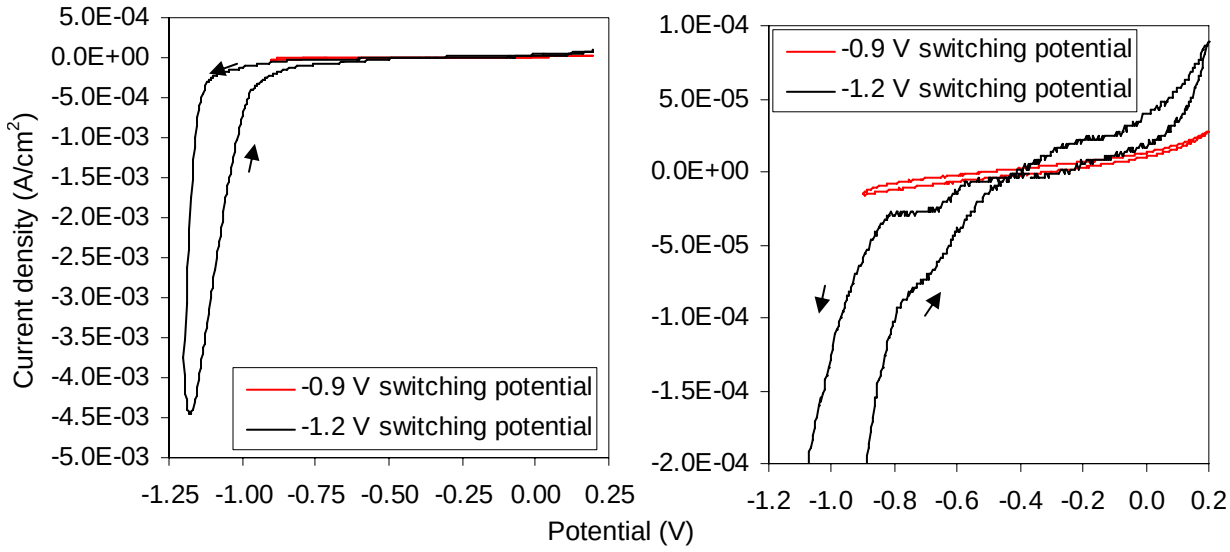

Figure 6-21: Deposition on liquid gallium WE from solution B, higher switching potentials
Scan rate is 10 mV/sec.

A further decrease in the switching potential to -2.5 V, as shown in Figure 6-22, leads to the appearance of the peak at -0.70 V (marked with *) during the anodic sweep. This peak is at a similar potential to the one observed in Figure 6-7 for a type one deposit on gold. The behavior shown in Figure 6-22 lends further credence to the theory that this peak is due to electrochemistry occurring on type one deposit and not on the working electrode surface.

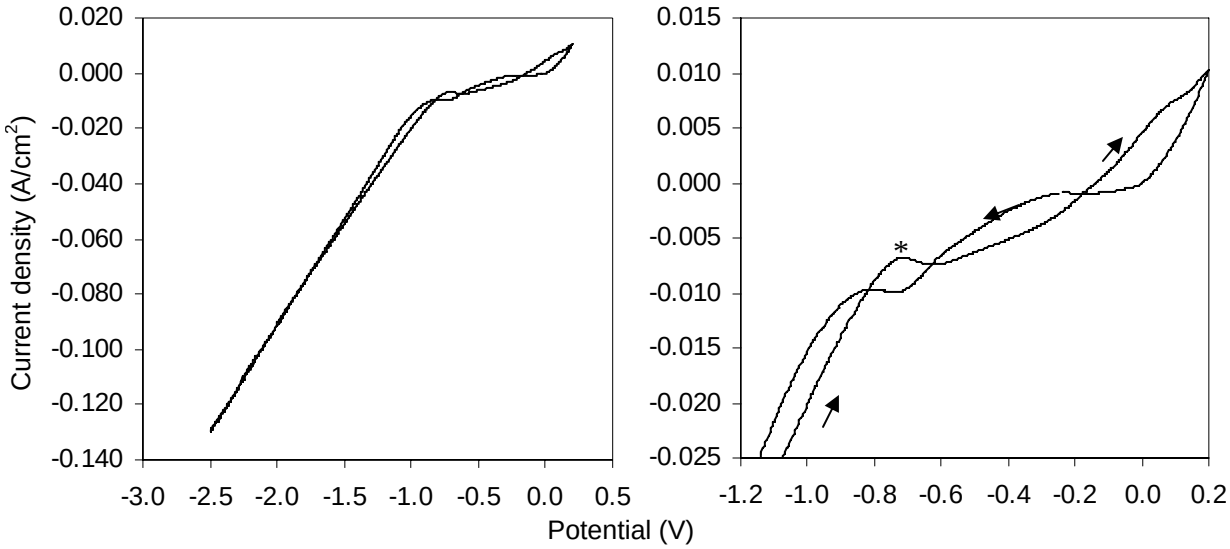

Figure 6-22: Deposition on liquid gallium WE from solution B, lower switching potential
Scan rate is 10 mV/sec.

The BSE SEM image in Figure 6-23 shows closely packed tendrils of deposit. The morphology of this deposit is similar to the general morphology of the deposit shown in the GSE SEM image in Figure 6-3 for codeposition of arsenic and copper on a liquid gallium working electrode and to the morphology of the type one deposit shown in Figure 6-11(b). In all experiments, the deposit was a soft black powder.

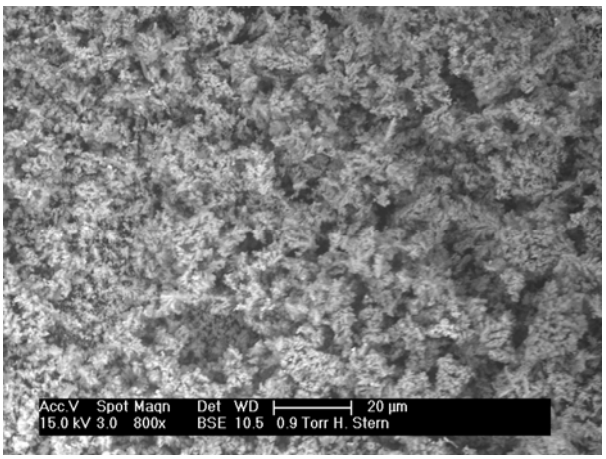

Figure 6-23: BSE SEM image of type one deposited on liquid gallium WE

6.5 Conclusions

As, Cr, and Cu have been successfully deposited from binary and ternary component dilute sulfuric acid solutions. Unlike the deposition of As from a single component solution (Section 5.3), deposition of As with Cu and/or Cr opens up a potential window where arsine is not evolved. Arsine is still evolved at more cathodic potentials along with deposition of As, Cr, and Cu. Three types of deposits were formed from the ternary solution. Deposition from solutions A, B, and C (see Table 6-1 for solution compositions) yielded three types of deposits. The first type, similar to that deposited in the arsenic-copper deposition experiments, was black and sponge-like. It was deposited from all three solutions and contained As (35%), Cr (20%), and Cu (45% of the total metal), with oxygen accounting for about half of the atoms detected. Type one deposit was formed over a narrow potential range from all three solutions without arsine and then with arsine at more cathodic potentials. This type of deposit was formed at a faster rate than the other types. The second type of deposit formed at more anodic potentials than the first type and only from solutions B and C. It changed from medium gray to light-bluish gray upon exposure to air. It contained a different balance of As (60%), Cr (30%), and Cu (10% of the total metal), with oxygen again accounting for about half of the atoms detected, and deposited only on solid electrodes without evolving arsine. Based on appearance, a mixture of type one and two deposits were formed during the arsenic-chromium experiments. The third type of deposit was thin and silvery, deposited as a smooth layer, and was only formed on gold and copper working electrodes. Its deposition was confirmed for solution A and C and was probably also formed from solution B, but the experiments to check for its existence were not performed. Type three was deposited at more anodic potentials than the other two types of deposits and did so without the evolution of any gas. It contained only As (35%) and Cu (65%

total metal) with small amounts of oxygen and was only deposited in very limited quantities. The second type of deposit offers the best method for arsenic, copper, and chromium removal from both solutions B and C since it can be produced in larger quantities than type three, contains a distribution of the metals close to that in CCA type-C, and can be produced without the evolution of arsine.

XRD analysis of the deposit from the arsenic-copper experiments and the type one deposit revealed the presence of Cu_3As (of the type domeykite high). The presence of Cu_3As is consistent with the electrochemical stability analysis from Section 2.1 for mixed copper-arsenic systems. Complete analysis of all of the XRD peaks in the spectrum was not possible due to high levels of background noise from the sample mounting material. There is also a strong possibility that much of the deposit was not crystalline and, therefore, could not be analyzed with XRD.

XPS analysis of the deposits yielded incomplete results because there was not a match in the databases to some of the peaks. The peaks that were identified correspond to As and CuO for the As-Cu solution deposit and to Cu and As for the type one deposit. Cu_3As was not in the database. These peak identifications would be strengthened by collected XPS data on As, CuO, Cu_3As, and other arsenic and copper oxides.

6.6 References

Baraldi, P., E. Soragni, C. Fontanesi and V. Ganzerli (2001). "On the kinetics of chromium electrodeposition on copper electrodes." Journal of Alloys and Compounds **317-318**: 612-618.

Pourbaix, M. (1974). Atlas of Electrochemical Equilibria in Aqueous Solutions. Houston, National Association of Corrosion Engineers.

7 Assessment of Electrolytic CCA Remediation

This phase of the research investigated the feasibility of capturing and removing arsenic, chromium, and copper from three concentrations of model CCA waste solutions (Table 7-1) along with solutions containing one or two-component combinations of CCA waste solutions (Chapters 5 and 6). The behavior of the electrolytic deposition of arsenic, chromium, and copper from these solutions can be used as the foundation for evaluating the engineering feasibility of electrolytic remediation of aqueous CCA wastes.

Table 7-1: Concentration of solutions for arsenic, copper, and chromium codeposition

Solution	Concentration, mM			
	As_2O_5	$CuSO_4$	CrO_3	H_2SO_4
A	4.1	0.77	2.5	0.025
B	41	7.7	25	0.25
C	206	39	125	2.5

One of the basic operating requirements in an electrolytic CCA remediation process would be the avoidance of arsine production. Our research shows that it is possible to deposit all three metals from an aqueous solution over a range of concentrations without producing arsine; however, careful control of the system is necessary to prevent it from moving into an arsine-producing regime. All of the electrode materials tested (copper, gold, 304 stainless steel, liquid gallium) exhibited a range of potentials in which arsenic, chromium, and copper were deposited without the evolution of arsine. Copper working electrodes produced the smallest amount of arsine in comparison to the other electrodes under the same deposition conditions.

Three types of deposits (Section 6.4) were formed from model CCA solutions. Table 7-2 shows a comparison of the atom percents of the components in the model CCA type-C solution to that contained in each type of deposit, rounded to the nearest 5%. The type three deposit is not useful for bulk removal of all the metals because it does not contain chromium and only

forms as a thin layer on the electrode surface. Both type one and type two deposits were formed in more substantial quantities, contained all three components, and, under a limited potential range (usually from the potential at which the deposit first formed to 0.2±0.1 V lower), formed without the evolution of arsine. Type two deposit most closely matches the composition of the CCA type-C solution, which makes it the best candidate for bulk removal of all three metals. Type one could also be employed for CCA removal, but extra copper would probably have to be added to the solution to achieve more complete and efficient removal of arsenic and chromium.

Table 7-2: Atom percent of As, Cr, and Cu in CCA type-C and the three deposit types

	CCA Type-C	Type One	Type Two	Type Three
Arsenic	55	35	60	35
Chromium	35	20	30	0
Copper	10	45	10	65

The concentration of the CCA solution played an important role in the electrolytic deposition of arsenic, chromium, and copper. The threshold potential for deposition became more cathodic as the concentration of the solution decreased. Type two deposit was formed only from solutions B and C, the more concentrated solutions, and not from solution A. The only type of deposit that was formed in more than trace amounts from solution A was type one. Formation of type one deposit from solution A was observed only after the start of hydrogen evolution whereas deposition of type two material in solutions B and C could be observed before the evolution of any visible gas. Thus, the efficiency of the deposition (percent of total current that produces a deposit) was significantly less (<50% of max observed) for deposition from solution A than from solutions B and C. Power in a deposition process is also lost due to the potential drop caused by forcing a current to pass through a resistive bulk solution. This power loss is minimized by decreasing the solution resistance, which is usually accomplished by depositing from a concentrated solution. Therefore, an electrolytic CCA remediation process would

perform more efficiently using high concentration solutions (solution C) rather than low (solution A).

Removal rate of CCA from solution C via type two deposit on a copper electrode can be estimated from peak current (at -0.66 V) in Figure 6-8 and the type two composition in Table 7-2 to be 8 hr to deposit 1 kg on a one square meter electrode assuming 100% current efficiency. When solution C is changed to solution A (Figure 6-6), type one deposit would form at a rate of 63 hr per kg per square meter assuming 100% current efficiency. Thus, the rate of deposition drops by a factor of about 8 when the solution concentration drops by a factor of 50.

The results from this study indicate that CCA remediation via electrolytic deposition of arsenic, chromium, and copper is probably feasible from an engineering standpoint. The second part of the remediation process would be processing the deposits into reusable materials, such as pure arsenic, chromium, and copper. The deposits need to be more fully characterized before a refining process can be designed and evaluated.

8 Conclusions

The underlying engineering science for remediation of aqueous CCA wastes via electrolytic deposition of neutral arsenic, chromium, and copper was developed as a major focus of this research. To that end, electrolytic deposition of arsenic, chromium, and copper from model aqueous CCA wastes was performed and characterized with the following specific contributions.

8.1 Copper sulfate reference electrode

Copper sulfate electrode (CSE) was specially constructed, developed and used as a reference electrode for the electrolytic deposition experiments. Since the deposition experiments were performed in solutions of dilute sulfuric acid, the CSE's copper sulfate and sulfuric acid electrolyte solution was the best compositional match to the deposition solution of the commonly used reference electrodes. The CSE was chosen in order to minimize the liquid junction potential during deposition experiments and to avoid the introduction of contaminating ions into the deposition solutions. The potential of the CSE as a function of temperature over the range of 5 to 45 °C was measured and related to the normal hydrogen electrode (NHE) potential using the saturated calomel reference electrode as intermediary. The variation of potential with temperature (slope of 0.17 ± 0.02 mV/°C) was found to be similar to previously measured values that used slightly different experimental setups (Ewing 1939; Pawel 1998). The value of the CSE in reference to the NHE at 25°C, 317 mV, is bracketed by the commonly accepted values of 316 and 318 mV (Potter 1956; Uhlig and Revie 1985; Jones 1996). Simulation of the CSE electrolyte solution using the ELECNRTL property model was performed to determine the activity of the Cu^{2+} ion and the other charged species in the liquid junction between the CSE and the saturated calomel reference electrode. The aqueous system in the liquid junction region

involved reacting species and concentrated solutions and proved to be too complicated to be modeled accurately using the conventional assumptions employed for this type of analysis.

8.2 Electrochemical stability analysis

The thermodynamically preferred forms of As, Cr, and Cu, in an aqueous system as a function of pH and electrochemical potential were determined using an electrochemical stability analysis of the individual components. The most stable species in each aqueous metal system at the deposition conditions for the other metals were also identified. Stability analysis revealed that codeposition of arsenic and copper would produce Cu_3As, and under the conditions of codeposition of all three metals arsine, a toxic gas, is also produced. Hydrogen would be an additional byproduct of the deposition. The addition of Cu to the As system does not move the As/AsH_3 stability boundary far enough in the negative electrochemical potential direction to allow chromium deposition without arsine evolution.

8.3 Electrolytic deposition

In contradiction of the results of the electrochemical stability analysis, conditions were found experimentally where As, Cr, and Cu were deposited from model aqueous CCA type-C solutions without the formation of arsine or hydrogen. Electrolytic deposition of arsenic, chromium, and copper was performed using working and reference electrodes specially designed and fabricated for this study. Deposition phenomena were investigated using one-, two-, and three-component solutions containing dilute sulfuric acid. Three concentration levels of model CCA type-C solutions (Table 8-1) were investigated on gold, copper, 304 stainless steel, and liquid gallium working electrodes. The results from the one- and two-component deposition experiments were employed to understand the three-component deposition phenomena.

Table 8-1: Concentration of solutions for arsenic, copper, and chromium codeposition

Solution	Concentration, mM			
	As_2O_5	$CuSO_4$	CrO_3	H_2SO_4
A	4.1	0.77	2.5	0.025
B	41	7.7	25	0.25
C	206	39	125	2.5

Three types of deposits were formed at different concentrations and potentials, designated herein as types 1, 2, and 3. Type one and two deposits were shown to contain arsenic, chromium, and copper by EDAX SEM measurements. For all three solutions, at least one of these deposits could be formed without the evolution of arsine. This finding demonstrates the strong influence of kinetics on the deposition system in that the electrochemical stability analysis, which does not include kinetics, predicted that arsine would always be formed when Cu, Cr, and As are deposited together.

The concentration of the CCA solution played an important role in the electrolytic deposition of arsenic, chromium, and copper. The threshold potential for deposition became more cathodic as the concentration of electroactive species decreased. Type two was the most preferred deposit of the three because it contained a ratio of arsenic, chromium, and copper that was close to that of CCA type-C.

Table 8-2: Atom percent of As, Cr, and Cu in CCA type-C and the three deposit types

	CCA Type-C	Type One	Type Two	Type Three
Arsenic	55	35	60	35
Chromium	35	20	30	0
Copper	10	45	10	65

Type two deposit was formed only from solutions B and C. In contrast, type one deposit, which was rich in copper compared to CCA type-C, is the only option for bulk deposition from solution A, the most dilute solution. Thus, the best deposit of the three could be formed only from solutions B and C, which had higher concentrations of the electroactive species. The most

efficient deposition was found to occur from solutions B and C, since hydrogen was the dominant product for solution A. Removal of, chromium, copper, and arsenic was possible for all three solutions studied, but the efficiency of the removal decreased by at least 50% when the concentration of the electroactive species was decreased by a factor of ten (solution A in comparison to solution B).

8.4 Practical implications for CCA remediation

CCA remediation via electrolytic deposition of chromium, copper, and arsenic is probably feasible from an engineering standpoint. The process efficiency increases with concentration due to the increases in current efficiency, deposition rate, and solution conductivity and a reduction in the cathodic potential (more positive potential). Key questions remain about the effect of contaminants, such as potassium and sodium, that are sometimes found in CCA treatment solutions, and the acceptable range of sulfuric acid for the deposition process. The discovery of deposition of all three metals from CCA model solutions without the formation of arsine or hydrogen under certain conditions suggests that conditions for an industrial electrolytic recovery process for CCA wastes can be identified and potentially utilized to develop a practical means for remediation.

8.5 References

Ewing, S. (1939). "The copper-copper sulfate half-cell for measuring potentials in the earth." American Gas Association, Proceedings **21**: 624-634.

Jones, D. A. (1996). Principles and Prevention of Corrosion. Upper Saddle River, NJ, Prentice Hall.

Pawel, S. J., R. J. Lopez and E. Ondak (1998). "Chemical and environmental influences on copper/copper sulfate reference electrode half cell potential." Materials Performance **37**(5): 24-29.

Potter, E. C. (1956). Electrochemistry Principles & Applications. London, Cleaver-Hume Press Ltd.

Uhlig, H. H. and R. W. Revie (1985). Corrosion and Corrosion Control An Introduction to Corrosion Science and Engineering. New York, John Wiley & Sons.

9 Recommendations

While the results of this study have identified some promising methods for electrolytic remediation of CCA wastes, there are several areas where this study would greatly benefit from further inquiry. Key areas are refinement of the copper sulfate electrode modeling, measurement of electrolyte deposition over a wider range of conditions, and detailed characterization of the deposits. Specific suggestions follow for ways to build on and improve the results of this study.

9.1 Copper sulfate electrode modeling

An approach to the calculation of the liquid junction potential that could yield more accurate results than the method employed in this study (Section 3.5) is digital simulation. The general approach is to divide the liquid junction region into small regions in space and simultaneously solve for the concentration and activity of all species in each zone. By using small increments, the controlling equations for the model can be linearized. The digital simulation model should include the ELECNRTL property model, or another appropriate property model for concentrated electrolyte solutions, for the reaction system, the diffusion equations for transport of the species between each section, and the boundary conditions of the composition of the electrolyte solutions at either end of the liquid junction region. A challenging part of the digital simulation would probably be incorporation of the ELECNRTL model since AspenPlus 2004 or other available software do not have an appropriate interface. One way to attempt to work around this problem would be to use commercially available software to find the concentration and activity of all the species in the system for a set of concentrations that span the range of expected values. The results would require a large number of runs to yield detailed data and could be curve fit to multiple species concentrations. The resulting simplified equations for the property model would then be inputted into the digital simulation.

9.2 Electrolytic deposition

A more accurate evaluation of the process feasibility would benefit from additional measurements of the effects of solution concentration and composition on metal deposition. Exploring the role of contaminants, such as potassium and sodium, which are sometimes used in CCA treatment solutions in the deposition process, or other common ions found in soils or ground and surface waters is important as they could severely limit the deposition range and rate. This effect was observed for chromium deposition in this study (Section 5.2). Furthermore, bulk deposition experiments, as opposed to the electro-analytical experiments in this study, would elucidate the effects of decreasing solution concentration over the course of a single experiment, which would more closely mimic processes that would be used at an industrial scale. An important aspect of changing the metal concentration over the course of the remediation process is that the sulfuric-acid-to-chromium ratio could change by several orders of magnitude. Such large changes could severely limit or stop chromium deposition.

9.3 Analysis of the deposits

Characterization of the deposits was controlled by the small amount of each type of deposit that was obtained over the course of the experiments. Elemental compositions were measured with EDAX SEM and the morphology was examined with GSE and BSE detectors using SEM. In order to design and evaluate a process for refining the deposits into reusable materials, such as pure arsenic, chromium, and copper, they need to be more fully characterized. The composition of the deposit is important information for evaluating the recycling options. Bulk deposition would yield a greater quantity of material than currently available for XRD analysis, which would lead to more accurate and less noisy results. XRD analysis would probably be able to determine the compounds present. If XRD fails, then X-ray photoelectron

spectroscopy (XPS) may be able to provide chemical data, but XPS results can be difficult to interpret for a mixed species like the deposits. Knowing bulk properties such as conductivity, density, and maximum thickness of the deposit would also be valuable for designing both a recycling process and the initial bulk deposition process.

10 Appendix

10.1 Symbols

a_i	Activity of species *i*
c_i	Concentration of species *i*, molarity
c_i^*	Bulk concentration of species *i*
$\mathscr{E}$	Electric field strength
E^0	Standard state electrochemical potential
E_i	Electrical potential of electrochemical couple *i* with reference to the NHE unless otherwise noted
E_j	Liquid junction potential
E_λ	Switching potential
$\dot{E}$	AC variation of the potential, phasor quantity
e	Electronic charge (1.60×10^{-19} C)
D_i	Diffusion coefficient of species *i*
f	F/RT
F	Faraday constant, 96485.3 C/mol equivalent
ΔG	Change in Gibbs free energy
I	Total current
I_i	Current due to species *i*
I_D	Diffusion current
$\dot{I}$	AC variation of the current, phasor quantity
k	Rate constant
k^0	Standard rate constant
K_i	Equilibrium constant of species *i*
$\mathfrak{M}_i$	Molecular weight of species *i*, (g/mol)
n	Stoichiometric number of electrons in an electrochemical reaction
P	Pressure
r	Radius of an ion
R	Molar gas constant
T	Temperature
t_i	Transference number of species *i*
u_i	Electronic mobility
v	(a) Linear velocity of solution flow (b) Linear potential scan rate
x	Length
z_i	Electronic charge on species *i*
Z	Impedance
α	Transfer coefficient
γ_i	Activity coefficient of species *i*
η	(a) Viscosity of the medium (b) Overpotential
ν_i	Stoichiometric coefficient in electrochemical reaction

ρ_i Density of species *i*, (kg/m^3)
ϕ Phase angle
ω Angular frequency

10.2 Abbreviations

AC	Alternating current
BPD	Bulk potential deposition
BPS	Bulk potential stripping
CE	Counter electrode
CSE	Copper sulfate electrode
DC	Direct current
EDTA	Ethylenediaminetetraacetic acid
ELECNRTL	Electrolyte Non-Random Two Liquid equation of state
LJP	Liquid junction potential
NHE	Normal hydrogen electrode
RE	Reference electrode
SCE	Saturated calomel electrode
WE	Working electrode
UPD	Underpotential deposition
UPS	Underpotential stripping

10.3 XRD Spectra

Spectrum one is of a deposit formed on a liquid gallium working electrode from a solution of 7.7 mM copper sulfate, 41 mM arsenic pentoxide, and 61 mM sulfuric acid at -2.5 V vs. CSE. Spectrum two is of a deposit formed on a liquid gallium working electrode from a solution of 7.7 mM copper sulfate, 41 mM arsenic pentoxide, 25 mM chromium trioxide, and 0.25 mM sulfuric acid at -1.5 V vs. CSE. The peak at 22 degrees two-theta in both spectra is from the background. The rest of the background was subtracted from the spectra.

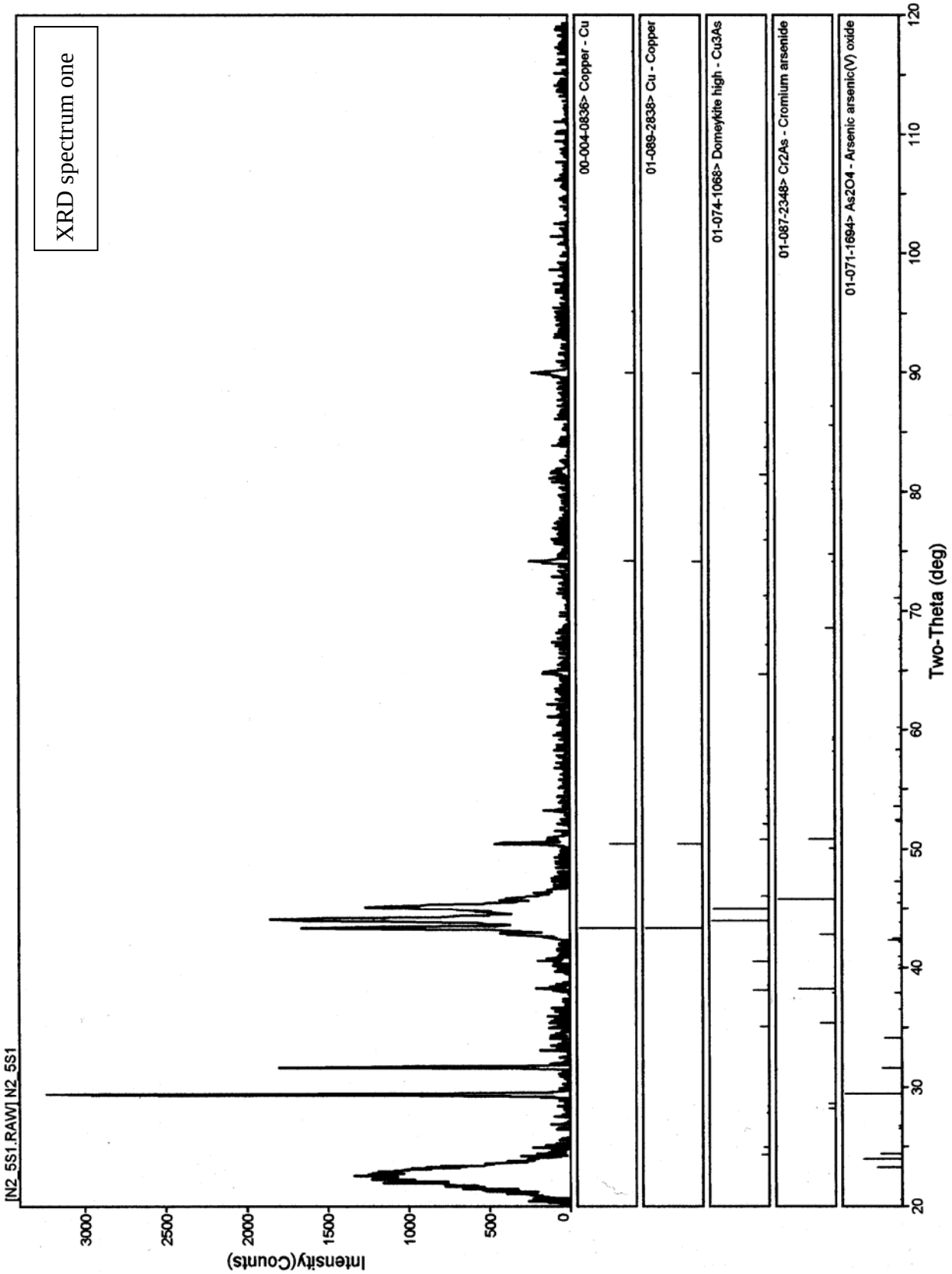
XRD spectrum one
[N2_5S1.RAW] N2_5S1
Intensity(Counts)
3000
2500
2000
1500
1000
500
0
00-004-0836> Copper - Cu
01-089-2838> Cu - Copper
01-074-1068> Domeykite high - Cu3As
01-087-2348> Cr2As - Cromium arsenide
01-071-1694> As2O4 - Arsenic arsenic(V) oxide
20
30
40
50
60
70
80
90
100
110
120
Two-Theta (deg)

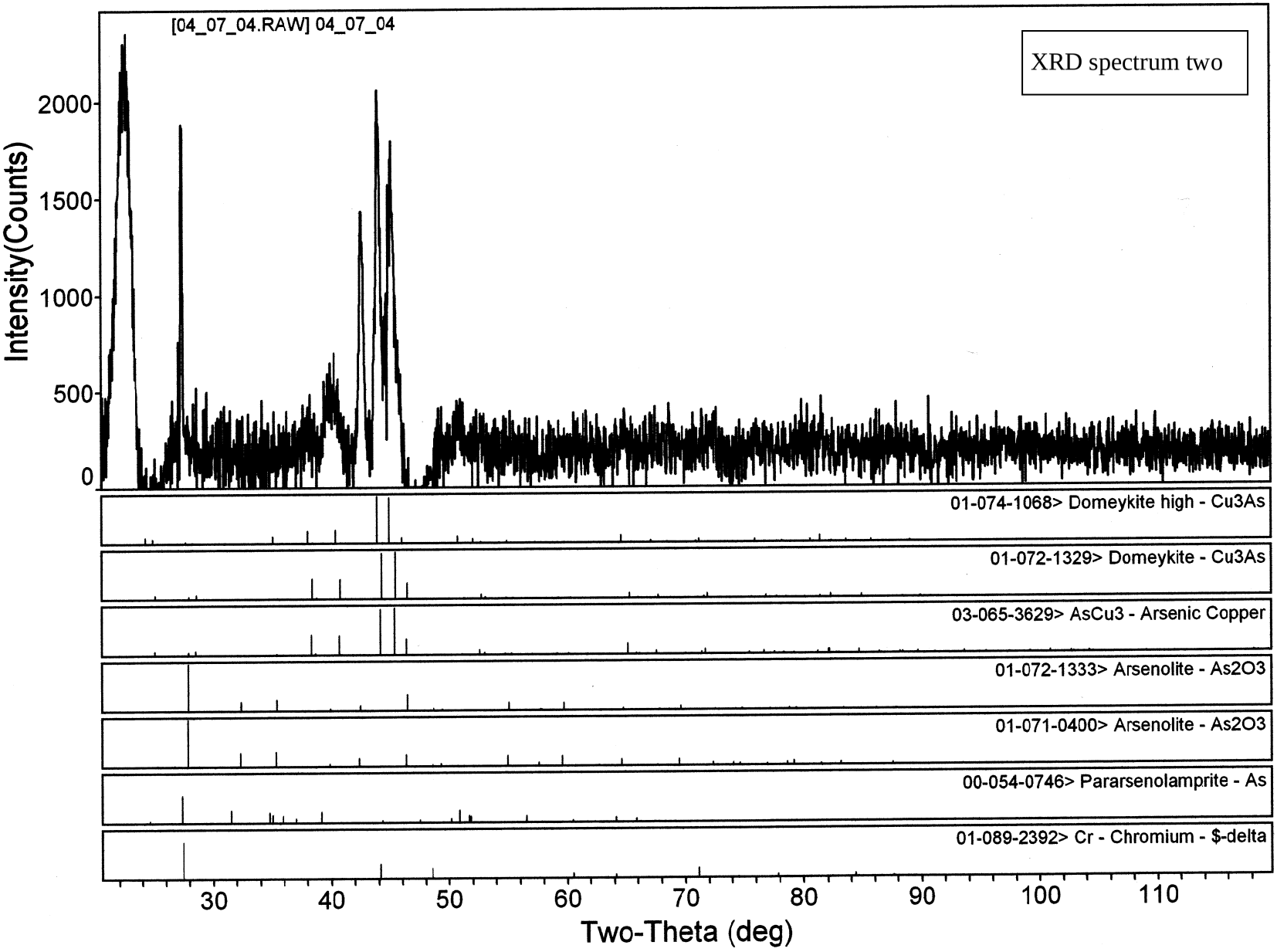
[04_07_04.RAW] 04_07_04
XRD spectrum two
Intensity(Counts)
2000
1500
1000
500
0
01-074-1068> Domeykite high - Cu3As
01-072-1329> Domeykite - Cu3As
03-065-3629> AsCu3 - Arsenic Copper
01-072-1333> Arsenolite - As2O3
01-071-0400> Arsenolite - As2O3
00-054-0746> Pararsenolamprite - As
01-089-2392> Cr - Chromium - $-delta
30
40
50
60
70
80
90
100
110
Two-Theta (deg)

10.4 XPS Spectra

Sample one (spectra three - six) is a mixture of deposits formed on a liquid gallium working electrode from a solution of 7.7 mM copper sulfate, 41 mM arsenic pentoxide, 25 mM chromium trioxide, and 0.25 mM sulfuric acid at -1.5, -2.0 and -2.5 V vs. CSE. Sample two (spectra seven - nine) is a deposit formed on a liquid gallium working electrode from a solution of 7.7 mM copper sulfate, 41 mM arsenic pentoxide, and 61 mM sulfuric acid at -2.5 V vs. CSE. Spectrum one and two are an overview of the XPS spectra of the two samples where S1 = sample one and S2 = sample two. The curve fit of the peaks was done so as to yield the sum of the peaks (dotted line) that most closely matches the data. The carbon peak was used as the internal sample reference.

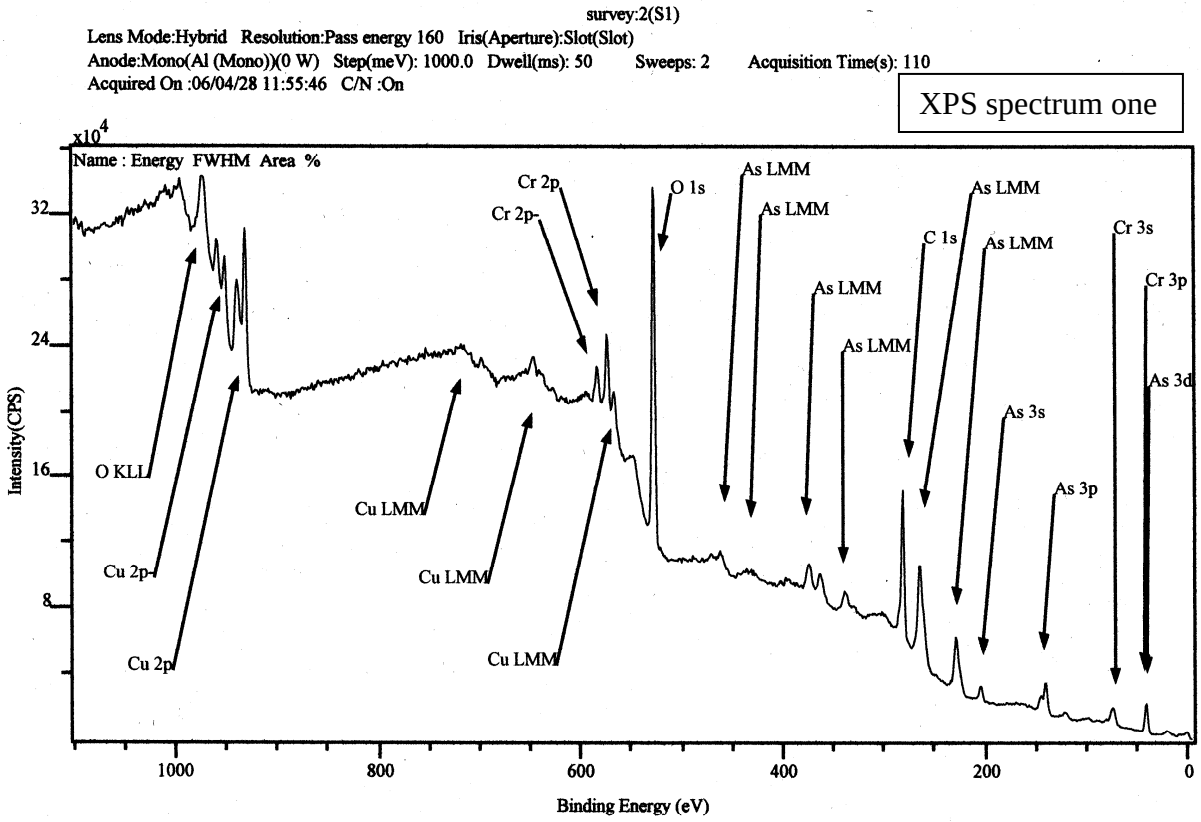
survey:2(S1)
Lens Mode:Hybrid Resolution:Pass energy 160 Iris(Aperture):Slot(Slot)
Anode:Mono(Al (Mono))(0 W) Step(meV): 1000.0 Dwell(ms): 50 Sweeps: 2 Acquisition Time(s): 110
Acquired On :06/04/28 11:55:46 C/N :On
XPS spectrum one
x10^4
Name : Energy FWHM Area %
Intensity(CPS)
Binding Energy (eV)
O KLL
Cu 2p
Cu 2p
Cu 2p
Cu LMM
Cu LMM
Cu LMM
Cr 2p
Cr 2p
O 1s
As LMM
As LMM
As LMM
As LMM
As LMM
As LMM
C 1s
Cr 3s
Cr 3p
As 3d
As 3s
As 3p

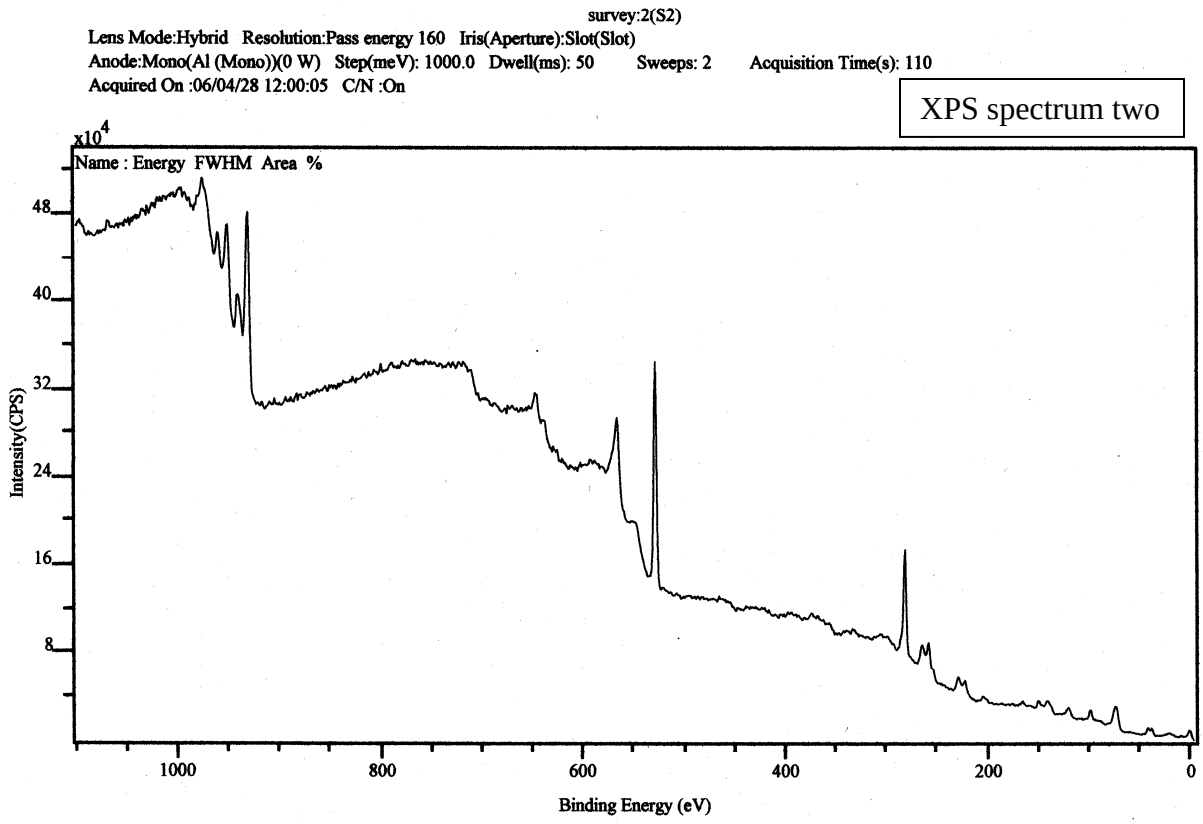
survey:2(S2)
Lens Mode:Hybrid Resolution:Pass energy 160 Iris(Aperture):Slot(Slot)
Anode:Mono(Al (Mono))(0 W) Step(meV): 1000.0 Dwell(ms): 50 Sweeps: 2 Acquisition Time(s): 110
Acquired On :06/04/28 12:00:05 C/N :On
XPS spectrum two
x10^4
Name : Energy FWHM Area %
Intensity(CPS)
Binding Energy (eV)

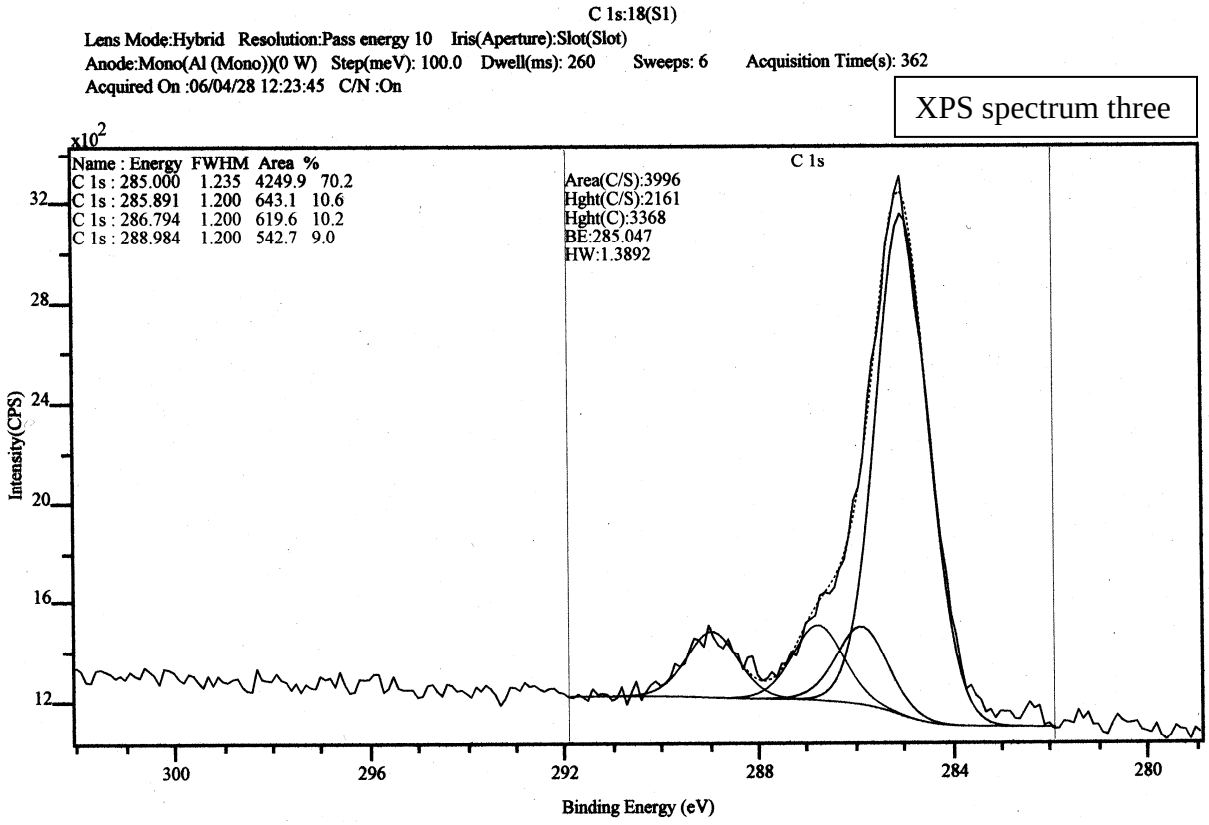
C 1s:18(S1)
Lens Mode:Hybrid Resolution:Pass energy 10 Iris(Aperture):Slot(Slot)
Anode:Mono(Al (Mono))(0 W) Step(meV): 100.0 Dwell(ms): 260 Sweeps: 6 Acquisition Time(s): 362
Acquired On :06/04/28 12:23:45 C/N :On
XPS spectrum three
x10^2
Name : Energy FWHM Area %
C 1s : 285.000 1.235 4249.9 70.2
C 1s : 285.891 1.200 643.1 10.6
C 1s : 286.794 1.200 619.6 10.2
C 1s : 288.984 1.200 542.7 9.0
C 1s
Area(C/S):3996
Hght(C/S):2161
Hght(C):3368
BE:285.047
HW:1.3892
Intensity(CPS)
Binding Energy (eV)

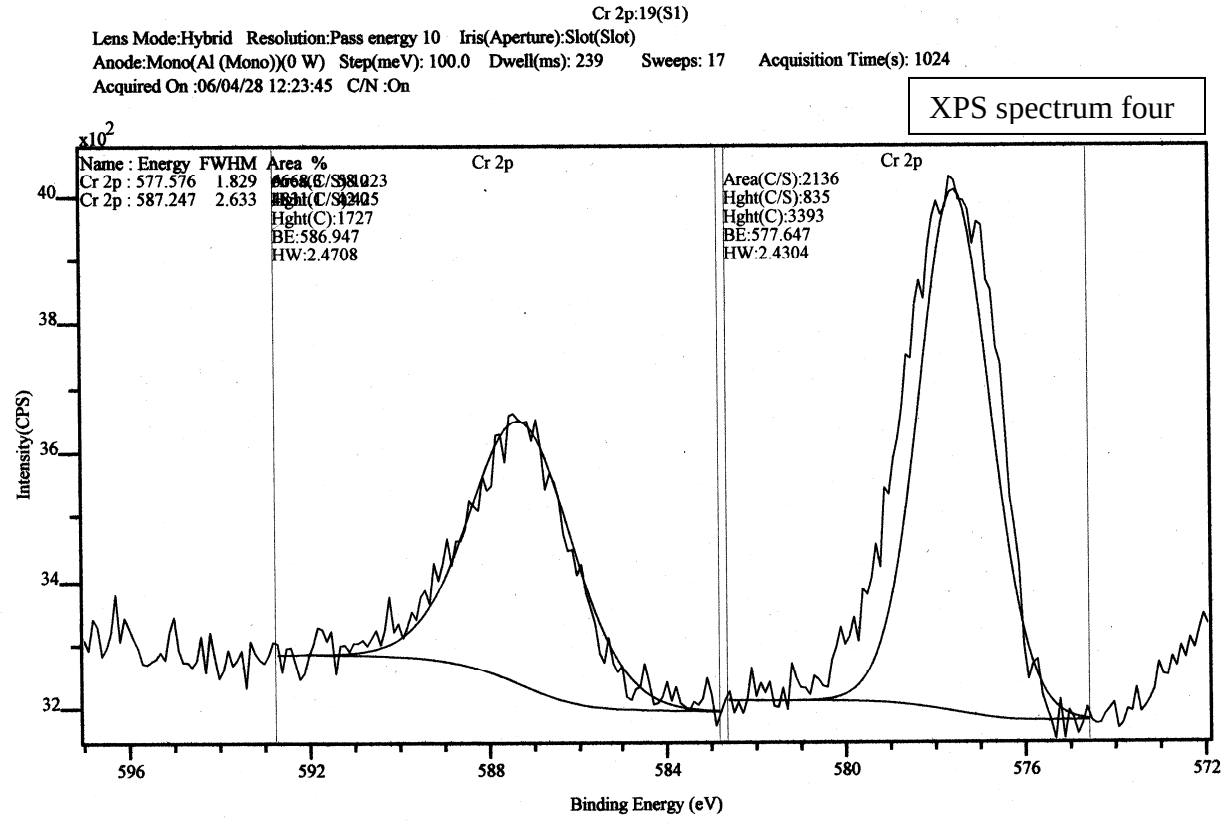
Cr 2p:19(S1)
Lens Mode:Hybrid Resolution:Pass energy 10 Iris(Aperture):Slot(Slot)
Anode:Mono(Al (Mono))(0 W) Step(meV): 100.0 Dwell(ms): 239 Sweeps: 17 Acquisition Time(s): 1024
Acquired On :06/04/28 12:23:45 C/N :On
XPS spectrum four
x10^2
Name : Energy FWHM Area %
Cr 2p : 577.576 1.829
Cr 2p : 587.247 2.633
Cr 2p
Hght(C):1727
BE:586.947
HW:2.4708
Cr 2p
Area(C/S):2136
Hght(C/S):835
Hght(C):3393
BE:577.647
HW:2.4304
Intensity(CPS)
Binding Energy (eV)

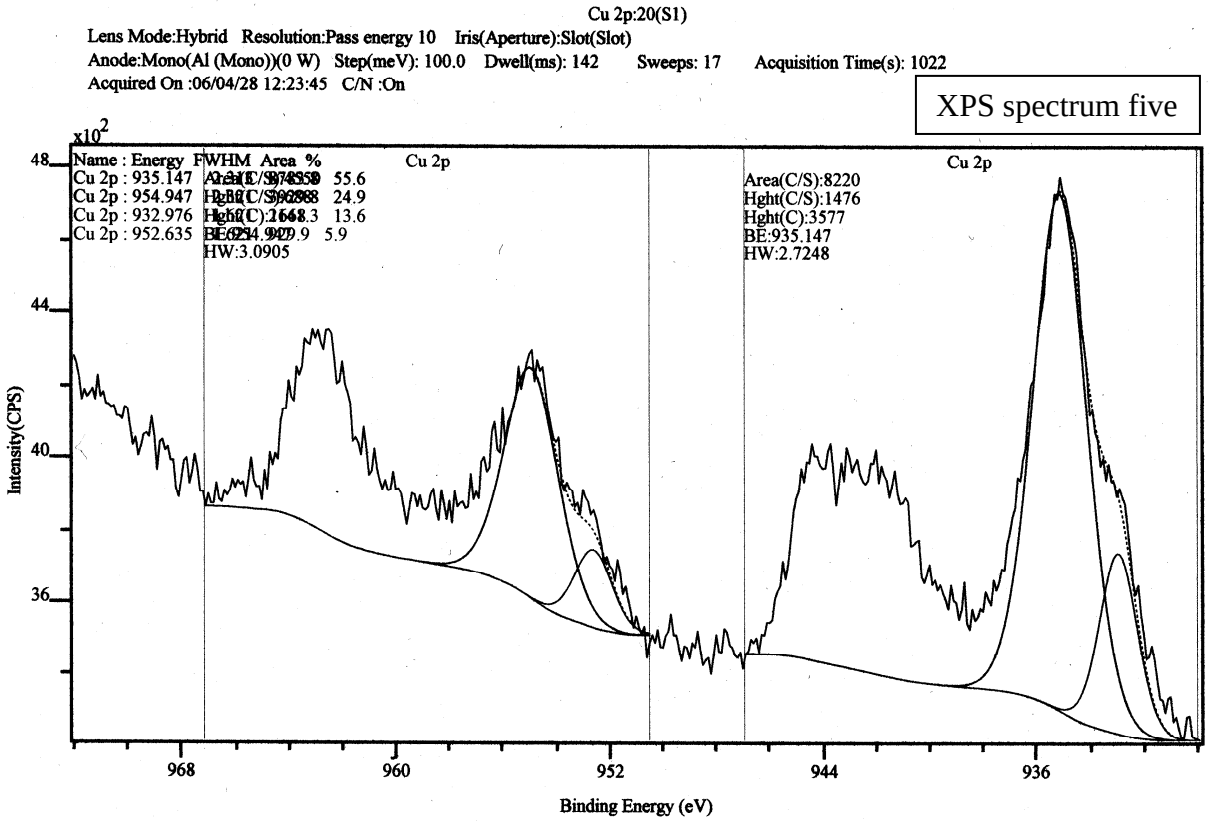
Cu 2p:20(S1)
Lens Mode:Hybrid Resolution:Pass energy 10 Iris(Aperture):Slot(Slot)
Anode:Mono(Al (Mono))(0 W) Step(meV): 100.0 Dwell(ms): 142 Sweeps: 17 Acquisition Time(s): 1022
Acquired On :06/04/28 12:23:45 C/N :On
XPS spectrum five
x10^2
Name : Energy FWHM Area %
Cu 2p : 935.147
Cu 2p : 954.947
Cu 2p : 932.976
Cu 2p : 952.635
HW:3.0905
Cu 2p
Area(C/S):8220
Hght(C/S):1476
Hght(C):3577
BE:935.147
HW:2.7248
Intensity(CPS)
Binding Energy (eV)

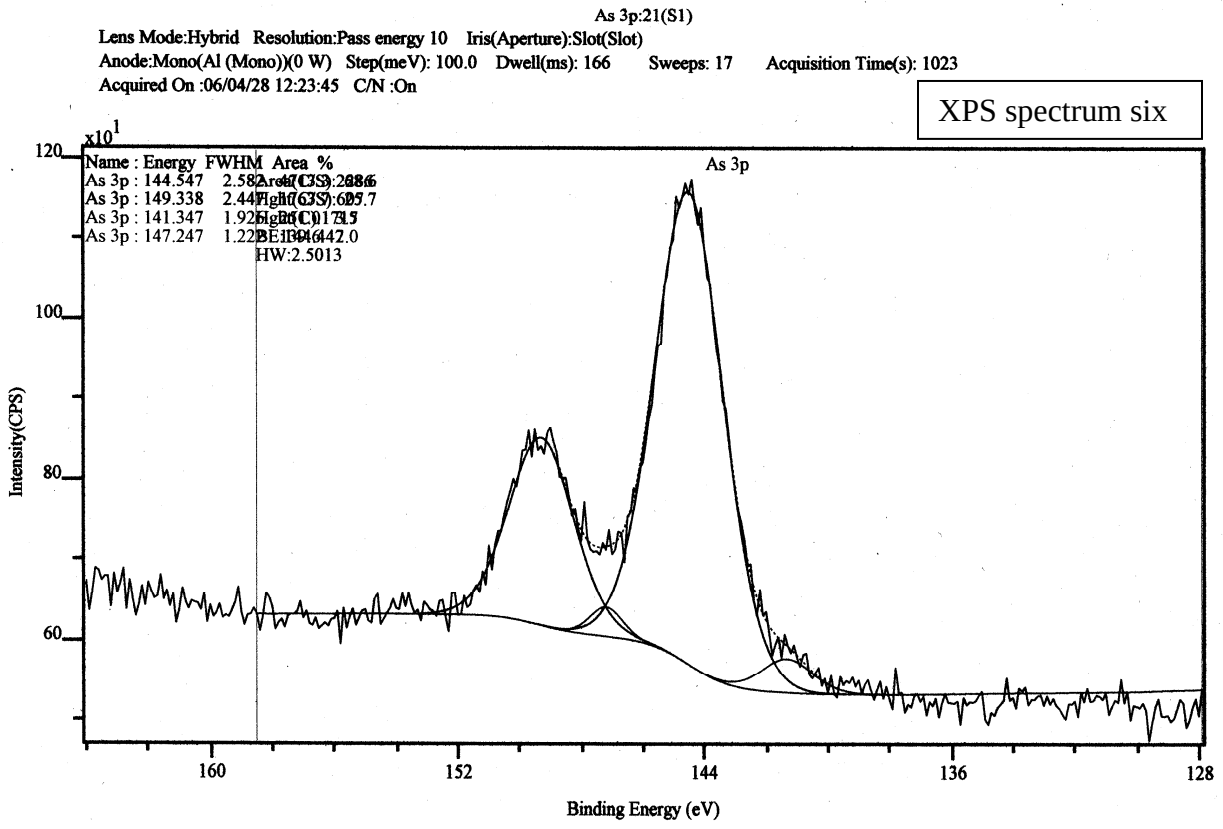
As 3p:21(S1)
Lens Mode:Hybrid Resolution:Pass energy 10 Iris(Aperture):Slot(Slot)
Anode:Mono(Al (Mono))(0 W) Step(meV): 100.0 Dwell(ms): 166 Sweeps: 17 Acquisition Time(s): 1023
Acquired On :06/04/28 12:23:45 C/N :On
XPS spectrum six
x10^1
Name : Energy FWHM Area %
As 3p : 144.547 2.582
As 3p : 149.338 2.447
As 3p : 141.347 1.925
As 3p : 147.247 1.22
HW:2.5013
As 3p
Intensity(CPS)
Binding Energy (eV)

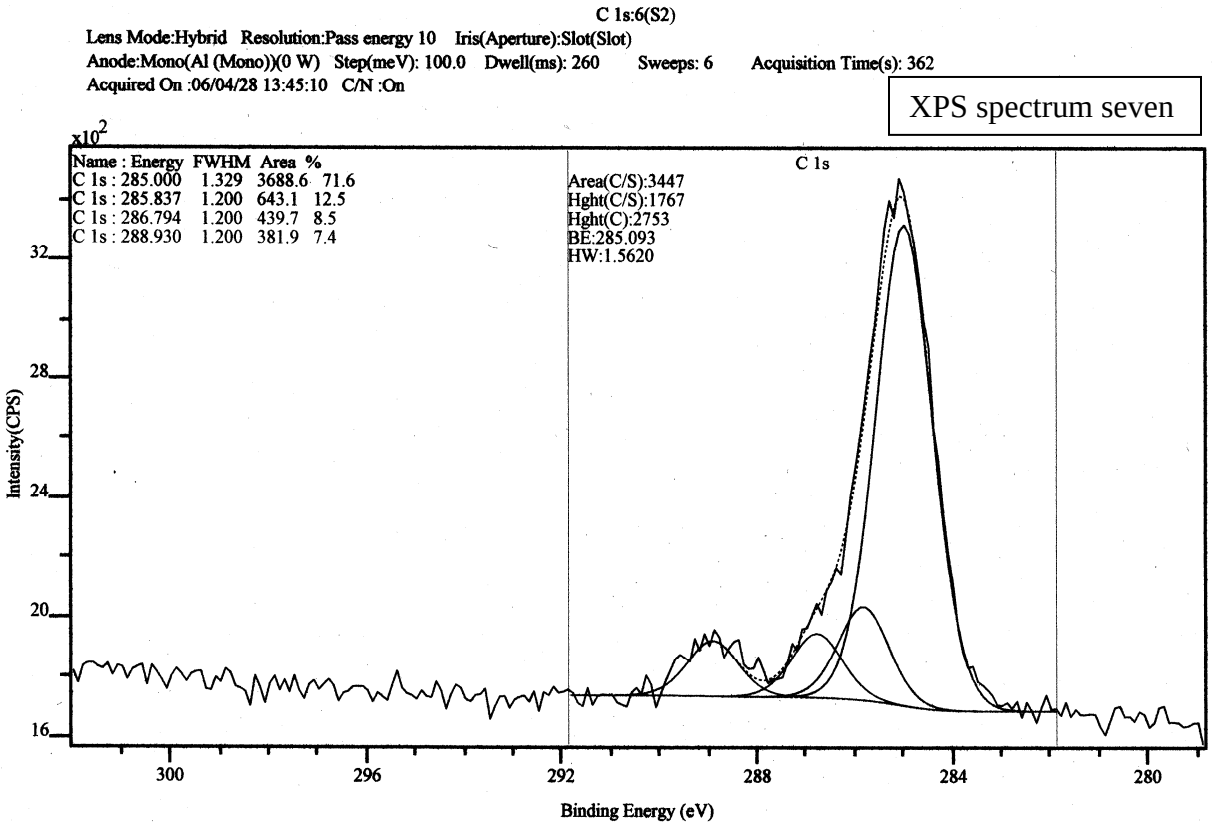
C 1s:6(S2)
Lens Mode:Hybrid Resolution:Pass energy 10 Iris(Aperture):Slot(Slot)
Anode:Mono(Al (Mono))(0 W) Step(meV): 100.0 Dwell(ms): 260 Sweeps: 6 Acquisition Time(s): 362
Acquired On :06/04/28 13:45:10 C/N :On
XPS spectrum seven
x10^2
Name : Energy FWHM Area %
C 1s : 285.000 1.329 3688.6 71.6
C 1s : 285.837 1.200 643.1 12.5
C 1s : 286.794 1.200 439.7 8.5
C 1s : 288.930 1.200 381.9 7.4
C 1s
Area(C/S):3447
Hght(C/S):1767
Hght(C):2753
BE:285.093
HW:1.5620
Intensity(CPS)
Binding Energy (eV)

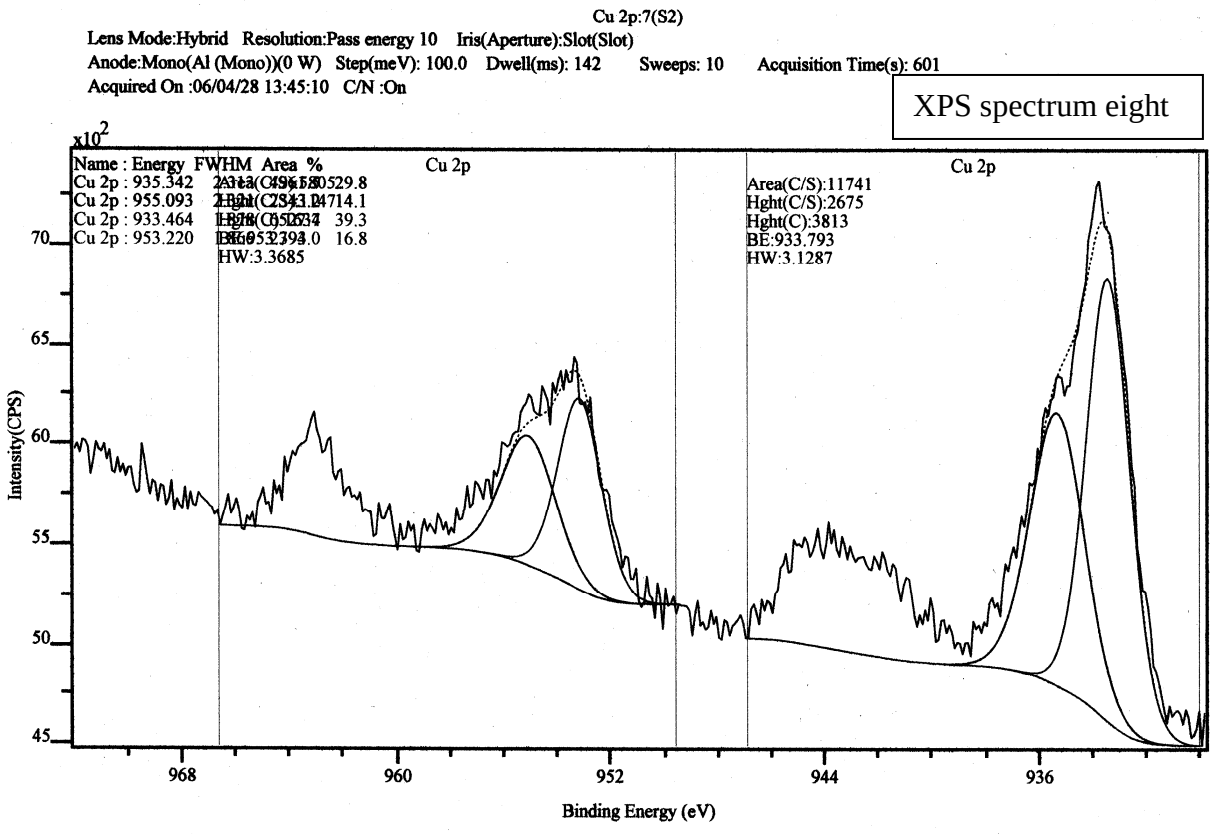
Cu 2p:7(S2)
Lens Mode:Hybrid Resolution:Pass energy 10 Iris(Aperture):Slot(Slot)
Anode:Mono(Al (Mono))(0 W) Step(meV): 100.0 Dwell(ms): 142 Sweeps: 10 Acquisition Time(s): 601
Acquired On :06/04/28 13:45:10 C/N :On
XPS spectrum eight
x10^2
Name : Energy FWHM Area %
Cu 2p : 935.342
Cu 2p : 955.093
Cu 2p : 933.464
Cu 2p : 953.220
HW:3.3685
Cu 2p
Cu 2p
Area(C/S):11741
Hght(C/S):2675
Hght(C):3813
BE:933.793
HW:3.1287
Intensity(CPS)
Binding Energy (eV)

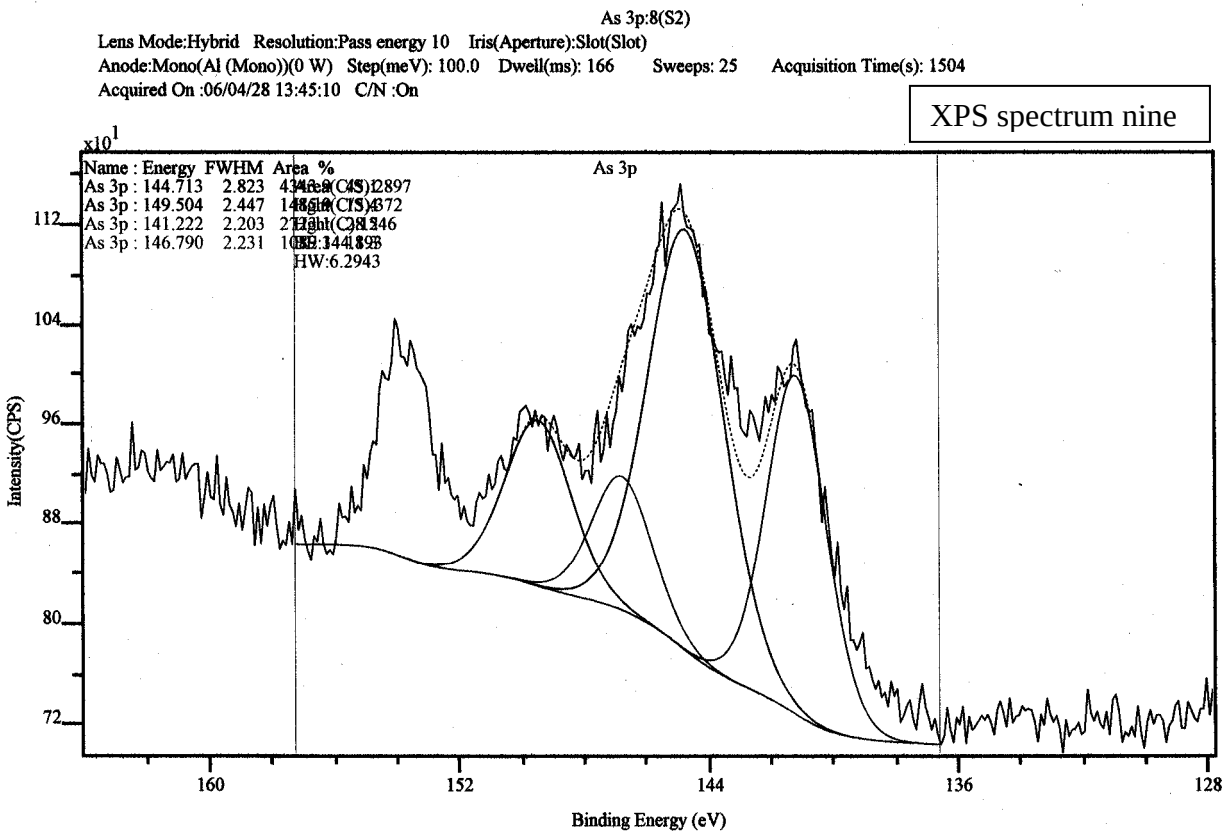
As 3p:8(S2)
Lens Mode:Hybrid Resolution:Pass energy 10 Iris(Aperture):Slot(Slot)
Anode:Mono(Al (Mono))(0 W) Step(meV): 100.0 Dwell(ms): 166 Sweeps: 25 Acquisition Time(s): 1504
Acquired On :06/04/28 13:45:10 C/N :On
XPS spectrum nine
x10^1
Name : Energy FWHM Area %
As 3p : 144.713 2.823
As 3p : 149.504 2.447
As 3p : 141.222 2.203
As 3p : 146.790 2.231
As 3p
HW:6.2943
Intensity(CPS)
112
104
96
88
80
72
160
152
144
136
128
Binding Energy (eV)